UNIVERSIDADE ESTADUAL DE CAMPINAS
Faculdade de Engenharia Mecânica

DOUGLAS DANIEL DE CARVALHO

Motion of intruders in granular media

Movimento de intrusos em meios granulares

Campinas

2024

DOUGLAS DANIEL DE CARVALHO

Motion of intruders in granular media

Movimento de intrusos em meios granulares

Doctoral Thesis presented to the Faculdade de Engenharia Mecânica of the Universidade Estadual de Campinas as part of the requirements for obtaining the title of Doctor of Philosophy in Mechanical Engineering, in the Area Thermal and Fluids.

Tese de Doutorado apresentada à Faculdade de Engenharia Mecânica da Universidade Estadual de Campinas como parte dos requisitos exigidos para a obtenção do título de Doutor em Engenharia Mecânica, na Área de Térmica e Fluidos.

Orientador: Prof. Dr. Erick de Moraes Franklin

ESTE TRABALHO CORRESPONDE À VERSÃO FINAL DA TESE DE DOUTORADO DEFENDIDA PELO ALUNO DOUGLAS DANIEL DE CARVALHO, E ORIENTADA PELO PROF. DR. ERICK DE MORAES FRANKLIN.

Campinas

2024

Ficha catalográfica
Universidade Estadual de Campinas (UNICAMP)
Biblioteca da Área de Engenharia e Arquitetura
Rose Meire da Silva - CRB 8/5974

C253m
Carvalho, Douglas Daniel de, 1991-
Motion of intruders in granular media / Douglas Daniel de Carvalho. – Campinas, SP : [s.n.], 2024.

Orientador(es): Erick de Moraes Franklin.
Tese (doutorado) – Universidade Estadual de Campinas (UNICAMP), Faculdade de Engenharia Mecânica.

1. Materiais granulados. 2. Materiais granulados - Microestrutura. 3. Materiais granulados - Propriedades mecânicas. 4. Fluxo granular. 5. Matéria mole e granular, fluidos complexos e microfluídica. 6. Crateras de impacto. 7. Método dos elementos discretos. I. Franklin, Erick de Moraes, 1974-. II. Universidade Estadual de Campinas (UNICAMP). Faculdade de Engenharia Mecânica. III. Título.

Informações complementares

Título em outro idioma: Movimento de intrusos em meios granulares
Palavras-chave em inglês:
Granular materials
Granular materials - Microstructure
Granular materials - Mechanical properties
Granular flow
Soft and granular matter, complex fluids and microfluidics
Impact craters
Discrete element method
Área de concentração: Térmica e Fluídos
Titulação: Doutor em Engenharia Mecânica
Banca examinadora:
Erick de Moraes Franklin [Orientador]
Antoine Seguin
Baptiste Darbois Texier
Yuri Dumaresq Sobral
Rafael Gabler Gontijo
Data de defesa: 18-12-2024
Programa de Pós-Graduação: Engenharia Mecânica

Identificação e informações acadêmicas do(a) aluno(a)
- ORCID do autor: https://orcid.org/0000-0003-2426-8928
- Currículo Lattes do autor: http://lattes.cnpq.br/6073161093351917

UNIVERSIDADE ESTADUAL DE CAMPINAS
FACULDADE DE ENGENHARIA MECÂNICA

TESE DE DOUTORADO ACADÊMICO

Motion of intruders in granular media

Movimento de intrusos em meios granulares

Autor: Douglas Daniel de Carvalho
Orientador: Prof. Dr. Erick de Moraes Franklin

A Banca Examinadora composta pelos membros abaixo aprovou esta Tese de Doutorado:

Prof. Dr. Erick de Moraes Franklin, Presidente
Universidade Estadual de Campinas (UNICAMP)

Prof. Dr. Antoine Seguin
Université Paris-Saclay - FAST (Fluides, Automatique et Systèmes Thermiques)

Dr. Baptiste Darbois Texier
Université Paris-Saclay - FAST (Fluides, Automatique et Systèmes Thermiques)

Prof. Dr. Yuri Dumaresq Sobral
Universidade de Brasília (UnB)

Prof. Dr. Rafael Gabler Gontijo
Universidade de Brasília (UnB)

A Ata de Defesa com as respectivas assinaturas dos membros encontra-se no SIGA/Sistema de Fluxo de Dissertação/Tese e na Secretaria do Programa da Unidade.

Campinas, 18 de dezembro de 2024

DEDICATION

To my beloved family, the main strings of my life, whose unwavering support has provided harmony throughout this long journey. Like the finely tuned strings of an instrument, each of you resonates in a unique way — some firm and steady, others loose and soft — but together, you create the melody that keeps me balanced and functioning. José, Wilma, Maycon, Jhonie, and Alice, without your love, encouragement, and belief in me, this work would have been impossible. You are the foundation that has sustained me through the many ups and downs, through all the challenges and triumphs. Thank you so much, I love you!

To R. F. M., for being a part of this journey. Our time together has shaped many moments of growth, and I am grateful for the lessons learned, all the moments spent together, and the experiences and love we have shared along the way. You will always be remembered!

To the artists whose creations have helped me endure the long hours. Your art has been a refuge, an escape, and a source of inspiration when I needed it most. You have shown me that creativity, in all its forms, is vital to sustaining the human spirit.

And finally, to all who dedicate their time to the pursuit of science and art, for it is through your tireless work that the world becomes a little brighter, a little more bearable, and a little more understandable every single day. Your contributions, no matter how great or small, are the threads that weave the fabric of progress and beauty in our world. This work is as much yours as it is mine.

ACKNOWLEDGEMENTS

I would like to thank my friends, whose laughter, advice, and companionship were the melody that filled the quiet spaces, offering solace when the road seemed long and winding (sorry Sir Paul McCartney, but I had to use those verses somewhere). Old friends who have always been a constant presence (Mineiros, Candangos, and Cariocas) and new friends I have made along the way (Brazilians, Ecuadorians, French, and Chileans), thank you for reminding me that life outside of work is just as (if not more) important, and for walking alongside me on this adventure.

To my colleagues and collaborators, thank you for your collaboration, insight, and the shared moments of struggle and joy that have helped me refine my work. Whether in the lab, in the office, or in conversation, your ideas and efforts have enriched this project in countless ways. Also thanks to the technical team, for your tireless efforts to ensure that the tools of my research were always in perfect harmony. Your work behind the scenes has allowed science to flow smoothly (at least most of the time), and for that I am deeply grateful.

Thanks to my professors, for sharing your vast knowledge and instilling in me the curiosity to ask bigger, more complex questions. Your lessons have been the foundation on which this Thesis stands. Special thanks to my M.Sc. advisor, Rafael Gontijo, for all the inspiration given throughout the years. Many thanks to my supervisors, for their patience, guidance, and unwavering belief in me: Antoine Seguin, Baptiste Texier, and Yann Bertho, thank you so much, you have pushed me beyond what I thought I was capable of and helped me navigate the many complexities of this field. I will always be grateful for your teachings. And finally, I would like to express my deepest gratitude to my advisor, Erick Franklin, for being a constant source of support and guidance throughout my research journey. The lessons you have taught me as a student have been invaluable. Your presence at the many conferences we attended together was always a reassuring constant, and I deeply appreciate how you encouraged my growth in the scientific community. From long discussions in the lab to sharing moments outside of work, your companionship has made this journey all the more meaningful. Thank you for not only being a mentor, but also a friend who was always there when I needed it.

This study was financed in part by the São Paulo Research Foundation (FAPESP), grants No. 2020/04151-7 and No. 2022/12511-9.

RESUMO

Esta Tese explora a dinâmica de materiais granulares na presença de objetos sólidos (intrusos). A interação entre intrusos e materiais granulares ocorre frequentemente na natureza e na indústria, desde a preparação do solo para práticas agrícolas até a formação de crateras devido a impactos de meteoros. A pesquisa apresentada aqui emprega uma combinação de simulações numéricas, investigações experimentais e modelagem matemática para fornecer novos insights sobre essas interações complexas.

Na primeira parte do estudo, investigamos o movimento de intrusos se movendo em baixas velocidades, em um regime quase estático. Começamos estudando numericamente o comportamento de um sistema granular (pequenos discos) deslocado por um intruso em movimento (disco maior). Analisamos as forças resultantes no intruso e a rede de forças de contato instantâneas na escala dos grãos. Nossas descobertas revelam uma rede de sustentação distinta que transmite grandes forças do intruso em direção às paredes, causando bloqueio localizado e altas forças de arrasto, e uma rede dissipativa que carrega forças menores. Além disso, desvendamos o mecanismo de colapso das redes de sustentação. O comportamento de múltiplos intrusos se movendo juntos em tal meio também é investigado. Ao simular grupos de intrusos com configurações iniciais variadas, descobrimos que eles exibem um comportamento cooperativo, com uma distância ótima entre eles para a qual o arrasto é mínimo, o que tem implicações práticas para projetar dispositivos que interagem com superfícies granulares, como máquinas de aração. Também identificamos padrões de comportamento de intrusos associados ao seu arranjo inicial no espaço. Experimentalmente, investigamos como as forças de arrasto em pares de intrusos esféricos variam com sua separação transversal e profundidade dentro de um leito granular. Nossos resultados indicam um efeito cooperativo que reduz o arrasto médio em cada intruso quando eles estão próximos, e que essa redução relativa de arrasto aumenta com a profundidade. Propomos um modelo fenomenológico baseado na quebra de redes de contato para modelar essas observações.

Na segunda parte desta Tese, exploramos o movimento de intrusos se movendo em velocidades mais altas, no chamado regime colisional. Começamos explorando numericamente a formação de crateras por projéteis esféricos (intrusos) impactando um leito granular, focando nos efeitos da fração de empacotamento, atrito entre os grãos e rotação do projétil. Descobrimos que, embora o diâmetro da cratera permaneça inalterado pela fração de empacotamento, a profundidade de penetração é significativamente influenciada por ela, levando à proposição de uma lei de escala *ad hoc* para unificar as correlações existentes para a profundidade de penetração. Em seguida, exploramos numericamente o impacto de projéteis granulares rotativos (agregados), focando nos efeitos das tensões de ligação e rotações iniciais. Descobrimos que, à medida que as tensões de ligação diminuem e a rotação inicial aumenta, os grãos do projétil se espalham para mais longe do ponto de impacto, levando a crateras mais planas com picos distintos na borda e no centro, fornecendo insights sobre os formatos de crateras geralmente observados na natureza. Finalmente, o impacto de projéteis rotativos é examinado experimentalmente, mostrando que a velocidade rotacional aumenta a profundidade de penetração. Um modelo atualizado incorporando efeitos rotacionais fornece uma lei de escala refinada para a profundidade de penetração, com aplicações potenciais em engenharia geotécnica e exploração planetária. Desta forma, esta Tese contribui para uma compreensão mais profunda da dinâmica da interação entre materiais granulares e intrusos, oferecendo insights valiosos para aplicações teóricas e práticas.

Palavras–chave: Materiais granulares, Intrusos sólidos, Regime quase estático, Forças de contato, Redução de arrasto, Comportamento cooperativo, Regime colisional, Formação de crateras, Projéteis rotativos, Profundidade de penetração.

ABSTRACT

This Thesis explores the dynamics of granular materials in the presence of solid objects (intruders). Interaction between intruders and granular materials occurs frequently in nature and industry, from soil preparation for agricultural practices to crater formation due to meteor impacts. The research presented here employs a combination of numerical simulations, experimental investigations, and mathematical modeling to provide new insights into these complex interactions.

In the first part of the study, we investigate the motion of intruders moving at low velocities, in a quasi-static regime. We begin by numerically studying the behavior of a granular system (small disks) displaced by a moving intruder (larger disk). We analyze the resulting forces on the intruder and the network of instantaneous contact forces at the grain scale. Our findings reveal a distinct load-bearing network that transmits large forces from the intruder toward the walls, causing localized jamming and high drag forces, and a dissipative network that carries smaller forces. Furthermore, we uncover the mechanism of the collapse of bearing chains. The behavior of multiple intruders moving together in such a media is also investigated. By simulating groups of intruders with varying initial configurations, we find that they exhibit a cooperative behavior, with an optimal distance between them for which the drag is minimum, which has practical implications for designing devices that interact with granular surfaces, such as plowing machines. We also identify patterns of intruder behavior associated with their initial arrangement in space. Experimentally, we investigate how the drag forces on pairs of spherical intruders vary with their transverse separation and depth within a granular bed. Our results indicate a cooperative effect that reduces the average drag on each intruder when they are close together, and that this relative drag reduction increases with depth. We propose a phenomenological model based on the breaking of contact chains to model these observations.

In the second part of this Thesis, we explore the motion of intruders moving at higher velocities, in the so-called collisional regime. We start by numerically exploring the formation of craters by spherical projectiles (intruders) impacting a granular bed, focusing on the effects of packing fraction, grain friction, and projectile spin. We find that while the crater diameter remains unaffected by the packing fraction, the penetration depth is significantly influenced by it, leading to the proposition of an *ad hoc* scaling law to unify existing correlations for penetration depth. We then explore numerically the impact of projectiles consisting of aggregated particles, focusing on the effects of bond stresses and initial spins. We find that as bond stresses decrease and initial spin increases, projectile grains spread further away from the impact point, leading to flatter craters with distinct peaks at the rim and center, providing insights into crater shapes usually observed in nature. Finally, the impact of rotating projectiles is examined experimentally, showing that rotational velocity increases penetration depth. An updated model incorporating rotational effects provides a refined scaling law for penetration depth, with potential applications in geotechnical engineering and planetary exploration.

In this way, this Thesis contributes to a deeper understanding of the dynamics of the interaction between granular materials and intruders, offering valuable insights for theoretical and practical applications.

Keywords: Granular materials, Solid intruders, Quasi-static regime, Contact forces, Drag reduction, Cooperative behavior, Collisional regime, Crater formation, Spinning projectile, Penetration depth.

“La libertad, Sancho, es uno de los más preciosos dones que a los hombres dieron los cielos; con ella no pueden igualarse los tesoros que encierra la tierra ni el mar encubre; por la libertad así como por la honra se puede y debe aventurar la vida, y, por el contrario, el cautiverio es el mayor mal que puede venir a los hombres.”

— Don Quijote de la Mancha, Miguel de Cervantes

LIST OF FIGURES

LIST OF TABLES

LIST OF ABBREVIATIONS AND ACRONYMS

Chapter 1: Introduction

NASA	National Aeronautics and Space Administration
JPL	Jet Propulsion Laboratory
MSSS	Mars Science Laboratory Mission
USGS	United States Geological Survey
DEM	Discrete Element Method

Chapter 2: Historical overview of the interaction of intruders with granular materials

RFT	Resistive Force Theory
2D	Two-dimensional
3D	Three-dimensional

Chapter 3: Methodology

LIGGGHTS	LAMMPS Improved for General Granular and Granular Heat Transfer Simulations
LAMMPS	Large-scale Atomic/Molecular Massively Parallel Simulator
DESIgn	Discrete-Element, Bonded-particle Sea Ice
ROI	Region of Interest

LIST OF SYMBOLS

Chapter 2: Historical overview of the interaction of intruders with granular materials

μ	Macroscopic friction coefficient (ratio of shear to normal stresses)
E	Available energy at impact
D_c	Crater diameter
h_c	Crater depth
V_p	Velocity of the projectile at collision
D_p	Projectile diameter
g	Modulus of gravity acceleration
ρ_p	Density of the projectile
ρ	Density of the grains
σ	Material strength (yield stress)
Π_σ	Dimensionless pressure ratio for material strength
Fr	Froud number
y	Vertical coordinate oriented downwards
$\vec{F}_p$	Resultant force on a solid projectile
$\vec{g}$	Gravity acceleration
ξ	Inertial term constant (drag model)
κ	Friction term constant (drag model)
δ	Penetration depth
h	Releasing height

H	Total drop distance
t_c	Impact time
ϕ	Packing fraction
ϕ_{cps}	Critical packing

Chapter 3: Methodology

$\vec{u}$	Velocity of a particle
$\vec{g}$	Acceleration due to gravity
m	Mass of a particle
I	Moment of inertia
$\vec{\omega}$	Angular velocity of a particle
$\vec{F}_c$	Resultant of contact forces between solids
$\vec{T}_c$	Resultant of contact torques between solids
$\vec{F}_{c,ij}$	Contact forces between particles i and j
$\vec{F}_{c,iw}$	Contact forces between particle i and the wall
$\vec{T}_{c,ij}$	Torque due to the tangential component of the contact force between particles i and j
$\vec{T}_{c,iw}$	Torque due to the tangential component of the contact force between particle i and the vertical wall
N_c	Number of particles in contact with particle i
N_w	Number of particles in contact with the wall
v_i	Speed of grain i
v'	Threshold velocity
$\mu_{d,g}$	Dynamic friction coefficient

$\mu_{s,g}$	Static friction coefficient
$\vec{F}_{c,ij}$	Contact force between particles i and j
$F_{c,n}$	Normal component of the contact force
$F_{c,t}$	Tangential component of the contact force
δ_n	Normal displacement
δ_t	Tangential displacement
κ_n	Normal stiffness coefficient
κ_t	Tangential stiffness coefficient
γ_n	Damping coefficient for normal contact
γ_t	Damping coefficient for tangential contact
E_i	Young's modulus of particle i
E_j	Young's modulus of particle j
ν_i	Poisson's ratio of particle i
ν_j	Poisson's ratio of particle j
r_i	Radius of particle i
r_j	Radius of particle j
h_i	Thickness of particle i
h_j	Thickness of particle j
h_m	Minimum thickness of the two particles in contact
r_c	Effective radius for contact
m_c	Effective mass for contact
E_c	Effective contact modulus
G_c	Effective shear modulus

δ_n	Normal overlap (displacement)
β	Damping ratio
ϵ	Restitution coefficient
$\mathbf{x}_i$	Position of the center of particle i
$\mathbf{x}_j$	Position of the center of particle j
μ	Microscopic coefficient of friction
μ_r	Coefficient of rolling resistance

A_b	Cross-sectional area of the bond material
$\vec{v}_n$	Normal component of the relative velocity between two particles
$\vec{v}_t$	Tangential component of the relative velocity between two particles
Δt	Time step of DEM computations
$k_{b,n}$	Normal stiffness constant for bonds
$k_{b,t}$	Tangential stiffness constant for bonds
I_p	Polar moment of inertia
I_a	Second area moment of inertia
$\vec{\omega}_n$	Normal component of the relative angular velocity
$\vec{\omega}_t$	Tangential component of the relative angular velocity
E_b	Bond Young's modulus
l_b	Bond equilibrium length
ν	Poisson's ratio
R_c	Effective radius

d	Diameter of the polyamide spheres (intruders)
V_0	Constant velocity of the intruders
ρ	Density of the glass spheres
ϕ	Packing fraction of the granular bed
h	Depth of immersion of the intruder
g	Acceleration due to gravity
F	Force experienced by the intruder
F_0	Drag force of a single the intruder
h_{rod}	Length of the cylindrical rod below the surface of the granular media
Δ	Distance separating two intruders

d	Diameter of the projectile
ρ	Density of the projectile
D	Diameter of the cylindrical container
b	Height of the cylindrical container
d_g	Diameter of the glass spheres
ρ_g	Density of the glass spheres
ϕ	Packing fraction
v_i	Speed at impact
h	Distance above the granular surface
ω_i	Angular velocity
V	Applied voltage in the power supply

ω_c	Critical rotation rate
D	Diameter of the cylinder
δ	Penetration depth

Chapter 4: Results and discussions - Quasi-static regime - Intrusion problems

F_D	Drag force
N_s	Number of small particles
N_l	Number of large particles
N	Total number of grains
d_{int}	Diameter of the intruder
h_{int}	Height of the intruder
d_s	Small particle diameter
d_l	Large particle diameter
h_g	Height of granular disks
ϕ	Packing fraction
L_x	Longitudinal length
L_y	Transverse length
ϵ_{gg}	Restitution coefficient (grain-grain)
ϵ_{gi}	Restitution coefficient (grain-intruder)
ϵ_{gw}	Restitution coefficient (grain-wall)
μ_{gg}	Dynamic friction coefficient (grain-grain)
μ_{gi}	Dynamic friction coefficient (grain-intruder)

μ_{iw}	Dynamic friction coefficient (intruder-bottom wall)
μ_{gw}	Dynamic friction coefficient (grain-walls)
$\mu_{s,gw}$	Static friction coefficient (grain-bottom wall)
v'	Threshold velocity
A_{ROI}	Area of the region of interest
ΔS	Total distance traveled by the intruder
t_R	Rayleigh time
G	Shear modulus
E	Young's modulus
ν	Poisson ratio
ρ	Material density
$\vec{F}_D$	Instantaneous drag force on the intruder
F_D	Magnitude of the drag force
$\langle F_D \rangle$	Mean drag force
t	Time
V_0	Initial velocity of the intruder
ρ	Anisotropy of the contact network
Z	Average number of contacts per particle
N	Number of non-rattler particles
$\hat{R}$	Fabric tensor
$\mathbf{r}_{ij}$	Contact vector from the center of particle i to the contact between particles i and j
$\lvert\mathbf{r}_{ij}\rvert$	Magnitude of the contact vector

d_g	Mean grain diameter
V_0	Initial velocity of the intruder
ΔS	Displacement of grains
Δt	Duration of creeping
t_c	Characteristic time ($t_c = d_g/V_0$)
μ_{iw}	Coefficient of basal friction for the intruder
μ_{gw}	Coefficient of basal friction for the grains
$\mu_{s,gw}$	Coefficient of static basal friction for the grains
$\langle L \rangle$	Time-averaged length of chains
$\langle F_D \rangle$	Time-averaged drag

ϵ	Restitution coefficient
μ	Friction coefficient
Δx	Initial separation in the longitudinal direction
Δy	Initial separation in the transverse direction
ϕ	Packing fraction
Δy	Initial separation of intruders
D_{opt}	Optimal distance for minimum drag
$\lvert \vec{F}_D \rvert$	Magnitude of the drag force
$\langle Z \rangle$	Mean number of contacts per particle averaged over time
$\langle \rho \rangle$	Time-averaged anisotropy
D_{att}	Characteristic distance between intruders

Δy_{final}	Final separation in the transverse direction
F_T	Thrust force
τ	Total time of the intruders' motion

h	Depth of the intruder (distance from the free surface of grains to the center of the intruder)
$f_0(t)$	Longitudinal time-varying drag force
F_0	Mean drag force experienced by a single intruder
Δ	Distance between the intruders
V_0	Velocity of the intruders
F	Overall drag force of the system
$\tilde{F}$	Normalized drag force
$\tilde{\delta}$	Normalized distance between intruders
Λ	Coefficient corresponding to the relative reduction in drag
$\tilde{\delta}_s$	Normalized characteristic screening length
d	Diameter of the intruder
r	Radial coordinate in cylindrical coordinates
θ	Angular coordinate in cylindrical coordinates
λ_0	Characteristic length over which velocity varies
λ_s	Velocity slip tangential to the object surface
f_r	Force coefficient in the radial direction
f_θ	Force coefficient in the tangential direction
$\mathbf{v}(r, \theta)$	Velocity field around the intruder

$\mathbf{f}$	Force per unit area in the granular material
$\mathbf{f}_1$	Force field around the first intruder
$\mathbf{f}'_1$	Perturbed force field around the first intruder
α	Nondimensional coefficient representing the strength of the interaction
F_S	Side force
η	Viscosity of a fluid

Chapter 5: Results and discussions - Collisional regime - Impact problems

d	Diameter of the grains
ρ	Density of the grains
D_p	Diameter of the projectile
ρ_p	Density of the projectile
μ_{gg}	Grain-grain friction coefficient
ϕ	Packing fraction
ϵ_{gg}	Restitution coefficient (grain-grain)
ϵ_{gp}	Restitution coefficient (grain-projectile)
ϵ_{gw}	Restitution coefficient (grain-wall)
μ_{gp}	Friction coefficient (grain-projectile)
μ_{gw}	Friction coefficient (grain-wall)
$\mu_{r,gg}$	Coefficient of rolling friction (grain-grain)
$\mu_{r,gp}$	Coefficient of rolling friction (grain-projectile)
$\mu_{r,gw}$	Coefficient of rolling friction (grain-wall)

N	Number of spheres in the simulation
h	Free-fall height
V_p	Collision velocity of the projectile
Fr^{-1}	Inverse Froude number
δ	Penetration depth
E	Young's modulus
ν	Poisson's ratio
D_{bed}	Diameter of the granular bed
h_{bed}	Height of the granular bed
N_d	Number of grains for each diameter
t_R	Rayleigh time
G	Shear modulus
D_c	Crater diameter
H	Total drop distance
μ_{rep}	Macroscopic friction measured as the tangent of the angle of repose
m_p	Mass of the projectile
g	Acceleration due to gravity
d_1	A constant related to the drag model
κ	A constant used in the drag equations
$\mathcal{W}(x)$	Lambert function
A	Constant in the correlation proposed by Seguin *et al.* (2008)
β	Exponent in the correlation proposed by Seguin *et al.* (2008)
λ	Exponent in the correlation proposed by Seguin *et al.* (2008)

n	Coefficient in the proposed fitting equation
t_c	Time taken for reaching full stop
$\vec{a}$	Projectile acceleration
$\vec{F}_p$	Resultant force on the projectile
a_y	Vertical component of projectile deceleration
V_y	Vertical velocity of the projectile
$a_{y,peak}$	Maximum values of deceleration
$a_{y,inertial}$	Inertial term of the vertical deceleration
ξ	Coefficient in the drag force equation
θ	Granular temperature
$\Delta y_{rebound}$	Vertical displacement during rebound
μ_{gp}	Grain-projectile friction coefficient
μ_{gw}	Grain-wall friction coefficient
μ_{gg}	Grain-grain friction coefficient
$\bar{\theta}$	Space-averaged granular temperature
$\vec{\omega}$	Angular velocity of the projectile
ω_x, ω_y, ω_z	Components of angular velocity
K_v	Linear kinetic energy of the projectile
K_ω	Rotational kinetic energy of the projectile
I	Moment of inertia of the projectile
N_p	Number of projectile spheres

d_p	Diameter of projectile spheres
$\rho_{p,bulk}$	Bulk density of the projectile
ϕ_p	Packing fraction of the projectile
σ_p	Bonding stress
ϵ_{pp}	Restitution coefficient (projectile grain-projectile grain)
ϵ_{pw}	Restitution coefficient (projectile grain-wall)
μ_{pp}	Friction coefficient (projectile grain-projectile grain)
μ_{pw}	Friction coefficient (projectile grain-wall)
$\mu_{r,pp}$	Coefficient of rolling friction (projectile grain-projectile grain)
$\mu_{r,pw}$	Coefficient of rolling friction (projectile grain-wall)
Δt	Time step
K_ω/K_v	Ratio of rotational to linear kinetic energies

d	Diameter of the spherical projectile
ρ	Density of the spherical projectile
D	Diameter of the cylindrical container
b	Height of the cylindrical container
d_g	Diameter of the granular material
v_i	Speed at impact
ω_i	Angular velocity of the rotating granular medium
δ_0	Penetration depth
H_0	Total distance traveled by the projectile

z	Depth
T_v	Characteristic time of penetration
$\tilde{z}$	Dimensionless depth
$\tilde{t}$	Dimensionless time
$\tilde{\delta}_0$	Dimensionless penetration depth
$\tilde{H}_0$	Dimensionless total distance
K_v	Coefficient for velocity-dependent force term in drag model
K_z	Coefficient for depth-dependent force term in drag model
ν	Velocity ratio defined as $\nu = \omega_i\, d/v_i$
A	Constant in the scaling law
α	Exponent in the power-law dependence
B	Constant in the penetration depth equation
T_ω	Characteristic time for stopping the rotation of an initially spinning projectile
C_f	Resisting torque exerted by the granular medium on the object during penetration
τ_f	Local solid friction force per unit area between the grains and the sphere
$\tilde{z}$	Nondimensional depth
$\tilde{t}$	Nondimensional time
$\tilde{H}$	Nondimensional total height
$\tilde{\delta}$	Nondimensional penetration depth
C	Coefficient in the relation for $\chi(\nu)$
$\chi(\nu)$	Function related to the effect of rotation on penetration depth
B	Coefficient from the fit of the relative penetration depth

LIST OF PUBLICATIONS

Peer-reviewed journal articles

1. Carvalho, D. D.; Lima, N. C.; Franklin, E. M. "*Contacts, motion, and chain breaking in a two-dimensional granular system displaced by an intruder*". *Physical Review E*, v. 105, p. 034903, 2022. DOI: <https://doi.org/10.1103/PhysRevE.105.034903>

2. Carvalho, D. D.; Franklin, E. M. "*Collaborative behavior of intruders moving amid grains*". *Physics of Fluids*, v. 34, n. 12, 2022. DOI: <https://doi.org/10.1063/5.0124556>

   Selected as "Featured".

   Featured in Scilight: <https://pubs.aip.org/aip/sci/article/2022/49/491107/2843820/Modeling-multiple-animal-movements-through-sand>

3. Carvalho, D. D.; Lima, N. C.; Franklin, E. M. "*Roles of packing fraction, microscopic friction, and projectile spin in cratering by impact*". *Physical Review E*, v. 107, n. 4, p. 044901, 2023. DOI: <https://doi.org/10.1103/PhysRevE.107.044901>

4. Carvalho, D. D.; Lima, N. C.; Franklin, E. M. "*Impact craters formed by spinning granular projectiles*". *Physical Review E*, v. 108, n. 5, p. 054904, 2023. DOI: <https://doi.org/10.1103/PhysRevE.108.054904>

   Featured in Physics Magazine: <https://physics.aps.org/articles/v16/s166>

   Featured in Popular Mechanics: <https://www.popularmechanics.com/space/solar-system/a46170498/barringer-crater-curveball/>

   Featured in The Science Times: <https://www.sciencetimes.com/articles/47657/20231214/curveball-asteroids-study-suggests-unusual-spins-shape-earths-craters-including.htm>

   Featured in Phys.org: <https://phys.org/news/2023-12-simulations-craters-reveal-characteristics-impactors.html#google_vignette>

   Featured in Space.com: <https://www.space.com/barringer-crater-formation-cosmic-curveball-asteroid>

5. Carvalho, D. D.; Bertho, Y.; Franklin, E. M.; Seguin, A. "*Penetration of a spinning sphere impacting a granular medium*". *Physical Review E*, v. 109, n. 5, p. 054902, 2024. DOI: <https://doi.org/10.1103/PhysRevE.109.054902>

   Featured in CNRS Ingénierie: <https://www.insis.cnrs.fr/fr/cnrsinfo/comment-la-rotation-des-projectiles-les-fait-senfoncer-dans-les-milieux-granulaires>

6. Carvalho, D. D.; Bertho, Y.; Seguin, A.; Franklin, E.; Texier, B. ''*Drag reduction during the side-by-side motion of a pair of intruders in a granular medium*". *Physical Review Fluids*, v. 9, p. 114303, 2024. DOI: <https://doi.org/10.1103/PhysRevFluids.9.114303>

   Featured in Phys.org: <https://phys.org/news/2024-12-cooperation-intruders-side-granular-media.html>

Conference proceedings

1. 26th International Congress of Mechanical Engineering - COBEM2021. "*Motion of a solid body within a granular medium*". 2021. Brazil.
2. 14th European Fluid Mechanics Conference - EFMC14. "*Motion of a solid body within granular media*". 2022. Greece.
3. 75th Annual Meeting of the APS Division of Fluid Dynamics. "*Cooperative motion of intruders amid smaller grains*". 2022. United States of America.
4. 19th Brazilian Congress of Thermal Sciences and Engineering - ENCIT2022. "*Locomotion of an intruder within granular media*". 2022. Brazil.
5. Landslide Mechanics: From Complex Granular Behavior to Field-scale Flow? Centre International des Sciences Mécaniques (CISM). 2023. Attendee. Italy.
6. Journées Écoulements & Fluides à Saclay (JEFS). "*Collaborative motion of intruders moving amid smaller grains*". 2023. France.
7. Journée de Non-Permanents et Stagiaires (JNPS). "*The cooperative nature of the motion of sets of intruders moving amid grains*". 2023. France.
8. Workshop Patterns in Granular Matter. "*The cooperative nature of a set of intruders moving between smaller grains*". 2023. Brazil.

9. Engineering Mechanics Institute (EMI) 2023 International Conference. "*The cooperative nature of the motion of sets of intruders moving amid grains*". 2023. Italy.

10. 1st European Fluid Dynamics Conference (EFDC1). "*Drag reduction in the side-by-side motion of intruders in a granular medium*". 2024. Germany.

11. 7th Southern Workshop on Granular Materials. "*Penetration of spinning projectiles impacting granular materials*". 2024. Chile.

CONTENTS

1 INTRODUCTION

1.1 General introduction to granular materials

Granular materials, consisting of discrete, macroscopic particles, are ubiquitous in our daily lives and play a crucial role in a wide array of natural and industrial processes. From the grains of sand in the desert, which cover more than 10% of the land surface on Earth (Duran, 1997), to the particles in pharmaceutical manufacturing or the everyday coffee, granular media are encountered across various scales and applications. Such diverse materials, with an enormous variety of sizes, shapes, mechanical and chemical properties, find extensive use in nature and industry. The processing of both granular media and its aggregates consumes approximately 10% of all the energy produced on the planet, in different industries such as mining, cosmetic, pharmaceutical and food (Duran, 1997). The current use of these materials dates back to ancient civilizations, being used in activities essential to human evolution, such as agriculture (grain cultivation and soil work), buildings (housing construction), timekeeping (hourglass), to name just a few examples. Even though the physics of granular materials is not a relatively new subject, having already been studied by illustrious scientists like Coulomb (Coulomb, 1773) and Reynolds (Reynolds, 1885), its mechanics remains poorly understood, and some important yet seemingly trivial questions still lack clear answers, as what is the nature of the contact force between two solid particles (Duran, 1997; Andreotti *et al.*, 2011). The Amontons-Coulomb's laws of friction themselves, traditionally used in modeling this effect and first observed by Leonardo Da Vinci, are still an open problem in physics (Andreotti *et al.*, 2011). Therefore, the study of these materials is crucial not only for understanding fundamental physical principles but also for addressing practical challenges in engineering, physics, geophysics, and planetary science, to cite but a few. Figure (1.1) gives some examples of granular materials found in natural and industrial contexts.

In geophysical applications, the study of these materials, especially how they move, is used to prevent and mitigate natural risks, such as landslides, avalanches, or to better understand the transport of sediments in rivers (Ren *et al.*, 2008; Ferdowsi *et al.*, 2017; Texier *et al.*, 2023; Gonzalez *et al.*, 2023); in civil construction, these materials find applications from the design of foundations to maintaining the stability of slopes and excavations (Jiang; Zhang, 2015); in industry, granular materials are involved, for example, in the production of food [Figs. (1.1)b

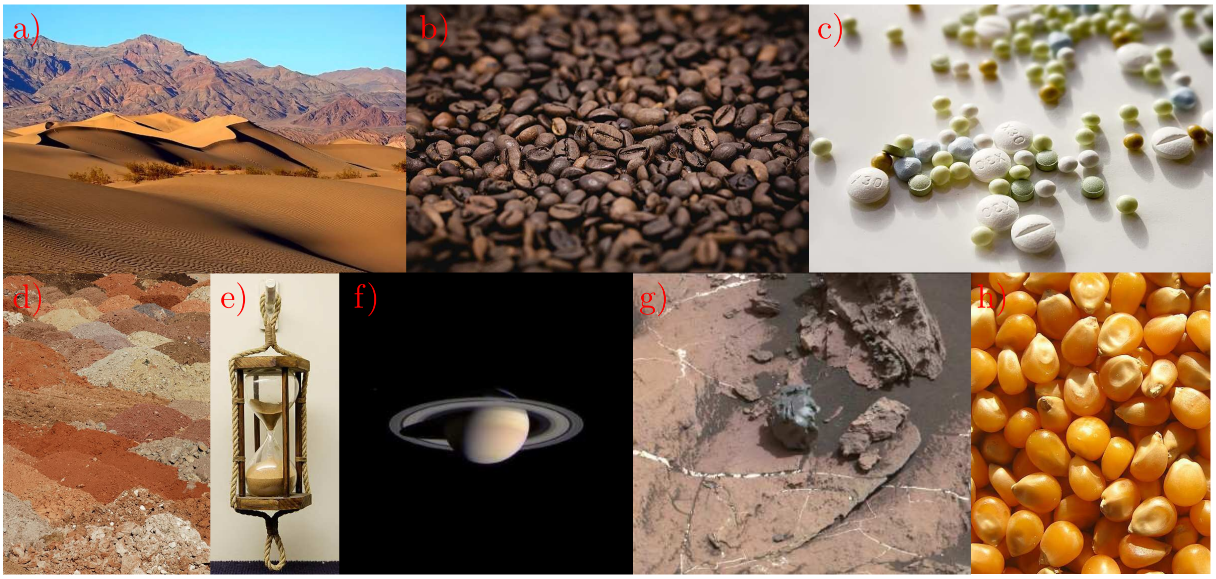

Figure 1.1 – Examples of the variety of granular materials. (a) Mesquite dunes in Death Valley National Park, United States. Credits: Brocken Inaglory (Inaglory,). (b) Coffee beans. Credits: Popo le Chien (Chien,). (c) Pharmaceutical pills. Credits: Takkk (Takkk,). (d) Piles of soil with various compositions. Credits: Alvesgaspar (Alvesgaspar,). (e) Hourglass. Credits: Marie-Lan Nguyen (Nguyen,). (f) Photo of Saturn taken by the Cassini spacecraft. Credits: NASA/JPL/Space Science Institute. (g) Iron-nickel meteorite photographed by the Curiosity rover on Mars. Credits: NASA/JPL-Caltech/MSSS. (h) Corn grains. Credits: Andrey Butko (Butko,).

and (1.1)h], pharmaceuticals [Fig. (1.1)c], and construction materials [Fig. (1.1)d], especially in the processes of storage, mixing, grinding, and transporting (Duran, 1997); in this context, the design of efficient hoppers and conveyors requires knowledge of how granular materials flow under different conditions (To *et al.*, 2001; Janda *et al.*, 2009; Tang; Behringer, 2011; Hilton; Cleary, 2011). In astrophysics, the formation of planets, moons, and other celestial bodies is believed to involve processes that are governed by the physics of granular materials (Blum, 2018; Hestroffer *et al.*, 2019). For instance, planetary rings, as the ones in planet Saturn [Fig. (1.1)f], are composed of countless granular particles orbiting in space (Andreotti *et al.*, 2011). In addition, in recent years, global warming is leading to the expansion of desert areas on our planet [Fig. (1.1)a], so that the delivery and transportation of goods in these areas is a challenge for the near future. Not to mention planetary exploration. A problem of this nature has been faced by the Mars rover Spirit, which became stuck in 2010 in the sandy Martian soil. Despite months of efforts to free the rover from a sand trap on Mars, the NASA probe now remains firmly lodged in the floor of a small crater on the red planet. Mission managers have announced that since Spirit cannot free itself, it will remain in its current position, spending its remaining operational days conducting science experiments from inside the crater, where its wheels can only move a few centimeters (Jaggard, 2010). To this end, the development of robots designed to operate in granular environments [Fig. (1.1)g], such as sand, gravel or regolith (Wei *et al.*, 2021) (as on Mars, where loose regolith represents a significant challenge for exploration missions, from rover mobility to drilling operations (Arvidson *et al.*, 2010; Jaggard, 2010)), is quite important and depends on a better understanding of the physics of granular materials for proper operation (like a detailed understanding of the forces that arise as these devices move and interact with these materials, for example). These robots, often inspired by the locomotion of animals such as snakes, lizards, or insects (Maladen *et al.*, 2009), must navigate complex terrains where traditional vehicles would have difficulty locomoting (Zhang *et al.*, 2013; Li *et al.*, 2013a). For instance, it has been shown that bioinspired designs, such as snake-like robots, can achieve more efficient locomotion in granular environments by mimicking the wave-like movement of real snakes (Marvi *et al.*, 2014).

Regarding the composition of granular materials, they are made up of particles large enough for thermal fluctuations to be insignificant or ignored. This differentiates them, for example, from colloids, where Brownian motion is present, and from powders (Andreotti *et al.*, 2011). The size of granular particles covers a wide range, ranging from particles with a diameter greater than 100 micrometers (Andreotti *et al.*, 2011), to others with millimeters (grains of sand) to meters (boulders), and they can be composed of various materials, including metals (e.g. steel), minerals (e.g. quartz sand), organic matter (e.g. grains), and synthetic substances (e.g. plastic pellets). Furthermore, particles can have different shapes, such as spherical (e.g., ball bearings), angular (e.g., gravel), rod-shaped or irregular (e.g., natural sand) (Duran, 1997; Andreotti *et al.*, 2011).

Since these materials are of a discrete nature, each particle interacts with its neighbors primarily through contact forces (Duran, 1997; Andreotti *et al.*, 2011). The contact force between two dry grains is usually decomposed into a normal and tangential reaction, which for particles large enough are dominated by the elastic repulsion (Hertz contact) and solid friction (Amontons-Coulomb's law), respectively (Andreotti *et al.*, 2011). These contact forces are applicable to permanent contacts, as those that exist in a granular pile, for instance; however, when flowing, these materials are also subjected to inelastic collisions between the particles. A brief description of these interactions is given in Appendix A and a thorough description can be found in Andreotti *et al.* (2011) (Andreotti *et al.*, 2011). Finally, although not important as the interactions already mentioned, others may arise under different scenarios. For example, particles may be subjected to electrostatic forces if they are charged; in the presence of an interstitial fluid in the contact region, a capillary cohesion between particles may be developed; and, for particles small enough, intermolecular forces of the van der Waals type can introduce a non negligible attraction. These interactions may become more complex if we consider wet granular materials (i.e. granular materials in the presence of an interstitial liquid). In one part, the fluid might be flowing in regard to the grains (as in the transport of sediments); on the other, the fluid may be carried away with the grains (as is the case of sub-aquatic avalanches) (Andreotti *et al.*, 2011). In both cases, the interstitial fluid influences or controls the dissipative processes within these flows and new interactions arise, such as hydrodynamic drag forces, Archimedes buoyancy, added mass force, Basset force, Magnus force, and lubrication forces (Andreotti *et al.*, 2011).

These mechanical interactions create complex stress networks within these materials, known as force chains [Fig. (1.2)], such that stress is not distributed uniformly throughout all particles, but rather transmitted through the contacts in these history-dependent networks (force chains) (Majmudar; Behringer, 2005). The force chains are elongated structures that carry most of the stress in a granular assembly, while particles outside these chains bear little or no load (Radjai *et al.*, 1996; Radjai *et al.*, 1998). The heterogeneous distribution of stress within granular materials leads to complex and often unpredictable behavior, since force chains are directly related to these materials' mechanical stability (Majmudar; Behringer, 2005). When external forces cause a redistribution of stress, the integrity of the force chains can be compromised, leading to localized failure or even catastrophic collapse. For example, in a sand pile, the stability of the pile depends on the network of force chains. If a force chain is broken, it can lead to the collapse of the pile. This is also one of the causes behind landslides and other natural events (Majmudar; Behringer, 2005; Tordesillas, 2007). These structures are not static, constantly evolving in response to external disturbances in these materials (Seguin *et al.*, 2016; Carvalho; Franklin, 2022b; Carvalho *et al.*, 2022). The distribution of forces within these chains tends to be highly anisotropic, which means that, as already mentioned, the stress is not distributed uniformly within these materials, but concentrated along specific directions (Majmudar; Behringer, 2005), sometimes leading to the formation of shear bands (regions where the material experiences large stresses while the surrounding material remains approximately undeformed) (Jiang; Zhang, 2015) and localized failures (Tordesillas, 2007). These dynamic structures can rearrange or collapse under stress, leading to an extremely important phenomenon in the physics of granular materials known as jamming, where the material transitions from a fluid-like to a rigid, solid-like state (Cates *et al.*, 1998; Bi *et al.*, 2011). One way to observe the distribution of contact forces is to use appropriate techniques, usually making use of photoelastic grains, together with illumination schemes and light polarizers (Majmudar; Behringer, 2005; Daniels *et al.*, 2017). This creates a visual pattern of alternating light and dark heterogeneous lines within the material, associated with the local internal stress [Fig. (1.2)b]. More on this technique to be presented in Sec. 3.2.2. Contact networks can also be visualized and quantified through numerical simulations [Fig. (1.2)a] (Herman, 2016; Carvalho *et al.*, 2022; Carvalho; Franklin, 2022b).

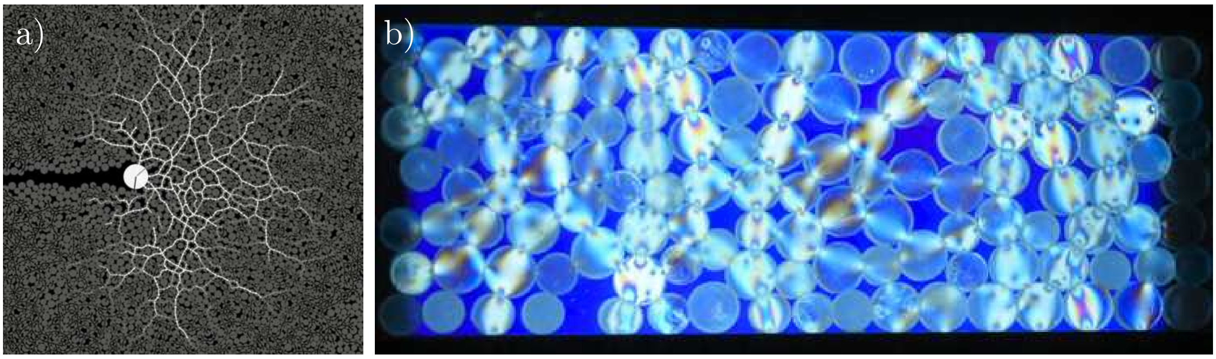

Figure 1.2 – Examples of force chains observed in granular materials. (a) Obtained numerically. Image adapted from (Carvalho *et al.*, 2022). (b) Obtained experimentally.

These materials also exhibit diverse mechanical behaviors that differentiate them from the traditional solid, liquid, and gaseous states of matter. Their behavior is highly dependent on factors related to the discrete nature of their composition, such as particle size, shape, density, and, most importantly, interparticle interaction forces (Duran, 1997; Andreotti *et al.*, 2011). Unlike the classical phases of matter (solid, liquid, and gas), granular materials do not fit perfectly into any of these categories individually; instead, they exhibit characteristics of all three, depending on the flow conditions (Jaeger *et al.*, 1996; Duran, 1997; Andreotti *et al.*, 2011). For example, when subjected to low stress, they can behave like solids, supporting their own weight and resisting deformation. However, when the stress exceeds a certain limit, they can flow like a fluid (Duran, 1997; Andreotti *et al.*, 2011). This defines some flow regimes (two of which will be explored in this Thesis) depending on factors such as applied stress, velocity, and concentration. The main flow regimes being: i) quasi-static regime: occurs at low shear rates, where the material behaves more like a solid and deformation is slow. Here, the flow is dominated by frictional forces between particles; ii) intermediate (dense) regime: at moderate shear rates, the material flows more readily, and both frictional and collisional forces are significant; iii) inertial (dilute) regime: at high shear rates, the material behaves more like a gas, with particles colliding frequently and moving independently of each other (Andreotti *et al.*, 2011; fr/MIDI/, 2004). Since granular flows are very important for the understanding of natural and artificial processes, some previous works have focused on understanding these flows. In particular, we can mention gravity-driven flows, found in events such as avalanches (which occur when the material on a slope exceeds a critical angle), landslides and grain discharge from hoppers (Pouliquen, 1999; Pouliquen; Forterre, 2002); well-controlled Couette flows, which have been used primarily to investigate the rheological properties of granular materials, particularly how they behave under shear (Pouliquen; Forterre, 2009; Pouliquen *et al.*, 2006); and finally, studies where objects move within these materials (Kolb *et al.*, 2013; Seguin *et al.*, 2016; Carvalho *et al.*, 2022; Carvalho; Franklin, 2022b; Carvalho *et al.*, 2023b; Carvalho *et al.*, 2023a; Carvalho *et al.*, 2024a; Carvalho *et al.*, 2024b), a topic to be covered in this Thesis. Some of these studies have led to the proposal of some continuum models to describe these materials, treating them approximately as continuous media, in order to propose constitutive relations that describe how stress and strain are related (Pouliquen *et al.*, 2006). Although there has been some advancement in recent years, the rheological properties of granular materials are very complex and usually exhibit nonlinear and sometimes unforeserable behavior, making it a challenge to predict their behavior in many scenarios (Andreotti *et al.*, 2011).

Another interesting aspect of granular materials is related to a property known as dilatancy, first observed by Osborne Reynolds in the 19th century (Reynolds, 1885). In short, we can define it as the tendency of granular materials to expand in volume when subjected to shear deformation. As a granular material is sheared, the particles must move past each other, usually leading to an increase in voids and, consequently, an increase in volume (Duran, 1997; Andreotti *et al.*, 2011). These volume changes are associated with the materials' packing, or how the particles are organized internally within a volume. The packing fraction refers to the proportion of space occupied by the particles within a given volume (Andreotti *et al.*, 2011). In granular materials, this can vary from loose packings, where the particles occupy a small fraction of the volume, to dense packings, where the particles are compacted together. Random close packing (RCP) is a state in which the particles are packed as densely as possible without any long-range order, typically reaching a packing density of about 0.64 for spherical particles (Torquato *et al.*, 2000). Ordered packing, on the other hand, refers to a crystalline arrangement of particles, such as close-packed face-centered cubic (FCC) structure, which can reach higher packing densities, up to about $\pi/\sqrt{18} \approx 0.74$ for identical spheres (Torquato *et al.*, 2000).

Finally, one of the most intriguing phenomena behind the physics of granular materials (and the central theme of this Thesis) are associated to the way they interact with intruders (solid objects moving through or over them). For instance, slowly moving intruders often experience resistance due to quasi-static forces, which are dominated by friction and cohesion between particles (Kolb *et al.*, 2013; Seguin *et al.*, 2016; Carvalho *et al.*, 2022; Carvalho; Franklin, 2022b; Carvalho *et al.*, 2024b). In contrast, rapidly moving intruders can generate shock waves and fluid-like responses in the granular medium (Seguin *et al.*, 2008; Seguin *et al.*, 2009; Carvalho *et al.*, 2023b; Carvalho *et al.*, 2023a; Carvalho *et al.*, 2024a; Bourrier *et al.*, 2008).

The purpose of this short section has been to give a brief overview of some topics related to granular materials, providing a shallow description of them. The reader is referred to the monographs of Duran (1997) (Duran, 1997) and Andreotti *et al.* (2011) (Andreotti *et al.*, 2011) for a complete description of the current state of research and understanding of these materials.

1.2 Relevance of intruder motion in granular materials

Most people have probably tried running on the sand on a beach and realized how difficult it is to do so, compared to trying to do the same movement on the asphalt of a street, for example. In the same context, under the pretext of getting rid of or alleviating the intense heat under the sun on a beach, the use of umbrellas becomes indispensable. However, anyone who has ever tried to stick an umbrella in the sand must have realized how difficult this task is. These are simple examples, derived from an observation made at the time this Thesis is being written, under the intense Brazilian summer sun, which reflect everyday situations in which intruders interact with granular materials, whether moving on their surface or within them. In a general perspective, the study of the motion of intruders over or within granular materials is of great interest in several practical, scientific and engineering contexts. In simple terms, an intruder can be defined as a solid object, usually distinct in size, shape or density from the surrounding granular medium. Understanding the dynamics of the motion of these objects in granular media is fundamental to a better understanding of natural and artificial (man-made) systems, ranging from biology and agriculture to planetary science and engineering. The interaction between an intruder and a granular medium is an extremely complex process, being influenced by several factors such as the geometry of the intruders, their velocities and types of motion (e.g. quasi-static or collisional regimes), as well as the properties of the surrounding granular medium itself. In this section, we highlight some scenarios where this type of motion can be found. Figure (1.3) gives some examples of intruders interacting with granular materials in both natural and industrial contexts.

Figure 1.3 – Examples of the motion of intruders on or within granular materials. (a) The De Winton's golden mole (*Cryptochloris wintoni*). Credits: JP Le Roux (Roux,). (b) A tunnel used by the De Winton's golden mole in Port Nolloth, South Africa. Credits: Samantha Mynhardt (Mynhardt,). (c) Roots growing in soil. Credits: Pixabay (Vogel,). (d) Roots of a tree. Credits: Pixabay (FelixMittermeier,). (e) Sandfish lizard (*Scincus scincus*). Credits: Wilfried Berns (Berns,). (f) Saharan Horned Viper (*Cerastes cerastes*). Credits: Holger Krisp (Krisp,). (g) Barringer Crater, impact crater with 1200 m in diameter in the desert of northern Arizona, United States. Credits: USGS/D. Roddy, Public Domain. (h) Curiosity rover on Mars. Credits: NASA/JPL-Caltech/MSSS. (i) Ancient way of plow activity. Credits: Ralf Roletschek (Roletschek,). (j) Modern plow. Credits: Joevilliers, Public Domain.

Although it may not seem so obvious, fundamental ecological processes such as soil penetration by animals [Figs. (1.3)a, (1.3)c, and (1.3)f] are examples of the motion of intruders in granular media. For example, burrowing animals such as moles, lizards, clams and earthworms must navigate the soil (or subsea soils) by moving the grains around them (Maladen *et al.*, 2009). Recently, the De Winton's golden mole (*Cryptochloris wintoni*) [Fig. (1.3)a], last seen in 1937 off the northwest coast of South Africa, was rediscovered in November 2023 after almost 90 years without being seen. This blind and elusive mole avoids human contact by "swimming" through sand dunes [Fig. (1.3)b], making it extremely difficult to spot (Mynhardt, 2023). The efficiency of these processes depends on the animal's ability to generate enough momentum to overcome the resistance of the granular material, typically associated with the force chains formed within them. For example, there are several burrowing and excavation strategies employed by different biological systems (Hosoi; Goldman, 2015), such as the Atlantic razor clam (*Ensis directus*), which uses deformations of its body to loosen and repack the underwater soil around it, leading to a unidirectional motion (Jung *et al.*, 2011). In general, these locomotion strategies involve a wave-like, snake-like motion (Maladen *et al.*, 2009; Jung, 2010), or a "two-anchor" mechanism (Jung *et al.*, 2011). The sandfish lizard [Fig. (1.3)e], for example, moves through sand by rhythmically rocking its body from side to side (Maladen *et al.*, 2009). This is also the case for smaller creatures such as the nematode *Caenorhabditis elegans*, which navigate granular environments effectively using wave-like motion (Jung, 2010). In contrast, soft-bodied animals in particulate substrates saturated with a pore liquid typically employ a "two-anchor" method of burrowing (Jung *et al.*, 2011). This involves expanding one part of the body to create a terminal anchor while another part contracts to minimize drag. As the contracted segment advances through the burrow, it expands to establish a new anchor, while the previous anchor contracts and moves forward (Jung *et al.*, 2011).

Another aspect of extreme environmental importance, especially in ecosystem conservation, is linked to the dispersal of seeds falling from trees, with subsequent penetration into the soil, revealing ballistic mechanisms directly associated to the physics of granular materials. A recent study showed how some types of seeds (*Erodium* and *Pelargonium* seeds) adopt a strategy of using their rotation as a way of reducing soil resistance to penetration by causing a change in the configuration of contact networks due to soil rearrangements (Jung *et al.*, 2017). This leads to root growth in plants [Figs. (1.3)c and (1.3)d], another area where the interaction of intruders (in this case roots) with granular materials plays a critical role. As roots penetrate the soil, they encounter resistance from surrounding grains, which can affect their direction of growth, since the trajectories are effected by the presence of obstacles in the granular material, like stones, usually generating tortuous paths (Kolb *et al.*, 2017). In addition, the root's growth rate is affected by the granular material properties; for instance, forces exerted on the root cap have been shown to reflect the interparticle's force networks (Fakih *et al.*, 2019) and the roots elongation tends to be attenuated the more compact the granular material is (Abdalla *et al.*, 1969). Thus, a better understanding of the physics of these movements can lead to the development of better agricultural soil management techniques in order to improve root penetration and, consequently, plant growth, with a considerable economic impact. Also in an agricultural context, the motion of tools and machinery through soil is found in many common activities such as plowing, planting, and harvesting [Figs. (1.3)i and (1.3)j] (Godwin; O'Dogherty, 2007).

In industry, the design of avalanche protection structures, such as the use of fences, barriers, or the implementation of reforestation zones, is linked to the understanding of how intruders (in this case, artificial structures or trees) interact with the layers of granular material during these critical events. Some works provided insights into the ideal design (disposition) of these structures to mitigate the risk of avalanches (Texier *et al.*, 2023); while others have shown, through experiments of the stability of a granular layer over a rough incline, that the presence of a nail forest increases the stability of the granular layer due to additional frictional forces exerted by the pillar forest on the granular layer (Benito *et al.*, 2012a).

In the field of intruder locomotion in granular media, we can mention the development of robots that are capable of moving efficiently on irregular granular terrains, as is the case in military applications or in search and rescue missions in areas affected by natural disasters (avalanches and landslides). Furthermore, moving away from terrestrial applications, the movement of intruders in granular media is also found, for example, in the exploration of extraterrestrial surfaces, such as those of Mars and the Moon. Rovers designed to traverse these surfaces, such as the Spirit and Curiosity rovers [Fig. (1.3)h], that spend many years of activity on Mars, making great scientific discoveries, must be able to deal with low gravity environments and the unique mechanical properties of extraterrestrial soils. In this context, there are several mobility challenges, especially aggravated by the need to avoid entrapment and ensure stability during movement. A famous example with a huge economic impact is the entrapment of the Mars rover Spirit in 2010, which became stuck in the sandy Martian soil in the floor of a small crater (Jaggard, 2010). This lead to the prediction of models to improve rover performance based on the interaction between the wheels and the granular substrate (terramechanics), leading to the optimization of wheel designs and steering strategies (Iagnemma *et al.*, 2004; Ishigami *et al.*, 2007). Recently, a great effort has been put on the development of bioinspired robots that mimic the locomotion strategies of animals such as snakes and lizards. These designs have shown promise in overcoming mobility challenges in loose and changing terrains, making them ideal for a wide range of applications (Maladen *et al.*, 2011b; Xiao; Murphy, 2018; Chen *et al.*, 2023).

Finally, cratering after projectile impact is also a process where this type of motion is encountered. Crater formation involves the rapid displacement and deposition of granular material, leading to the formation of craters of various shapes, as well as complex patterns of material ejection and, in some cases, wave propagation. Experiments and simulations have provided insights into the scaling laws that govern crater formation (Melosh; Ivanov, 1999; Uehara *et al.*, 2003b; Katsuragi; Durian, 2007; Seguin *et al.*, 2008; Carvalho *et al.*, 2023b; Carvalho *et al.*, 2023a; Carvalho *et al.*, 2024a). Such studies are not only important for understanding the geological history of planetary bodies (such as the event that caused the extinction of the dinosaurs on Earth), but also for predicting the effects of future impacts on Earth. Impact problems are also of utmost importance to understand the distribution of elements (heavy metals) under or within the surface, brought by the projectile after the impact (Carvalho *et al.*, 2023a). In the early 20th century, businessman Daniel Barringer spent a fortune searching for an iron meteorite that he believed was buried under the floor of a meteor crater in Arizona, United States [Fig. (1.3)g] (Stephens, 2023). Although we have had few opportunities to study large meteorite impacts, there is now an understanding in the scientific community that Barringer's search was probably in vain: the projectile that created that meteor crater vaporized largely upon impact (Stephens, 2023). However, the specifics of how meteorite debris is dispersed and how its impact shapes the resulting crater are still not well understood and studies on this topic are proving to be relevant.

Locomotion in granular materials, taking account the physical interactions between intruders and the surrounding granular material, and cratering by impact at low energy levels are the central themes of this Thesis, described in Sec. 1.3.

1.3 Central themes of this Thesis

As seen in Sec. 1.2, the displacement of a solid body (intruder) within a granular medium is ubiquitous in natural and man-made processes. However, the fundamental understanding of the interaction between one or more moving objects and a granular substrate remains a fundamental and practical challenge.

Depending on velocities, lengths, materials and concentrations involved, the granular system is forced to move in different manners. For instance, the motion can be highly inertial, with great part of the kinetic energy being dissipated through friction and collisions within grains (Bester; Behringer, 2017), or when the velocities involved are relatively small, it can be in quasi-static regime, being dominated by the formation and destruction of contact networks and stick-slip motion (Appendix A) (Kolb *et al.*, 2013; Tordesillas *et al.*, 2014; Kozlowski *et al.*, 2019; Carlevaro *et al.*, 2020; Kozlowski *et al.*, 2022; Kozlowski *et al.*, 2021; Pugnaloni *et al.*, 2022; Carvalho *et al.*, 2022; Carvalho; Franklin, 2022b; Carvalho *et al.*, 2024b). This regime can be observed in the thrusting of ploughs in agricultural activities, in avalanche protection devices aimed at slowing down the flow (Benito *et al.*, 2012b; Texier *et al.*, 2023), in root growth (Kolb *et al.*, 2017; Fakih *et al.*, 2019), or in the motion of animals in the soil (Hosoi; Goldman, 2015). For higher velocities, a dilute regime appears, in which solid-solid collisions dominate (Andreotti *et al.*, 2011), such as happens in crater formation (Uehara *et al.*, 2003b; Seguin *et al.*, 2008; Seguin *et al.*, 2009; Carvalho *et al.*, 2023b; Carvalho *et al.*, 2023a; Carvalho *et al.*, 2024a)).

When intruders are set in motion in granular media, they may experience different phenomena. Their motion leads to local reorganizations of the granular packing around them (Houssais *et al.*, 2015; Kolb *et al.*, 2013), causing either breakage or formation of force chains [Fig. (1.2)]. This generates a strongly oscillating drag force on the intruder (Kolb *et al.*, 2013; Seguin *et al.*, 2016; Carvalho *et al.*, 2022; Carvalho; Franklin, 2022b; Carvalho *et al.*, 2024b) which, in some cases, may lead to creeping (Candelier; Dauchot, 2009) or to the formation of jammed regions, which can bring the intruder to a complete stop (Bi *et al.*, 2011; Zheng *et al.*, 2014). These forces have been, in some cases, previously measured. However, local variations of particle fractions, forming compressed fronts and expanded trails (Kolb *et al.*, 2013; Seguin *et al.*, 2016; Carvalho; Franklin, 2022b), together with the breaking and reorganization of the force networks around the intruder, make the prediction of granular motion and drag forces very complex (Carvalho *et al.*, 2022). On a small scale, some works focused on the motion of an intruder being pulled at a constant velocity amid smaller grains (Albert *et al.*, 1999; Albert *et al.*, 2001; Geng; Behringer, 2005; Costantino *et al.*, 2008; Kolb *et al.*, 2013; Seguin *et al.*, 2016; Kozlowski *et al.*, 2019; Carlevaro *et al.*, 2020; Carvalho *et al.*, 2022; Carvalho; Franklin, 2022b), while others focused on the motion of intruders being pulled at a constant force (Candelier; Dauchot, 2009; Reichhardt; Reichhardt, 2010; Candelier; Dauchot, 2010). Although similar, the case of a group of intruders moving simultaneously through grains has been substantially less studied and many questions remain to be answered. This sort of motion can be found, for instance, in the displacement of animals in the soil (Hosoi; Goldman, 2015) or in the growth of roots (Kolb *et al.*, 2017; Fakih *et al.*, 2019). When more than one intruder move within grains, the motion of each intruder can affect those of others, establishing a sort of cooperative behavior. Cooperative effects are constantly observed in nature when intruders move within a fluid. We can cite, for example, the reduction of drag when two spheres move side-by-side in a viscous flow (Happel; Brenner, 1983) or the flight of migration birds in a V-shaped formation. In this context, some investigations were carried out. The first type of study concerned intruders that moved freely in low-density grains (Pacheco-Vázquez; Ruiz-Suárez, 2010; Solano-Altamirano *et al.*, 2013; Carvalho; Franklin, 2022b) and the second type concerned threaded objects placed at a constant separation distance (Cruz; Caballero-Robledo, 2016; Merceron *et al.*, 2019; Dhiman *et al.*, 2020; Caballero-Robledo *et al.*, 2021; Pravin *et al.*, 2021; Carvalho; Franklin, 2022b; Carvalho *et al.*, 2024b). Some of these studies led to the prediction of side forces (of both attractive and repulsive natures, depending on the intruders' separation) between the intruders and the physical mechanisms behind them, while other studies predicted drag reduction, evincing a cooperative dynamics when intruders move together within a granular material.

From a different but similar perspective, on relatively larger and faster scales, we can observe the movement of a projectile (intruder) within grains, following its impact on granular targets, with the consequent formation of craters and the projectile penetration, which is often observed in nature at different scales. For instance, we find it in ballistics problems, when a seed fall from a tree, or in rare events such as the collision of objects with celestial bodies. Understanding their behavior, especially when subjected to external forces like impacts, is essential not only for scientific curiosity but also for solving practical engineering challenges. Impact, defined as a sudden application of force or energy, can lead to a cascade of intricate interactions among granular particles. The outcome of these interactions can vary widely, ranging from simple grain rearrangements to complex phenomena like energy dissipation, wave propagation, and even the onset of granular flows. The interest in impact within granular media spans across multiple disciplines, including physics, engineering, geology, and material science. To this end, small-scale experiments (Uehara *et al.*, 2003b; Walsh *et al.*, 2003; Katsuragi; Durian, 2007; Goldman; Umbanhowar, 2008; Seguin *et al.*, 2008; Pacheco-Vázquez; Ruiz-Suárez, 2010; Pacheco-Vázquez; Ruiz-Suárez, 2011; Carvalho *et al.*, 2024a) and numerical simulations (Ciamarra *et al.*, 2004; Seguin *et al.*, 2009; Carvalho *et al.*, 2023b; Carvalho *et al.*, 2023a) have proven to be extremely useful for understanding crater formation and projectile dynamics, leading to scaling laws for the projectile's penetration depth and crater diameter, models for the drag force experienced by the projectile during the penetration process, and mechanisms of energy dissipation. However, most of those studies are limited to the case of pure translation of the sphere, with no rotational motion.

In summary, the study of granular materials is a multidisciplinary task that unites diverse topics in physics, engineering, geophysics, planetary science, among others. Understanding the complex behaviors of these materials is essential to address natural or industrial challenges. The continuous studies on these matters lead to innovations that can impact many fields, from building better harvesting equipment to exploring distant planets. In particular, the research presented in this Thesis, on the dynamics of intruders moving over or within granular materials, aims at giving a contribution to further our current scientific understanding of this topic. This Thesis is concerned with the study of the response of granular materials when in the presence of a solid intruder, either when the intruder moves at a very low velocity inside it (quasi-static regime) or when it is impacted by an intruder at higher velocities (collisional regime). The research presented here employs a combination of numerical simulations, experimental investigations, and mathematical modeling to provide new insights into these complex interactions.

One part of the work investigates how the movement of a single intruder affects the granular structure, leading to the perception of drag by the intruder. Using discrete element method (DEM) simulations, we confirm that force networks within the granular medium play a crucial role. Specifically, we identify a "bearing network" that transmits larger forces from the intruder toward the walls, leading, sometimes, to localized jamming and high drag forces, and a "dissipative network" that carries smaller forces, which percolates over long distances. We also demonstrate that the extent of these force networks, as well as the formation of void regions behind the intruder, are significantly influenced by factors such as basal friction and the granular media compactness (Carvalho *et al.*, 2022).

In addition to studies of individual intruders, this research delves into the cooperative dynamics of multiple intruders. By simulating groups of intruders moving through a granular medium, we found that they exhibit cooperative behavior even when they are relatively far apart. This cooperation, which can result in reduced mean drag, is facilitated by the compaction and expansion of the granular material in front of and behind each intruder and affected by contact chains in the media. This leads to the discovery of an optimal spacing to minimize drag, which has practical implications for designing devices that interact with granular surfaces. Our findings also show that the initial arrangement of intruders can lead to specific collaboration patterns (final arrangement in space) (Carvalho; Franklin, 2022b). Experimentally, we confirmed this tendency of collaborative movement with manifestations leading to a reduction in mean drag, which proved to be more intense with the depth of the intruders in the granular medium. These observations led to the proposal of a mathematical model that describes well the drag reduction due to the collaborative motion of intruders in granular media (Carvalho *et al.*, 2024b).

This Thesis also extends to the impact of projectiles on granular targets, a phenomenon relevant in natural and industrial contexts. Using DEM simulations, we examined how several factors, including projectile rotation, bed compaction, and grain friction, affect crater formation and the forces experienced by the projectile (intruder). We found that a denser region forms beneath the projectile, contributing to its rebound, and that projectile rotation significantly increases penetration depth and crater diameter. These findings led to the proposal of scaling laws that help explain some characteristics of crater formation observed in different environments (Carvalho *et al.*, 2023b). Furthermore, our investigations of rotating granular projectile impacts highlighted how projectile cohesion (in aggregates) and spin influence material dispersion and crater shapes, offering insights into natural impact events such as asteroid collisions, as well as technological applications such as planetary exploration (Carvalho *et al.*, 2023a). Experimentally, we validated and extended these numerical findings by showing that rotational motion increases the penetration depth of spherical projectiles in granular media, leading to the development of a model that accounts for rotational effects. This model successfully predicts the depth achieved by rotating projectiles, providing valuable predictions for scenarios ranging from agricultural seed dispersal to space probe landings (Carvalho *et al.*, 2024a).

Overall, our research provides a contribution to the understanding of the fundamental mechanics of granular materials and their response to the motion of an intruder within it. By exploring isolated and cooperative behaviors of intruders and projectiles, this Thesis offers some insights that are applicable to a wide range of scientific and engineering fields. In Sec. 2, a brief historical overview of the interaction of intruders with granular materials is given. In

Sec. 3, the numerical and experimental methodologies employed throughout this Thesis are explained. In Sec. 4, numerical and experimental results concerning the quasi-static motion of intruders within a granular material are presented. In Sec. 5, numerical and experimental results concerning the collisional motion of projectiles impacting a granular material are presented. Finally, Sec. 6 presents the main conclusions of this Thesis and some topics to be investigated in the future.

2 HISTORICAL OVERVIEW OF THE INTERACTION OF INTRUDERS WITH GRANULAR MATERIALS

2.1 Quasi-static regime - Intrusion problems

The motion of a solid intruder in a granular medium is commonly found in nature and human activities. For example, we find it in the motion of animals and machines over and within granular matter (snakes, worms, vehicles, etc.), the penetration of solid bodies in sand (such as ballistic objects), and the impact of objects on sandy surfaces (such as the landing of space probes on other planets) (Askari; Kamrin, 2016; Zheng *et al.*, 2018). Depending on velocities, lengths, materials and concentrations involved, the granular system is forced to move in different manners. For instance, the motion can be highly inertial, with great part of the kinetic energy being dissipated through friction and collisions within grains (Bester; Behringer, 2017), or when the velocities involved are relatively small, it can be in quasi-static regime, being dominated by the formation and destruction of contact networks and stick-slip motion (Kolb *et al.*, 2013; Tordesillas *et al.*, 2014; Kozlowski *et al.*, 2019; Carlevaro *et al.*, 2020; Kozlowski *et al.*, 2022; Kozlowski *et al.*, 2021; Pugnaloni *et al.*, 2022; Carvalho *et al.*, 2022; Carvalho; Franklin, 2022b; Carvalho *et al.*, 2024b). This regime can be observed in the thrusting of ploughs in agricultural activities, in avalanche protection devices aimed at slowing down the flow (Benito *et al.*, 2012b; Texier *et al.*, 2023), in root growth (Kolb *et al.*, 2017; Fakih *et al.*, 2019), or in the motion of animals in the soil (Hosoi; Goldman, 2015). For higher velocities, a dilute regime appears, in which solid-solid collisions dominate (Andreotti *et al.*, 2011).

Given their importance, many studies were devoted over the last decades to stress transmission and jamming in granular matter under normal and shear stresses (Radjai *et al.*, 1998; Cates *et al.*, 1998; Majmudar; Behringer, 2005; Bi *et al.*, 2011; Seguin, 2020). Radjai *et al.* (1998) (Radjai *et al.*, 1998) showed that the stress transmission in a two-dimensional (2D) packing of rigid spheres under biaxial compression occurs through two complementary networks: a load-bearing network and a dissipative network. The former is a network of nonsliding contacts that transmit strong forces (higher than the average), carrying the deviatoric load and presenting anisotropy induced by shear, while the latter is a network of sliding contacts that transmit weak forces (smaller than the average), carrying only load contributing to the average pressure and presenting anisotropy in a direction orthogonal to that of the load-bearing network.

Later, Seguin (2020) (Seguin, 2020) investigated the force network of a monolayer of disks under vibration compressed above the limit for jamming. The results corroborate the existence of load-bearing and dissipative networks, and show that the latter is characterized by cycles consisting of 3 to 8 grains that are linked to the load-bearing chains, relieving part of the load. Cates *et al.* (1998) (Cates *et al.*, 1998) investigated fragile states in colloidal suspensions and granular materials, being defined as those whose internal structure has organized itself to support loads in certain directions, but not in others. They showed that those states result from the formation of force chains aligned in preferential directions, and, therefore, fragile matter undergoes jamming and is able to support loading in such directions, while it undergoes unjamming and suffers plastic deformation in others. Bi *et al.* (2011) (Bi *et al.*, 2011) showed that granular materials sheared by external stresses present not only the isotropic jamming observed in shear-free conditions, but also fragile states and shear jamming that appear at particle fractions lower than those necessary for isotropic jamming. They showed also that the fragile state appears under small shear stresses and is characterized by force chains that are one-directional, while the shear jamming results from stronger shear stresses with a force network that percolates in different directions.

For the case of an intruder moving in granular matter, local variations of particle fraction, forming compressed fronts and expanded trails (Kolb *et al.*, 2013; Seguin *et al.*, 2016), together with the breaking and reorganization of the force networks around the intruder, make the prediction of granular motion and drag forces complex. Many studies were therefore devoted to the drag force on intruders (Albert *et al.*, 1999; Albert *et al.*, 2001; Stone *et al.*, 2004; Geng; Behringer, 2005; Costantino *et al.*, 2008; Kolb *et al.*, 2013; Seguin *et al.*, 2016; Kozlowski *et al.*, 2019; Carlevaro *et al.*, 2020). In particular, Kolb *et al.* (2013) (Kolb *et al.*, 2013) investigated experimentally the drag force on the intruder and the motion of grains around it as the intruder was driven within a bidimensional granular system consisting of disks. They showed the formation of a region in front (upstream) of the intruder where grains reach the jamming packing fraction (compression), and a region behind (downstream) the intruder where a cavity without grains (expansion) appears. As the intruder moves, grains recirculate intermittently from the compressed front toward the downstream region with the occurrence of chain breaking and unjamming, making the drag force on the intruder to fluctuate, sometimes very strongly, around a mean value. They showed also that the cavity tends to disappear and the drag to increase greatly as the average particle fraction grows because the compressed front is confined by lateral walls, leaving no room for local compression/expansion in the limit of the highest possible packing fraction. Seguin *et al.* (2016) (Seguin *et al.*, 2016) inquired further into the motion around an intruder in a granular system similar to that of Ref. (Kolb *et al.*, 2013), but using simultaneously photoelastic and tessellation techniques to measure the strain and stress rates at the grain scale. They showed that, although the strain and shear are localized, the macroscopic friction coefficient μ (ratio of shear to normal stresses) depends on the azimuthal direction, indicating that a local rheology is not adequate to describe the motion of grains around the intruder.

More recently, Kozlowski *et al.* (2019) (Kozlowski *et al.*, 2019) and Carlevaro *et al.* (2020) (Carlevaro *et al.*, 2020) investigated the effects of the packing fraction and the interparticle and basal frictions (the latter between the bottom wall and the grains, excluding the intruder) on the motion of an intruder moving within a bidimensional granular system in a Couette geometry. The experiments (Kozlowski *et al.*, 2019) made use of photoelastic disks moving over either a glass plate or a layer of water, while the numerical simulations (Carlevaro *et al.*, 2020) were 2D and varied the friction coefficient (static and dynamic) over broader ranges. In both, the intruder was driven by the continuous loading of a spring. The experiments showed that in the presence of basal friction there are two regimes depending on the particle fraction: at low particle fractions, an intermittent regime where the intruder moves freely between clogging events appears, while at high particle fractions a stick-slip regime takes place, where the intruder moves through fast slip events alternated with long periods of creep. In the absence of basal friction (water layer), only the intermittent regime is observed. The numerical simulations showed that the intermittent to stick-slip transition is highly affected by the dynamic coefficient of basal friction, with the intermittent regime occurring for values below 0.1 and the stick-slip for higher values, while it is virtually independent of the static coefficient, which contributes mainly to the duration of stick events. Later, Pugnaloni *et al.* (2022) (Pugnaloni *et al.*, 2022) showed that the stick-slip dynamics depends only on the sizes involved, being independent of friction coefficients, and proposed a model for the energy released by the spring as a function of the packing fraction. Tripura *et al.* (2022) (Tripura *et al.*, 2022) studied numerically how a two-dimensional granular medium consisting of single and pairs of disks (dumbbells) behaves when displaced by a larger intruder (single disk). They found that the drag force on the intruder increases with the proportion of dumbbells in the system, that the additional resistance caused by dumbbells is negligible when the microscopic friction is set to zero, and that the stress propagated in front of the intruder increases with its diameter. The problem was inquired further by Refs. (Kozlowski *et al.*, 2021; Kozlowski *et al.*, 2022), who measured the effects of grain angularity on the stress propagation and stick-slip dynamics, showing that angular grains resist to motion under lower packing fractions and have higher shear strengths. Recently, Carvalho *et al.* (2022) (Carvalho *et al.*, 2022) investigated numerically the motion of an intruder within a two-dimensional granular medium using a setup similar to that of Ref. (Seguin *et al.*, 2016). Among other findings, they showed that the force network can reach regions far downstream of the intruder, and that grains within the bearing chains creep while the chains break. The latter result explains how the load chains break and allow the intruder to proceed with its motion.

In the light of the complex constitutive behavior of granular media, partly due to its non-linearity, history-dependence and non-locality, forces on arbitrarily shaped granular intruders have been described by simple and yet empirical "resistive force hypotheses" (RFT), being more of a hypothesis than a theory due to the lack of physical explanations (Askari; Kamrin, 2016). The resisting force against the motion of the intruder is represented by a simple superposition principle (Maladen *et al.*, 2011a), where the intruder's boundary is divided into differential elements and the total force equals the sum of the forces on each element as if it were moving on its own. Despite the lack of physical explanation, Ref. (Askari; Kamrin, 2016) shows that granular RFT arises due to frictional yield criterion in the absence of other cohesion forces, both being mechanical features of dry granular media.

Given the problem complexity, most of previous studies were devoted to the motion of one intruder within a granular medium (Albert *et al.*, 1999; Albert *et al.*, 2001; Stone *et al.*, 2004; Geng; Behringer, 2005; Costantino *et al.*, 2008; Kolb *et al.*, 2013; Seguin *et al.*, 2016; Kozlowski *et al.*, 2019; Carlevaro *et al.*, 2020; Pugnaloni *et al.*, 2022; Carvalho *et al.*, 2022), in general using two-dimensional systems, and, although using relatively simple setups, they brought important insights into the problem. One case of particular interest is when several intruders move within grains, since the motion of each intruder can affect those of others (Carvalho; Franklin, 2022b), establishing a cooperative behavior. Some applications can be envisaged: if one intruder affects the motion of others, the ground can be probed to detect the presence of solid objects, such as buried rocks or ice. This opens new opportunities for prospecting the soil of planets and moons for the presence of ice and other materials, for instance.

Although there are not many studies concerning groups of intruders moving through grains, some model experiments were carried out to elucidate this problem (Pacheco-Vázquez;

Ruiz-Suárez, 2010; Solano-Altamirano *et al.*, 2013; Dhiman *et al.*, 2020; Kawabata *et al.*, 2020; Pravin *et al.*, 2021; Espinosa *et al.*, 2022). The first type of study concerns intruders that move freely in low-density grains (densities much lower than those of intruders, also known as light granular medium). For example, Pacheco-Vázquez and Ruiz-Suárez (2010) (Pacheco-Vázquez; Ruiz-Suárez, 2010) showed that a pair of intruders that impact a light granular medium side by side and are let to sink, first repel themselves (in the horizontal plane, transverse to their motion) once the impact has taken place and afterward attract each other. They explained these observations by an increase in the granular pressure between the intruders (initial repulsion) and a Bernoulli-like mechanism (attraction). For a number of intruders slightly larger (five, for instance) placed initially side by side, Pacheco-Vázquez and Ruiz-Suárez (2010) (Pacheco-Vázquez; Ruiz-Suárez, 2010) showed that they assume upward and downward convex configurations in succession, depending on the initial intruder-intruder separation (above a certain value they fall in parallel). They explained this behavior based on a sequential increase and decrease of the drag on the central intruders caused by the compaction and expansion of the bed, respectively. Finally, they showed that the intruders always finish horizontally aligned, irrespective of their number, initial configuration (vertical, horizontal or grouped distributions of intruders), sizes and densities, which they explained by the compaction-expansion mechanism. Later, Solano-Altamirano *et al.* (2013) (Solano-Altamirano *et al.*, 2013) studied a similar impact configuration in a quasi 2D geometry, observing attractive and repulsive behaviors between the intruders. They also invoked a Bernoulli-like effect to explain the attractive behavior, and justified the repulsive effect as due to a granular jamming in the region between the intruders. They found that the initial repulsion exists only when the separation between intruders is less than 6 grain diameters and attraction when the separation is less than 5-6 times the intruder diameter and sinking velocities higher than 1 m/s. The behaviour of several intruders has also been investigated numerically in the case of pairs and trios of larger disks (intruders) moving freely amid smaller disks (quasi two-dimensional granular medium) (Carvalho; Franklin, 2022b). These simulations showed the existence of a cooperative dynamics between the intruders, even when they were at relatively large distances from each other. They also revealed that the type of cooperation depends on the initial arrangement of intruders, with the same spatial configuration eventually reached for some of the arrangements. The cooperative dynamics were rationalised as the result of compaction and expansion of granular matter in front and behind each intruder, respectively.

A second type of study concerns threaded objects placed at a constant separation distance. Caballero *et al.* (2021) studied the side force experienced by a pair of cylindrical intruders placed in a discharging granular silo (Caballero-Robledo *et al.*, 2021). They observed attractive side forces for intermediate separations and repulsive forces at very small separations. They correlated these observations with the difference of granular temperature between the left and right regions of the granular flow around the intruders. Analogous observations were made by a previous numerical study carried out in a similar configuration (Cruz; Caballero-Robledo, 2016). Other numerical simulations were conducted by Dhiman *et al.* (2020) to explore the interaction between a pair of spherical intruders forced to move horizontally within a 3D granular bed (Dhiman *et al.*, 2020). They found that the side force acting on intruders varies with separation, from repulsive for small values to attractive for relatively higher values, with an equilibrium separation in the repulsive-attractive transition for which the transverse force is zero. However, they showed that the Bernoulli-like effect proposed previously cannot explain alone the forces acting on intruders. Based on their findings, they proposed that repulsion and attraction are given, respectively, by the formation and break up of contact chains linking the intruders, which depend, in their turn, on the intruders' surfaces and the shear zones close to them: the intruders' surfaces tend to stabilize contact chains, while the shear zones tend to destabilize them. They also found that the drag force acting on each intruder does not vary significantly with their separation, although it is lower than in the case of a single intruder. Carvalho and Franklin (2022) (Carvalho; Franklin, 2022b) investigated numerically the motion of pairs of larger disks (intruders) moving horizontally amid smaller disks (quasi two-dimensional granular medium) at a constant velocity. They observed a non-monotonic behavior of the drag force with the separation of the intruders: first the drag increases with the separation between the intruders' centroids, then it reaches a maximum, next it decreases until reaching a minimum, and finally it increases again until reaching the same value found for an individual intruder. Recently, Carvalho *et al.* (2024) (Carvalho *et al.*, 2024b) conducted an experimental investigation to examine how the drag forces acting on a pair of transversely aligned intruders vary with their depth and transverse separation as they move at constant speed through a granular bed. Their findings revealed that the mean drag experienced by each intruder is lower than that of a single intruder when the separations are small. As the separation increases, the drag rises until it reaches a plateau equivalent to the drag experienced by a single intruder at large separations, indicating a cooperative dynamic within a specific distance range. Additionally, they observed that the drag reduction for small separations increases with depth, and that the mean drag data varies exponentially with intruder-intruder separation.

Interaction effects between threaded objects were also observed experimentally and numerically for a pair of rods penetrating vertically into a granular bed (Pravin *et al.*, 2021). Pravin *et al.* (2021) investigated how the resisting forces and work acting on a pair of rods varied with their separation during the penetration. In addition to the transverse separation of intruders (rods in this case), they varied also the sizes of grains and intruders, and the friction coefficient of grains, and in all cases they found that the work for penetration varies non-monotonically with the intruders' separation. Beginning from touching intruders, the work first increases with increasing the separation while the gap remains small enough to hinder the passage of grains in the region between the intruders (i.e., the work increases due to the growth of the effective cross-sectional area). When the separation becomes enough to allow the flow of grains in the gap, the work decreases until reaching a plateau at a separation of approximately 11 grain diameters. In the increasing-decreasing transition, there is a maximum value of work that is approximately 25% higher than that at large separations (plateau), the corresponding separation being of 2-3 grain diameters.. In order to characterize the interaction between two intruders, Merceron *et al.* (2018) (Merceron *et al.*, 2018) carried out experiments where they visualized the granular flow around a pair of intruders placed side by side. They investigated a confined 2D system where two intruders were forced to move upwards into an assembly of small bidisperse disks (which density was similar to that of intruders). They showed that there is a separation distance between the intruders below which the motion of grains in front of one intruder is affected by the other, and that, in opposition in some way to previous works, this distance is independent of the intruders' size.

2.2 Collisional regime - Impact problems

The impact of projectiles onto granular targets, with the resulting crater formation and projectile penetration, is frequently observed in nature at different scales. We find it in the collision with the ground of seeds falling from trees, which, when small and light, involves mass, lengths and velocities of the orders of 10 g, 1 cm and 1 cm/s, respectively, corresponding to energy levels of the order of 10^{-7} J (the equivalent of lighting a LED lamp for approximately 0.0000001 s) and forming cm-size craters. We find it also in the collision of km-size asteroids impacting planets and moons at 10^3-10^4 km/h, which corresponds to energies of the orders of

10^{16} (equivalent to a hydrogen bomb) to 10^{18} J, and forms km-size craters. However, the values involved can be much higher: for instance, the *Tycho* and *Posidonius* craters found on Earth's moon have diameters of approximately 100 km (85 and 95 km, respectively) (Ruiz-Suárez, 2013; Krüger *et al.*, 2016), and the *Odisseus* crater found on Saturn's moon Tethys (Barlow *et al.*, 2017) a diameter of 445 km.

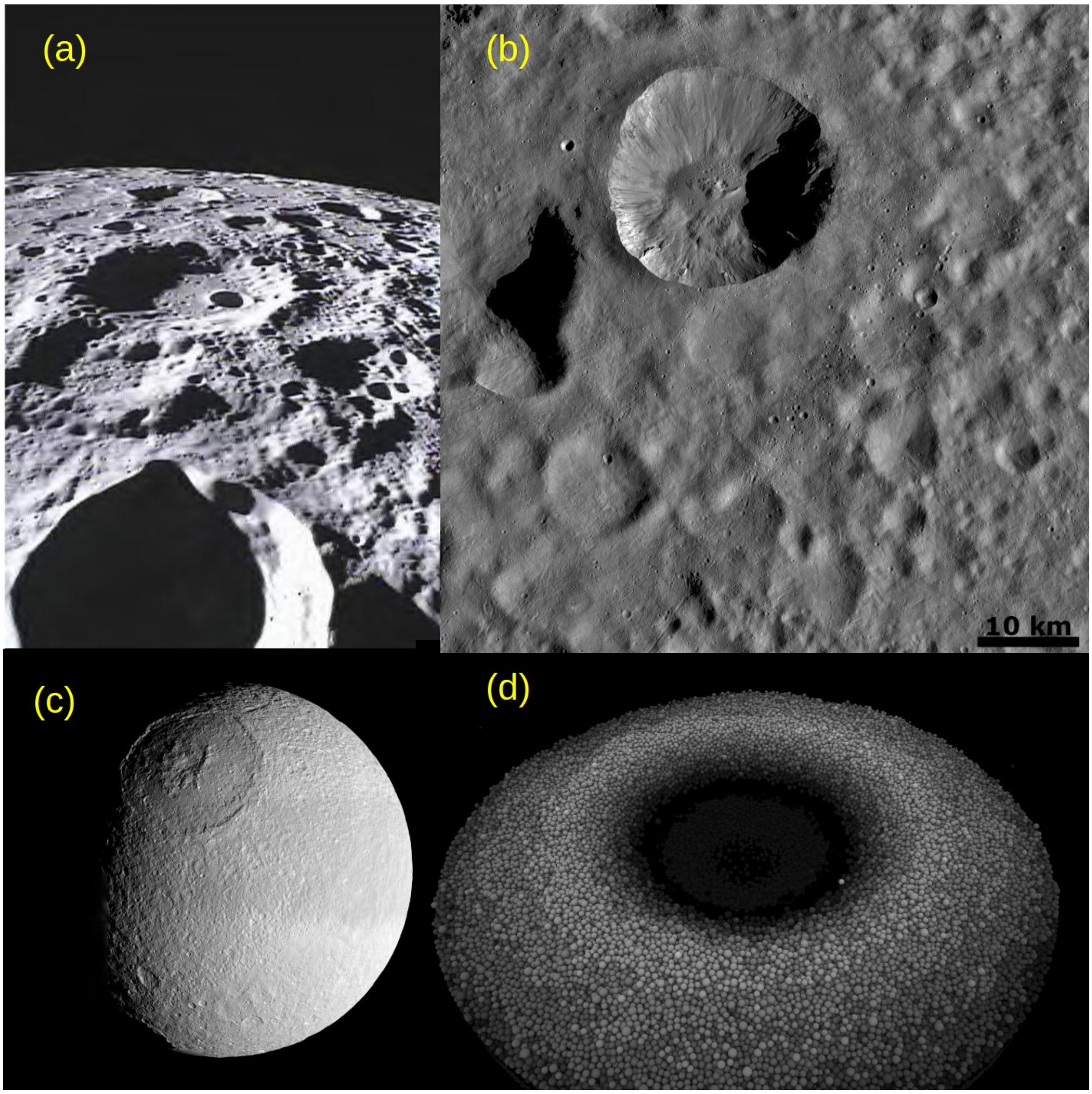

Figure 2.1 – (a) Craters on Earth's moon (in the middle, with a smaller bow-shaped crater inside, is Poinsot crater); (b) Craters on Vesta, with a recent 20-km-diameter crater on the top of image; (c) 445-km-diameter crater on Saturn's moon Tethys; (d) 76-mm-diameter crater obtained numerically from the impact of a 25-mm-diameter steel sphere falling from 50 mm onto a bed of particles (glass spheres with mean diameter of 1 mm). Images (a), (b) and (c): Courtesy NASA/JPL-Caltech. Image adapted from (Carvalho *et al.*, 2023a).

The different scales of impacting objects found in nature imply in huge differences in collisional processes and resulting craters. For example, under small energies (low masses and velocities) the impact results only in partial penetration of the projectile and ejection of part of the grains, while under large energies it involves also melting and evaporation of part of the material. Concerning the resulting crater, there are different types that depend basically on its size and gravity acceleration (Melosh; Ivanov, 1999), but strong variations occur and a classification is not straightforward (Barlow *et al.*, 2017; Arvidson, 1974). In general, small craters have a bowl shape (also called simple craters), with roughly a parabolic profile [Fig. (2.1)b], and as the craters become larger, they present a flat floor and a central peak or peak rings. For even larger craters, they have, in addition to the flat floor and central peak (or peak rings), external rings that are formed from the partial collapse of steep walls [Fig. (2.1)c]. For reference, lunar craters with diameters smaller than approximately 10 km are bowl-shaped, those with diameters of the order of 100 km have the external rings, flat floor and peak rings, and craters within those values generally vary between bowl-shaped and flat floor with central peak (Melosh; Ivanov, 1999). Notwithstanding their ubiquitous nature, the mechanisms leading to different crater shapes are far from being completely understood.

Besides the involved energies, other properties such as the projectile and ground compositions (Pacheco-Vázquez; Ruiz-Suárez, 2011), confinement (Seguin *et al.*, 2008), projectile spin (Carvalho *et al.*, 2023b), and microscopic friction (Carvalho *et al.*, 2023b) can strongly influence the crater shape. The diversity of scales and parameters makes of cratering an intricate problem. Although the collisional processes of different systems are different, they bear similarities if we consider the dynamics of the granular material alone, which can be explored if we assure that some proportions and ratios are within the same ranges (scaling laws). By using dimensional analysis, Holsapple (1993) (Holsapple, 1993) showed that the dimensionless volume of the crater is a function of two pressure ratios and the density ratio ρ_p/ρ, where ρ_p and ρ are the densities of the projectile and grains, respectively. One dimensionless pressure ratio, Π_σ, is the material strength (yield stress) σ of the target normalized by the dynamic pressure $\rho_p V_p^2$,

$$\Pi_\sigma = \frac{\sigma}{\rho_p V_p^2}\,, \tag{2.1}$$

where V_p is the velocity of the projectile at the collision. The other one is the projectile weight divided by its surface area and normalized by the dynamic pressure,

$$Fr^{-1} = \frac{D_p g}{V_p^2}\,, \tag{2.2}$$

where D_p is the projectile diameter and g is the modulus of gravity acceleration $\vec{g}$. This pressure ratio is the equivalent of the inverse of a Froude number Fr^{-1}: gravitational effects compared to inertia. If we neglect ρ_p/ρ, since in many cases it is of order one, it is important to assure that we are considering similar dimensionless pressures when comparing collisions of different scales: in cases where the target strength is higher than the lithostatic pressure, Π_σ is dominant (strength regime), and for the inverse, Fr^{-1} dominates (gravity regime) (Holsapple, 1993). Therefore, for small objects colliding with resistant targets, such as a small seed falling on Earth, Π_σ dominates, while for km-size projectiles under strong gravity accelerations Fr^{-1} dominates. In geophysical problems, typical Froude numbers are within $10^{-6} \lesssim Fr^{-1} \lesssim 10^{-2}$, where the upper end is sometimes considered in the strength regime, but usually acknowledged as being in the gravity regime (Holsapple, 1993; Ruiz-Suárez, 2013).

Because impacts of km-scale asteroids are extraordinarily rare events on the human timescale (every few hundred million years on Earth's surface, for example), laboratory-scale experiments and numerical simulations have proven essential in the investigation of crater formation, part of them carried out in the strength regime (given the relatively small velocities). However, by decreasing D_p and/or increasing V_p, some experiments and grain-scale simulations reached $Fr^{-1} \leq 10^{-4}$, being in the gravity regime. In addition, as pointed out by Holsapple (1993) (Holsapple, 1993), the range of Fr^{-1} for the gravity regime is larger when the target consists of cohesionless grains, so that some experiments and simulations with $Fr^{-1} = 10^{-2}$ can be considered in that regime. This has allowed us to perform extrapolations of laboratory results to geophysical problems in order to obtain hints about the granular behavior and, perhaps most important, discard wrong assumptions (Ruiz-Suárez, 2013).

Bearing in mind the two different regimes, the scales of the crater diameter D_c and depth h_c can be obtained from physical arguments (Amato; Williams, 1998; Uehara *et al.*, 2003b; Uehara *et al.*, 2003a; Walsh *et al.*, 2003). For the gravity regime, it is expected that the available energy at the impact E is dissipated by excavating the crater, i.e., displacing the crater volume ($\sim D_c^3$) by a distance proportional to h_c. By hypothesizing that $h_c \sim D_c$ in this regime, we find $D_c \sim E^{1/4}$ and, therefore, $h_c \sim E^{1/4}$. For the strength regime, cratering is dominated by the target strength, i.e., the crater volume is excavated by plastic deformation, giving thus $D_c \sim E^{1/3}$. However, more sophisticated computations and/or experiments are necessary to better understand the physical mechanisms of cratering.

Because impacts of km-scale asteroids are extraordinarily rare events within the human timescale (of the order of millions of years on Earth's surface, for example), laboratory-scale experiments and numerical simulations have proven essential in the investigation of crater formation (Uehara *et al.*, 2003b; Walsh *et al.*, 2003; Ciamarra *et al.*, 2004; Katsuragi; Durian, 2007; Vet; Bruyn, 2007; Goldman; Umbanhowar, 2008; Seguin *et al.*, 2008; Seguin *et al.*, 2009; Umbanhowar; Goldman, 2010; Katsuragi; Durian, 2013). By assuring $\mathrm{Fr}^{-1} \lesssim 10^{-1}$ in most cases and using targets consisting of cohesionless grains, those works allowed extrapolations of laboratory results to geophysical problems, so that hints about the granular behavior were obtained and wrong assumptions discarded (Ruiz-Suárez, 2013). The penetration dynamics of a sphere in a granular medium has been extensively studied both experimentally (Uehara *et al.*, 2003b; Ambroso *et al.*, 2005; Bruyn; Walsh, 2004; Seguin *et al.*, 2009; Carvalho *et al.*, 2024a), numerically (Seguin *et al.*, 2009; Carvalho *et al.*, 2023b; Carvalho *et al.*, 2023a), and by modeling (Goldman; Umbanhowar, 2008; Hinch, 2014; Katsuragi; Durian, 2007; Guo, 2018).

Concerning the experiments and numerical simulations of a solid sphere impacting a dry granular medium, important aspects were commonly observed for the gravity regime. In general, it was found that the collision has two distinct phases: In the first phase, the grains in the impact region are fluidized and the projectile penetrates the target with a predominant inertial drag, while in the second phase the bed hardens again and the projectile continues its penetration with a depth-dependent frictional drag (Goldman; Umbanhowar, 2008). The projectile thus decelerates while penetrating the granular medium because of the opposing drag and, just before reaching a full stop, suffers a discontinuity in its acceleration: the dynamic drag is changed to a static force that supports the projectile (Goldman; Umbanhowar, 2008; Katsuragi; Durian, 2007). The crater diameter D_c has been reported (Uehara *et al.*, 2003b; Uehara *et al.*, 2003a; Walsh *et al.*, 2003; Vet; Bruyn, 2007) to, indeed, scale as $D_c \sim E^{1/4}$, but different scalings were obtained for h_c. For the latter, some authors found that $h_c \sim D_c$ and then $h_c \sim E^{1/4}$ (as expected for the gravity regime) (Walsh *et al.*, 2003; Vet; Bruyn, 2007), but others found different scales, such as $h_c \sim V_p^{2/3}$ (Uehara *et al.* (2003) (Uehara *et al.*, 2003b; Uehara *et al.*, 2003a), where in their case h_c was equal to the depth δ reached by the projectile) or $h_c \sim V_p$ (proportional thus to the momentum of the projectile at the impact, as shown by de Bruyn and Walsh (2004) (Bruyn; Walsh, 2004)).

In particular, Ciamarra *et al.* (2004) (Ciamarra *et al.*, 2004) investigated experimentally and numerically the impact of a projectile onto a two-dimensional granular medium (disks), and found that the impact time t_c (time interval from reaching the target to full stop) is independent of V_p, so that the projectile penetration δ depends on the impact velocity. They found a constant deceleration that is proportional to V_p, which explains the independence of t_c, but that is in disagreement with the direct measurements made later by Goldman and Umbanhowar (2008) (Goldman; Umbanhowar, 2008). Uehara *et al.* (2003) (Uehara *et al.*, 2003b; Uehara *et al.*, 2003a) released spheres of different densities ρ_p from different initial heights h onto cohesionless beads and, for partially penetrating spheres ($\delta = h_c$), found that $D_c \sim \left(\rho_p D_p^3 H\right)^{1/4}$ $\sim E^{1/4}$ (according to predictions), where H is the total drop distance (vertical distance traveled by the projectile, including the penetration depth δ, so that $H = h + \delta$). However, they found that $h_c \sim H^{1/3}$, h_c not scaling with E, so that the crater aspect ratio is not necessarily fixed. They also found that the friction and restitution coefficients of the projectile and diameter of the grains do not affect the crater morphology. Besides the scaling laws for the crater h_c and penetration δ depths, many other aspects remain without a consensus, such as the shape of craters, the role of force chains and jamming, the effects of the packing fraction and friction, etc.

The first description of the resultant force on a projectile moving within a granular medium is probably that done by Poncelet (1829) (Poncelet, 1829), as the sum of the projectile weight, an inertial force, and a friction term. As pointed out by Ruiz-Suárez (2013) (Ruiz-Suárez, 2013), Poncelet did not consider that the friction term should vary with the penetration depth, which was included later in the model (Tsimring; Volfson, 2005; Katsuragi; Durian, 2007). The mechanical actions involved when an object impacts a granular material are often related to the drag force. This drag force generates penetration resistance, and, for a sphere impacting a granular material, it consists of a sum of two terms. The first term is frictional, linked to the hydrostatic pressure prevailing beneath the sphere during penetration. The second term is of collisional origin, linked to the dissipation of energy by collisions between grains. Considering a vertical coordinate y oriented downwards and a force drag $\vec{F}_{drag}$ oriented upwards (with respect to gravity acceleration $\vec{g}$), the resultant force $\vec{F}_p$ (oriented upwards) acting on a solid projectile of mass m_p while it penetrates the granular bed is given by Eq. (2.3),

$$F_p = m_p \frac{d^2y}{dt^2} = -m_p g + F_{drag}\,, \tag{2.3}$$

where F_p and F_{drag} are the moduli of $\vec{F}_p$ and $\vec{F}_{drag}$, respectively, $V = dy/dt$ is the instantaneous velocity of the projectile, and $F_{drag} = \xi V^2 + \kappa y$ (inertial and friction terms), ξ and κ being parameters that depend on the projectile characteristics (density and shape) (Katsuragi; Durian, 2007; Pacheco-Vázquez; Ruiz-Suárez, 2010). Umbanhowar and Goldman (2010) (Umbanhowar; Goldman, 2010) proposed that Eq. (2.3) is incomplete to describe projectiles impacting targets with different packing fractions ϕ, being valid only close to a critical packing ϕ_{cps}.

Goldman and Umbanhowar (2008) (Goldman; Umbanhowar, 2008) observed fluctuations during the inertial phase, and they conjectured that such fluctuations are due to the formation and collapse of granular chains. They showed that, at the acceleration discontinuity that occurs at the end of the motion, the projectile moves upwards before reaching full stop, and also observed that t_c is approximately independent of V_p above a threshold value. Finally, they proposed that in Eq. (2.3) the inertial term dominates at high velocity and shallow penetration, while at low velocities and deep penetrations a viscous-like term linear in V must be added and dominates the drag force together with the frictional term. For oblique collisions, Ye *et al.* (2021) (Ye *et al.*, 2021) also proposed that a viscous-like force, added to the frictional and inertial ones, is important for the projectile dynamics.

Another important question is how the available energy is distributed/dissipated during the impact. Tsimring and Volfson (2005) (Tsimring; Volfson, 2005) proposed that the impact energy is dissipated through three mechanisms: the lifting of grains, inelastic collisions, and microscopic solid friction, in proportions of approximately 10, 20 and 70%, respectively. By carrying out 2D (two-dimensional) DEM (discrete element method), Kondic *et al.* (2012) (Kondic *et al.*, 2012) corroborated that solid friction dissipates a significant part of the available energy, but Seguin *et al.* (2009) (Seguin *et al.*, 2009) found the contrary: that impact on frictionless grains causes the same penetration depths and stopping times. Seguin *et al.* (2009) (Seguin *et al.*, 2009) argue that inelastic collisions are the main responsible for the energy dissipation. One possible explanation for an independence on the solid friction is that the quasi-static motion of grains would by turns form and break granular chains, whose compressive stresses would engender jammed and unjammed states (Ruiz-Suárez, 2013). Although light was shed on the dissipation issue, it remains an open question.

Recently, Carvalho *et al.* (2023) (Carvalho *et al.*, 2023b) carried out 3D (three dimensional) DEM (discrete element method) simulations and showed that microscopic friction affects considerably the crater morphology. In addition, they showed that differences in initial packing fractions can engender the diversity of scaling laws found in the literature (Uehara *et al.*, 2003b; Uehara *et al.*, 2003a; Walsh *et al.*, 2003; Seguin *et al.*, 2008; Katsuragi; Durian, 2013), and proposed an *ad hoc* scaling that collapsed their data for the penetration length and can perhaps unify the existing correlations.

However, most of those studies are limited to the case of pure translation of the sphere, with no rotational motion. Taking this rotational movement into account is important for many problems of locomotion (Li *et al.*, 2013b; Zhang; Goldman, 2014; Hosoi; Goldman, 2015; Kumar *et al.*, 2019; Seguin *et al.*, 2022), physical biology (Jung *et al.*, 2017), and military applications (Robins, 1742). Rotational effects were recently observed to alter significantly the dynamics of penetration. Carvalho *et al.* (2023) (Carvalho *et al.*, 2023b) investigated numerically the initial spin of the projectile and showed that both δ and D_c increase with the projectile spin, that large asymmetries can appear depending on the spin axis, and that the final rebound of the projectile is suppressed by the spin. In a more recent study, the authors confirmed experimentally that the rotational velocity of a projectile increases its penetration depth into granular material. However, the influence of rotation on penetration depth was shown to be less significant than that of impact velocity. The authors incorporated the effect of rotation into the penetration depth by modifying the conventional scaling law for penetration depth without rotation. Furthermore, by accounting for rotational effects, they have adapted the dynamics equation [Eq. (2.3)] governing the penetration of a projectile into granular materials (Carvalho *et al.*, 2024a). Although substantially less studied in granular materials (Ye *et al.*, 2012; Ye *et al.*, 2015; Kumar *et al.*, 2019; Carvalho *et al.*, 2023b; Carvalho *et al.*, 2023a; Carvalho *et al.*, 2024a), the effect of rotation has been widely studied in Newtonian fluids. The Magnus effect is a well-known phenomenon that finds applications ranging from boat sailing to the physics of sports. In those situations, the rotation applied perpendicular to the direction of the flow creates lift forces on the object. The Magnus effect has also been observed for granular materials; however, the direction of the lifting force was found to be opposite to that normally found in viscous fluids (Kumar *et al.*, 2019). Considering the flow of a Newtonian fluid around a sphere, the drag force, i.e., parallel to the flow direction, is not significantly affected by the rotation of the object. In particular, if the axis of rotation is aligned with the flow direction, then the drag force remains similar to the case without rotation for both high and low Reynolds numbers (Gladkov, 2022). Granular media exhibit a different behavior in comparison with a Newtonian fluid, their ability to modify the pressure under shear being a major feature of those materials.

Although most of experiments on impact cratering were for solid projectiles, many problems, in particular in geophysics, concern the impact of aggregates. For example, in the case of asteroids or meteors impacting the surface of a planet, aggregates can be divided into smaller parts which, in their turn, penetrate into the target and excavate the crater. This process can be responsible for the spreading of materials on Earth, just below the ground surface, such as nickel, platinum and gold (Ganapathy, 1980; Sawlowicz, 1993; McDonald *et al.*, 2001). The impact of non-spinning projectiles consisting of aggregated materials was inquired into by Pacheco-Vázquez and Ruiz-Suárez, who investigated first the sinking of collections of a few intruders in low-density granular medium (Pacheco-Vázquez; Ruiz-Suárez, 2010) and afterwards the impact of aggregates onto a granular bed (Pacheco-Vázquez; Ruiz-Suárez, 2011). In general, they showed that, although the formation of complex craters is affected by the packing fraction of the projectile, the same scale $D_c \sim h^{1/4}$ found for solid projectiles remains valid. However, D_c is larger for granular projectiles (aggregates), with a discontinuity accounting for the cohesion of grains (energy necessary for fragmentation). They also showed that $h_c \sim h^{1/3}$ is valid only for small energies: h_c decreases abruptly above a threshold value and remains constant for higher energies. If the fragments once forming the projectile sink in the granular bed (which can happen for low-density beds), they move with a cooperative dynamics (Pacheco-Vázquez; Ruiz-Suárez, 2010).

Recently, Carvalho *et al.* (2023) (Carvalho *et al.*, 2023a) numerically investigated how projectile spin and cohesion influence crater shapes and the spread of projectile material both on and beneath the surface. The study found that as bonding stresses decrease and initial spin increases, the projectile's grains spread farther radially from the impact point, remain closer to the surface with shallower penetration depths, and disperse over larger horizontal distances. They also showed that some grains become deeply buried in the granular bed, while others accumulate above the surface, forming peaks or populating the crater's corona. As a result, the crater shape flattens, with peaks appearing around the rim and at the crater's center. They also observed that the penetration depth of rotating projectiles depends on angular velocity and the degree of collapse, measured by the number of detached particles, rather than bonding stresses themselves. At high spinning velocities, excess breaking energy leads mainly to greater horizontal spreading and peak formation, without significantly affecting penetration depth.

3 METHODOLOGY

3.1 Numerical Methodology

All numerical simulations in this Thesis were performed using the Discrete Element Method (DEM) (Cundall; Strack, 1979). DEM is a numerical technique used to simulate the behavior of granular materials (discrete media) by modeling the interactions between individual particles and boundaries. Originally developed by Cundall and Strack (Cundall; Strack, 1979), DEM has become an essential tool in the study of granular materials, providing insights into their mechanical behavior (Zhu *et al.*, 2008). DEM solves the dynamics of each individual particle, which can move both translationally and rotationally, by computing the forces and torques on each of them (Newton's laws of motion). It accounts for the forces and torques acting on each particle due to contact with neighboring particles, the boundaries, and external force fields. It uses several models to describe how particles interact, typically including models for normal and tangential forces, damping, and friction. These models have parameters (friction coefficients, coefficients of restitution, material properties, etc.) that can be adjusted to represent different types of granular materials (Kloss *et al.*, 2012; Kloss; Goniva, 2010; Berger *et al.*, 2015). Furthermore, DEM simulations can incorporate various boundary conditions, such as fixed or periodic walls, to mimic real-world scenarios. A major advantage of this type of simulation is that, although they are numerically expensive due to the high number of particles and interactions (Derakhshani *et al.*, 2015), they provide valuable dynamic information, such as the trajectories and forces acting on each individual particle, which can be very difficult to obtain through experimental methods (Zhu *et al.*, 2008).

We used the open-source code LIGGGHTS (Kloss *et al.*, 2012; Kloss; Goniva, 2010; Berger *et al.*, 2015) to carry out the computations (<http://www.cfdem.com>). LIGGGHTS is an open-source DEM particle simulation software whose main developer and author is Christoph Kloss. LIGGGHTS stands for LAMMPS Improved for General Granular and Granular Heat Transfer Simulations (LIGGGHTS(R)-PUBLIC..., 2016). On its turn, LAMMPS (Large-scale Atomic/Molecular Massively Parallel Simulator) is a classic and widely used molecular dynamics simulator (<http://lammps.sandia.gov>) that, thanks to physical and algorithmic analogies, offers basic functionalities for DEM simulations (LIGGGHTS(R)-PUBLIC..., 2016), the main adaptions in LIGGGHTS regarding the addition of mesh geometry support and granular models for particle–particle and particle–wall interactions (Berger *et al.*, 2015). LIGGGHTS is currently used by a variety of research institutions worldwide in diverse areas such as chemistry, physics, pharmaceuticals, engineering, food production, mining, among others. Furthermore, it is capable of modeling a variety of systems at various scales, from just a few particles to millions of them (LIGGGHTS(R)-PUBLIC. . . , 2016). In the most general sense, LIGGGHTS integrates (using Velocity-Verlet time integration (Berger *et al.*, 2015)) Newton's equations of motion for collections of atoms, molecules, or macroscopic particles interacting through short or long-range forces with a variety of initial and/or boundary conditions (LIGGGHTS(R)-PUBLIC. . . , 2016; Berger *et al.*, 2015). Additionally, it tracks the trajectory of each particle, while modeling particle-particle and particle-wall collisions with a soft-sphere approach. It applies spring-dashpot models to calculate forces caused by particle-particle interactions and particle-wall interactions, in addition to considering volume forces, such as gravity, for example. For computational efficiency, it makes use of optimized neighbor lists (Yao *et al.*, 2004) to track down the closest particles. On parallel machines, the software uses spatial decomposition techniques to partition the simulation domain into small 3D subdomains, one of which is assigned to each processor, thus performing more rapidly the desired computations (LIGGGHTS(R)-PUBLIC. . . , 2016).

In this Thesis, two different types of simulations were performed: i) Two-dimensional simulations (2D) of disks settled over a horizontal wall and confined by vertical walls (although the solid objects are three-dimensional (3D) disks, we employ the terminology *two-dimensional granular system* since they form a monolayer of particles); ii) 3D simulations of spheres confined in a cylindrical container. The formulation for both kinds of simulations is very similar, with some slight differences concerning the way some parameters for the particles interactions are modeled (Secs. 3.1.1.1 and 3.1.2.1 clarify those differences).

In order to perform the numerical simulations with disks (2D), we used an additional toolbox called "Discrete-Element, bonded-particle Sea Ice – DESIgn" (Herman, 2016). DESIgn is a toolbox carefully adapted for use with the open-source code LIGGGHTS (Kloss *et al.*, 2012; Kloss; Goniva, 2010; Berger *et al.*, 2015). The source files, together with the complete technical documentation, including basic tutorials and validation, can be found in Herman (2016) (Herman, 2016). Originally, the DESIgn toolbox was developed as a tool to study the processes that model a wide range of sea ice types. But as Herman (2016) (Herman, 2016) points out, it can be applied to other 2D materials composed of disk-shaped grains (as is our case). The version used in this Thesis (DESIgn 1.3a) is an extension of previous versions described in other works by Herman (Herman, 2013b; Herman, 2013a). The model considers the interactions between neighboring particles in direct contact (based on Hertzian contact mechanics - Appendix A), taking into account repulsive and frictional forces between them (Herman, 2016). The complete set of equations used in this model are shown in Sec. 3.1.1. Since this is an open library, it is possible to implement new features in the toolbox. In particular, in order to produce disks that have friction with the bottom walls, we implemented this force in the DESIgn code (please check Sec.3.1.1 for a description of this implementation and (Lima *et al.*, 2021) for the source code implemented in the toolbox). More details regarding this toolbox can be found in (Herman, 2016).

In the following, Sec. 3.1.1 presents the numerical methodology for the 2D case while Sec. 3.1.2 presents the numerical methodology for the 3D case.

3.1.1 2D simulations - Quasi-static regime - Intrusion problems

The methodology presented in this section will later be employed to study numerically the displacement of intruders (larger disks) amid smaller disks, with the results obtained being presented in Sec. 4.1.

The dynamics of each particle is computed by the linear and angular momentum equations, given by Eqs. (3.1) and (3.2), respectively,

$$m\frac{d\vec{u}}{dt} = \vec{F}_c + m\vec{g}; \tag{3.1}$$

$$I\frac{d\vec{\omega}}{dt} = \vec{T}_c, \tag{3.2}$$

where $\vec{g}$ is the acceleration of gravity and, for each particle, m is the mass, $\vec{u}$ is the velocity, I is the moment of inertia, $\vec{\omega}$ is the angular velocity, $\vec{F}_c$ is the resultant of contact forces between solids, and $\vec{T}_c$ is the resultant of contact torques between solids. The contact forces and torques are computed by Eqs. (3.3) and (3.4), respectively,

$$\vec{F}_c = \sum_{i\neq j}^{N_c}\left(\vec{F}_{c,ij}\right) + \sum_{i}^{N_w}\left(\vec{F}_{c,iw}\right); \tag{3.3}$$

$$\vec{T}_c = \sum_{i\neq j}^{N_c}\vec{T}_{c,ij} + \sum_{i}^{N_w}\vec{T}_{c,iw}, \tag{3.4}$$

where $\vec{F}_{c,ij}$ and $\vec{F}_{c,iw}$ are the contact forces between particles i and j and between particle i and the wall, respectively, $\vec{T}_{c,ij}$ is the torque due to the tangential component of the contact force between particles i and j, and $\vec{T}_{c,iw}$ is the torque due to the tangential component of the contact force between particle i and the vertical wall. N_c is the number of particles in contact with particle i, and N_w the number of particles in contact with the wall. Since the grains are disks lying on a horizontal wall, $\vec{F}_{c,iw}$ includes the friction force between the bottom wall and each grain, which follows the Coulomb law with static and dynamic values (Andreotti *et al.*, 2011).

For the contact forces between particles ($\vec{F}_{c,ij}$), and between particles and the lateral walls (included in $\vec{F}_{c,iw}$), the elastic Hertz-Mindlin contact model (Di Renzo; Di Maio, 2005) is used. Additional details of the Hertzian model in a more general context can be found in (Brilliantov *et al.*, 1996; Zhang; Makse, 2005; Schwager, 2007; Zhou, 2011), while a brief description of Hertz's contact model is given in Appendix A. This model consists in the combination of two spring-dashpots, the first one including the normal interactions and a Coulomb friction coefficient, and the second one including the tangential forces, as schemed in Fig. (3.1)a. Equations for computing the normal and tangential forces based on particle overlaps (modeling deformations) are shown in Sec. 3.1.1.1.

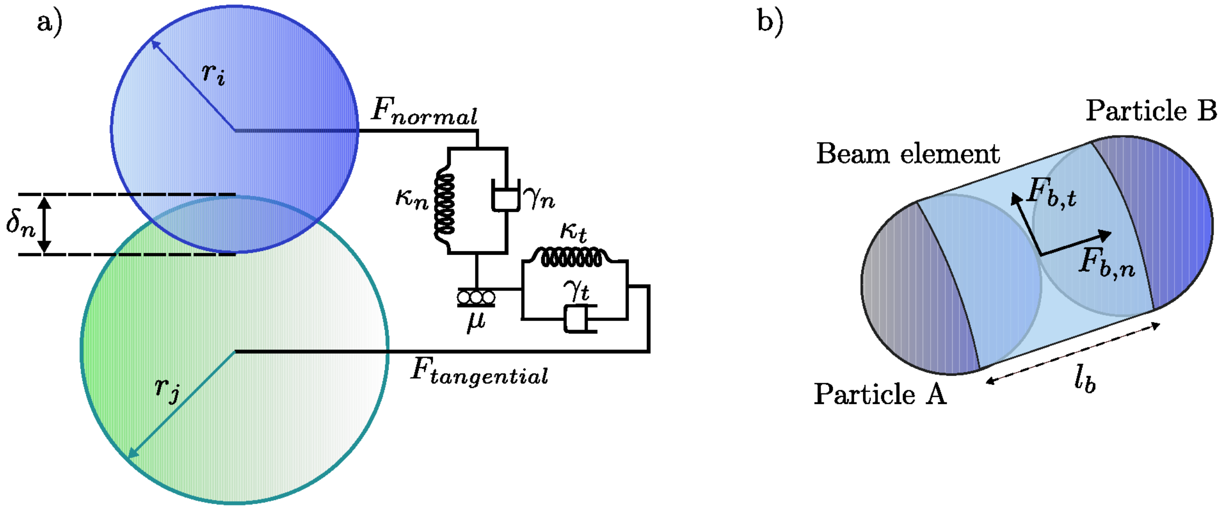

Figure 3.1 – (a) Scheme of the spring-dashpot model (Hertz-Mindlin) used in the numerical simulations. Image adapted from (Sun *et al.*, 2023). (b) Schematic of a bond connecting two particles. Image adapted from (Guo *et al.*, 2013; Chen *et al.*, 2022b).

Because the DESIgn toolbox (Herman, 2016) originally does not compute the friction between the grains and the bottom wall (included in $\vec{F}_{c,iw}$), we implemented that in its library (the source code for this implementation can be found at (Lima *et al.*, 2021)). The friction force was modeled in a similar manner as in Carlevaro *et al.* (2020) (Carlevaro *et al.*, 2020): if a grain i is moving at a speed $v_i = |\vec{u}_i|$ above a threshold value v' ($v_i > v'$), then a dynamic friction force with the bottom wall is considered as being $\vec{F}_{c,iw} = -\mu_{d,g} m_i |\vec{g}| \vec{u}_i / |\vec{u}_i|$. Conversely, if it is moving with a velocity v_i smaller than or equal to the threshold value v' ($v_i \leq v'$), then a static friction force with the bottom wall $\vec{F}_{c,iw} = -\mu_{s,g} m_i |\vec{g}| \vec{u}_i / |\vec{u}_i|$ is applied and the particle is stopped by setting $v_i = 0$. This ensures that a grain will only resume its motion if the forces exerted by the other grains exceed the static friction force (Carlevaro *et al.*, 2020). In this model, we do not consider rotational friction between the grains and the bottom wall. We intend to implement other dry friction models (Pennestrì *et al.*, 2016; Modesto *et al.*, 2022) in the future and see how the results obtained with the presented model would compare with those obtained under different models.

3.1.1.1 Contact model - 2D simulations

This section describes the contact model used in our simulations using the open-source code LIGGGHTS (Kloss *et al.*, 2012; Kloss; Goniva, 2010; Berger *et al.*, 2015) together with the DESIgn toolbox (Herman, 2016) for the 2D simulations of this Thesis. The contact force between particles i and j, $\vec{F}_{c,ij}$, is usually decomposed into its normal and tangential components, whose magnitudes are given, respectively, by:

$$F_{c,n} = \kappa_n \delta_n - \gamma_n \frac{d\delta_n}{dt}; \tag{3.5}$$

$$F_{c,t} = \kappa_t \delta_t - \gamma_t \frac{d\delta_t}{dt}. \tag{3.6}$$

The two terms in Eq. (3.5) correspond to a repulsive force and a viscoelastic damping. As for the case of Eq. (3.6), the tangential force is the sum of a shear force and a damping term. In Eqs. (3.5) and (3.6), δ_n is the normal displacement and $\delta_n \geq 0$ when two grains are in contact; δ_t is the tangential displacement, measured in the direction perpendicular to the plane of contact. In addition, the coefficients κ_n, κ_t, γ_n, and γ_t are functions of the displacements as well of the shape, size and material properties of the particles in contact. Please check the scheme in Fig. (3.1)a for a clearer picture. The exact form of such coefficients depend on the contact model chosen. All damping components depend on the relative velocity between the interacting particles: $d\delta_n/dt$ denotes the normal and $d\delta_t/dt$ the tangential component of the relative velocity of the interacting particles.

For the case of two interacting particles i and j, characterized by Young moduli E_i and E_j, Poisson's ratios ν_i and ν_j, radii r_i and r_j, and thicknesses h_i and h_j, with $h_m = \min\{h_i, h_j\}$, one can define an effective radius r_c, an effective mass m_c, an effective contact modulus E_c and an effective shear modulus G_c as:

$$r_c = \frac{r_i r_j}{r_i + r_j}, \tag{3.7}$$

$$m_c = \frac{m_i m_j}{m_i + m_j}, \tag{3.8}$$

$$E_c = \left(\frac{1-\nu_i^2}{E_i} + \frac{1-\nu_j^2}{E_j} \right)^{-1}, \tag{3.9}$$

$$G_c = \frac{1}{2}\left[\frac{(1+\nu_i)(2-\nu_i)}{E_i} + \frac{(1+\nu_j)(2-\nu_j)}{E_j} \right]^{-1}. \tag{3.10}$$

In addition, the normal overlap (displacement) δ_n between the disks in contact [please check the scheme in Fig. (3.1)a)] is measured along $\mathbf{r}_{ij}$ and is defined as:

$$\delta_n = r_i + r_j - |\mathbf{x}_i - \mathbf{x}_j|. \tag{3.11}$$

The equations presented above are also valid if one of the materials in contact is a wall. In this case, for a flat wall, $r_j \to \infty$, δ_n is computed using the normal distance of the grain to the wall, and δ_t is computed as the displacement parallel to the wall of the center of grains. Some contact models also relate the damping ratio β with the restitution coefficient ϵ of underdamped systems, leading to:

$$\beta = \frac{\ln(\epsilon)}{\sqrt{\ln^2(\epsilon) + \pi^2}}. \tag{3.12}$$

For the case of two elastic cylinders, the normal displacement is given by (Herman, 2016):

$$\delta_n = \frac{F_{c,n}}{\pi h_m E_c}\left[1 + \ln\left(\frac{2\pi h_m^3 E_c}{r_c F_{c,n}} \right) \right], \tag{3.13}$$

and an approximate expression for the normal contact force can be given by (Herman, 2016):

$$F_{c,n} = \pi E_c h_m \delta_n f\left(\frac{\delta_n r_c}{2h_m^2} \right). \tag{3.14}$$

In this way, κ_n is defined as:

$$\kappa_n = \pi E_c h_m f\left(\frac{\delta_n r_c}{2h_m^2}\right); \qquad f(x) = \frac{p_1 x^2 + p_2 x + p_3}{x^2 + q_1 x + q_2}. \tag{3.15}$$

In the DESIgn toolbox (Herman, 2016), the expression for f, as denoted by the second expression in the right-hand side of Eq. (3.15), is modeled with coefficients for, $x \in [0, 0.2]$, given by: $p_1 = 0.9117$, $p_2 = 0.2722$, $p_3 = 0.003324$, $q_1 = 1.524$, and $q_2 = 0.03159$.

In many viscoelastic contact models, the Hertzian theory is used to compute the normal repulsive force (i.e., the κ_n coefficient), as well as to estimate the shear and damping terms in Eqs. (3.5) and (3.6). In the DESIgn toolbox (Herman, 2016), κ_n is computed from Eq. (3.15) and the remaining coefficients by:

$$\kappa_t = 6\frac{G_c}{E_c}\kappa_n, \tag{3.16}$$

$$\gamma_n = -\beta\sqrt{5\kappa_n m_c}, \tag{3.17}$$

$$\gamma_t = -2\beta\sqrt{5\frac{G_c}{E_c}\kappa_n m_c}. \tag{3.18}$$

The reader can find a more complete description of this model in (Herman, 2016), along with additional information.

3.1.2 3D simulations - Collisional regime - Impact problems

The methodology presented in this section will later be employed to study numerically the impact of spherical projectiles onto a granular bed, with the results obtained being presented in Sec. 5.

This section describes the contact model used in our simulations using the open-source code LIGGGHTS (Kloss *et al.*, 2012; Kloss; Goniva, 2010; Berger *et al.*, 2015) for the 3D simulations of this Thesis. The equations presented in this section bear a lot of similarities with those presented in Sec. 3.1.1.1, the main difference being that in this case we are working with spherical particles, whereas in the other we were working with cylindrical particles. In the case of spherical particles, the contact area between them is circular, with a radius increasing as the normal force is increased; in the case of discs, the contact area is rectangular, with a constant height equal to h_m and the width increasing with the increase in the normal force (Herman, 2016). Here, the Newton's law of motion is computed for each individual particle. Basically, as in the 2D simulations (Sec. 3.1.1) the code computes the linear [Eq. (3.1)] and angular [Eq. (3.2)] momentum equations at each time step, however here considering rolling resistance. The contact forces ($\vec{F}_{c,ij}$ and $\vec{F}_{c,iw}$) are computed using the elastic Hertz-Mindlin contact model (Di Renzo; Di Maio, 2005), described in Sec. 3.1.2.1. Please check the scheme presented in Fig. (3.1)a for a clearer picture. In the contact torques ($\vec{T}_{c,ij}$ and $\vec{T}_{c,iw}$), the rolling resistance is considered through a coefficient of rolling friction μ_r, also described in Sec. 3.1.2.1. The torque due to rolling resistance is important if angular grains (sand, for example) are modeled as spherical particles with the angularity effects embedded in the rolling friction (Derakhshani *et al.*, 2015). Such effects are negligible for perfect spherical grains.

3.1.2.1 Contact model - 3D simulations

The contact force between particles i and j , $\vec{F}_{c,ij}$, or between a particle i and the wall, $\vec{F}_{c,iw}$, is usually decomposed into normal and tangential components, given by Eqs. (3.19) and (3.20), respectively.

$$F_{c,n} = \kappa_n \delta_n - \gamma_n \frac{d\delta_n}{dt}; \tag{3.19}$$

$$F_{c,t} = \kappa_t \delta_t - \gamma_t \frac{d\delta_t}{dt}. \tag{3.20}$$

The two terms in the right hand side of Eq. (3.19) correspond to a repulsive force and a viscoelastic damping, and $\delta_n \geq 0$ is the normal displacement of two solids in contact. When two spherical particles are in contact, δ_n is given by Eq. (3.11).

For the contact between a spherical particle and a wall, δ_n is computed as the normal displacement between the center of the grain and the contact point. The two terms in the right hand side of Eq. (3.20) correspond to a shear force and a viscoelastic damping, and δ_t is the tangential displacement measured in the direction perpendicular to the plane of contact. Please check the scheme in Fig. (3.1)a for a clearer picture. $F_{c,t}$ is given by Eq. (3.20) until it reaches $F_{c,t} = \mu F_{c,n}$, where μ is the microscopic coefficient of friction. From that moment, slip occurs and the tangential force becomes governed by the Coulomb's Law,

$$F_{c,t} = \mu F_{c,n}, \tag{3.21}$$

until the contact is finished. Coefficients κ_n, κ_t, γ_n, and γ_t are functions of the displacements and grain properties. They are computed by Eqs. (3.22) to (3.25), based on the effective radius r_c, mass m_c, contact modulus E_c, and shear modulus G_c [Eqs. (3.7) to (3.10)] of particles i and j with, respectively, Young moduli E_i and E_j and Poisson's ratios ν_i and ν_j,

$$\kappa_n = \frac{4}{3} E_c \sqrt{R_c \delta_n}; \tag{3.22}$$

$$\kappa_t = 8 G_c \sqrt{R_c \delta_n}; \tag{3.23}$$

$$\gamma_n = -2\sqrt{\frac{5}{6}} \beta \sqrt{2 E_c \sqrt{R_c \delta_n} m_c}; \tag{3.24}$$

$$\gamma_t = -2\sqrt{\frac{5}{6}} \beta \sqrt{8 G_c \sqrt{R_c \delta_n} m_c}, \tag{3.25}$$

where β is a damping coefficient based on the restitution coefficient ϵ, computed as in Eq. (3.12).

For a particle of radius r, contact torques are computed as the sum of the torques due to $F_{c,t}$ and rolling friction, for all its contacts. For $\vec{T}_r$ representing the torque caused by rolling friction, contact torques can thus be summarized as in Eq. (3.26):

$$\vec{T}_c = \sum \left(r F_{c,t} \vec{n} \times \vec{t} + \vec{T}_r \right), \tag{3.26}$$

where $\vec{n}$ and $\vec{t}$ are unit vectors in the normal and tangential directions, respectively. $\vec{T}_r$ can be modeled as having spring and damping components, but Derakhshani *et al.* (2015) (Derakhshani *et al.*, 2015) showed that the damping component is negligible for DEM computations. Therefore,

$$\vec{T}_r = -k_r \Delta\theta_r \vec{n} \times \vec{t}, \tag{3.27}$$

where θ_r is the incremental rolling at the considered contact and k_r is the rolling stiffness, given by Eq. (3.28).

$$k_r = \mu_r R_c \frac{F_{c,n}}{\theta_r^m}. \tag{3.28}$$

In Eq. (3.28), θ_r^m is the angle for incipient rolling and μ_r is the coefficient of rolling resistance.

More details regarding this formulation can be found in (LIGGGHTS(R)-PUBLIC…, 2016; Derakhshani *et al.*, 2015).

3.1.2.2 3D simulations - Cohesive projectile (aggregate)

In this section, we describe the model we used to carry out 3D DEM computations of spinning granular projectiles (aggregates) impacting onto a granular bed, for different bonding stresses (between the projectile's grains), initial spins and initial heights. The results obtained can be seen in Sec. 5.1.2.

To begin, we need to build the aggregate (shown in Fig. 5.20b) that will later form the projectile used in our simulations. To do that, firstly a shell of spherical shape and same size of solid projectiles investigated in Carvalho *et al.* (Carvalho *et al.*, 2022) is created. Afterward, 1 mm diameter particles are randomly generated inside the shell until filling the entire space. The particles in contact are then bonded together [please check the scheme in Fig. (3.1)b)], and their density is slightly altered so that the aggregate reaches a bulk density of 7865 kg/m^3, identical to solid projectiles. Finally, the spherical shell is deleted.

When in the presence of bonds [Fig. (3.1)b)], the relative motion of spheres leads also to bond deformation. Therefore, additional force $\vec{F_b}$ and moment $\vec{T_b}$ are induced on the spheres to resist deformation. These additional terms can be decomposed into normal and tangential components, as shown in Guo *et al.* (2013) (Guo *et al.*, 2013) and Schramm *et al.* (2019) (Schramm *et al.*, 2019):

$$\vec{F_b} = \vec{F}_{b,n} + \vec{F}_{b,t}; \tag{3.29}$$

$$\vec{T_b} = \vec{T}_{b,n} + \vec{T}_{b,t}. \tag{3.30}$$

The material that bonds two or more particles together acts also as a spring and damper system. Thus, based on the model presented in (Guo *et al.*, 2013), each component of Eqs. (3.29) and (3.30) can be written as:

$$\vec{F}_{b,n} = k_{b,n} A_b \vec{v}_n \Delta t + 2\beta_b \vec{v}_n \sqrt{m k_{b,n}}; \tag{3.31}$$

$$\vec{F}_{b,t} = k_{b,t} A_b \vec{v}_t \Delta t + 2\beta_b \vec{v}_t \sqrt{m k_{b,t}}; \tag{3.32}$$

$$\vec{T}_{b,n} = k_{b,t} I_p \vec{\omega}_n \Delta t + 2\beta_b \vec{\omega}_n \sqrt{I k_{b,t} I_p}; \tag{3.33}$$

$$\vec{T}_{b,t} = k_{b,n} I_a \vec{\omega}_t \Delta t + 2\beta_b \vec{\omega}_t \sqrt{I k_{b,n} I_a}. \tag{3.34}$$

The first terms on the right-hand side of Eqs. (3.31)–(3.34) correspond to the incremental normal force, shear force, torsional moment, and bending moment, respectively. The terms in these equations are defined as follows: A_b is the cross sectional area of the bond material; $\vec{v}_n$ and $\vec{v}_t$ are the normal and tangential components of the relative velocity between the two particles, respectively; Δt is the time step of DEM computations; β_b is the local damping coefficient of bonds, which in our case is equal to 0.5; m is the mass each particle; I_p and I_a are the polar and second moments of inertia, respectively; $\vec{\omega}_n$ and $\vec{\omega}_t$ are the normal and tangential components of the relative angular velocities between two particles, respectively; I is the moment of inertia; and $k_{b,n}$ and $k_{b,t}$ are the normal and tangential stiffness constants for bonds, respectively. These two last quantities are given by:

$$k_{b,n} = \frac{E_b}{l_b}; \tag{3.35}$$

$$k_{b,t} = \frac{k_{b,n}}{2(1-\nu)}, \tag{3.36}$$

where E_b is the bond Young's modulus (kept equal to the particle Young's modulus in our case); l_b is the bond equilibrium length, considered here as the particle radius; and ν is the Poisson's ratio. We note that $k_{b,n}$, $k_{b,t}$, $k_{b,t} I_p$ and $k_{b,n} I_a$ represent the normal, shear, torsional and bending stiffness of the bond, respectively.

Finally, if the magnitude of forces and moments surpass, at any time, the maximum normal or tangential bond strength, respectively, the bond is broken.

3.2 Experimental Methodology

3.2.1 Quasi-static regime - Intrusion problems - Cooperative motion

The experiments consist in pulling intruders [polyamide spheres with a diameter $d = 20$ mm - Fig. (3.3)a] at a constant velocity V_0 inside a granular medium made of slightly polydisperse glass spheres [diameter $d_g = 1 \pm 0.3$ mm and density $\rho \simeq 2.5 \times 10^3$ kg m^{-3} - Fig. (3.15)a]. The grains are contained in a rectangular box 365 mm long, 270 mm wide, filled to a height of 97 mm [Fig. 3.2(a)]. To ensure the randomness of the initial conditions and the homogenization of the granular bed, the box is vibrated manually along the transverse y-direction before each experiment takes place, which results in a flattened free surface bed with an initial packing fraction of $\phi = 0.60 \pm 0.02$, measured by weighing the contents of the box. We find that this procedure leads to reproducible measurements.

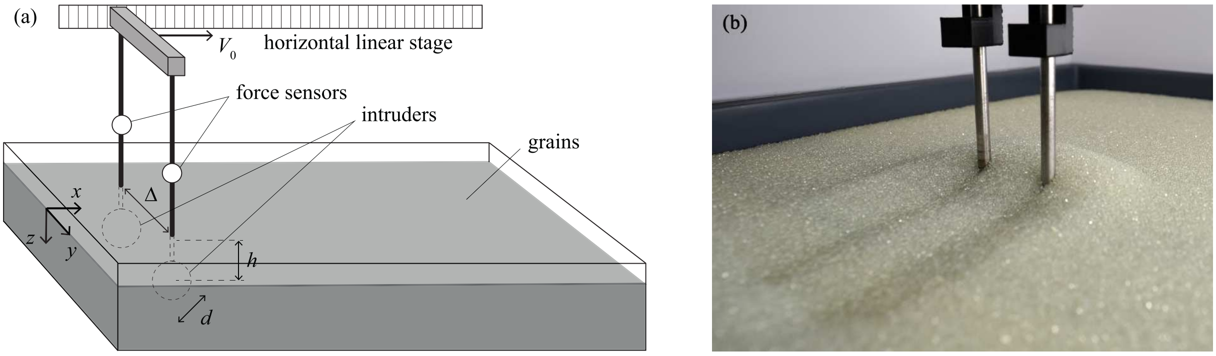

Figure 3.2 – (a) Sketch of the experimental setup for the displacement along the x-axis of two spherical intruders of diameter d, immersed in grains at the depth h. (b) Picture of an experiment for two immersed intruders $\Delta = 30$ mm apart, at depth $h = 14$ mm and moving at the velocity $V_0 = 2.7$ mm s^{-1} during the forward journey.

The intruders are attached to cylindrical rods of 5 mm in diameter, preventing any tilting or rotation, as shown in Fig. (3.3)c, and immersed in the bed at depth h (h being the distance separating the free surface of grains from the center of the intruder). The rods are connected to force gauges (*single point load cell 780 g, ID3132_0, Phidgets Inc.*) that measure (indirectly) the longitudinal time-varying drag force $f_0(t)$ at a frequency of 60 Hz. The rods are attached to the moving device via adapters that were 3D printed. The output voltage signal of the load cells is acquired through a high-resolution 24-bit analog-to-digital converter four-input *PhidgetBridge* circuit [*ID 1046_0B*, showed in Fig. (3.3)b], with data acquisition controlled by an in house code.

The force gauges were calibrated by attaching standard masses [Fig. (3.4)d] of a known weight to them (this process was repeated several times before and after the experiments, in different days). The results of these calibrations are presented in Figs. (3.4)a and (3.4)b, where one notes a linear relation between the applied mass and the resulting voltage signal. The little differences given by the results presented in Figs. (3.4)a and (3.4)b are due to small adjustments in the screws that connect the force gauges to the cylindrical rods. Note that by rotating the force sensors 90° over their main axis, one is able to measure side forces (perpendicular to the drag force but in the same plane) between the intruders (Dhiman *et al.*,

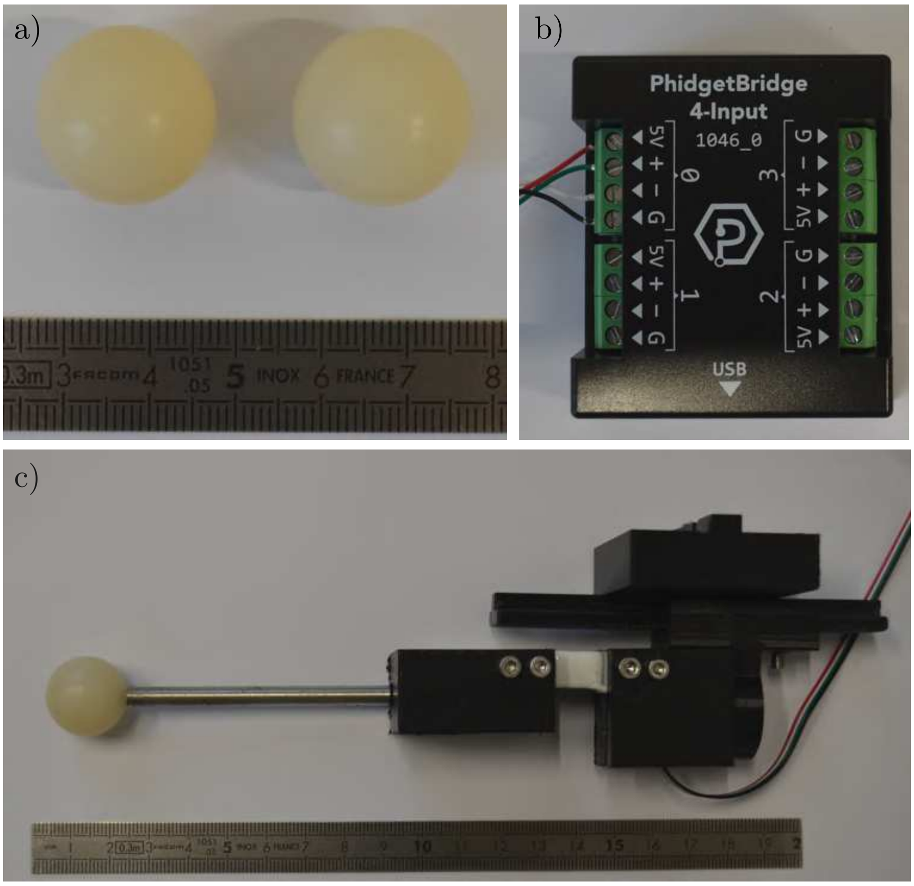

Figure 3.3 – (a) Polyamide spheres (intruders) with diameter $d = 20$ mm. (b) Analog-to-digital converter four-input *PhidgetBridge* circuit. (c) Assemble of the moving parts, showing an intruder, a cylindrical attaching rod, a load cell (in white), and a 3D printed adapter (in black), which is fixed at the moving device.

2020). The calibration curves under these circumstances are shown in Fig. (3.4)c.

By using the linear relations of the form $V = aM + b$ in the caption of Fig. (3.4), where a and b are coefficients, forces F can then be calculated by:

$$F = \frac{(V - a)g}{b}, \tag{3.37}$$

where g is the acceleration of gravity.

The whole system is fixed to an x-direction moving plate, controlled by a linear stepper motor ensuring the displacement of the intruders at a constant velocity V_0 from 10^{-1} to 10 mm s^{-1} [Fig. 3.2(a)].

Two distinct configurations will be considered: (i) the displacement of a single intruder in the x-direction from one edge of the box to the other, and initially placed at $y = 0$ and depth $z = h$; (ii) the displacement of two side-by-side intruders at the same abscissa x and same depth $z = h$, located initially at $y = \pm\Delta/2$ and separated by a distance Δ measured from

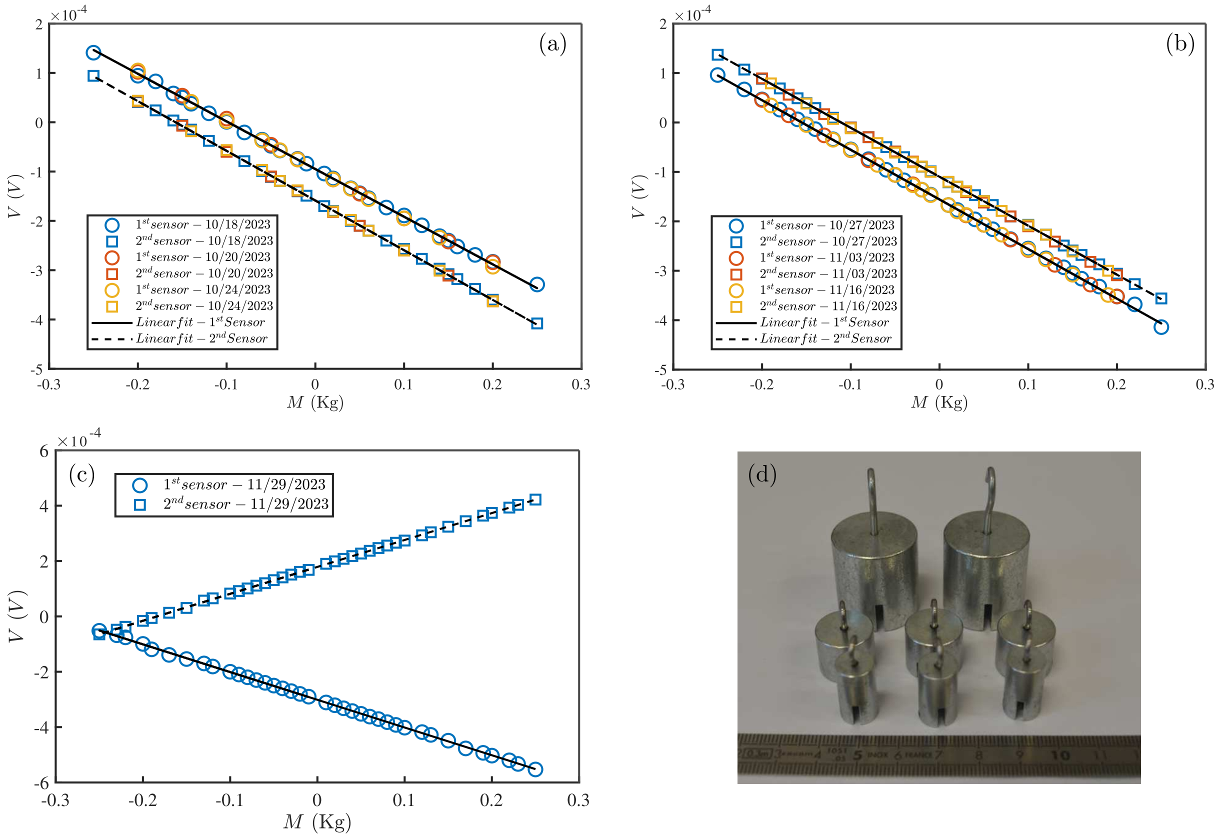

Figure 3.4 – Calibration curves (mass M as a function of voltage V) for measuring drag [(a), (b)] and side forces [(c)]. (a) Linear fit for the 1^{st} force sensor given by the solid line (—): $V = -0.000966M - 0.000095$; linear fit for the 2^{nd} force sensor given by the dashed line (- - -): $V = -0.001008M - 0.000159$. (b) Linear fit for the 1^{st} force sensor given by the solid line (—): $V = -0.001004M - 0.000156$; linear fit for the 2^{nd} force sensor given by the dashed line (- - -): $V = -0.000990M - 0.000110$. (c) Linear fit for the 1^{st} force sensor given by the solid line (—): $V = -0.001002M - 0.000301$; linear fit for the 2^{nd} force sensor given by the dashed line (- - -): $V = 0.000973M + 0.000179$. (d) Standard masses of a known weight used in the calibration process.

their centers, as seen in Fig. 3.2(a) and Fig. 3.5(b), presented here for illustration purposes only. To prevent any wall effects (Seguin *et al.*, 2008), we ensure to stay far enough from the side walls during an experiment, with an intruder/wall distance of approximately $3\,d$, and we restrict immersion depths to $h \leq 49$ mm to maintain a distance greater than $2.5\,d$ between the intruders and the bottom wall. Finally, note that one experiment consists of moving the intruder forward (along positive x) in the undisturbed granular medium [Fig. (3.2)b], and then, in a second step, making the return path (towards negative x) in the wake generated by the forward path and seen in Fig. (3.5)a.

Finally, in all drag measurements acquired during this experimental study and presented in Sec. 4.2, the drag force measured during the movement of the rod alone (i.e., without

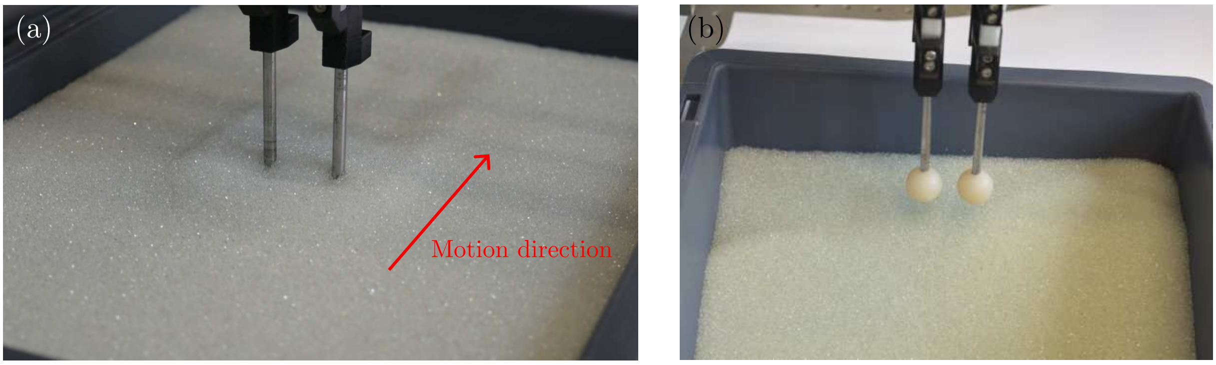

Figure 3.5 – (a) Example of a backward motion (intruders moving in their own wake). (b) Intruders inside the granular bed (illustration purposes only).

the intruder attached to its end) has been subtracted from the force signal for each probed depth h, so as to retain only the force experienced by the intruder. The drag forces measured F_0 (defined in Sec'. 4.2.2) for each probed length of the cylindrical rod below the surface of the granular media h_{rod} are shown in Fig. (3.6). Note that the power fit coefficients calculated are close to those found in the literature (Albert *et al.*, 1999; Wieghardt, 1975).

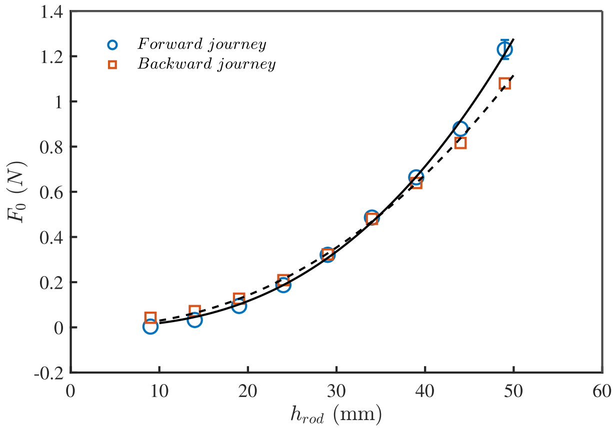

Figure 3.6 – Mean drag force F_0 as a function of the cylindrical rod height h_{rod}. Power law fit for the forward journey given by the solid line (—): $F_0 = (4.5938 \times 10^{-5})h_{rod}^{2.62}$; power law fit for the backward journey given by the dashed line (- - -): $F_0 = (1.6752 \times 10^{-4})h_{rod}^{2.25}$.

The results obtained with these experiments can be seen in Sec. 4.2.

3.2.2 Visualization of contact forces - Photoelasticity

One way to observe the distribution of contact forces inside a granular material is to use appropriate photoelastic techniques, making use of photoelastic disks, illumination schemes, and polarizers (Majmudar; Behringer, 2005; Daniels *et al.*, 2017; Zadeh *et al.*, 2018; Zadeh *et al.*, 2019). The photoelastic technique for quantifying internal stresses in some types of materials is based on the fact that light can be polarized in different ways in birefringent materials. When a photoelastic material is placed between two polarizers and is subjected to the application of stresses, each region of the stressed material rotates the polarization of light according to the amount of local stress. This creates a visual pattern of alternating light and dark heterogeneous lines within the material, associated with the local internal stress. This pattern depends on how the polarizers are oriented, the geometric shape and composition of the material, and the way it is stressed (Daniels *et al.*, 2017; Zadeh *et al.*, 2019). This optical technique for visualizing internal forces has allowed a better understanding of the physics of granular materials, and several works have used the visualization of photoelastic forces to quantify different physical phenomena (Majmudar; Behringer, 2005; Majmudar *et al.*, 2007; Zhang *et al.*, 2010; Seguin *et al.*, 2016).

A brief description of the process involved in manufacturing photoelastic particles and how to observe the contact networks is given in Secs. 3.2.2.1 and 3.2.2.2, respectively. The interested reader is referred to the works of Daniels *et al.* (2017) (Daniels *et al.*, 2017) and Zadeh *et al.* (2019) (Zadeh *et al.*, 2019) for further explanations on the matter and to the excellent *wiki* (Zadeh *et al.*, 2018) for more complete details.

3.2.2.1 Manufacturing photoelastic particles

Cylindrical particles with different diameters were manufactured using a photoelastic material (polyurethane rubber). Briefly, the manufacturing steps for these particles are presented below:

1. Fabrication of a positive mold (3D printed) for the later fabrication of a silicone mold (negative) of the samples

   A block mold of the particles shape is made by means of 3D printing [Fig. (3.7)a], which is later used as a model for the creation of a silicone mold [green material in Fig. (3.7)b], over which the photoelastic material (polyurethane rubber) will be poured for the manufacturing of the particles. We fabricated molds with particles of different diameters, according to Fig. (3.7)a, namely: $d = 4mm$, $d = 5mm$, $d = 6mm$, $d = 8mm$ and $d = 10mm$. The block molds as well as their respective silicone negatives are shown in Fig. (3.7)b.

2. Fabricating a silicone mold for the samples

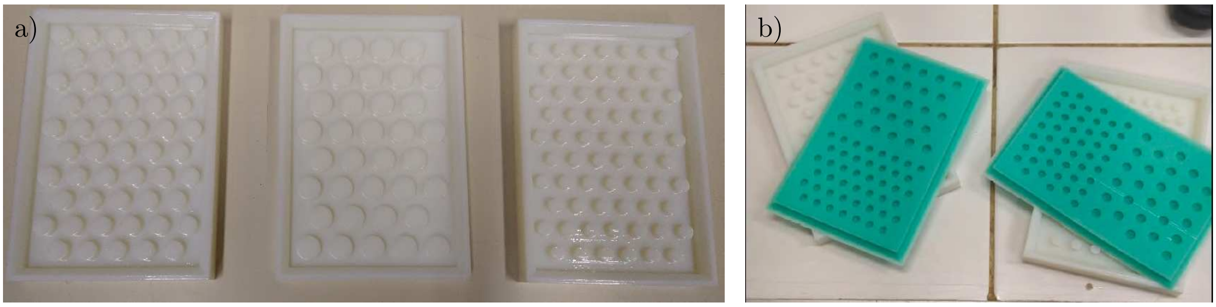

Figure 3.7 – (a) Block molds made by 3D printing. (b) Block molds and their respective silicone negatives.

In this step, we carefully fabricate (according to the material manufacturer's instructions) the silicone negative molds, using a mixture of its both constituents [Fig. (3.8)a]. After complete curing, the molds are ready to be used as "reservoirs" for manufacturing the particles. The final molds can be seen in Fig. (3.8)b.

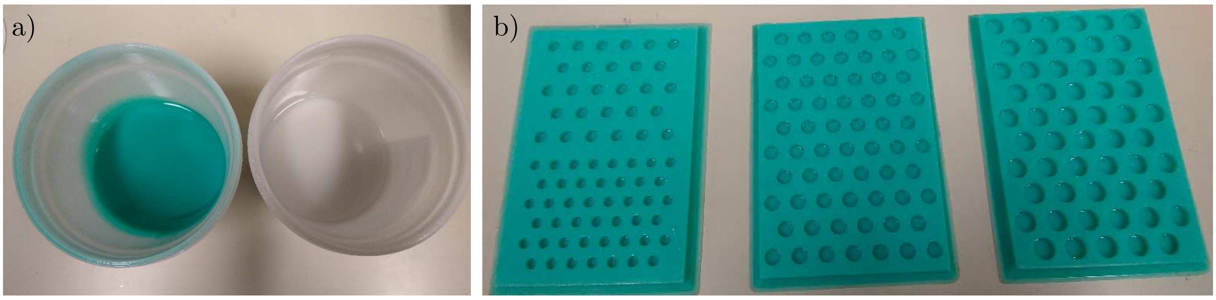

Figure 3.8 – (a) Silicone constituents used to make the molds. (b) Silicone molds after complete curing.

3. Creating the polyurethane rubber material

   Following the manufacturer's instructions, we mix the polyurethane rubber components [Fig. (3.9)a] and add a small quantity of pigment to it (blue for the time being). We then place the resulting mixture in a degasser [vacuum chamber coupled with a vacuum pump - Fig. (3.9)b)] to eliminate residual gases introduced during the mixing process of the components. The degassing process can be seen in Fig. (3.10)a.

4. Manufacturing the photoelastic particles

   After the polyurethane rubber has completely degassed [Fig. (3.10)a], it is carefully placed, using syringes, into the prefabricated silicone molds (item 2). After each particle has been individually filled with the polyurethane rubber, the particles are ready and must rest until they are completely cured, according to Fig. (3.10)b. The curing process

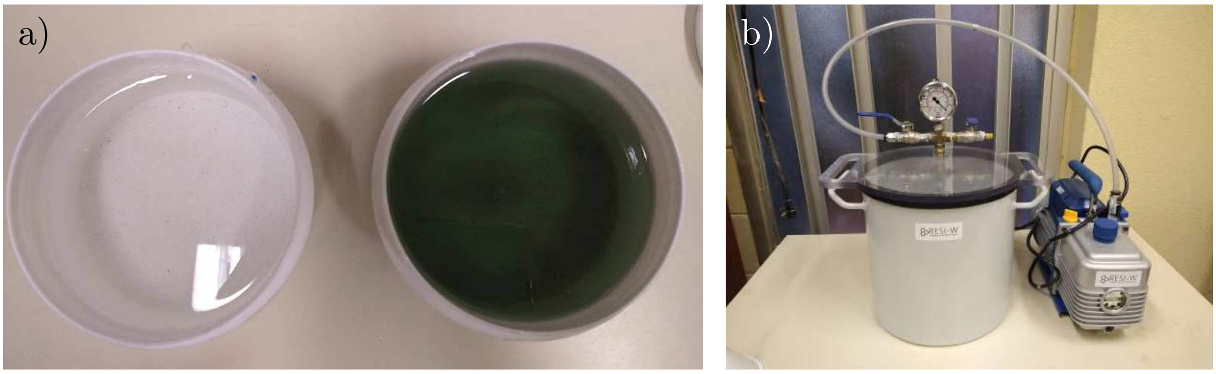

Figure 3.9 – (a) Polyurethane rubber used to manufacture particles. (b) Degasser used to remove bubbles from the mixture.

is accelerated by using an oven [in the laboratory, we make use of the one showed in Fig. (3.10)c].

Figure 3.10 – (a) Polyurethane rubber degassing process. (b) Final particles removed from silicone molds in the curing process. (c) Oven used in the curing process of the particles.

After the final curing process, the particles are finally ready and undergo a quality control process in order to check for any flaws, such as trapped bubbles or a shape different from the expected one. Figure (3.11) shows some particles already manufactured.

3.2.2.2 Visualizing the force networks

The photoelastic effect relies on the birefringent properties of certain transparent materials. In birefringent materials, the speed of light, and consequently the refractive index, varies with the wave's polarization and the eigenvalues of the local stress tensor. Through photoelasticity, we can measure internal stresses in a material, with optimal results achieved using circularly polarized light, which offers isotropic polarization. Circularly polarized light

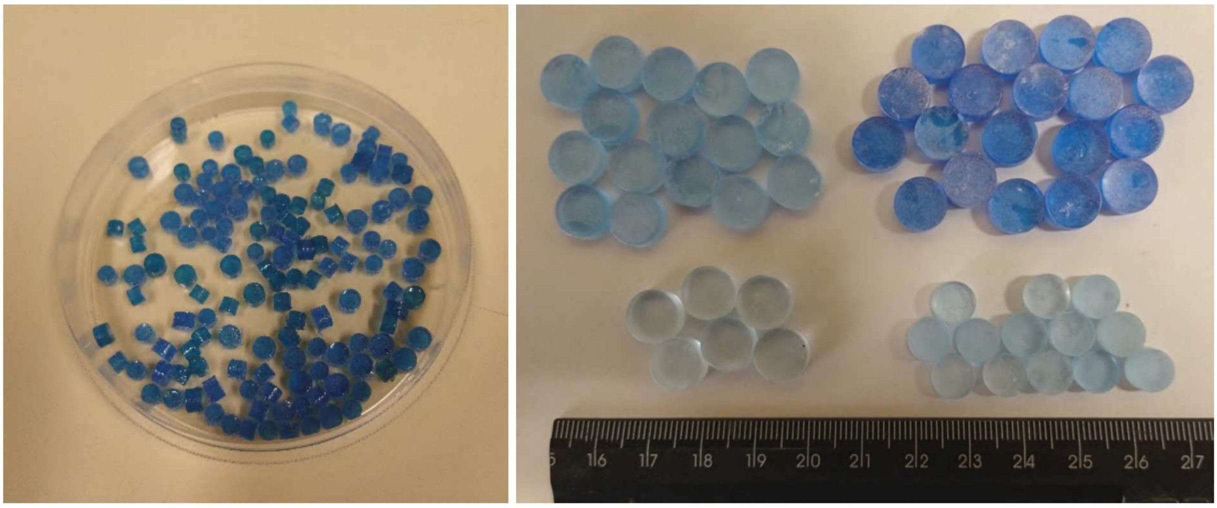

Figure 3.11 – Manufactured particles with different diameter after curing process. Note that particles on the right are covered in talcum powder to avoid sticking and present different colors according to the amount of pigment added in the polyurethane mixture before degassing.

is formed by two orthogonal linearly polarized waves with a quarter-wave phase shift (Daniels *et al.*, 2017; Zadeh *et al.*, 2018; Zadeh *et al.*, 2019).

When a photoelastic material under stress is placed between polarizers, the wave components, polarized in the principal directions of the local stress tensor, travel at different velocities. This variation causes phase shifts in the wave components, converting the circularly polarized light into elliptically polarized light. As a result, part of the altered wave is not completely blocked by the second polarizer and passes through, allowing it to be captured by the camera (Daniels *et al.*, 2017; Zadeh *et al.*, 2018; Zadeh *et al.*, 2019).

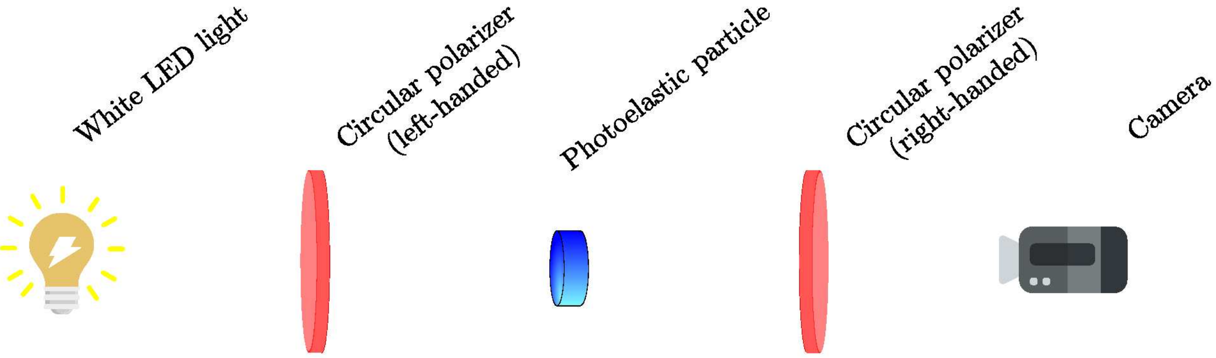

Figure 3.12 – Scheme of the photoelastic technique used for visualizing contact networks (polariscope). Image adapted from (Zadeh *et al.*, 2019).

Figure (3.12) depicts of a scheme of the apparatus (polariscope) used for the forces visualization: polarization is induced by passing unpolarized light through a right-handed circular polarizer. On the opposite side, a circular polarizer with reverse polarity (left-handed), placed in front of the camera, blocks undisturbed light. When the photoelastic material experiences anisotropic stress, the wave components aligned with the principal stress directions travel at different rates, causing phase shifts. This converts the circularly polarized light into elliptical polarization. The shifted portion of the wave passes through the second circular polarizer and is recorded by the camera, allowing for the visualization of the force chains (Daniels *et al.*, 2017; Zadeh *et al.*, 2018; Zadeh *et al.*, 2019).

By assembling a system similar to the scheme presented in Fig. (3.12), one is able to observe the contact networks between the particles when these are under an external stress, as observed in Fig. (3.13), where the figures on the left present states before the application of an external stress, and those on the right, the particles (and consequent force chains) after stress is applied.

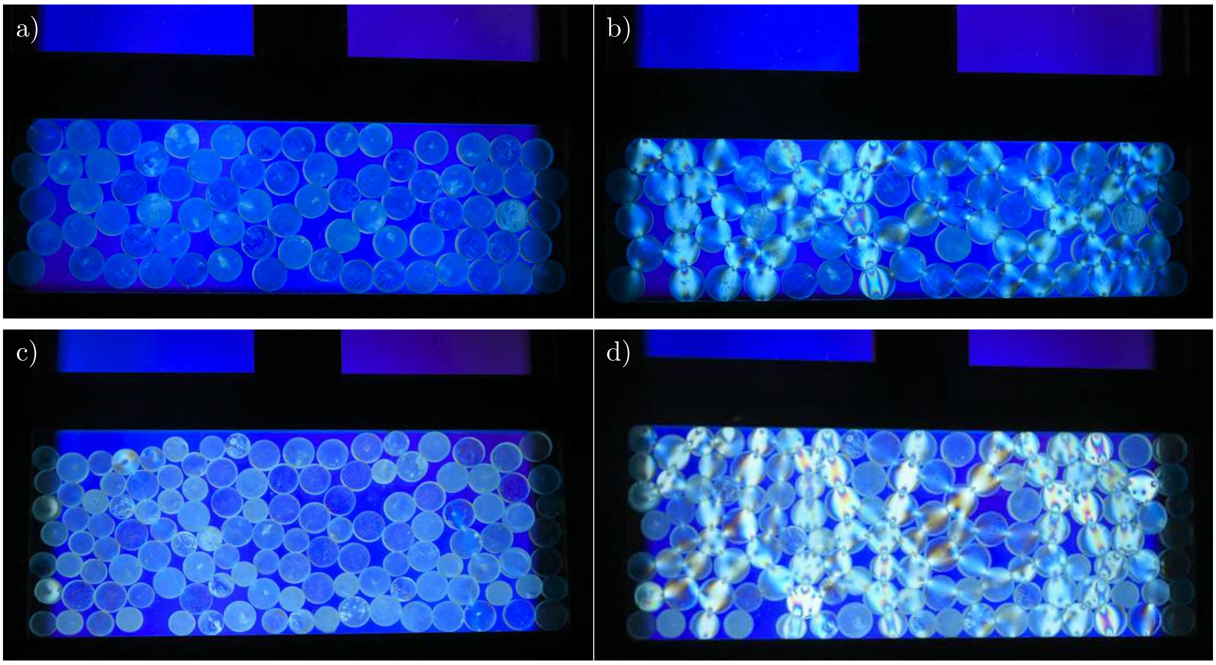

Figure 3.13 – Photoelastic particles under an axial compression through a polariscope as the one schemed in Fig. (3.12). Panels (a) and (b) with monodisperse particles before and after the compression, respectively. Panels (c) and (d) for bidisperse particles before and after the compression, respectively.

We intend to employ this technique in future works to study experimentally the dynamics of force chains in granular materials when disturbed by an intruder.

3.2.3 Collisional regime - Impact problems - Impact with spinning

The penetration depth δ of a spherical projectile of diameter d and density ρ is investigated by dropping it onto a fine granular material confined in a cylindrical container of

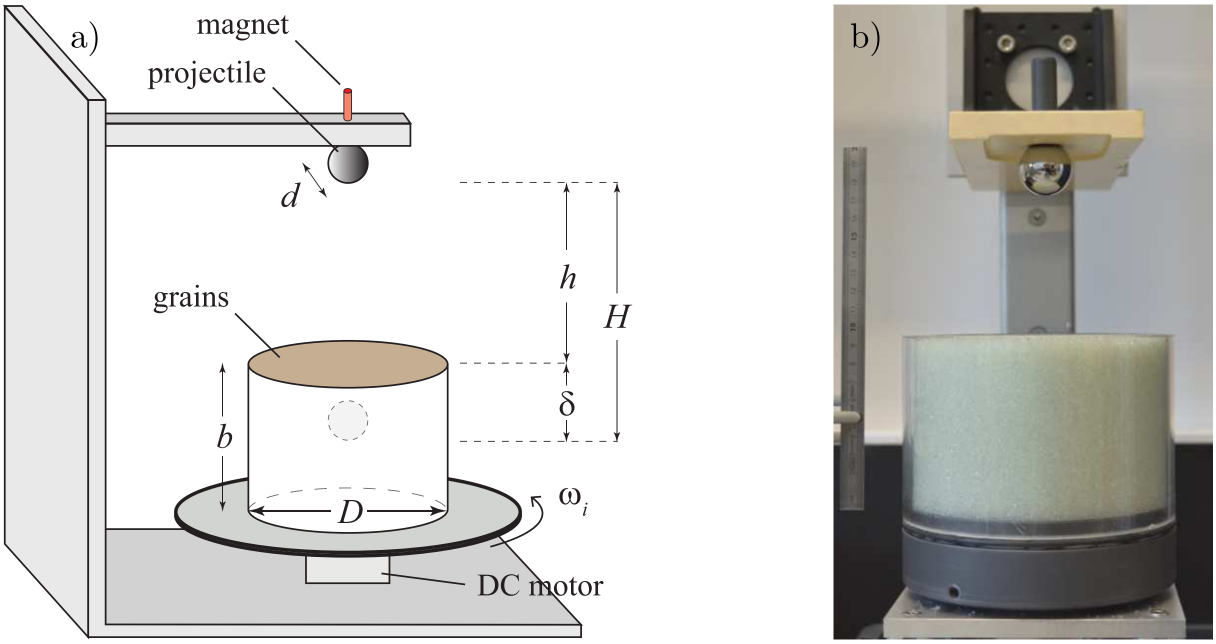

Figure 3.14 – (a) Sketch of the experimental setup and notations introduced. Image taken from (Carvalho *et al.*, 2024a). (b) Photograph of the actual experimental setup.

diameter D and height b, as indicated in the scheme presented in Fig. (3.14)a. The granular medium consists of slightly polydisperse glass spheres (diameter $d_g = 1 \pm 0.3$ mm and density $\rho_g \simeq 2.5 \times 10^3$ kg m^{-3}), as shown in Fig. (3.15)a. To ensure the randomness of the initial conditions of the granular bed, the cylindrical container is overfilled with grains which are gently mixed with a thin rod before each experiment, then the free surface is flattened using a straight edge. We found that this procedure leads to reproducible measurements, with only small variations and an initial packing fraction of $\phi \approx 0.6$ (measured by weighing the container's contents).

Different materials and sizes of spherical projectiles were used to highlight the influence of the sphere density ρ and diameter d on the penetration depth δ. For a container of diameter $D = 140$ mm and height $b = 90$ mm [Fig. (3.14)b], three different metallic projectiles were used, with diameters $d = 20$, 25, and 30 mm [Fig. (3.15)b] and densities $\rho \simeq 14920$, 8160, and 7710 kg m^{-3}, respectively. For a plastic projectile with diameter $d = 80$ mm and density $\rho \simeq 1150$ kg m^{-3} [Fig. (3.15)c], two different cylindrical containers were used, with diameter $D = 400$ mm and heights equal to $b = 50$ mm and $b = 180$ mm. This allows us to keep a ratio $D/d \gtrsim 5$, avoiding any confinement effects (Seguin *et al.*, 2008). Note that for all cases studied here, the grain size d_g remains much smaller than the projectile diameter d, with $d_g/d \leq 0.05$.

The projectile is initially held by a magnet at a distance h above the granular surface [Fig. (3.14)b], so that it is released without any initial velocity nor rotational motion (the non-

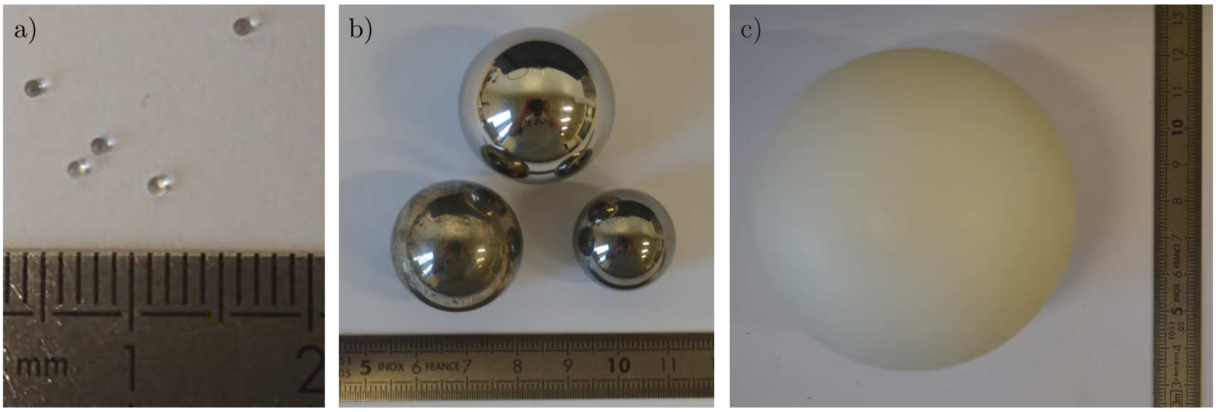

Figure 3.15 – (a) Polydisperse glass spheres with diameter $d_g = 1 \pm 0.3$ mm. (b) Different metallic projectiles with diameters $d = 30$, 25, and 20 mm (counterclockwise starting from the top). (c) Plastic projectile with diameter $d = 80$ mm.

metallic sphere is held by inserting a small magnet inside it). The impact velocity is adjusted by varying the releasing height h from 2 mm to 2.17 m. Hence, the corresponding speed at impact v_i, given by $v_i = \sqrt{2gh}$, where g is the gravitational acceleration, varies from 0.2 to 6.5 m s^{-1}. Note that the projectile is released just above the center of the cylindrical container and falls along its axis.

Rather than releasing a rotating projectile to impact a nonrotating granular bed (Carvalho *et al.*, 2023b; Carvalho *et al.*, 2023a), experimentally it is more feasible to release a nonrotating projectile onto a rotating granular medium. In the absence of relatively strong centrifugal effects, these situations are equivalent, since they induce the same relative motion between the projectile and grains. Hence, the cylindrical container is placed on a rotating platform allowing its rotation around its main axis at a constant angular velocity ω_i in the range 0 – 10 rad s^{-1}. In this way, the relative angular velocity between the projectile and the granular bed reaches a zero value at the end of each experiment. To be clearer, in both the experiments (Carvalho *et al.*, 2024a) and the DEM simulations (Carvalho *et al.*, 2023b; Carvalho *et al.*, 2023a), we impose an initial angular velocity (initial spin) to the projectile with respect to the bed. After the projectile impacts and penetrates the bed, it is free to decelerate and eventually reach zero angular velocity. The difference between the present experiments (Carvalho *et al.*, 2024a) and the DEM simulations (Carvalho *et al.*, 2023b; Carvalho *et al.*, 2023a) is that, with respect to the "laboratory" (Earth) frame of reference, in the experiments the bed rotates while in the simulations the projectile has an initial spin, but in both cases the projectile eventually reaches the angular velocity of the bed (non-zero in one case and zero in the other). A video showing one of these experiments can be seen in (CNRS-Ingénierie, 2024).

The cylindrical container is connected to a rotating platform which is in turn attached to an axis connected to a DC motor [*Cerclet, Ref 3445* - (Fig. (3.16)b]. The DC motor rotation is then controlled by a programmable DC power supply [*RSPRO, RS-3005P, 0-30V, 0-5A* - (Fig. (3.16)c]. The whole system, for illustration purposes only, is shown in Fig. (3.16)a. By varying the voltage in the power supply, one is able to precisely control the rotation of the axis attached to the motor and, consequently, that of the rotating cylinder itself.

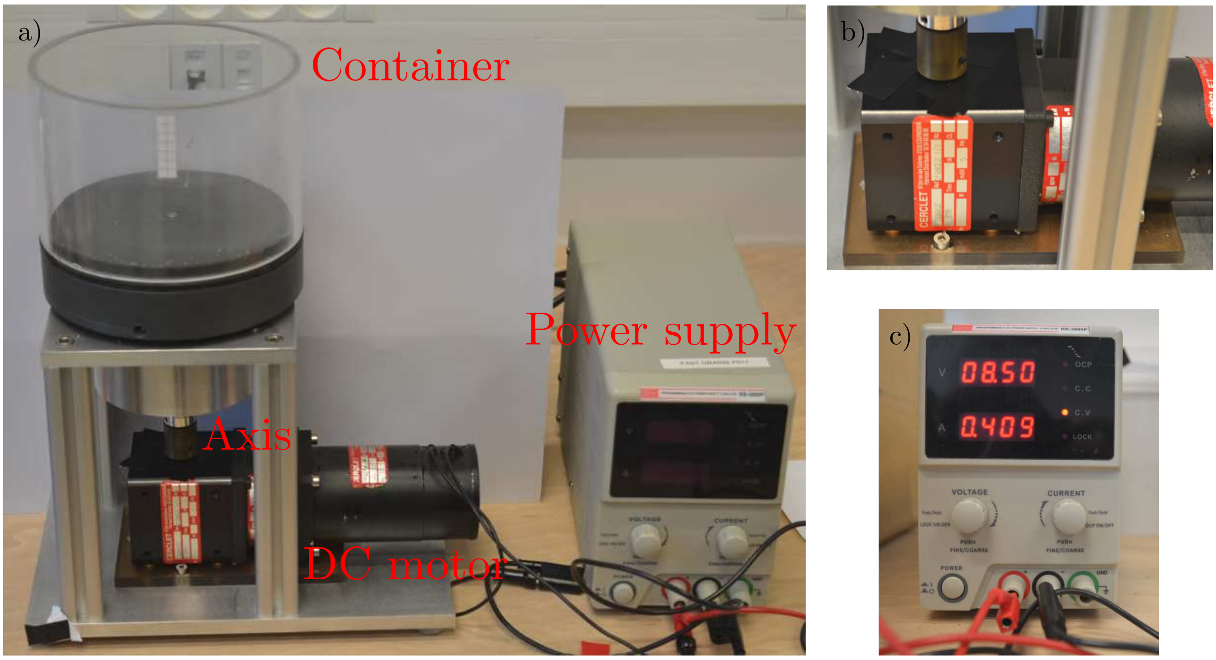

Figure 3.16 – (a) Assembled components of the experimental setup (empty reservoir) with the motion device. (b) Details of the DC motor. (c) Details of the power supply.

A calibration of the system was performed in order to produce a relation between the applied voltage V in the power supply and the effective rotation rate ω_i at the cylindrical container. Voltage V was varied from 2 to 8.75 V in steps of 0.25 V. Lower voltage values would not allow for the rotation of the cylinder and higher ones would cause the grains to be ejected due to centrifugal forces. Beginning from a non-rotating cylinder (ω_i = 0 rad s^{-1}), the voltage would slowly be increased (starting from V = 0 V) in the power supply until the desired value was reached. Once this happened, the system would be recorded with a high resolution camera at a high frequency of image acquisition (580 fps). By following a small marker attached to the cylinder wall, one is able, after carrying out an image analysis, to estimate the rotation of the cylinder. In order to know if the rotation rate would change after the ejecta of grains caused by the impact process (some grains eventually leave the cylinder boundaries after the impact of the projectile takes place), for the container with diameter $D = 140$ mm, 3 different cases were considered, where the cylinder was filled up with grains up to 3 different heights: i) b = 90 mm (completely full); ii) b = 75 mm; and iii) b = 60 mm. These cases are shown in Fig. (3.17). A similar calibration process was performed for the cylindrical container with diameter $D = 400$ mm and height $b = 50$ mm. However, in this case, depth variations were not considered since no grains were ejected away from the cylinder boundaries in all experiments performed in this container. In addition, voltage V was varied from 2.25 to 6 V in steps of 0.25 V.

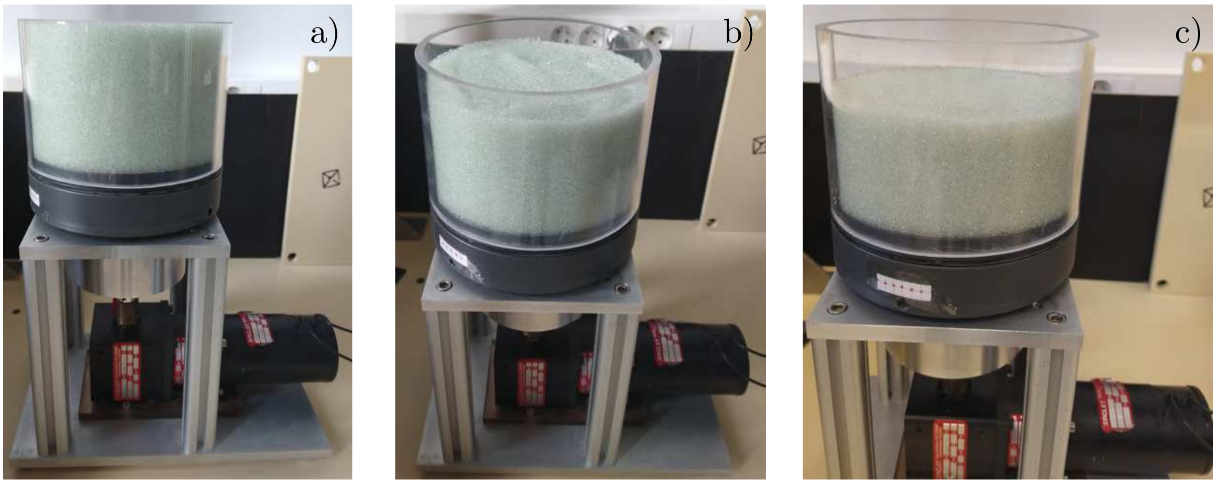

Figure 3.17 – Different cylinders used in the calibration process. (a) $D = 140$ mm and b = 90 mm. (b) $D = 140$ mm and b = 75 mm. (c) $D = 140$ mm and b = 60 mm.

Calibration curves obtained for the 4 different configurations discussed above are shown in Fig. (3.18). We note a linear relation between voltage V and angular velocity ω_i for all cases [see caption of Fig. (3.18)]. Moreover, no differences in rotation rates were measured for the cases with different filling height b in the cylinder with $D = 140$ mm.

We note that the experiments are limited to angular velocities of the order of 10 rad s^{-1} since beyond this value, grains begin to be ejected due to the centrifugal force. In addition, the experimental rotation rates are small enough to allow neglecting surface deformation. The critical rotation rate is obtained for $\omega_c = (6g/D)^{1/2}$ (Huang *et al.*, 2021; Irie *et al.*, 2021). In our case, $\omega_c = 20.5$ rad.s^{-1}, which is greater than the maximum rotation rate $\omega_{max} \approx 10$ rad.s^{-1} in our experiments. Therefore, at the maximum rotation rate of the system, we do not observe any surface deformation (Huang *et al.*, 2021; Irie *et al.*, 2021).

At the end of a release experiment, the angular velocity of the container is slowly reduced until it stops completely. The penetration depth δ is then measured using a thin probe [Fig. (3.19)a], pushed vertically to the impact point, that locates the top of the projectile with an

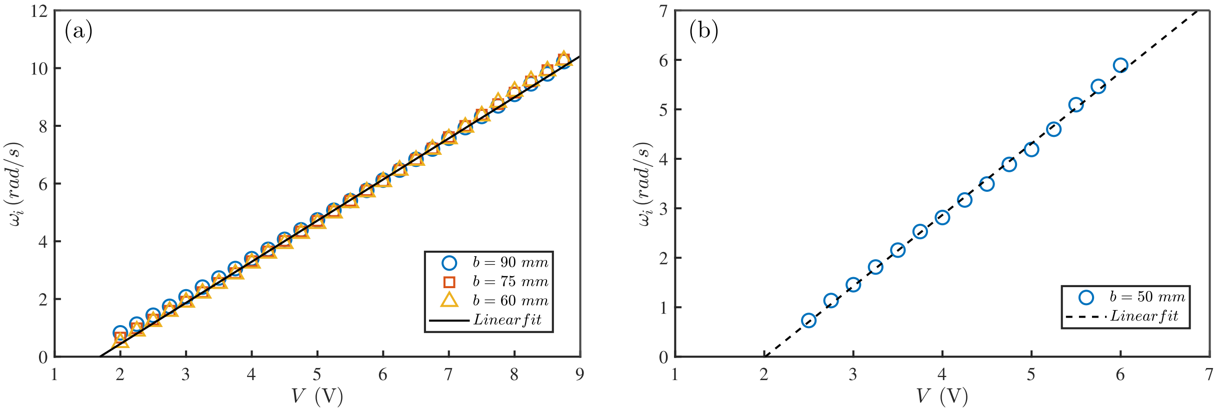

Figure 3.18 – Calibration curves (rotation rate ω_i as a function of voltage V) for the different cases studied. (a) Cylinders with $D = 140$ mm. Linear fit given by the solid line (—): $V = 1.425\omega_i - 2.406$. (b) Cylinder with $D = 400$ mm. Linear fit given by the dashed line (- - -): $V = 1.442\omega_i - 2.899$.

accuracy higher than 1 mm [Fig. (3.19)b]. Note that we ensure that the sphere has not deviated significantly from the vertical trajectory after impact, by probing a few points in the vicinity. Since one knows the original size of the measuring probe, through image analysis (we made use of the free software *ImageJ*) one is able, through size comparison with a scale, to determine the penetration depth of the projectile. A top view of a shallow crater (when the projectile does not sink completely below the granular medium) formed after impact is shown in Fig. (3.19)c.

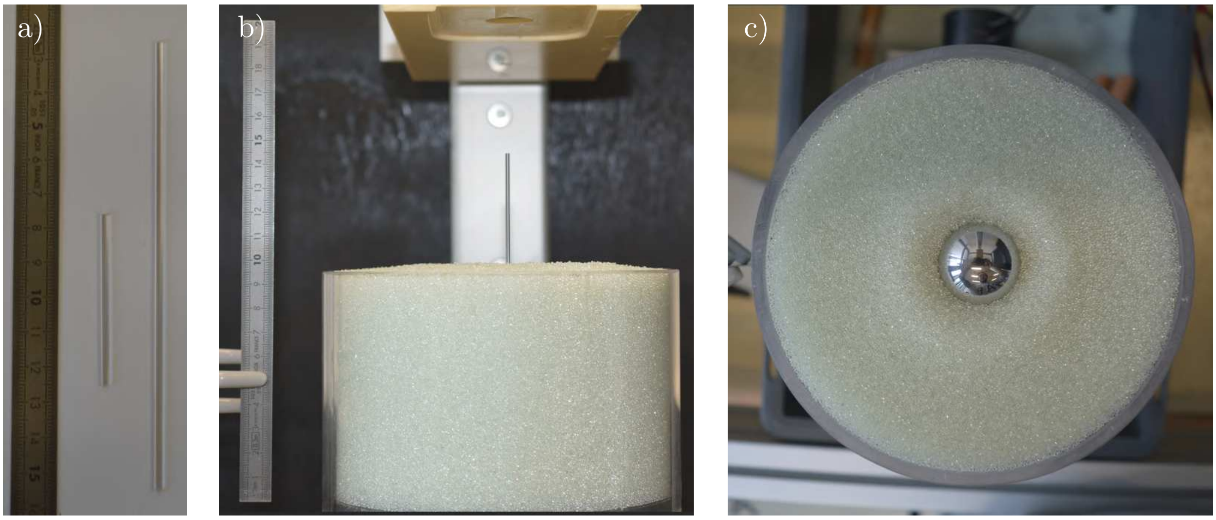

Figure 3.19 – (a) Measuring thin probe. (b) The probe locates the top of the projectile for depth measuring purposes. (c) Top view of a shallow crater.

The results obtained with these experiments can be seen in Sec. 5.2.

4 RESULTS AND DISCUSSION - QUASI-STATIC REGIME - INTRUSION PROBLEMS

4.1 Numerical Investigation

4.1.1 Motion of a single intruder

This section (Sec. 4.1.1) reproduces material from Douglas D. Carvalho, Nicolao C. Lima, and Erick M. Franklin, "Contacts, motion, and chain breaking in a two-dimensional granular system displaced by an intruder", Phys. Rev. E **105**, 034903 (2022), with permission from the American Physical Society (Carvalho *et al.*, 2022).

When the intruder's displacement promotes the quasi-static motion of grains, contact chains appear and collapse successively, forming a time-varying contact network that percolates forces within the granular medium. This intermittent network implies history dependence in the stress distribution, with the occurrence of local anisotropy, local packing variations, and jamming and unjamming regions as the contact chains persist or fail, respectively (Radjai *et al.*, 1998; Majmudar; Behringer, 2005; Cates *et al.*, 1998; Bi *et al.*, 2011; Seguin, 2020; Behringer; Chakraborty, 2018; Featherstone *et al.*, 2021). On the intruder, it causes a strongly oscillating drag force (Kolb *et al.*, 2013; Seguin *et al.*, 2016; Carvalho *et al.*, 2022). Therefore, the problem is intricate even in the case of a single intruder. Although already partially studied, the physics involved in a granular medium displaced by an intruder remains to be fully understood and important issues need to be investigated further. In this section we present a numerical investigation of a three-dimensional (3D) cylindrical intruder (disk) driven at constant speed within an assembly of smaller bidisperse disks (3D cylinders) confined in a rectangular cell, with the same configuration of the experiments of Seguin *et al.* (2016) (Seguin *et al.*, 2016) (quasi-static regime). We performed Discrete Element Method (DEM) computations for an ensemble of disks with static and dynamic coefficients of friction, in accordance to the methodology presented in Sec. 3.1.1. We first validate our numerical computations by replicating some of the experimental results obtained by (Seguin *et al.*, 2016), and we afterward investigate further the motion of particles and force transmission. In summary, we find that there is a bearing network that percolates large forces from the intruder toward the walls, being responsible for jammed regions and high values of the drag force, and a dissipative network that percolates small forces, in agreement with previous observations for compressed 2D granular systems (Radjai *et al.*, 1998;

Seguin, 2020). In addition, we find the anisotropy levels of the contact network for different force magnitudes and regions, that bearing chains occur preferentially in long chains in front of the intruder (which we associate with local jamming induced by shear), and that the force network can reach regions far downstream of the intruder by the end of the intruder's motion. By varying the coefficients of basal friction, we show that bearing networks transmit stronger forces within longer distances for higher basal friction, and that the void region (cavity) that appears downstream of the intruder tends to disappear for lower values of basal friction. Interestingly, our results show that grains within the bearing chains creep while the chains break, revealing the mechanism by which bearing chains collapse, and allowing the intruder to proceed with its motion.

4.1.1.1 Numerical setup

The computed system consisted basically of an assembly of 3D disks settled over a horizontal wall and confined by vertical walls, and of a larger 3D solid disk (intruder) that moved at constant velocity amid the other disks (the top wall was absent). Although the solid objects are 3D disks, we employ the terminology *two-dimensional granular system* since they form a monolayer of particles. The dimensions and properties are roughly the same as in Seguin *et al.* (2016) (Seguin *et al.*, 2016), the steel intruder having diameter and height of $d_{int} = 16$ mm and $h_{int} = 3.6$ mm, respectively, and the granular system consisting of a bidisperse mixture of polyurethane (PSM-4) disks with small and large diameters of $d_s = 4$ mm and $d_l = 5$ mm, respectively (in order to prevent crystallization (Speedy, 1999)), and height $h_g = 3.2$ mm. We forced the intruder to move within the disks at a constant velocity that varied within 10^{-1} mm/s $\leq V_0 \leq 10$ mm/s. The disks were distributed in a proportion of $N_l/N_s \approx 0.64$, where N_s and N_l are the numbers of small and large particles, respectively, in a way that the areas occupied by the small and large grains were almost the same. The disks were placed over a horizontal glass plate and were enclosed by vertical glass walls, so that the system dimensions were of $L_x \times L_y$ = 400 mm × 400 mm, where L_x and L_y are the longitudinal and transverse lengths, respectively. All simulations were performed with a fixed cell size (total domain), in a way that the mean packing fraction is kept constant for each computed case, being varied within $0.76 \leq \phi \leq 0.83$ by varying the number of disks in each tested case. The number of disks and the corresponding packing fractions can be seen in Tab. (4.1), and an example of setup of one simulation can be seen in Fig. (4.1)a.

Table 4.1 – Mean packing fraction ϕ, number of small N_s and large N_l grains, and total number of grains N.

ϕ	N_s	N_l	N
0.76	4832	3092	7924
0.77	4896	3133	8029
0.78	4959	3174	8133
0.79	5023	3215	8238
0.80	5087	3256	8343
0.81	5150	3296	8446
0.82	5214	3337	8551
0.83	5277	3377	8654

Although the Young's modulus of the steel is $E = 1.96 \times 10^{11}$ Pa, we used a value two orders of magnitude smaller in the numerical simulations in order to increase the time step without considerably affecting the accuracy of the results (Lommen *et al.*, 2014). The properties of the materials used in the numerical simulations are summarized in Tab. (4.2). We do not consider any motion in the direction perpendicular to the xy plane, so that there is no collision between the disks and bottom wall. The intruder is placed initially at the location x_i = -160 mm , y_i = 0 mm, in the left side of the simulation cell, and is moved at a constant velocity V_0 from left to right, through the granular medium, toward its final position at x_i = 160 mm , y_i = 0 mm [Fig. (4.1)a]. Therefore, for all values of V_0 and ϕ used in the simulations, the intruder traveled a total distance equal to $\Delta S = 320$ mm. The drag force F_D exerted by the grains onto the intruder, the forces on each grain, their displacements, and the contact network are computed at every time step. We defined a region of interest (ROI) of size A_{ROI} = 160 mm $\times$ 160 mm in the center of the domain [green-dashed area in Fig. (4.1)a] for computing time averages while avoiding intense boundary effect [see Fig. (4.3)c for a figure showing the effect of considering the entire domain on time averages]. The remaining computations considered the entire domain.

Table 4.2 – Properties of materials used in the simulations: E is the Young's modulus, ν is the Poisson ratio, ρ is the material density, and d is the particle diameter.

	Material	E **(Pa)**	ν	ρ **(kg/m^3)**	d **(mm)**
Intruder	Steel$^{(1)}$	1.96×10^9	0.29	7800	$d_{int} = 16$
Grains	Polyurethane$^{(1),(2)}$	4.14×10^6	0.50	1280	d_s = 4; d_l = 5
Walls	Glass$^{(1)}$	0.64×10^{11}	0.23	2500	L_x = 400; L_y = 400

$^{(1)}$ Hashemnia and Spelt (Hashemnia; Spelt, 2014)

$^{(2)}$ Gloss (Gloss, 2000)

Values for the coefficient of restitution were 0.3 for the grain-grain and 0.7 for the

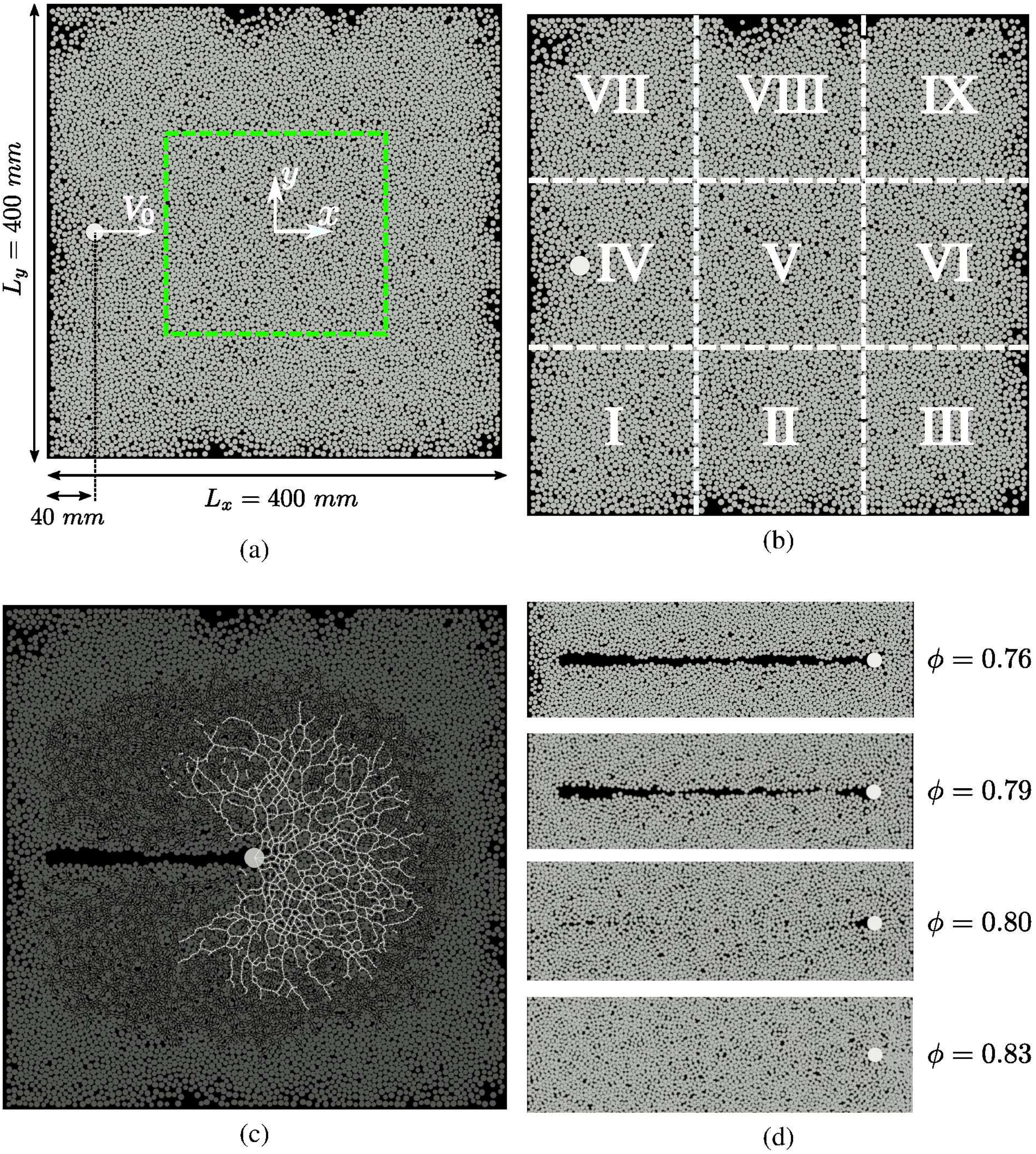

(a) (b) (c) (d)

Figure 4.1 – (a) Numerical setup for $\phi = 0.76$. (b) Different sub-regions of the entire domain analyzed individually. (c) Force chains formed during the motion of the intruder. Clear networks correspond to bearing (stronger) chains and darker networks to dissipative (weaker) chains. (d) Cavity formed downstream of the intruder for different packing fractions. Images taken from (Carvalho *et al.*, 2022).

grain-wall and grain-intruder interactions (Gondret *et al.*, 2002; Hashemnia; Spelt, 2014). For the friction coefficients, we considered only the dynamic coefficient for interactions occurring on surfaces oriented in the vertical plane (grain-grain, intruder-grain and grain-vertical wall interactions), for which we applied the Hertz-Mindlin contact model. Values for the polyurethane-

polyurethane and polyurethane-steel found in the literature are relatively high (Hashemnia; Spelt, 2014; Carlevaro *et al.*, 2020) when compared to the other materials involved. The friction between both the intruder and disks with the bottom wall was implemented by ourselves, for which we considered both the static and dynamic coefficients. For that, we defined a threshold velocity $v' = 5 \times 10^{-4}$ m/s for the transition between static and dynamic conditions. Values of the coefficients of restitution (ratio between the momentum just after and prior collision) and friction (Coulomb law) and the threshold velocity used in the simulations are listed in Tab. (4.3). Most of the coefficients were obtained from the literature (Carlevaro *et al.*, 2020; Hashemnia; Spelt, 2014; Gondret *et al.*, 2002), and sensitivity tests varying the coefficients are shown in Fig. (4.2).

Table 4.3 – Coefficients and threshold used in the numerical simulations.

Coefficient	**Symbol**	**Value**
Restitution coefficient (grain-grain)	ϵ_{gg}	0.3
Restitution coefficient (grain-intruder)$^{(2)}$	ϵ_{gi}	0.7
Restitution coefficient (grain-wall)$^{(3)}$	ϵ_{gw}	0.7
Dynamic friction coefficient (grain-grain)$^{(1)}$	μ_{gg}	1.2
Dynamic friction coefficient (grain-intruder)$^{(2)}$	μ_{gi}	1.8
Dynamic friction coefficient (intruder-bottom wall)	μ_{iw}	0.7
Dynamic friction coefficient (grain-walls)$^{(1)}$	μ_{gw}	0.4
Static friction coefficient (grain-bottom wall)	$\mu_{s,gw}$	0.7
Threshold velocity (dynamic/static friction)	v'	$v' = 5 \times 10^{-4}$ m/s

(1) Carvelaro *et al.* (Carlevaro *et al.*, 2020)

(2) Hashemnia *et al.* (Hashemnia; Spelt, 2014)

(3) Gondret *et al.* (Gondret *et al.*, 2002)

With the total domain and the particle fraction to be simulated defined, the set of disks with the desired proportion is generated. First, the particles are randomly distributed over a square space larger than the computational domain. Afterward, the space occupied initially by the disks is compressed from the external limits toward its interior until reaching the size of the computational domain. In this initialization process, the number of generated particles is the necessary to achieve the desired packing fraction ϕ, according to Eq. (4.1) (Kolb *et al.*, 2013).

$$\phi = \frac{\frac{\pi}{4}(N_s d_s^2 + N_l d_l^2)}{L_x L_y - \frac{\pi}{4} d_{int}^2}. \tag{4.1}$$

This initialization is necessary because the software is not capable of randomly inserting disks at high particle fractions in the domain within reasonable times (it takes much greater times than those of simulations themselves). Finally, the disks are allowed to relax and,

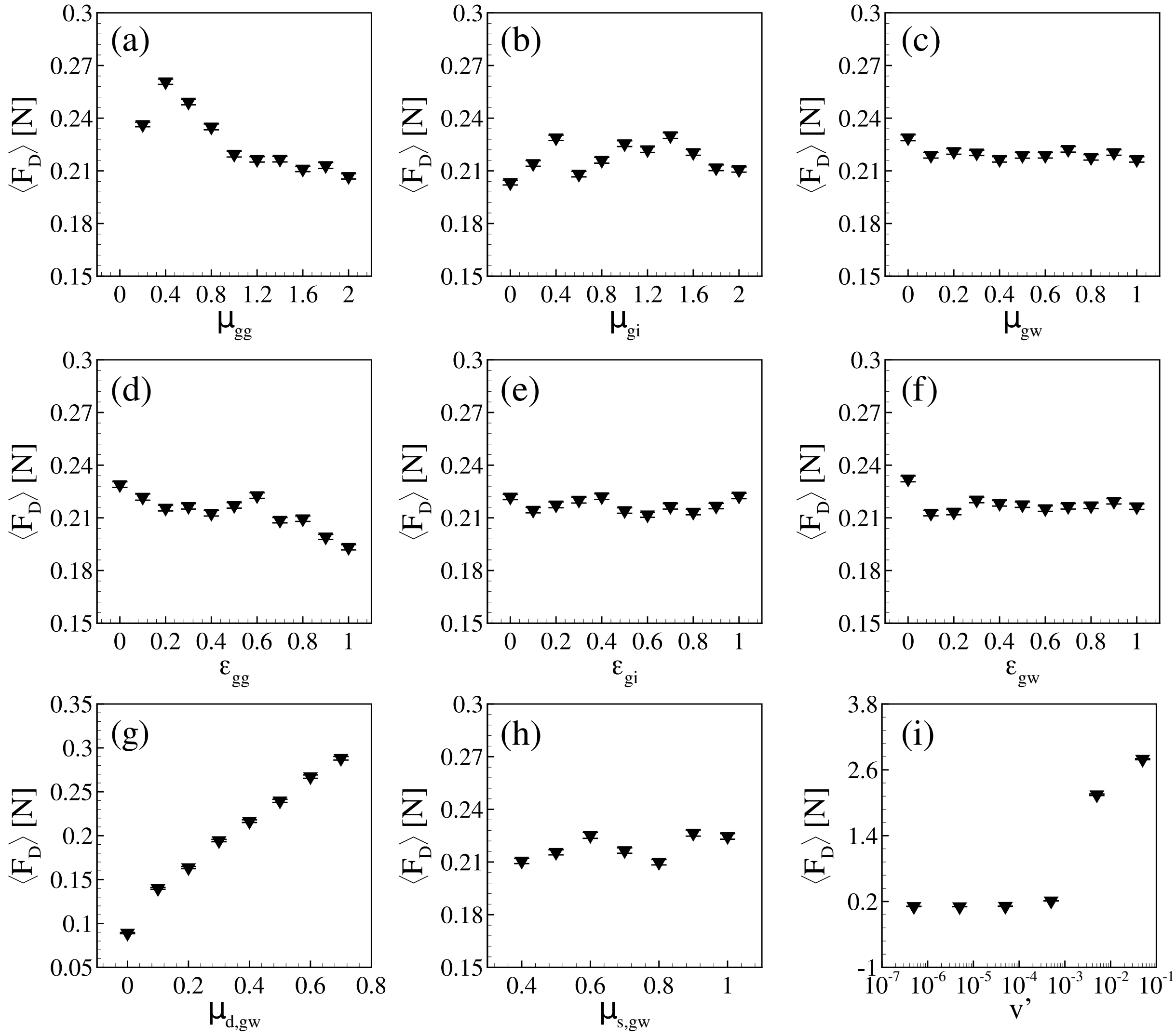

Figure 4.2 – Sensitivity tests: $\langle F_D \rangle$ as function of the coefficients listed in Tab. (4.3) as each one of them is varied separately. The symbol $\mu_{d,gw}$ corresponds to the dynamic coefficient of basal friction implemented by ourselves, while μ_{gw} corresponds to the dynamic coefficient intrinsic to the Hertz-Mindlin contact model, already implemented in LIGGGHTS. Because the results are for $\mu_{d,gw} = \mu_{gw}$, we used only one symbol in the following. In the graphics, symbols correspond to the measured values and bars to the standard errors. Images taken from (Carvalho *et al.*, 2022).

afterward, the simulation starts by setting the intruder into motion at a constant speed. All computations were performed with a time step $\Delta t = 3.2 \times 10^{-6}$ s, which, in the worst scenario, is less than 10 % of the Rayleigh time (timescale for Rayleigh waves resulting from collisions), given by:

$$t_R = \frac{\pi \left(d/2\right) \left(\rho/G\right)^{1/2}}{0.163\nu + 0.8766}, \tag{4.2}$$

where G is the shear modulus (Derakhshani *et al.*, 2015).

4.1.1.2 Drag force on the intruder

For each simulated condition, we computed the resultant force on the intruder at each time step and associated it with the instantaneous drag force on the intruder $\vec{F}_D$. We then obtained its magnitude F_D and, for each different condition, the mean $\langle F_D \rangle$. Figure (4.3)a presents F_D as a function of time t when the intruder moves with V_0 = 2.7 mm/s in a system with mean packing fraction ϕ = 0.76. We observe an initial transient, when the intruder begins moving and F_D increases due to an increasing number of contacts [shown next in Fig. (4.4)b], and that afterward the mean value remains roughly constant, with very high oscillations with peaks reaching values 3 times the mean value. Those strong oscillations are caused by the formation and destruction of contact networks that percolate forces within the bed, as shown next. The same behavior was found experimentally by Seguin *et al.* (2016) (Seguin *et al.*, 2016). Figure (4.3)b shows the time-averaged magnitude of the drag force $\langle F_D \rangle$ as a function of the intruder velocity V_0 for ϕ = 0.76. We obtain values that are roughly independent of V_0 (as in Refs. (Seguin *et al.*, 2016) and (Seguin *et al.*, 2013)), with a mean value $\langle F_D \rangle \approx 0.21$. For the same case, Seguin *et al.* (2016) (Seguin *et al.*, 2016) found experimentally $\langle F_D \rangle \approx$ 0.22. Fig. (4.3)c shows that, by considering all the domain (Global) to calculate the averages (red circles), although there are some small differences in values, we observe that the behavior is approximately the same for both regions. Finally, Fig. (4.3)d presents $\langle F_D \rangle$ as a function of ϕ for V_0 = 2.7 mm/s, showing that the mean force remains roughly constant until $0.80 \leq \phi \leq 0.81$, and from $\phi \approx 0.81$ on $\langle F_D \rangle$ increases strongly with ϕ, similar to results obtained experimentally by Kolb *et al.* (2013) (Kolb *et al.*, 2013). Considering that experimental uncertainties are expected in Refs. (Kolb *et al.*, 2013; Seguin *et al.*, 2016) and that we obtained the particle properties (with the exception of the diameter) from other works, the agreement is good.

We observed also the formation of a cavity (void region) downstream the intruder, whose size decreases with increasing the packing fraction, as shown in Fig. (4.1)d for $0.76 \leq \phi \leq 0.83$. We observe that for ϕ = 0.80 the cavity has almost disappeared, and for ϕ = 0.83 it no longer exists, in accordance with the experimental observations of Kolb *et al.* (2013) (Kolb *et al.*, 2013).

Altogether, the resultant drag and cavity agree with experimental observations and validate part of our numerical results. More information on the numerical simulations (input and output files, numerical scripts for post-processing the outputs, etc.) are available on a public repository (Lima *et al.*, 2021).

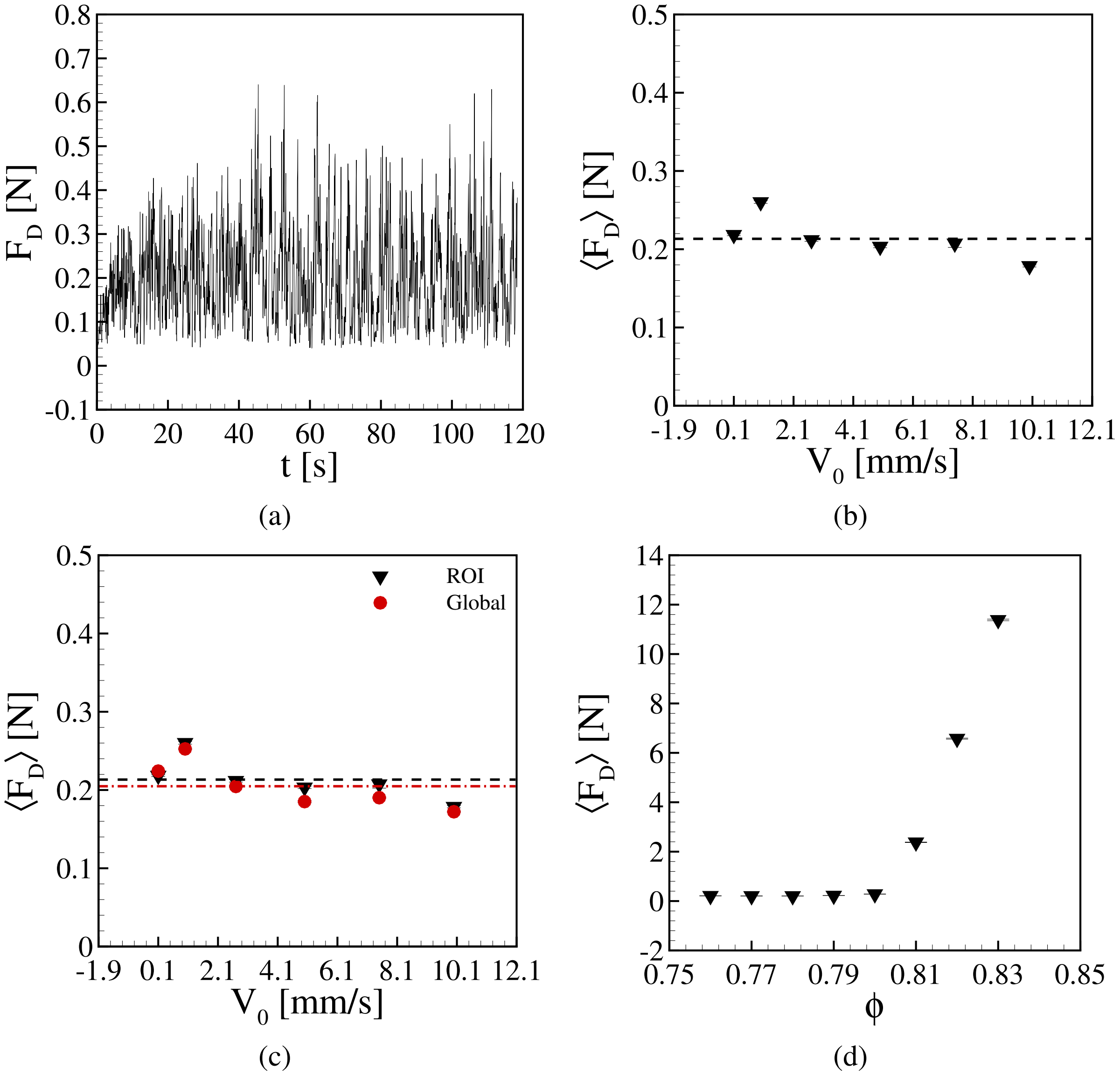

Figure 4.3 – (a) Magnitude of the resultant force on the intruder F_D when the mean packing fraction is $\phi = 0.76$ and $V_0 = 2.7$ mm/s as a function of time t. (b) Time-averaged magnitude of the resultant force on the intruder $\langle F_D \rangle$ as a function of its velocity for $\phi = 0.76$. (c) Same as (b) but black triangles correspond to averages considering only the ROI (as in shown in (b)) and red circles all the domain (Global). (d) $\langle F_D \rangle$ as a function of ϕ for $V_0 = 2.7$ mm/s. In Figs. (b), (c), and (d), symbols correspond to the average values and bars to the standard errors. Images taken from (Carvalho *et al.*, 2022).

4.1.1.3 Network of contact forces

In the following, we analyze the network of contact forces and the behavior of individual grains within specific contact chains. For that, we fixed the mean particle fraction to $\phi = 0.76$ and the intruder velocity to $V_0 = 2.7$ mm/s. From images of the force chains, such as Fig. (4.1)c, we observe that forces from the intruder propagate through contact networks whose anisotropy and size depend on the force level and region within the system. In what follows, we investigate the anisotropy of the system (i) as a whole, (ii) for different force levels (below and above an average value), and (iii) for different regions within the domain. For that, we computed the fabric tensor $\hat{R}$ (Bi *et al.*, 2011),

$$\hat{R} = \frac{1}{N} \sum_{i \neq j} \frac{\mathbf{r}_{ij}}{|\mathbf{r}_{ij}|} \otimes \frac{\mathbf{r}_{ij}}{|\mathbf{r}_{ij}|}, \tag{4.3}$$

where N is the number of non-rattler particles (particles with at least two contacts), $\mathbf{r}_{ij}$ is the contact vector from the center of particle i to the contact between particles i and j, and $\otimes$ denotes the vector outer product. With the eigenvalues R_1 and R_2 of the tensor $\hat{R}$, we computed the average number of contacts per particle $Z = R_1 + R_2$ and the anisotropy of the contact network $\rho = R_1 - R_2$ (Bi *et al.*, 2011). More details regarding the fabric tensor $\hat{R}$ can be seen in Appendix B.

Figures (4.4)a, (4.4)b, and (4.4)c present the contact anisotropy ρ, average number of contacts per particle Z, and number of non-rattler particles N, respectively, for the entire domain as functions of time. We observe that Z increases and ρ decreases during the first 20 s. The strong initial variations of Z and ρ are mainly due to adaptations of the initial conditions of the system as the intruder starts moving, with more grains being put into contact and a general decrease in anisotropy. After this time interval, mean values present lower variations. At the stable intervals ($t >$ 30 s), time averages computed for the ROI are $\langle \rho \rangle$ = 0.041 and $\langle Z \rangle$ = 2.903, showing that, when considered as a whole in terms of regions and force magnitudes, the contact network has a low degree of anisotropy. However, since the intruder moves in one direction, we expect load-bearing chains aligned in preferential directions in order to resist to the intruder's motion (Cates *et al.*, 1998; Majmudar; Behringer, 2005; Bi *et al.*, 2011). Load-bearing chains that transmit strong forces have been shown to exist in compressed 2D granular systems (Radjai *et al.*, 1998; Seguin, 2020), to be more anisotropic than the dissipative chains, and, in addition, to be related to jamming by shear (Bi *et al.*, 2011). We investigate next if this is also the case for a 2D system displaced by an intruder, and, in addition, if anisotropy varies in space.

4.1.1.3.1 Force levels

Following the same idea of Radjai *et al.* (1998) (Radjai *et al.*, 1998), we divided the network of contact forces into a bearing network, for which transmitted forces are higher than the average value (ensemble average at each considered instant), and a dissipative network, with

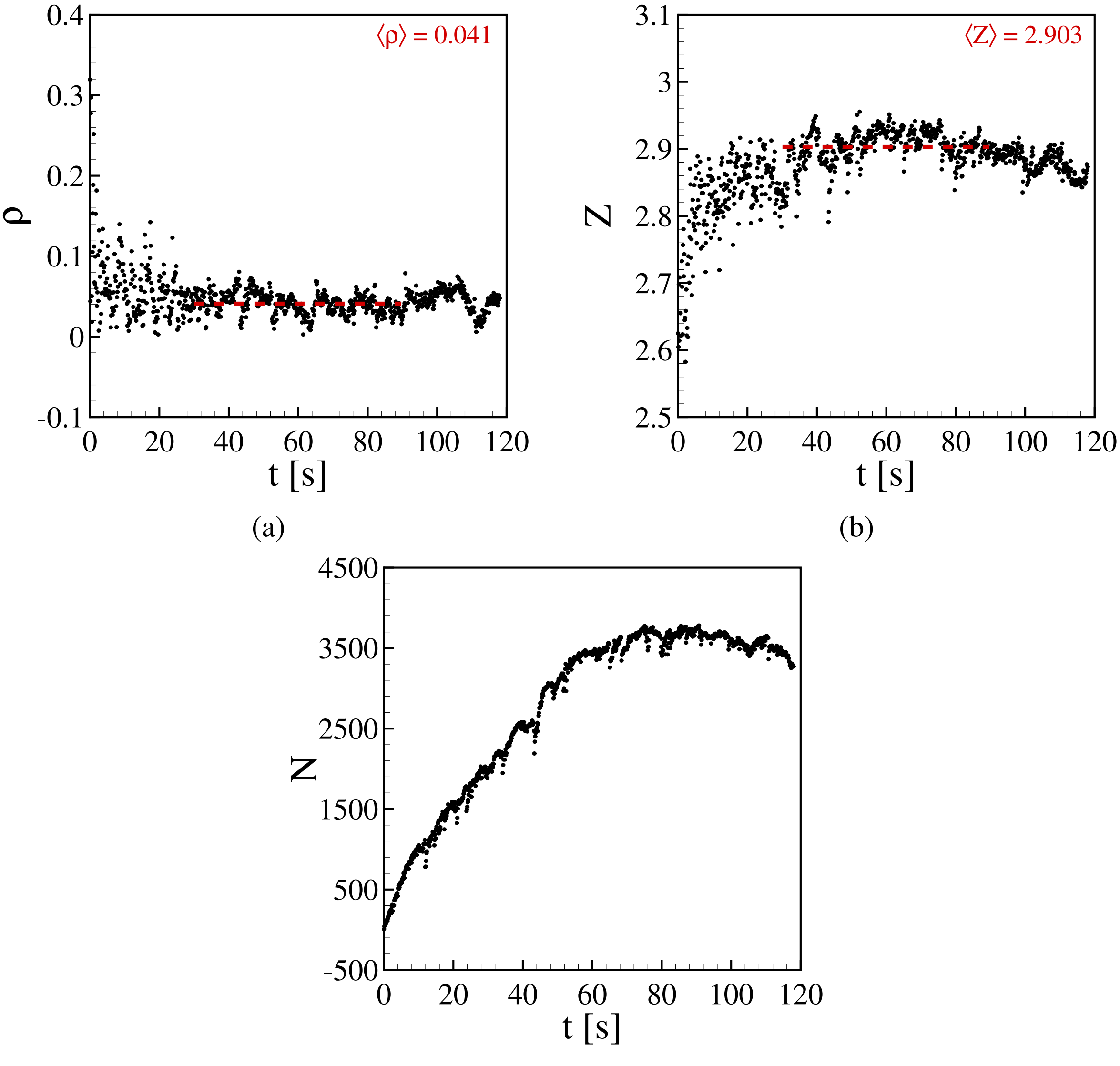

(a)

(b)

(c)

Figure 4.4 – Time evolution of (a) contact anisotropy ρ, (b) average number of contacts per particle Z, and (c) number of non-rattler particles N for the entire system. Images taken from (Carvalho *et al.*, 2022).

values lower than the average. Once identified the type of network, we computed $\hat{R}$, ρ and Z for each network (all chains), which are shown in this subsection. We also followed the evolution of specific chains and the motion of their grains, which are shown in Sec. 4.1.1.3.3.

Figures (4.5)a, (4.5)b, and (4.5)c present the time evolution of the contact anisotropy ρ, average number of contacts per particle Z, and number of non-rattler particles N, respectively, for the bearing (strong) and dissipative (weak) networks for the entire domain. We observe an increase in Z during the first 20 s for the dissipative network while for the bearing network the mean value of Z remains roughly constant, with values for the dissi-

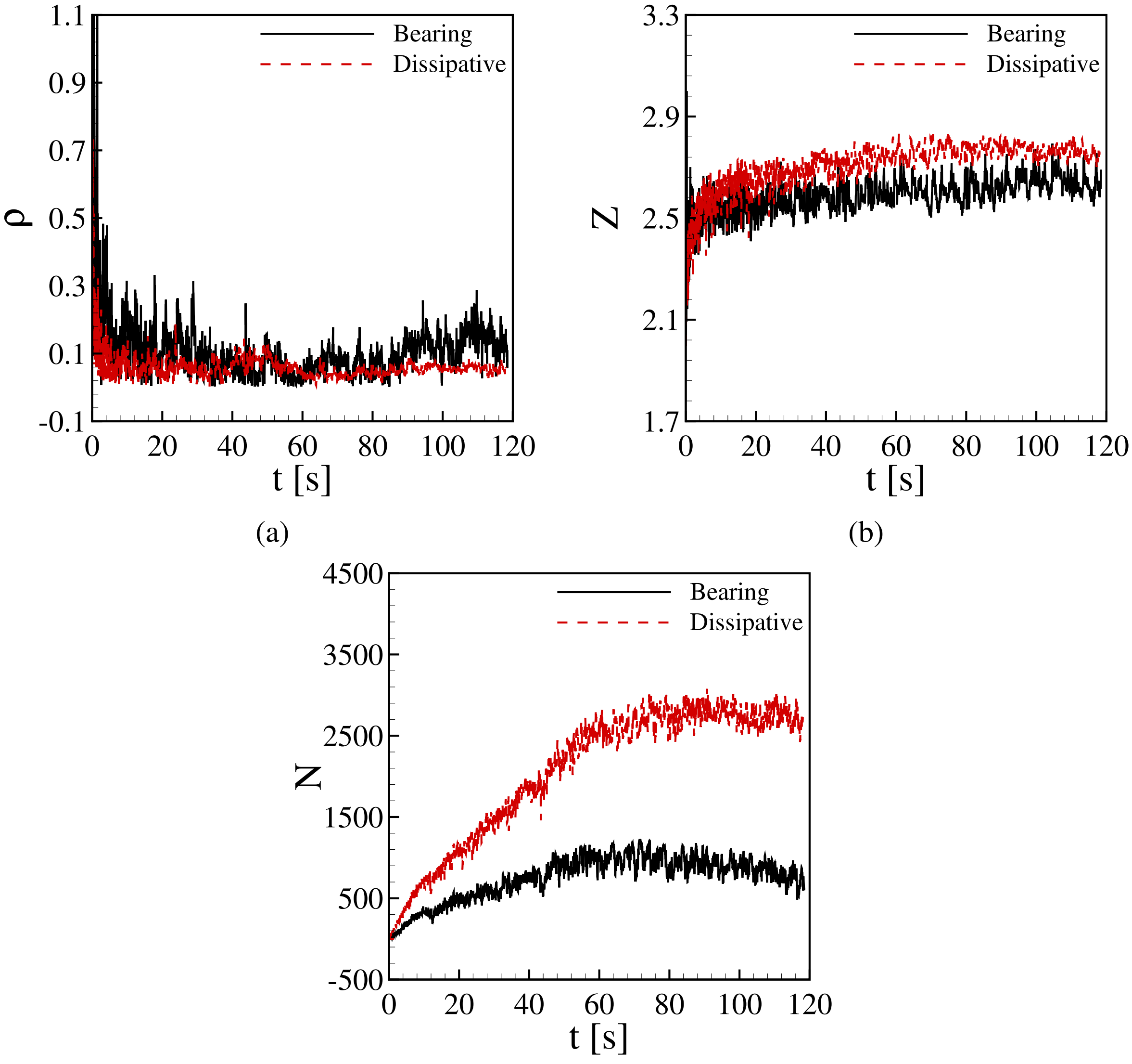

(a) (b)

(c)

Figure 4.5 – Time evolution of (a) contact anisotropy ρ, (b) average number of contacts per particle Z, and (c) number of non-rattler particles N computed for the bearing (continuous line) and dissipative (dashed-red line) networks. Time average values are $\langle\rho\rangle$ = 0.107 and $\langle Z\rangle$ = 2.592 for the bearing network, and $\langle\rho\rangle$ = 0.060 and $\langle Z\rangle$ = 2.711 for the dissipative network. Images taken from (Carvalho *et al.*, 2022).

pative network being 5 % higher than those for the bearing network. During the first 10-20 s for both networks, ρ decreases, with values 80 % higher for the bearing network in comparison with the dissipative network. These values indicate that anisotropy is maintained mostly by the load-bearing chains. From direct observations of figures of the network of contact forces, such as Figs. (4.1)c and (4.11), or from the animation available at <https://journals.aps.org/pre/supplemental/10.1103/PhysRevE.105.034903>, we observe that bearing chains percolate in various directions, but mostly in the front (upstream) region of the intruder. This characteristic, which is similar to the shear jammed state described by Bi *et al.* (2011) (Bi *et al.*, 2011) for the case of a sheared cell, explains the higher anisotropy of the bearing network. This is also in accordance with the description given by Kolb *et al.* (2013) (Kolb *et al.*, 2013) of a jammed region in front of the intruder, with load-bearing chains being formed and collapsing as the intruder moves, making the drag force to fluctuate strongly around a mean value, as shown in Fig. (4.3)a. We investigate the bearing chains in detail (at the grain scale) in Sec. 4.1.1.3.3.

4.1.1.3.2 Spatial distribution

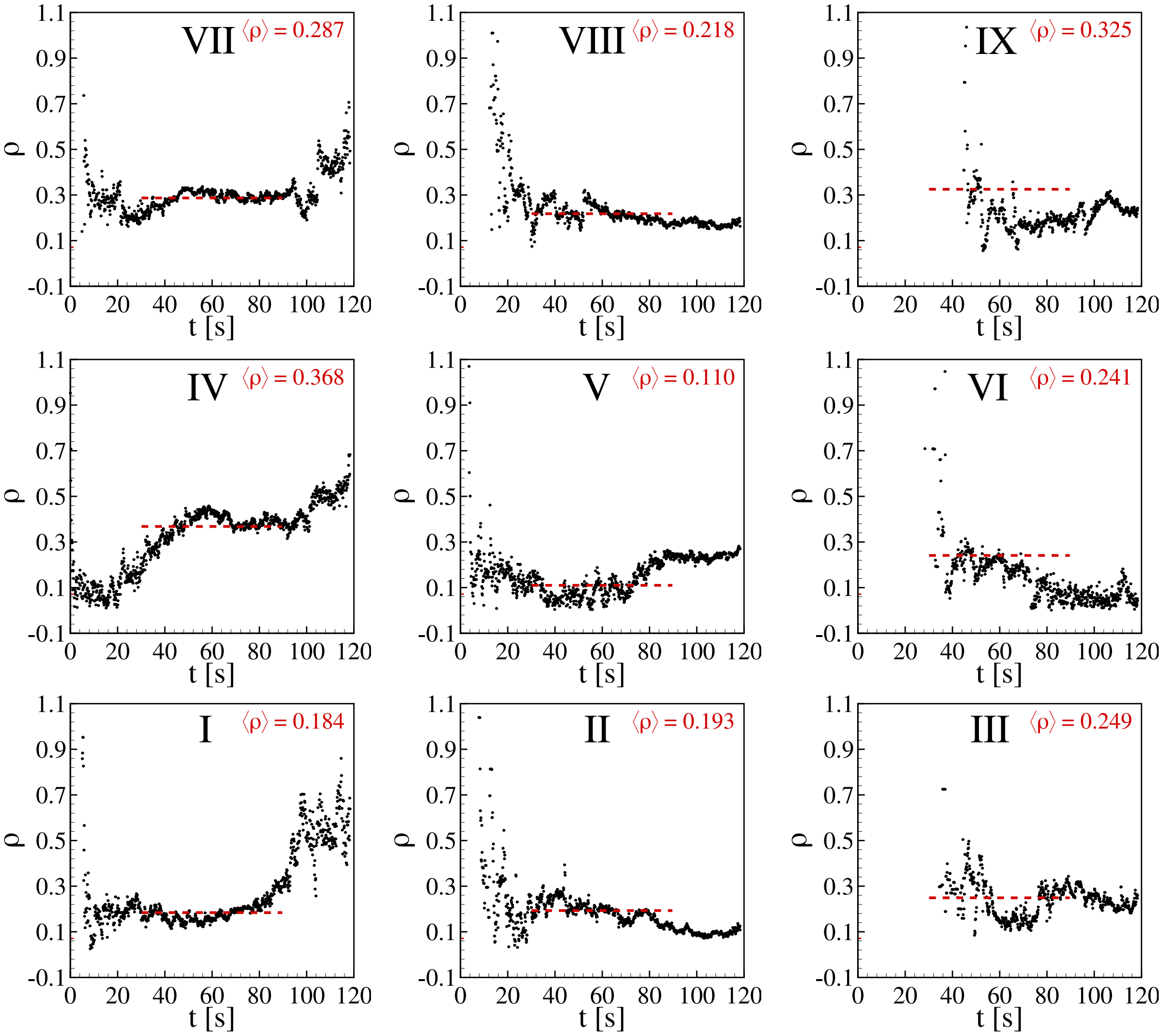

Figure 4.6 – Time evolution of the anisotropy of the contact network ρ for each individual region of Fig. (4.1)b. Images taken from (Carvalho *et al.*, 2022).

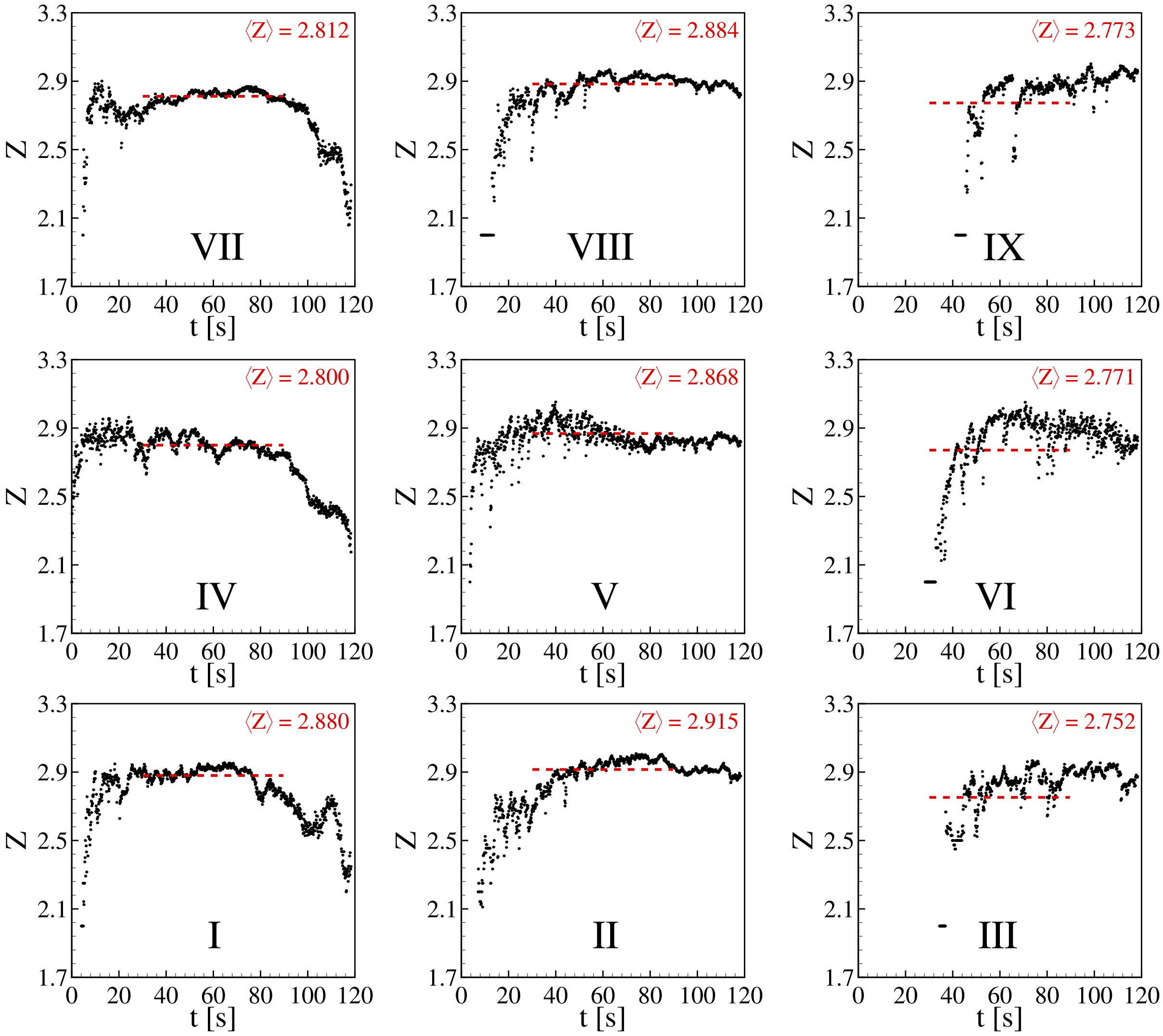

Figure 4.7 – Time evolution of the average number of contacts per particle Z for each individual region of Fig. (4.1)b. Images taken from (Carvalho *et al.*, 2022).

In order to investigate if the time evolution of anisotropy varies in space, we divided the domain in nine different regions as shown in Fig. (4.1)b. Figure (4.6) presents the anisotropy of the contact network ρ for each individual region of Fig. (4.1)b as a function of time (the relative positions of graphics correspond to the spatial distribution in the domain). Interestingly, ρ decreases in regions mainly upstream the intruder (regions II, III, V, VI, VIII and IX) as the latter moves from the left to the right [Fig. (4.1)], while ρ increases in the regions farther downstream the intruder (regions I, IV and VII) as it approaches the right boundary of the domain. In addition, values of ρ are much higher in the left regions by the end of the intruder's motion (values at least three times greater on the left than on the right regions). This behavior is corroborated by the time evolution of Z, shown in Fig. (4.7) for each region. From this figure, we observe that the average number of contacts per particle decreases in the left regions

(regions I, IV, and VII) by the end of motion, compatible with anisotropic behaviors, while the same does not occur in the other regions.

The explanation for the long-range effects is the size of the contact network that, by the end of motion of the intruder, reaches regions far downstream of it (check <https://journals.aps.org/pre/supplemental/10.1103/PhysRevE.105.034903> for an animation showing the instantaneous contact network). Because chains arriving at the farther regions (I, IV and VII) by the end of the intruder's motion follow principal directions, as if irradiating from the intruder, anisotropy is larger in those regions. These results corroborate the necessity of a non-local rheology to describe a granular system displaced by an intruder, even if most of grain displacements occur in the vicinity of the intruder (as shown in Refs. (Kolb *et al.*, 2013; Seguin *et al.*, 2016) and in Sec. 4.1.1.3.3).

4.1.1.3.3 Grains within bearing chains

The experimental results of Kolb *et al.* (2013) (Kolb *et al.*, 2013) and Seguin *et al.* (2016) (Seguin *et al.*, 2016) showed strong fluctuations of F_D around a mean value that are associated with the formation and breaking of bearing chains, and the same behavior appears in our simulations. However, previous works did not show how grains within a bearing chain move nor how the chain breaks. We investigate this problem by choosing some bearing chains, labeling the grains of each chain, and following these grains along time. For the labels, the corresponding numbers start with the grain in contact with the intruder and increase as grains are farther from it, as shown in Fig. (4.8)a.

One example of bearing chain is shown in Fig. (4.8), where Fig. (4.8)a shows the grains just after the chain was formed and Fig. (4.8)b after the chain broke. We observe that during this period some chains broke while some others formed, and that the motions of the considered grains are very small. In order to inquire into the motions of these grains, we computed their fluctuations with respect to the ensemble of grains and their accumulated displacements, and found that chains break due to creep motion of some grains, with a very small degree of fluctuations of individual grains. Because the oscillation levels of load-bearing grains are negligible, we present next only their displacements.

Figure (4.9)a presents the displacements ΔS of each labeled grain at different instants for the chain shown in Fig. (4.8) (transverse to the intruder's motion), and Fig. (4.9)c for a chain parallel to the intruder's motion. Each symbol corresponds to one instant, and the

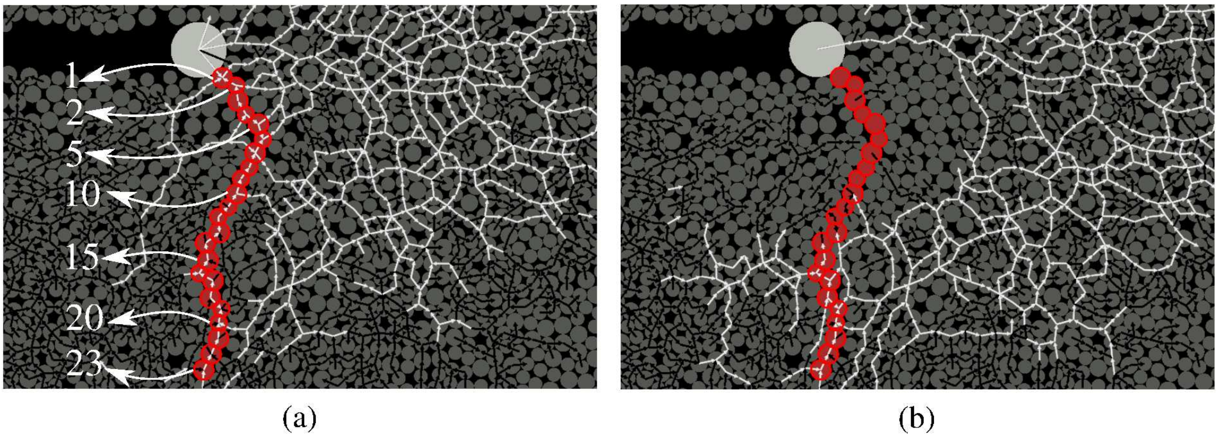

(a) (b)

Figure 4.8 – Grains within a bearing chain (shown in red) of the network shown in Fig. (4.1)c (bearing network in white). (a) Grains just after the chain was formed, with labels from 1 to 23 according to their distance from the intruder. (b) Grains just after the considered chain broke. Images taken from (Carvalho *et al.*, 2022).

figures represent the strain suffered by the chain. We observe that while the intruder is forced through the system the grains closer to it yield and move, while those farther [labeled 14 or more in Fig. (4.9)a and 19 or more in Fig. (4.9)c] do not move. In fact, we can observe from Fig. (4.8)b that the latter remain in contact with each other, so that the part of the chain that is not in contact with the intruder persists. The same behavior was observed for all the chains that we tracked. Figure (4.10) presents an ensemble average computed for 11 chains, for which we note that, in average, creep during chain breaking is localized around the intruder, decreasing fast as grains are farther from the intruder and being nonexistent from the 15^{th} grain on. The average duration of creeping Δt is of the order of 0.1 s, and normalizing Δt by the characteristic time $t_c = d_g/V_0$, where d_g = 4.5 mm is the mean grain diameter, we obtain $\Delta t/t_c$ of the order of 0.1. Table (4.4) shows the duration of each chain. In terms of drag on the intruder, Figs. (4.9)b and (4.9)d show the time evolution of F_D as the same bearing chains of Figs. (4.9)a and (4.9)c, respectively, break. We observe the same behavior shown by Kolb *et al.* (2013) (Kolb *et al.*, 2013): an increase in F_D while the bearing chain persists, and a fast decrease when the chain breaks.

In summary, we observe that the formation and breaking of bearing chains are responsible for the high oscillation levels of F_D, with F_D increasing during the lifetime of the bearing chain as the intruder is forced against it and decreasing as the chain breaks. In addition, we observe that the breaking occurs due to creeping of grains closer to the intruder while those farther from it do not move, and that, once broken, part of the former chain persists.

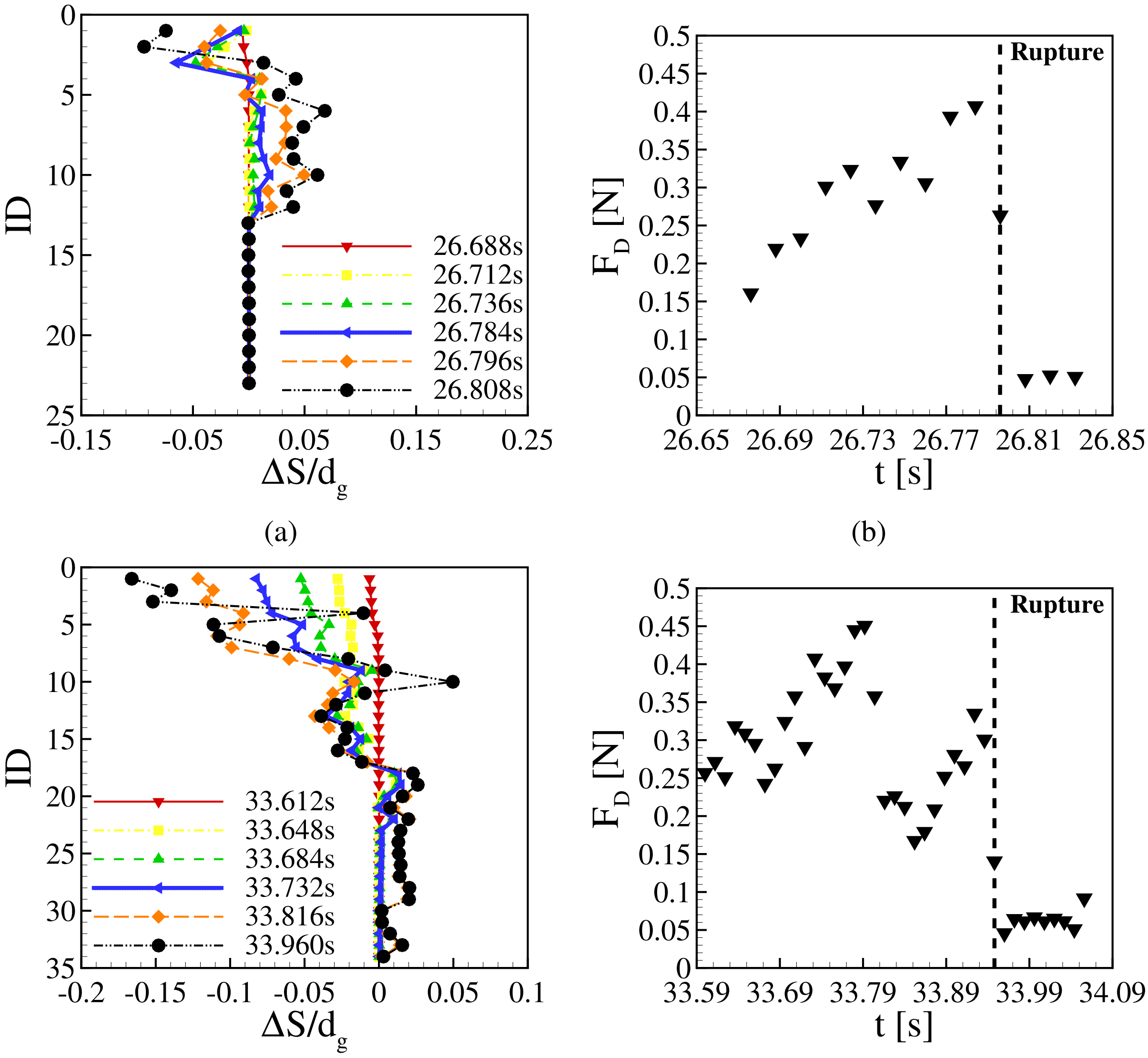

(a) (b)

(c) (d)

Figure 4.9 – Displacements of each labeled grain for different instants during the breaking of a bearing chain (a) transverse and (c) parallel to the intruder's motion, normalized by the mean grain diameter d_g = 4.5 mm. Figure (a) corresponds to the same chain shown in Fig. (4.8). Magnitude of the drag force on the intruder F_D along time during the formation and breaking of the (b) transverse and (d) longitudinal bearing chains. The dashed line indicates the instant when the chain is present for the last time, i.e., just before its rupture. Images taken from (Carvalho *et al.*, 2022).

4.1.1.4 Basal friction

Depending on the surface on which the disks move, the basal friction can be different. For instance, the friction can be much smaller over Teflon or ice than over acrylic, glass or metal alloys. The diversity of materials found both in nature and industry has thus motivated investigations of monolayers of particles sliding with different frictions. Kozlowski *et al.* (2019)

Table 4.4 – Duration Δt of creeping of each followed chain, in dimensional form and normalized by the characteristic time $t_c = d_g/V_0$.

Chain number	Δt	$\Delta t/t_c$
...	s	...
1	0.144	0.09
2	0.132	0.08
3	0.192	0.12
4	0.276	0.17
5	0.288	0.18
6	0.312	0.19
7	0.180	0.11
8	0.204	0.12
9	0.156	0.09
10	0.108	0.06
11	0.156	0.09

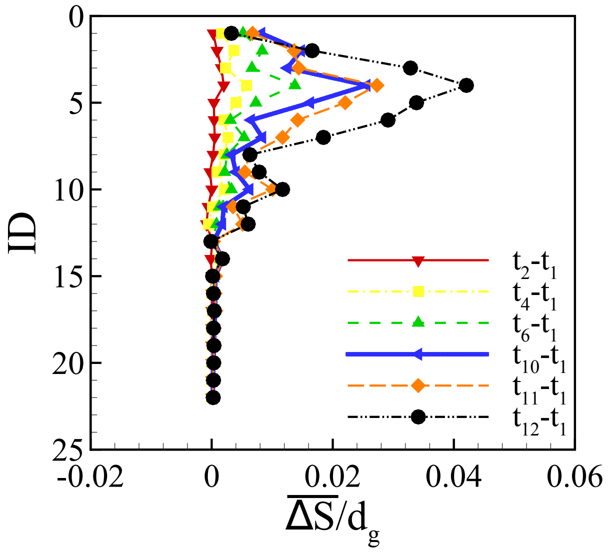

Figure 4.10 – Ensemble average of the displacements of grains $\overline{\Delta S}$ for different instants during the breaking of bearing chains transverse to the intruder's motion, normalized by the mean grain diameter d_g. Image taken from (Carvalho *et al.*, 2022).

Table 4.5 – Coefficients of basal friction: values used in the simulations.

Coefficients	Relative reductions						
	100%	75%	50%	25%	10%	1%	0.1%
μ_{iw}	0.7	0.525	0.35	0.175	0.07	0.007	0.0007
μ_{gw}	0.4	0.3	0.2	0.1	0.04	0.004	0.0004
$\mu_{s,gw}$	0.7	0.525	0.35	0.175	0.07	0.007	0.0007

(Kozlowski *et al.*, 2019) and Carlevaro *et al.* (2020) (Carlevaro *et al.*, 2020) investigated the effects of the basal friction of grains (μ_{gw} and $\mu_{s,gw}$) on the motion of an intruder with $\mu_{iw} = 0$ in a Couette geometry. They found that two regimes of motion appear depending on the friction

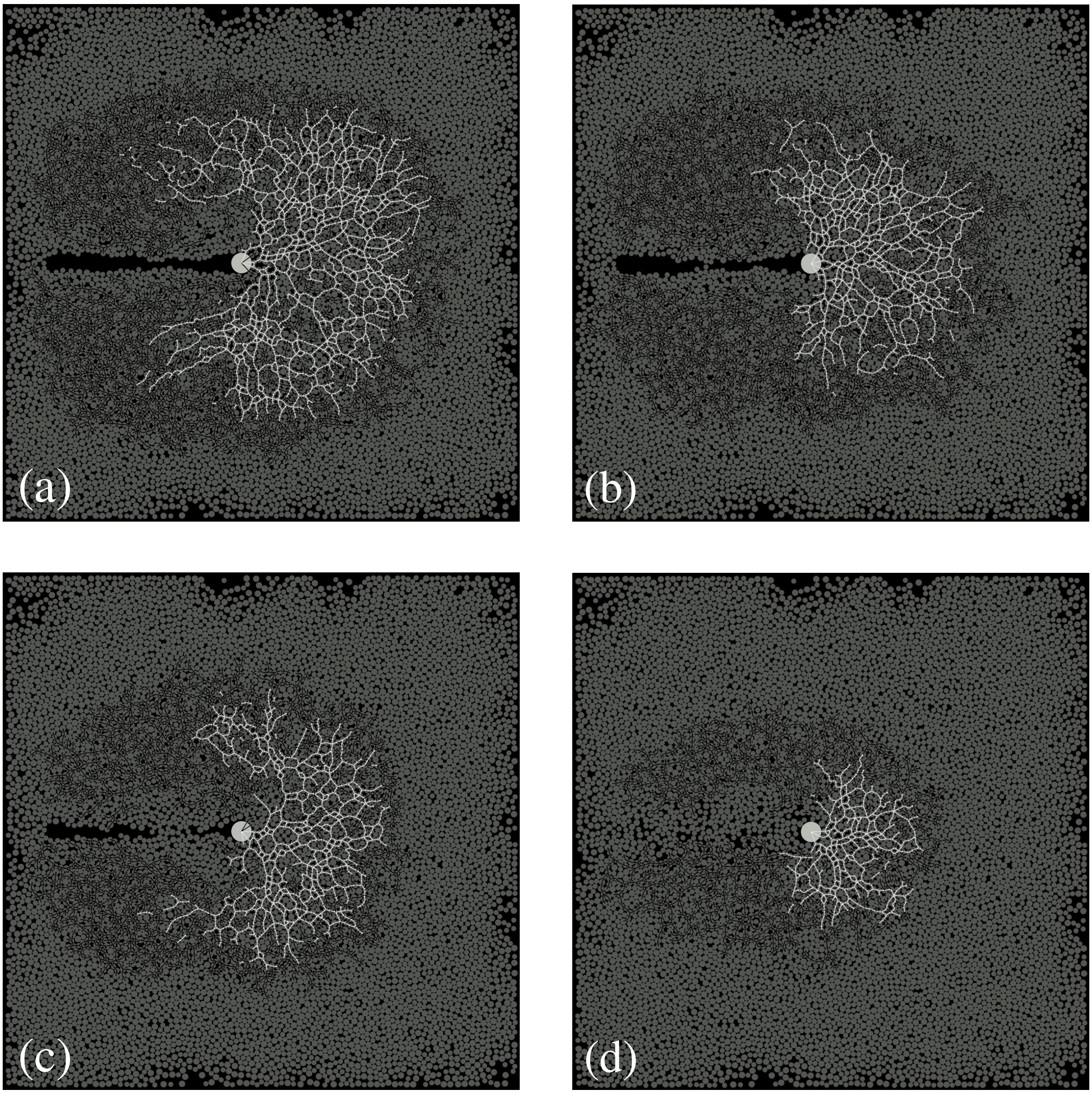

Figure 4.11 – Network of contact forces for different values of the coefficients of basal friction: (a) 100%, (b) 25%, (c) 10% and (d) 0.1% of the base values. Clear networks correspond to bearing (stronger) chains and darker networks to dissipative (weaker) chains, and all figures correspond to $t = 53.54$ s. Images taken from (Carvalho *et al.*, 2022).

coefficients, and that in the case without basal friction chains occur only in front of the intruder during stick events. Although they advanced valuable information about the general behavior of the system, knowledge on how the chain dynamics varies with the basal friction is still missing.

In the present section, we inquire further into the effect of the basal friction on the network of contact forces. For that, we reduced the values of the coefficients of basal friction for both the intruder and grains by the same proportions, as indicated in Tab. (4.5): values of

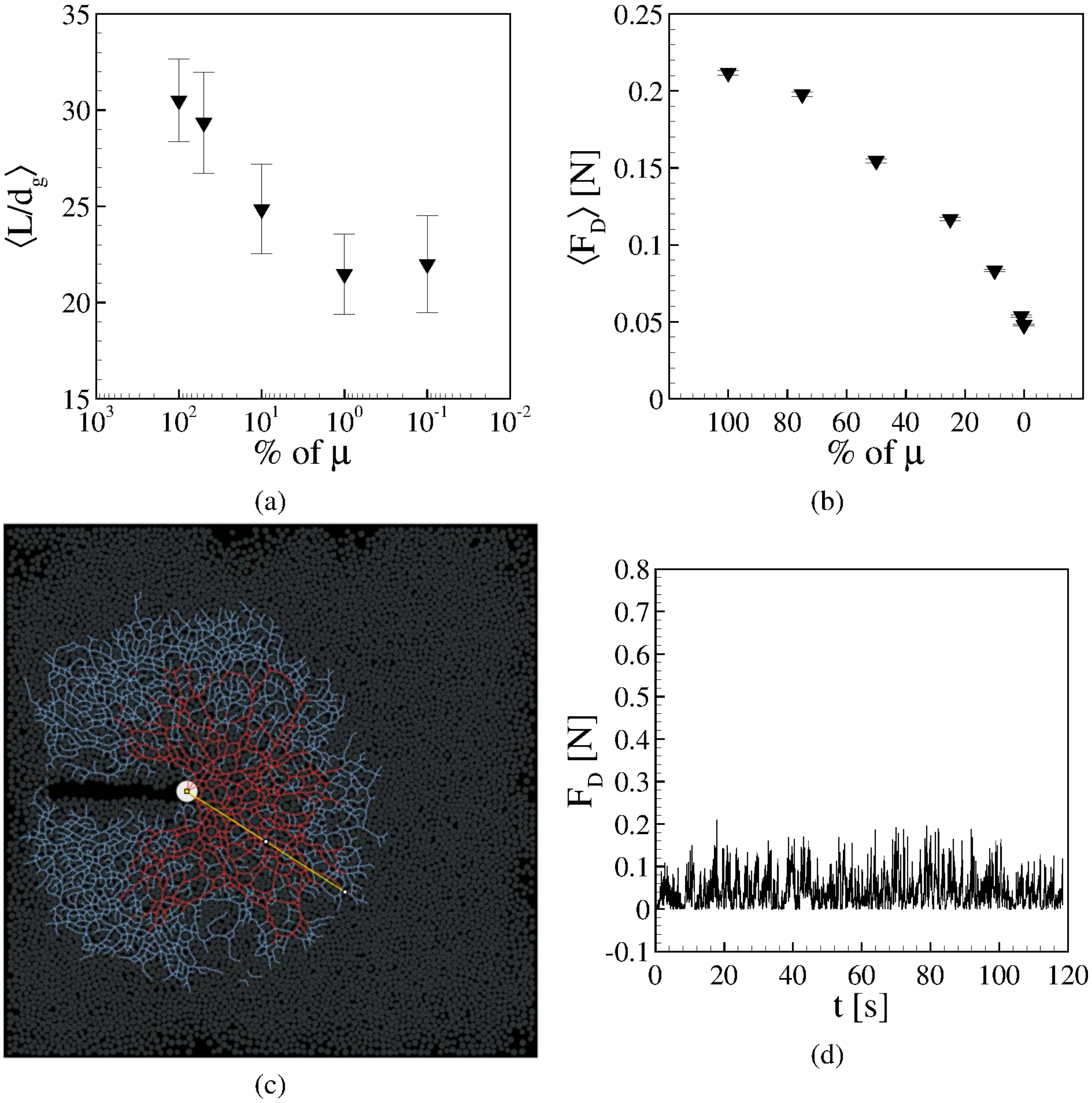

(a) (b)

(c) (d)

Figure 4.12 – (a) Time-averaged length of chains $\langle L \rangle$ normalized by d_g and (b) time-averaged drag $\langle F_D \rangle$ for different values of friction coefficients, in terms of percentages of the base values [see Tab. (4.5)]. (c) Diagram illustrating how the maximum distance reached by bearing chains is computed: a line (in yellow) with origin at the center of the intruder is rotated in the azimuthal direction in order to find the most distant points pertaining to bearing chains. In this figure, blue lines correspond to dissipative and red lines to bearing chains. (d) Magnitude of the resultant force on the intruder F_D as a function of time t when the basal friction is 0.1% of the base value. In Fig. (a) error bars correspond to standard deviations and in Fig. (b) to standard errors. Images taken from (Carvalho *et al.*, 2022).

the static and dynamic coefficients, μ_{iw}, μ_{gw} and $\mu_{s,gw}$, were reduced to 75, 50, 25, 10, 1, and 0.1% of the original values [shown in Tab. (4.3)]. We analyze next how the density of contact networks, typical lengths of chains, and behavior of the cavity vary with the basal friction.

Figure (4.11) shows the networks of contact forces for different values of the coefficients of basal friction, where Figs. (4.11)a to (4.11)d correspond to values of 100, 25, 10 and 0.1% of the base value [Tab. (4.5)]. The figures show that the extents of both bearing and dissipative chains decrease with decreasing the basal friction. In order to quantify that, we computed the typical length L of the bearing chains by measuring, along time, the maximum distance from the center of the intruder reached by bearing chains. Figure (4.12)c shows a diagram of how this distance is measured. Figure (4.12)a presents the time-averaged values of the typical length, $\langle L \rangle$, normalized by the mean grain diameter d_g for different values of friction coefficients (in terms of percentages of the base values). We observe that the extent of bearing chains decreases slightly with reducing the basal friction, the typical length decreasing by roughly 30% when the basal friction is reduced from 0.4 and 0.7 to virtually 0 (0.0004 and 0.0007, respectively). As a result of the lower extent of load-bearing chains, the resultant drag on the intruder also decreases with decreasing the basal friction, Fig. (4.12)b showing that $\langle F_D \rangle$ decreases one order of magnitude when basal frictions are reduced as before. Figure (4.12)d shows the temporal evolution of F_D for a basal friction of 0.1% of the base value, on which we observe a much lower level of fluctuations when compared with F_D for the base value.

The extent of bearing chains decreases under lower friction because in this case grains move easier when submitted to lower forces, breaking thus some of the chains. This is corroborated by the reductions of the downstream cavity as the basal friction decreases. Figure (4.13) shows the cavity for different basal frictions, Figs. (4.13)a to (4.13)d corresponding to 100, 25, 10 and 0.1% of the base value [Tab. (4.5)]. We observe a continuous reduction of the cavity size as the basal friction is reduced, with a very slight cavity (and wake) for the smallest value [Fig. (4.13)d], whose size is comparable to that for higher packing fractions ($\phi > 0.80$) and 100% of the basal friction [Fig. (4.1)d].

In summary, in Sec. 4.1.1 we investigated numerically the forces and structures in a two-dimensional granular system displaced by an intruder moving continuously. The granular system and the intruder consisted of 3D disks, all of them settled over a horizontal wall and confined by vertical walls, and, for the computations, we made use of the open-source DEM code LIGGGHTS (Kloss; Goniva, 2010; Berger *et al.*, 2015) together with the DESIgn toolbox (Herman, 2016). By varying the intruder's velocity and the basal friction, we obtained the resultant force on the intruder and the instantaneous network of contact forces, which we analyzed at both the cell and grain scales. We first validated our numerical computations by replicating

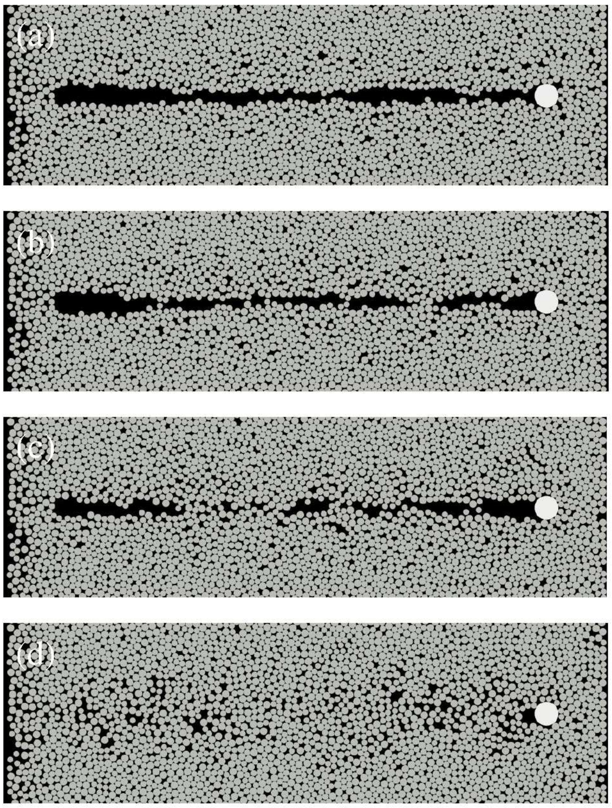

Figure 4.13 – Cavity for different basal frictions. Figures (a) to (d) correspond to 100, 25, 10 and 0.1% of the base value [Tab. (4.5)]. Images taken from (Carvalho *et al.*, 2022).

some of the experimental results obtained by Seguin *et al.* (2016) (Seguin *et al.*, 2016), and we afterward investigated the motion of particles and force transmission. We found that there is a bearing network that percolates large forces from the intruder toward the walls, being responsible for jammed regions and high values of the drag force, and a dissipative network that percolates small forces, in agreement with previous experiments on compressed granular systems. We then showed that anisotropy levels are higher for the bearing chains when compared with the dissipative ones, exhibiting some resemblance with shear jamming, and that anisotropy increases more in regions farther downstream of the intruder by the end of its motion, reaching values three times higher than those in upstream regions. We also found that the extent of the force network decreases with decreasing the basal friction, and that the void region (cavity) that appears downstream the intruder tends to disappear for lower values of basal friction. Finally, our results show that grains within the bearing chains creep while the chains break, revealing the mechanism by which bearing chains collapse.

In the next section (Sec. 4.1.2), we investigate numerically some aspects of the dynamics behind the motion of sets of intruders within a granular material.

4.1.2 Motion of sets of intruders

This section (Sec. 4.1.2) includes material from Douglas D. Carvalho and Erick M. Franklin, “Collaborative behavior of intruders moving amid grains”, Phys. Fluids **34**, (2022), reproduced with permission from the American Institute of Physics (Carvalho; Franklin, 2022b).

Even though the cooperative behavior of intruders was evinced and its mechanisms explained in previous works, many aspects remain open, such as the forced motion of intruders in the horizontal direction, and the roles of friction, mean packing fraction and contact chains on the overall dynamics. In this section, we investigate numerically how a group of intruders interact with each other while moving horizontally in a two-dimensional granular system. The numerical setup consists of two or three larger disks (intruders) driven either at constant speed or thrusting force within an assembly of smaller disks (grains) confined in a rectangular cell. As in Sec. 4.1.1, the disks are 3D objects (low height cylinders) sliding over a flat surface with both static and dynamic coefficients of friction, and we carried out DEM (discrete element method) computations, in accordance to the methodology presented in Sec. 3.1.1. In summary, we show that: (i) intruders cooperate even when at relatively large distances from each other; (ii) the cooperative dynamics is the result of contact chains linking the intruders as well as compaction and expansion of the granular medium in front and behind, respectively, each intruder; (iii) the collaborative behavior depends on the initial arrangement of intruders; and (iv) for some initial arrangements, the same spatial configuration is eventually reached. We propose a chart for the collaborative patterns, and we show the existence of an optimal distance for minimum drag for a given set of intruders, which can prove useful for devices stirring the ground or other granular surfaces.

4.1.2.1 Numerical setup

The numerical setup is similar to that of Sec. 4.1.1, excepting the size of the domain, the number of intruders, and the type of external forcing. The system consisted of an assembly of 3D disks (grains) over a horizontal wall, confined by vertical walls, and a set of two (duo) or three (trio) larger 3D disks (intruders) in different initial configurations. Both the grains and the intruders had one of their flat surfaces facing the bottom wall, and the intruders moved at either constant velocity or thrusting force among the grains. The dimensions and properties of each grain and intruder are the same as in Refs. (Seguin *et al.*, 2016; Carvalho *et al.*, 2022): the intruders were of steel with diameter $d_{int} = 16$ mm and height $h_{int} = 3.6$ mm, and the grains were of polyurethane (PSM-4) with height $h_g = 3.2$ mm and two different diameters, $d_s = 4$ mm and $d_l = 5$ mm, in order to prevent crystallization (Speedy, 1999). The areas occupied by the small and large grains were roughly the same by assuring a ratio $N_l/N_s \approx 0.64$ between the numbers of small (N_s) and large (N_l) disks.

The total domain varied depending on the simulation, being L_x = L_y = 0.4 m (for most simulations with two intruders) or L_x = 0.8 and L_y = 0.4 m (for all simulations with three and one with two intruders), where L_x and L_y are the longitudinal and transverse lengths, respectively. The domain was fixed for each simulation, so that the mean packing fraction ϕ remained constant in each run, but varied within $0.70 \leq \phi \leq 0.79$ for different runs by changing the number of disks in each simulation. The number of disks and the corresponding packing fractions are available in Tab. (4.6). We imposed the intruders to move at either a constant velocity of 2.7 mm/s (in cases with two intruders) or a constant external force (thrust) of 0.8 N (in cases with two and three intruders), and the motions were limited to the xy plane, x being the longitudinal and y the transverse direction. We made use of 2.7 mm/s to allow for comparisons with the experiments of Seguin *et al.* (2016) (Seguin *et al.*, 2016) (as done in Ref. (Carvalho *et al.*, 2022) and presented in Sec. 4.1.1), and 0.8 N to displace the intruders in the quasi-static regime (values slightly lower or higher would work as well). The 0.8 N thrust was imposed on each intruder, at each time step, in the x direction. Examples of setups can be seen in Fig. (4.14).

Table 4.6 – For each duo and trio (Config.): mean packing fraction ϕ, number of small N_s and large N_l grains, and total number of grains N.

Config.	ϕ	N_s	N_l	N
duo	0.76	4826	3089	7915
trio	0.70	8896	5693	14589
trio	0.71	9023	5775	14798
trio	0.72	9150	5856	15006
trio	0.73	9277	5937	15214
trio	0.74	9404	6019	15423
trio	0.75	9531	6100	15631
trio	0.76	9658	6181	15839
trio	0.77	9785	6262	16047
trio	0.78	9913	6344	16257
trio	0.79	10040	6426	16466

The intruders were placed initially in the left region of the domain, by either duos or trios with initial separations Δx and Δy in the longitudinal and transverse directions, respectively, and were afterward put into motion toward the right region. We varied the initial values

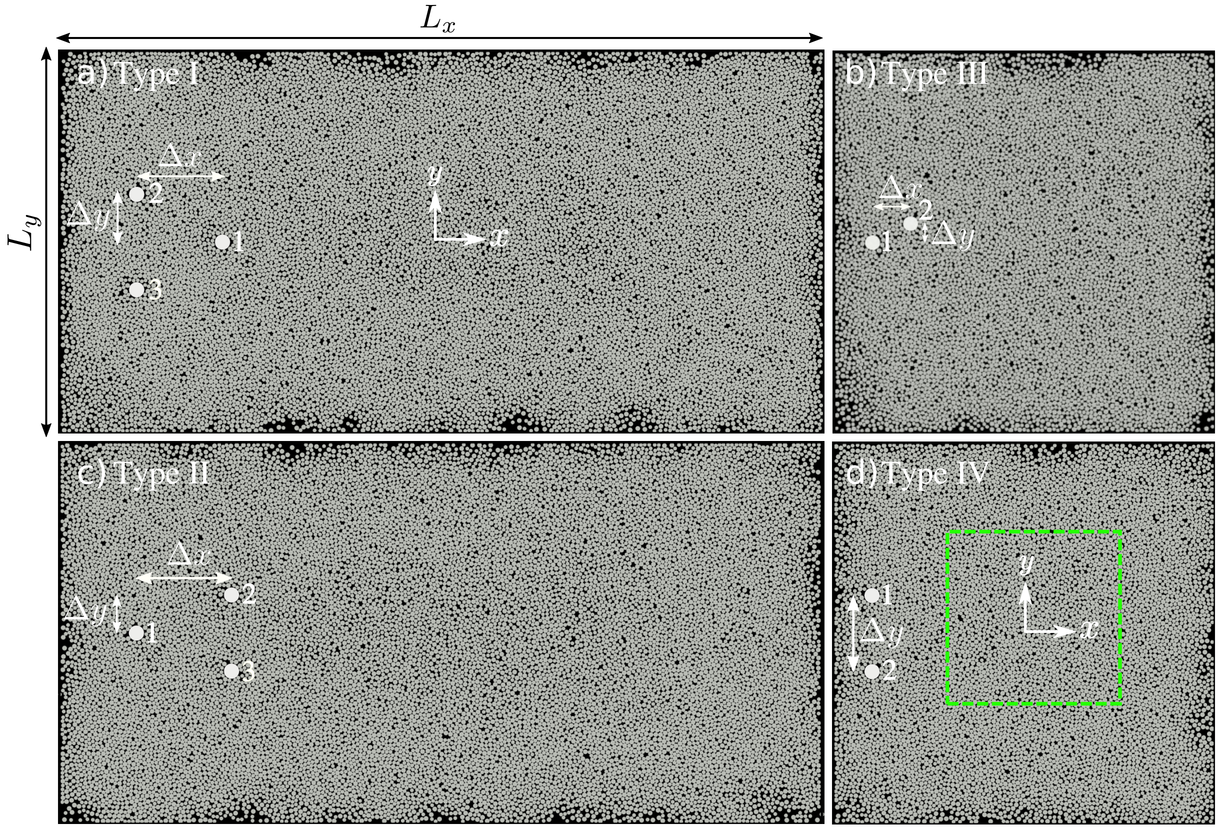

Figure 4.14 – Top-view images of the numerical setup for duos (d) aligned and (b) off-centered in the transverse direction, and trios with one intruder (a) in front and (c) behind two intruders initially aligned in the transverse direction. Figures (a) to (d) correspond to types I, III, II and IV, respectively. Δx and Δy are the initial separations in the longitudinal and transverse directions, respectively, and the area delimited by dashed-green lines in figure (d) is a static region of interest (ROI) used for some computations. Images taken from (Carvalho; Franklin, 2022b).

of Δx and Δy for different simulations, and, as the intruders were driven amid the grains, Δx and Δy were free to change along time in the cases of imposed thrust. Basically, four configurations were used: (i) one intruder in front of two intruders initially aligned in the transverse direction [Fig. (4.14)a]; (ii) one intruder behind two intruders initially aligned in the transverse direction [Fig. (4.14)c]; (iii) two intruders off-centered in the transverse direction [Fig. (4.14)b]; and (iv) two intruders initially aligned in the transverse direction [Fig. (4.14)d]. We call these configurations *types I to IV*, respectively. The simulations with imposed velocity were carried out only for type IV, for different initial Δy, but in these cases, due to the forcing characteristics, Δy remained constant along the time. Figure (4.14)d also shows a region of interest (ROI) delimited by dashed-green lines (fixed in space), measuring 160 mm × 160 mm (corresponding to approximately $35d_g \times 35d_g$, where d_g = 4.5 mm is the average diameter of disks) and used for computing the time-average forces on the intruders and anisotropy within the granular system.

Values of the coefficients of restitution ϵ and friction μ (both static and dynamic), Young's modulus E and Poisson ratio ν were obtained from the literature (Carlevaro *et al.*, 2020; Hashemnia; Spelt, 2014; Gondret *et al.*, 2002; Zaikin *et al.*, 2017), and sensitivity tests varying those coefficients are shown in Fig. (4.2). We note that we used a value of E for the steel two orders of magnitude smaller than the real one ($E = 1.96 \times 10^{11}$ Pa) in order to increase the time step while keeping a reasonable accuracy in the results (Lommen *et al.*, 2014). We implemented the basal friction, both static and dynamic, by defining a threshold velocity $v' = 5 \times 10^{-4}$ m/s for the transition between static and dynamic conditions. Sensitivity tests for v' are shown in Fig. (4.2)i, where we verified that the time-averaged drag force does not change considerably for $v' < 10^{-3}$ m/s. Table (4.7) summarizes the mechanical properties of objects as used in the simulations and Tab. (4.8) the values of friction and restitution coefficients.

Table 4.7 – Properties of materials as used in the simulations: E is the Young's modulus, ν is the Poisson ratio, ρ is the material density, and d is the particle diameter.

	Material	E **(Pa)**	ν	ρ **(kg/m^3)**	d **(mm)**
Intruder	Steel$^{(1)}$	1.96×10^9	0.29	7800	$d_{int} = 16$
Grains	Polyurethane$^{(1),(2)}$	4.14×10^6	0.50	1280	$d_s = 4$; $d_l = 5$
Walls	Glass$^{(1)}$	0.64×10^{11}	0.23	2500	$\cdots$

(1) Hashemnia and Spelt (Hashemnia; Spelt, 2014)

(2) Gloss (Gloss, 2000)

Table 4.8 – Friction and restitution coefficients used in the numerical simulations.

Coefficient	**Symbol**	**Value**
Restitution coefficient (grain-grain)	ϵ_{gg}	0.30
Restitution coefficient (grain-intruder)$^{(2)}$	ϵ_{gi}	0.70
Restitution coefficient (grain-wall)$^{(3)}$	ϵ_{gw}	0.70
Restitution coefficient (intruder-intruder)$^{(4)}$	ϵ_{ii}	0.56
Dynamic friction coefficient (grain-grain)$^{(1)}$	μ_{gg}	1.20
Dynamic friction coefficient (grain-intruder)$^{(2)}$	μ_{gi}	1.80
Dynamic friction coefficient (intruder-bottom wall)	μ_{iw}	0.70
Dynamic friction coefficient (grain-walls)$^{(1)}$	μ_{gw}	0.40
Dynamic friction coefficient (intruder-intruder)	μ_{ii}	0.57
Static friction coefficient (grain-bottom wall)	$\mu_{s,gw}$	0.70

(1) Carlevaro *et al.* (Carlevaro *et al.*, 2020)

(2) Hashemnia *et al.* (Hashemnia; Spelt, 2014)

(3) Gondret *et al.* (Gondret *et al.*, 2002)

(4) Zaikin *et al.* (Zaikin *et al.*, 2017)

Prior to each run, the grains were randomly distributed over a space larger than the computational domain, and then compressed toward the center until filling the desired domain.

Afterward, the grains were allowed to relax and the simulation started. This assured the desired packing fraction within reasonable times (computation times for placing random grains directly under high packing fractions are prohibitive). The simulations were carried out with a time step $\Delta t = 3.2 \times 10^{-6}$ s, which was less than 10 % of the Rayleigh time [Eq. (4.2)] (Derakhshani *et al.*, 2015) in all simulated cases, and our numerical computations were validated in Sec. 4.1.1 by replicating some of the experimental results of Seguin *et al.* (2016) (Seguin *et al.*, 2016). We present next the results for groups of two or three intruders moving within the granular system.

4.1.2.2 Results and discussion - Duos moving at constant velocity

We present in this subsection the results for a pair of aligned intruders moving at constant velocity V = 2.7 mm/s when ϕ = 0.76. For different computations, we varied the initial separation Δy of intruders and evaluated their drag force $\vec{F}_D$, the mean number of contacts per particle Z, the number of non-rattler particles N (particles with at least two contacts), and the anisotropy level ρ, Z and ρ given by the fabric tensor (Bi *et al.*, 2011)):

$$\hat{R} = \frac{1}{N} \sum_{i \neq j} \frac{\mathbf{r}_{ij}}{|\mathbf{r}_{ij}|} \otimes \frac{\mathbf{r}_{ij}}{|\mathbf{r}_{ij}|}, \tag{4.4}$$

where $\mathbf{r}_{ij}$ is the contact vector from the center of particle i to the contact between particles i and j, and $\otimes$ denotes the outer product. We then obtain the mean number of contacts per particle and the anisotropy level by computing $Z = R_1 + R_2$ and $\rho = R_1 - R_2$, respectively, where R_1 and R_2 are the eigenvalues of the tensor $\hat{R}$. More details regarding the fabric tensor $\hat{R}$ can be seen in Appendix B.

We computed also time averages of these quantities in the entire domain or by considering a moving ROI that followed the intruders along their motion Fig. (4.15)a. In the case of drag forces, we computed a mean value by averaging the values for both intruders. Those results are summarized in Fig. (4.15).

4.1.2.2.1 Drag force on the intruders

A snapshot showing a top-view image of grains and intruders for a typical simulation is shown in Fig. (4.15)a, where we observe the formation of a cavity (absence of grains) behind (downstream) each intruder in places previously visited by them (movies showing the time evolution of the granular system as the intruders move are available on a public repository

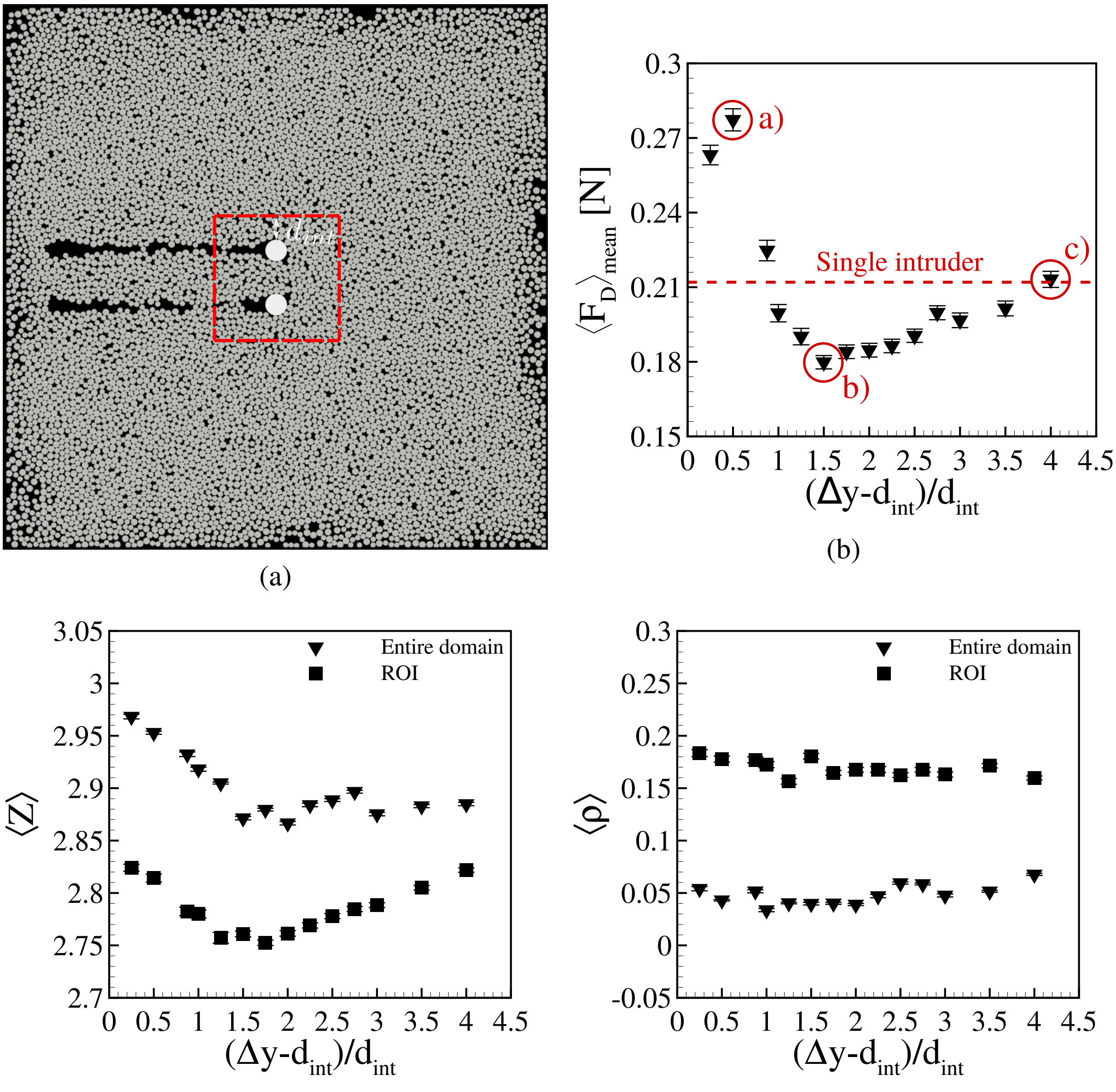

(a) (b) (c) (d)

Figure 4.15 – (a) Snapshot showing the intruders and grains (top-view image), and a moving ROI around the intruders (delimited by dashed-red lines). (b) Magnitude of the mean resultant force on each intruder $\langle F_D \rangle_{mean}$ as a function of their initial separation Δy normalized by the intruder diameter d_{int}. (c) Mean number of contacts per particle averaged over time $\langle Z \rangle$ and (d) time-averaged anisotropy $\langle \rho \rangle$ as functions of $(\Delta y - d_{int})/d_{int}$. In figures (b) to (d) triangles correspond to averages computed by considering the entire domain and squares by considering only particles in the moving ROI shown in figure (a), and bars correspond to the standard errors. In figure (b), the dashed-red line corresponds to the time-average drag force found for a single intruder in Ref. (Carvalho *et al.*, 2022), and the marked points indicate the conditions for which the networks of contact forces are shown in Fig. (4.18). All graphics are for $V = 2.7$ mm/s and $\phi = 0.76$. Images taken from (Carvalho; Franklin, 2022b).

(Carvalho; Franklin, 2022a)). The existence of a cavity downstream of a single intruder was measured experimentally by Kolb *et al.* (2013) (Kolb *et al.*, 2013) and Seguin *et al.* (2016) (Seguin *et al.*, 2016) and numerically by Carvalho *et al.* (2022) (Carvalho *et al.*, 2022). The figure also shows the region of interest around the intruders, which moves with them and is used in some computations presented next. The ROI was a square with side length equal to $\Delta y + 3d_{int}$.

As in Sec. 4.1.1, we computed the instantaneous drag force on the intruder $\vec{F}_D$, and then its time-averaged magnitude $\langle F_D \rangle$. Examples of the time evolution of $|\vec{F}_D|$ are shown in Fig. (4.16).

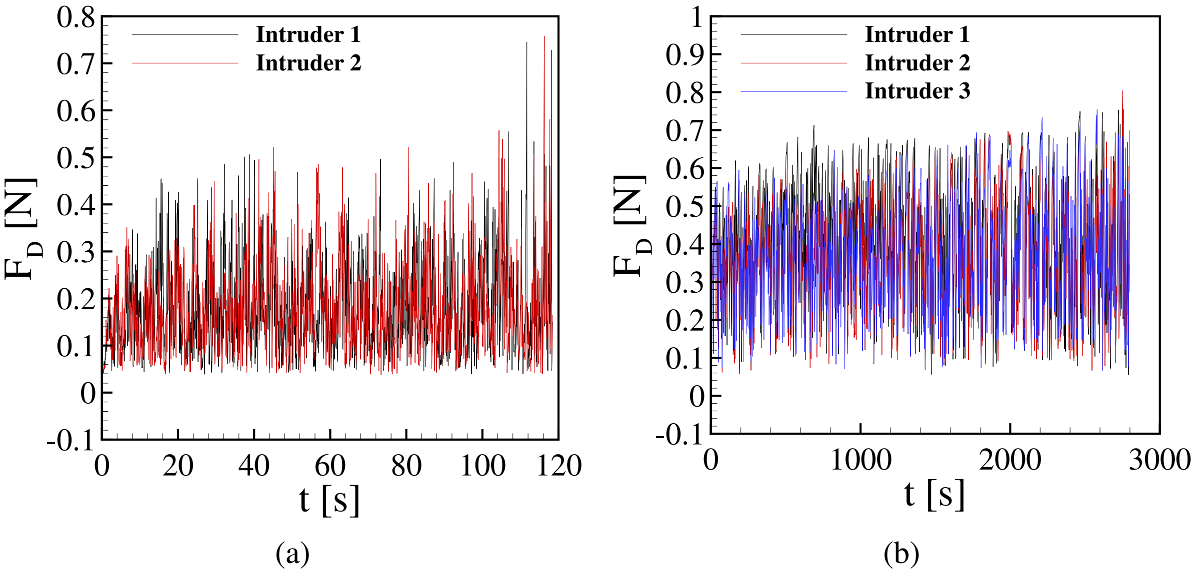

Figure 4.16 – Magnitudes of the resultant force on each intruder F_D as functions of time t. (a) Duos with $(\Delta y - d_{int})/d_{int}$ = 1.5 moving at V = 2.7 mm/s. (b) Trios moving at constant thrusting force (type I reaching D_{att}). Images taken from (Carvalho; Franklin, 2022b).

We afterward computed a mean value for the intruders, $\langle F_D \rangle_{mean}$, by adding their time averages and then dividing by two, for each transverse separation Δy. Figure (4.15)b presents $\langle F_D \rangle_{mean}$ as a function of $(\Delta y - d_{int})/d_{int}$, i.e., the separation between the surfaces of intruders normalized by the intruder diameter. We observe a non-monotonic variation, with a decrease in the mean drag force for $(\Delta y - d_{int})/d_{int} < 1.5$ as the separation between intruders increases, and an increase for $(\Delta y - d_{int})/d_{int} > 1.5$. Therefore, there is an optimal distance D_{opt} for minimum drag when the separation between the surfaces of intruders is 1.5 times their diameter ($D_{opt} \rightarrow \Delta y = 2.5 d_{int}$). Interestingly, in this condition the drag acting on each intruder is approximately 0.18 N, which corresponds to 85% of the value for a single intruder (Ref.

(Carvalho *et al.*, 2022) found 0.21 N for a single intruder under the same velocity and packing fraction). In fact, there is a range $1 \lessapprox (\Delta y - d_{int})/d_{int} \lessapprox 3.5$ where $\langle F_D \rangle_{mean}$ is smaller than the drag for a single intruder, indicating that some type of cooperative dynamics between the intruders is happening within the granular system. We note that the value of the minimum drag is repeatable, the value 0.18N being obtained in three simulations with different initialization in the same domain (confined by solid walls) and another one with periodic conditions, while a value of approximately 0.19N was obtained for a larger domain (L_x multiplied by 2, and confined by solid walls). Therefore, the results are roughly the same (variations being around 5% for different domains and initial conditions).

We note that we carried out simulations with different grain sizes (5 and 6 mm) [Fig. (4.17)a], and the results for the time-average drag are similar to previous ones: although the magnitude of the reduction changes with the size of disks, drag reduction occurs for the same range of $(\Delta y - d_{int})/d_{int}$, the minimum drag occurring for $(\Delta y - d_{int})/d_{int} \approx 1.5$. We thus used d_{int} as a scale for normalization, but further investigation is still necessary. We also carried out simulations with a different velocity of intruders (7.5 mm/s) [Fig. (4.17)b], and obtained similar results: the behavior and regions of drag reduction are the same though the values of drag are different. The results for different sizes of disks and intruder velocity are shown in Fig. (4.17).

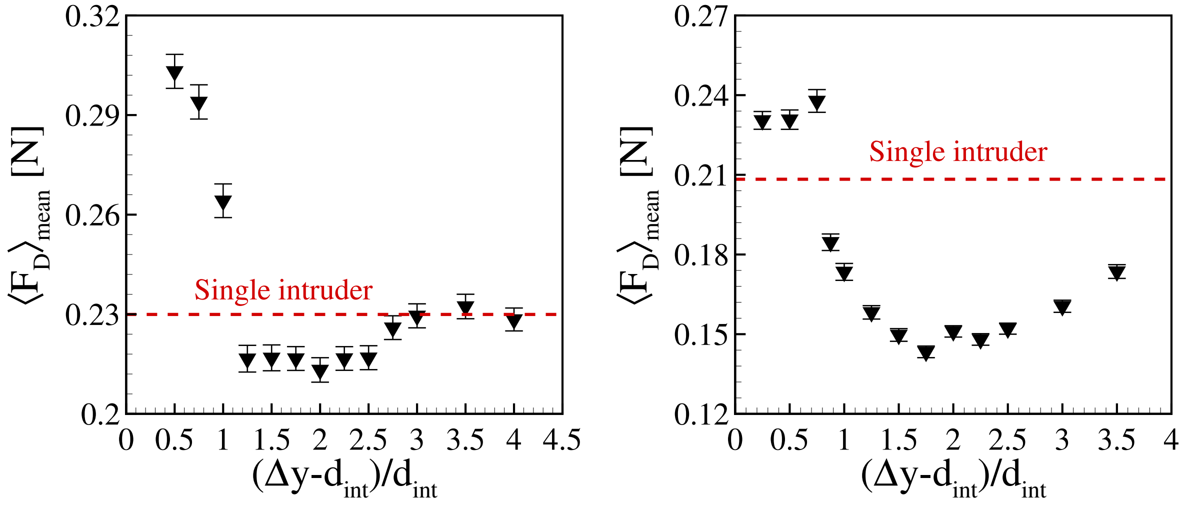

(a) (b)

Figure 4.17 – Magnitude of the mean resultant force on each intruder $\langle F_D \rangle_{mean}$ as a function of their initial separation Δy normalized by the intruder diameter d_{int}, for duos moving at constant speed. (a) Different size of disks: d_s = 5 mm and d_l = 6 mm. (b) Different velocity of intruders: V = 7.5 mm/s. Images taken from (Carvalho; Franklin, 2022b).

4.1.2.2.2 Network of contact forces

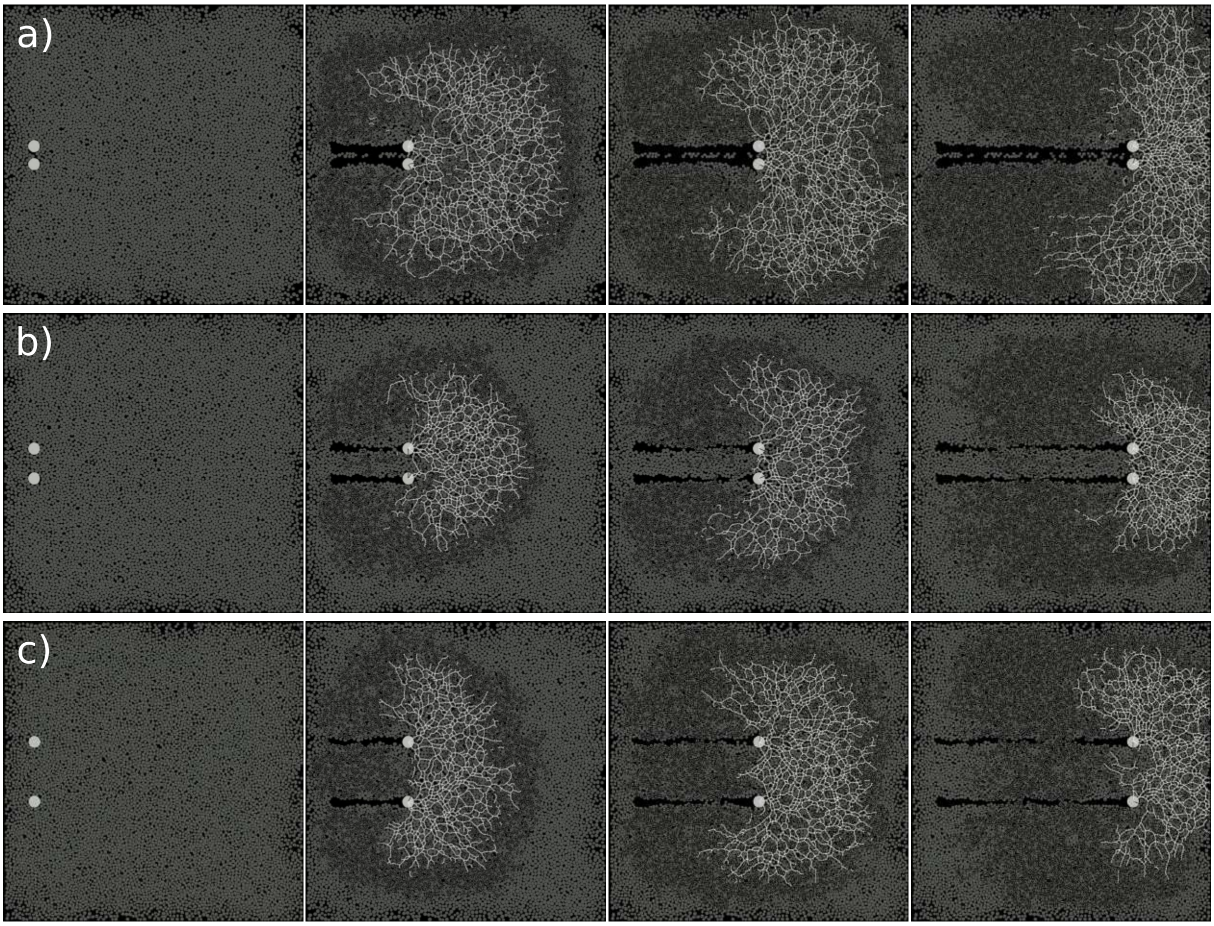

Figure 4.18 – From left to right, snapshots at t = 0, 35.532, 59.220 and 94.752 s of duos moving within grains at V = 2.7 mm/s for (a) $(\Delta y - d_{int})/d_{int}$ = 0.5; (b) $(\Delta y - d_{int})/d_{int}$ = 1.5; and (c) $(\Delta y - d_{int})/d_{int}$ = 4.0. The figures show the load-bearing (clear lines) and dissipative (dark lines) chains for the cases highlighted in Fig. (4.15)b, and ϕ = 0.76. Images taken from (Carvalho; Franklin, 2022b).

In the case of a cooperative dynamics, we expect that details of the network of contact forces change with the separation between intruders. Following Radjai *et al.* (1998) (Radjai *et al.*, 1998), we identified the contact chains and separated them into load-bearing chains, transmitting forces higher than the average value (ensemble average at each considered instant), and dissipative chains, transmitting values lower than that average. The ensemble average was computed at each time step by adding all the contact forces and dividing the result by the number of contacts. Those chains are intermittent, forming and collapsing successively. Figures (4.18)a to (4.18)c present snapshots at four different instants of duos moving at constant velocity for, respectively, $(\Delta y - d_{int})/d_{int}$ = 0.5, 1.5, and 4.0, showing also the load-bearing (clear lines) and dissipative (dark lines) chains. The cases $(\Delta y - d_{int})/d_{int}$ = 0.5 and 1.5 correspond, respectively, to the maximum and minimum drags found for V = 2.7 mm/s [Fig. (4.15)b]. For $(\Delta y - d_{int})/d_{int}$ = 0.5 [Fig. (4.18)a], we observe very sporadic load-bearing chains linking the intruders, indicating a low level of (positive) cooperation between the intruders, while load-bearing chains percolate over long distances from the intruders and reach the vertical walls toward the end of their motion. Dissipative chains also reach distances far from the intruders, and by the end of their motion percolate over almost the entire system. For $(\Delta y - d_{int})/d_{int}$ = 1.5 [Fig. (4.18)b], which corresponds to D_{opt}, we notice frequent load-bearing chains linking the intruders, indicating positive cooperation (resulting from one intruder pushing the other via load-bearing chains), and that load-bearing chains remain closer to the intruders, reaching the vertical walls only at the end of motion. Dissipative chains also remain closer to the intruders, reaching the right wall only by the end of their motion (implying less basal drag). For $(\Delta y - d_{int})/d_{int}$ = 4.0, [Fig.(4.18)c], which corresponds to an intermediate value of $\langle F_D \rangle_{mean}$, load-bearing chains link the intruders, but they also extend over distances farther from them. This, together with dissipative chains that percolate also over longer distances and reach the lateral walls before the end of motion, imply larger basal frictions and thus a higher drag force. Therefore, from the balance between chains connecting the intruders and those percolating over long distances, the intruders cooperate the most to move forward when $(\Delta y - d_{int})/d_{int}$ = 1.5 (Δy = D_{opt} = 2.5d_{int}), pushing each other and being subject to smaller drag.

Because the networks of contact forces are dense and intermittent, it is unfeasible to find small changes directly from their plots, such as those in Fig. (4.18). We thus investigated how the mean number of contacts per particle averaged over time $\langle Z \rangle$ and the time-averaged anisotropy $\langle \rho \rangle$ change with $(\Delta y - d_{int})/d_{int}$, which we show in Figs. (4.15)c and (4.15)d, respectively, computed for both the entire domain and the ROI.

By considering the entire domain, we observe that the profile of $\langle Z \rangle$ follows roughly that of $\langle F_D \rangle_{mean}$, with $\langle Z \rangle \approx$ 2.9 in the region $1 \leq (\Delta y - d_{int})/d_{int} \leq 4$, which is approximately the value for the single intruder (2.903) (Carvalho *et al.*, 2022). The anisotropy $\langle \rho \rangle$ considering the entire domain is roughly constant, with values of the order of 0.05, also close to that for the single intruder (0.041) (Carvalho *et al.*, 2022). Therefore, the granular system as a whole does not seem to play a large role on drag reduction, except when the intruders are too close from each other ($(\Delta y - d_{int})/d_{int} < 1$), being in that case almost one single and large intruder. By considering now only the ROI, the general behaviors of both $\langle Z \rangle$ and $\langle \rho \rangle$ with $(\Delta y - d_{int})/d_{int}$

remain as for the entire region, but the magnitudes are different: $\langle Z \rangle$ varies around 2.8 (smaller than that for the single intruder) and $\langle \rho \rangle$ remains constant at approximately 0.1 (larger than that for the single intruder). The network of contact forces is thus different in the neighborhood of the intruders, with less contacts between grains and higher anisotropy, indicating preferential directions for percolating loads. These preferential directions are connected with the motion of disks shown in Sec. 4.1.2.3.2.

Our results show that: (i) there exists a cooperative dynamics between the intruders; and (ii) in cases of constant velocity, there is an optimal separation between intruders for not only reaching minimum drag, but also drag reduction (with respect to single intruders). The latter can be proven useful for designing devices stirring the ground or other granular surfaces.

Additional graphics for the number of contacts per particle Z, number of non-rattler particles N and anisotropy ρ for the extreme cases [(a) - maximum drag] and [(b) - minimum drag] of Fig. (4.15)b are presented in Figs. (4.19), (4.20), and (4.21), respectively.

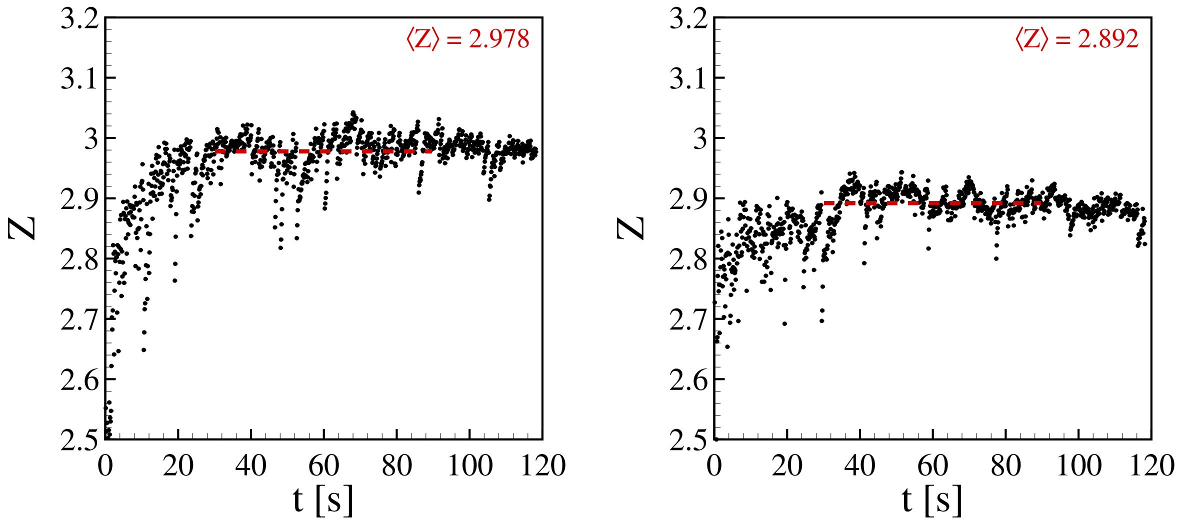

(a) (b)

Figure 4.19 – Time evolution of the mean number of contacts per particle Z for duos with (a) $(\Delta y - d_{int})/d_{int}$ = 0.5 and (b) $(\Delta y - d_{int})/d_{int}$ = 1.5. The time-averaged value is shown in the figure, ϕ = 0.76 and V_0 = 2.7 mm/s. Images taken from (Carvalho; Franklin, 2022b).

4.1.2.3 Results and discussion - Constant thrusting force

We investigate now the behavior of the entire system when a constant external force (thrust) of 0.8 N in the longitudinal direction is imposed on each intruder of either duos or trios (ϕ = 0.76, unless where otherwise mentioned). In these cases, because the drag force oscillates

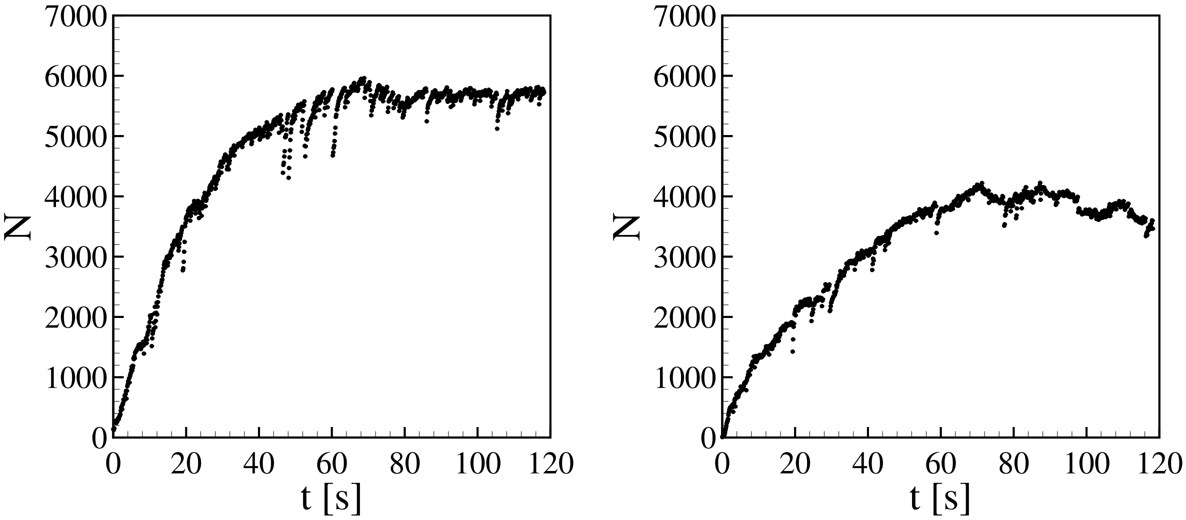

(a) (b)

Figure 4.20 – Time evolution of the number of non-rattler particles N for duos with (a) $(\Delta y - d_{int})/d_{int}$ = 0.5 and (b) $(\Delta y - d_{int})/d_{int}$ = 1.5. ϕ = 0.76 and V_0 = 2.7 mm/s. Images taken from (Carvalho; Franklin, 2022b).

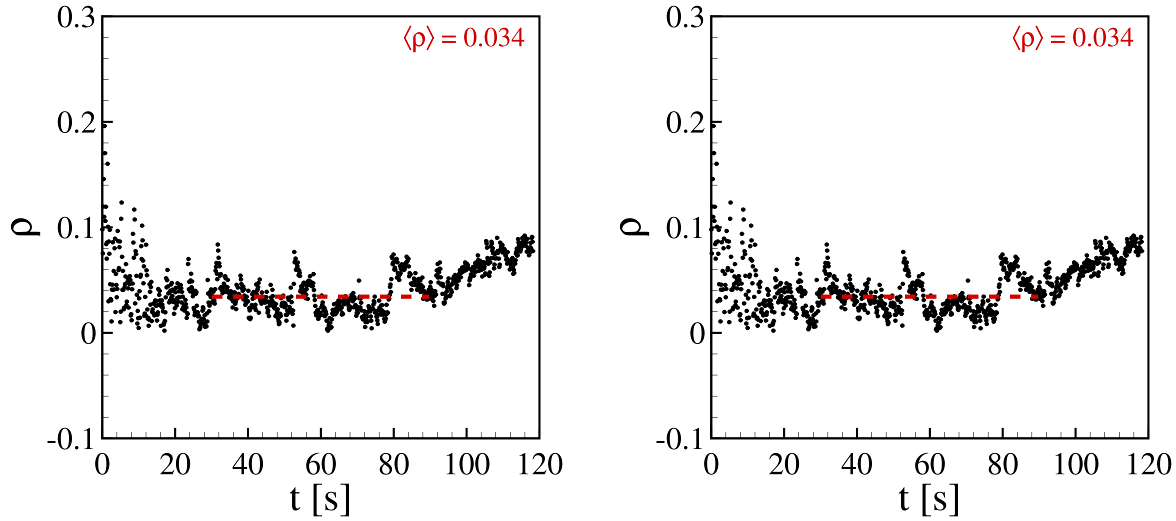

(a) (b)

Figure 4.21 – Time evolution of the anisotropy level ρ for duos with (a) $(\Delta y - d_{int})/d_{int}$ = 0.5 and (b) $(\Delta y - d_{int})/d_{int}$ = 1.5. The time-averaged value is shown in the figure, ϕ = 0.76 and V_0 = 2.7 mm/s. Images taken from (Carvalho; Franklin, 2022b).

along the motion and the intruders are free to move in the transverse direction, the cooperative behavior implies intruder velocities that vary along time and depend on the initial configuration, giving rise to different types of migration.

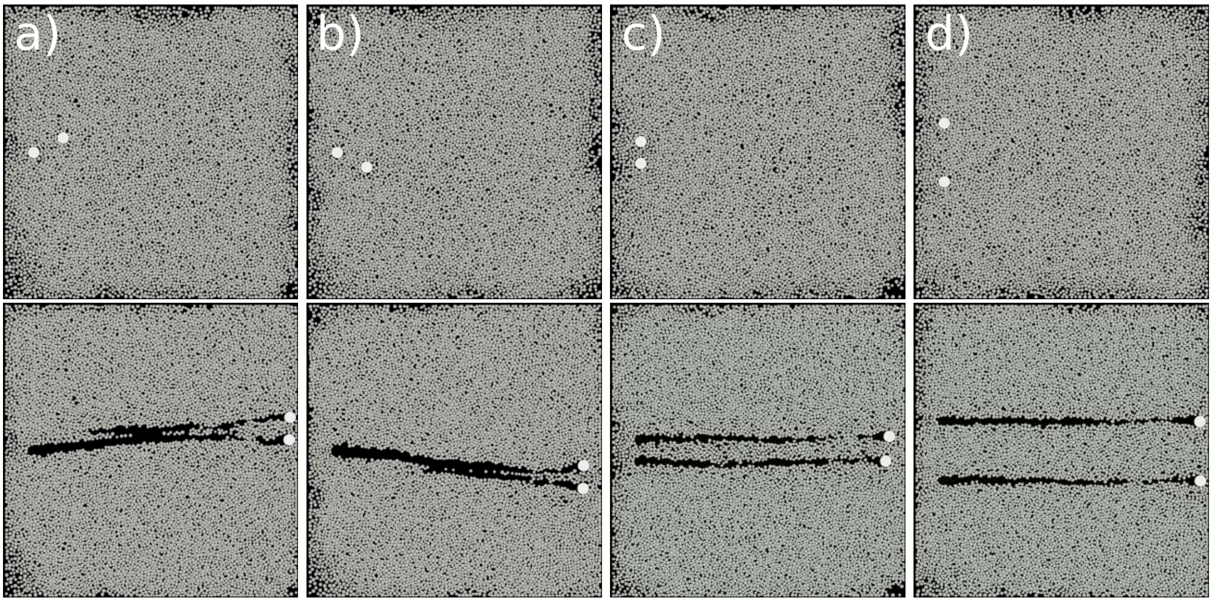

Figure 4.22 – Snapshots showing the intruders and grains (top-view images) for a pair of intruders: (a) and (b) off-centered (type III); and (c) and (d) aligned (type IV) in transverse direction. The initial condition is on the top and the final configuration on the bottom of each subfigure, and ϕ = 0.76. Images taken from (Carvalho; Franklin, 2022b).

4.1.2.3.1 Patterns: collaborative motion

By varying the initial configuration of duos and trios, both in terms of orientation and separations, we obtained different migration characteristics that can be classified in patterns. Beginning by duos, Fig. (4.22) shows the investigated cases, which consisted of intruders aligned [type IV, Figs. (4.22)c and (4.22)d], and off-centered (type III, Figs.(4.22)a and (4.22)b, which are symmetrical) in the transverse direction, with the initial condition on the top and the final on the bottom of each subfigure. We observe basically three patterns: (i) when the intruders are off-centered (type III), the cavity generated by the one that is in front (upstream) affects the intruder that is behind (downstream), which then moves faster in longitudinal direction with a component in the transverse direction toward the upstream intruder. Both intruders migrate with a small transverse component, and by the end of their motion are aligned in the transverse direction, separated by a characteristic distance D_{att} [Figs. (4.22)a and (4.22)b]. (ii) For aligned intruders (type IV) with Δy within a certain range, they approach or retreat until reaching Δy_{final} = D_{att}, and move afterward in aligned configuration, keeping Δy = D_{att} [Fig. (4.22)c]. (iii) For aligned intruders (type IV) with Δy above a given threshold, the intruders move in aligned configurations maintaining Δy approximately constant [Fig. (4.22)d].

Figure (4.23) shows the temporal evolution of Δy for the cases shown in Fig. (4.22).

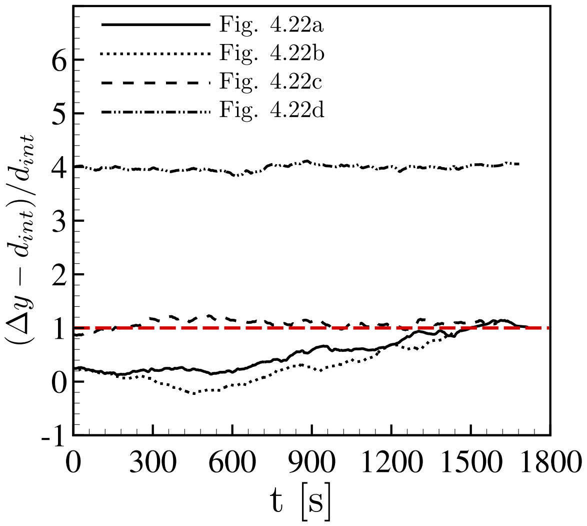

Figure 4.23 – Time evolution of the distance Δy in Fig. (4.22). The red-dashed line corresponds to the distance D_{att}. Image adapted from (Carvalho; Franklin, 2022b).

We note that the evolution toward D_{att} depends on the presence of solid boundaries: we computed one case with periodic boundaries and observed that, although there is still a collaborative motion, the grains did not evolve to D_{att} (at least in the simulated domain). However, we investigate here the confined case, and, therefore, we present next only the cases with solid boundaries.

For the trios, Fig. (4.24) shows the cases that we investigated, namely one intruder in front of two intruders initially aligned in the transverse direction [type I, Figs. (4.24)a to (4.24)c] and one intruder behind two intruders initially aligned in the transverse direction [type II, Figs. (4.24)d and (4.24)e]. We observe basically three patterns: (i) for type I with small separations (small values of Δy), the downstream intruders are exposed to the cavity of the upstream one, and thus move faster in the longitudinal direction and toward the upstream intruder in the transverse direction, forming a clump at the end of their motion [Fig. (4.24)a]. At that time, the drag force is highly increased so that the intruders stop, with indications of jamming (described in Sec. 4.1.2.3.4). (ii) Within a certain range of Δy in types I and II (for type II it is Δy lower than a given threshold), the downstream intruder(s) move(s) faster in the longitudinal direction and end(s) finally aligned with the upstream one(s), while in the transverse direction they move until reaching $\Delta y_{final} = D_{att}$ [Figs. (4.24)b and (4.24)d]. (iii) For Δy above a certain value (large separations) in types I and II, the downstream intruder(s) move(s) faster in the longitudinal direction and end(s) finally aligned with the upstream one without changing the transverse

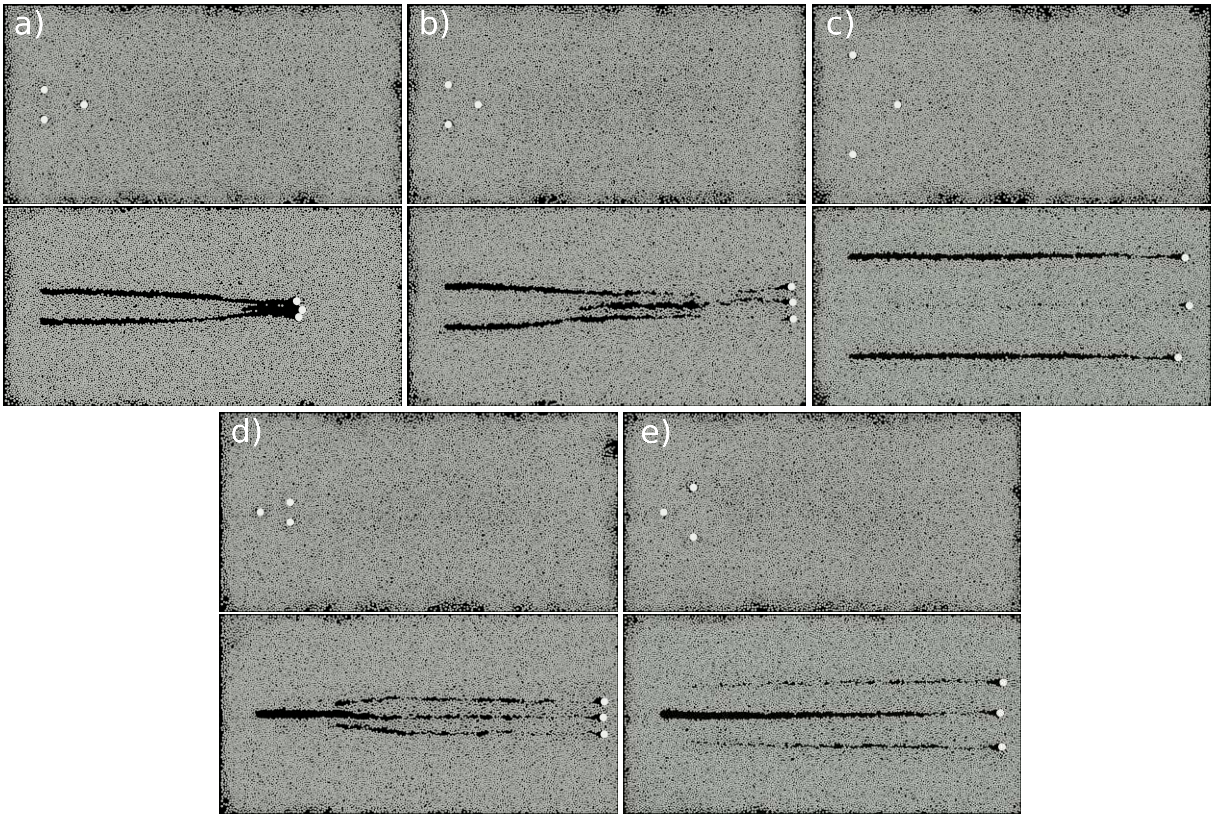

Figure 4.24 – Snapshots showing the intruders and grains (top-view images), for (a), (b) and (c) one intruder in front of two intruders initially aligned in the transverse direction (type I) and (d) and (e) one intruder behind two intruders initially aligned in the transverse direction (type II). The initial condition is on the top and the final configuration on the bottom of each subfigure, and ϕ = 0.76. Images taken from (Carvalho; Franklin, 2022b).

separation [Δy remains approximately constant, Figs. (4.24)c and (4.24)e].

The different patterns are summarized in Fig. (4.25), which shows the final separations Δy_{final} as functions of the initial ones Δy, normalized by the diameter of intruders d_{int}. In this figure, the dashed-red line corresponds to $(\Delta y_{final} - d_{int})/d_{int}$ = 1, and the symbols are listed in the figure key. We observe in Fig. (4.25) the behaviors described in previous paragraphs, but we can now find the respective ranges of initial separations and the value of D_{att}. For type I, within 1.5 $\leq (\Delta y - d_{int})/d_{int} \leq$ 2.2 the final distances reach $(\Delta y_{final} - d_{int})/d_{int} \approx$ 1 (i.e., D_{att} = 2d_{int}). For smaller values of Δy, the intruders form a clump ($\Delta y_{final} < \Delta y$) and for higher values they keep their separation ($\Delta y_{final} \approx \Delta y$). For type II with $(\Delta y - d_{int})/d_{int}$ $\leq$ 1 and types III and IV with $(\Delta y - d_{int})/d_{int} \leq$ 2, the intruders reach D_{att} = 2d_{int}, while for $(\Delta y - d_{int})/d_{int} >$ 1 or 2 (for types II or III and IV, respectively) the transverse separations remain constant ($\Delta y_{final} \approx \Delta y$). Therefore, within certain ranges of initial separations a fixed

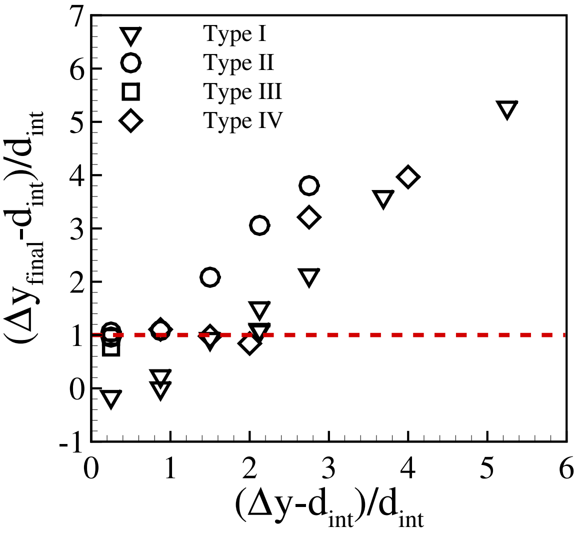

Figure 4.25 – Chart for collaborative patterns: final separations Δy_{final} as functions of initial separations Δy. The symbols are listed in the key and the dashed-red line corresponds to $(\Delta y_{final} - d_{int})/d_{int}$ = 1. Image taken from (Carvalho; Franklin, 2022b).

Δy_{final} is reached (an attractor-like behavior), corresponding to D_{att}/d_{int} = 2 (surface-surface separations equal to d_{int}). We note that one of the runs for type I within 1.5 $\leq (\Delta y - d_{int})/d_{int}$ $\leq$ 2.2 does not fall exactly on $(\Delta y_{final} - d_{int})/d_{int} \approx$ 1, but lies close to it. We consider this deviation rather small, resulting from the presence of one additional disk between two of the intruders at the final stage.

4.1.2.3.2 Motion of disks

The collaborative behavior can be examined in terms of motion of disks as the intruders are thrust within them. Figure (4.26) shows snapshots of the velocity fields of disks for one intruder in front of two intruders initially aligned in the transverse direction [type I, Figs. (4.26)a to (4.26)c] and one intruder behind two intruders initially aligned in the transverse direction [type II, Figs. (4.26)d and (4.26)e]. In Fig. (4.26), ϕ = 0.76 [corresponds to the same cases presented in Fig. (4.24)] and τ is the total time of the intruders' motion. With the exception of Fig. (4.26)a (clump), we observe that even if disks just in front of the intruder have higher velocities, the motion reaches regions far from the intruders, extending toward the walls by the end of the intruders' motion. Throughout the motion, we can also observe grains recirculating from the intruders' front toward their rear, and also migrating from the compacted regions toward the cavities. The migration toward cavities is particularly noticeable in Fig. (4.26)c,

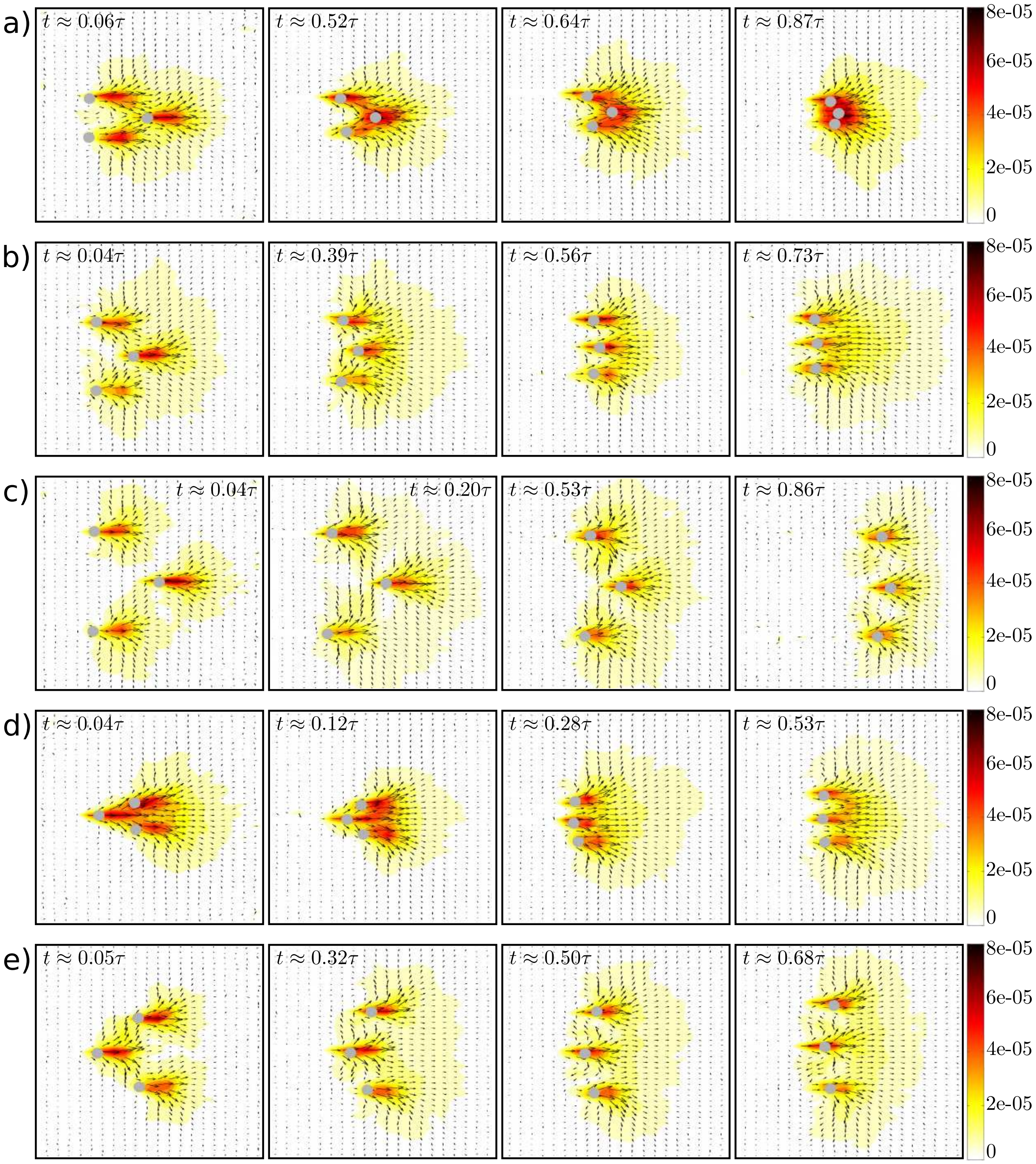

Figure 4.26 – Snapshots showing the velocity fields of disks as the intruders move, for (a), (b) and (c) one intruder in front of two intruders initially aligned in the transverse direction (type I) and (d) and (e) one intruder behind two intruders initially aligned in the transverse direction (type II). τ is the total time of the intrudes' motion, being 2064, 2796, 2928, 2964 and 2652 s for figures (a) to (e), respectively. The cases are in the same order of Fig. (4.24) ($\phi = 0.76$), and the scale of the colorbar is in m/s. Images taken from (Carvalho; Franklin, 2022b).

where vectors indicate migration to the central cavity and, indeed, Fig. (4.24)c shows that this cavity is almost suppressed, and in Fig. (4.26)e, where vectors indicate migration to the lateral cavities, also shown in Fig. (4.24)e (where those cavities are partially suppressed).

In the specific case of Fig. (4.26)a (clump), during roughly the first half of motion ($t \approx 0.06\tau$ to $t \approx 0.64\tau$) part of disks in front the downstream intruders move toward the upstream intruder and suppress its cavity, as can be seen in Fig. (4.24)a. During this time, disks recirculate around the downstream intruders, migrating from compacted regions toward their cavities. Close to the end of motion ($t \approx 0.87\tau$), we observe that the intruders are close to each other and the motion of disks is concentrated just in front of them, not reaching regions so far from the intruders as in the other four cases, indicating a compacted region in front of them. At the same time, a large cavity forms behind the intruders [shown in Fig. (4.24)a], the degree of velocities being small in the recirculation region. All that indicates that the intruders are about to be blocked.

In common, those cases show that part of grains in front of downstream intruders are pushed toward the cavity in front of them, generated by the upstream intruder. This facilitates the motion of downstream intruders, which move faster and reach eventually the upstream ones, whether to be transversely aligned or to form a clump. This picture is in agreement with experiments conducted with a single intruder moving in a system of disks with the same size as in our simulations. For instance, Kolb *et al.* (2013) (Kolb *et al.*, 2013) and Seguin *et al.* (2016) (Seguin *et al.*, 2016) showed that a compacted region forms in front of the intruder, with disks reaching the packing fraction for jamming, while a decompressed region, usually a cavity, forms behind the intruder, so that disks recirculate from the compacted front toward the cavity. The recirculation is intermittent, making the drag force to fluctuate around a mean value (as showed in Carvalho *et al.* (2022) (Carvalho *et al.*, 2022) and in Sec. 4.1.2.3.3).

4.1.2.3.3 Drag force on the intruders

We measured the magnitude of the instantaneous drag force on each intruder by computing $F_D = \sqrt{(F_x - F_T)^2 + F_y^2}$, where $F_T = 0.8$ N is the magnitude of the thrusting force imposed on each intruder, and F_x and F_y are the longitudinal and transverse components of the resultant force (so that the basal friction is included in F_D). We afterward time-averaged F_D for each intruder, obtaining $\langle F_D \rangle$ for different initial separations. The results are summarized in Tab. (4.9), where $\langle F_D \rangle_1$, $\langle F_D \rangle_2$ and $\langle F_D \rangle_3$ correspond to time-averaged drag forces on intruders labeled 1, 2 and 3, respectively, as shown in Fig. (4.14). Distances in Tab. (4.9) are normalized by the diameter of intruders, d_{int}, and forces by the thrusting force on each intruder, F_T.

Table 4.9 – Mean drag on each intruder for different types and separations: configuration type, initial separation in the longitudinal direction Δx, initial separation in the transverse direction Δy, and average forces on intruders 1, 2 and 3, $\langle F_D \rangle_1$, $\langle F_D \rangle_2$ and $\langle F_D \rangle_3$, respectively. Values are normalized by d_{int} and F_T.

Type	$\Delta x/d_{int}$	$\Delta y/d_{int}$	$\langle F_D \rangle_1 / F_T$	$\langle F_D \rangle_2 / F_T$	$\langle F_D \rangle_3 / F_T$
I	5.00	1.88	0.54	0.46	0.46
I	3.75	1.25	0.53	0.43	0.44
I	3.75	1.88	0.54	0.44	0.45
I	5.00	3.13	0.55	0.49	0.49
I	3.75	2.50	0.61	0.58	0.57
I	3.75	3.13	0.51	0.47	0.47
I	5.63	3.13	0.54	0.47	0.47
I	5.63	4.69	0.55	0.49	0.49
I	5.63	6.25	0.56	0.50	0.51
I	3.75	3.75	0.52	0.47	0.47
II	3.75	1.25	0.49	0.53	0.53
II	3.75	1.88	0.47	0.51	0.51
II	6.25	1.25	0.48	0.56	0.56
II	3.75	3.13	0.43	0.48	0.48
II	6.25	2.50	0.40	0.48	0.48
II	6.25	3.75	0.44	0.50	0.51
III	2.50	1.25	0.57	0.61	-
III	2.50	1.25	0.42	0.54	-
III	2.50	1.25	0.49	0.55	-
IV	0	1.88	0.53	0.52	-
IV	0	2.50	0.49	0.49	-
IV	0	3.00	0.53	0.52	-
IV	0	3.75	0.49	0.49	-
IV	0	5.00	0.54	0.55	-

From Tab. (4.9), we notice basically that the drag forces on the upstream intruders are larger than those on the downstream ones, being roughly equal for intruders aligned in the transverse direction. Figures (4.27) and (4.28) present graphics of the mean drag forces as functions of initial separations Δx and Δy, for the configurations of type I and II [Fig. (4.27)] and III and IV [Fig. (4.28)].

This corroborates the description given in the previous section. We note that the initial separation in the longitudinal direction (Δx) only affects the time for reaching the final configuration. As an example, the time to reach the final configuration (of type I) as a function of the initial separation between intruders is presented in Fig. (4.29).

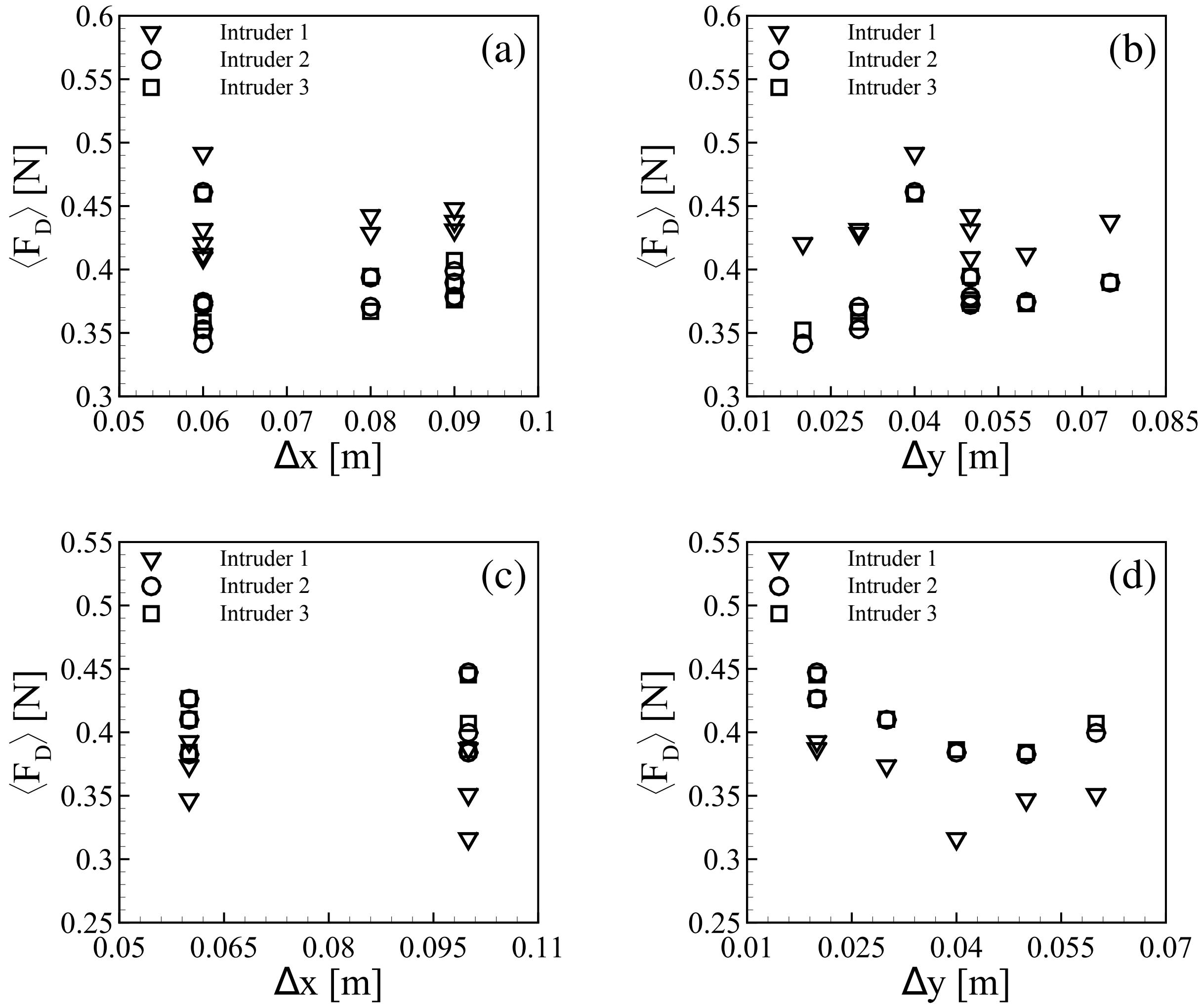

Figure 4.27 – Mean drag on each intruder as functions of initial separations Δx and Δy for (a) and (b) type I and (c) and (d) type II. Images taken from (Carvalho; Franklin, 2022b).

4.1.2.3.4 Network of contact forces

We examine now how the network of contact forces is related with drag reduction, increase, and even jamming in certain cases. For that, we proceeded as in Sec. 4.1.2.2.2 and computed the load-bearing and dissipative chains. Figure (4.30) shows the load-bearing and dissipative chains superposed with the particle positions at four different instants for the same case of Fig. (4.24)a (the three intruders form a clump which jams). Although load-bearing chains exist in the region between the intruders, we notice that they percolate over longer distances as the intruders come closer to each other. By the end of the intruders' motion [Fig. (4.30)d], load-bearing chains are dense and reach three of the vertical walls, blocking the motion of the intruders (and indicating a possible jamming state.).

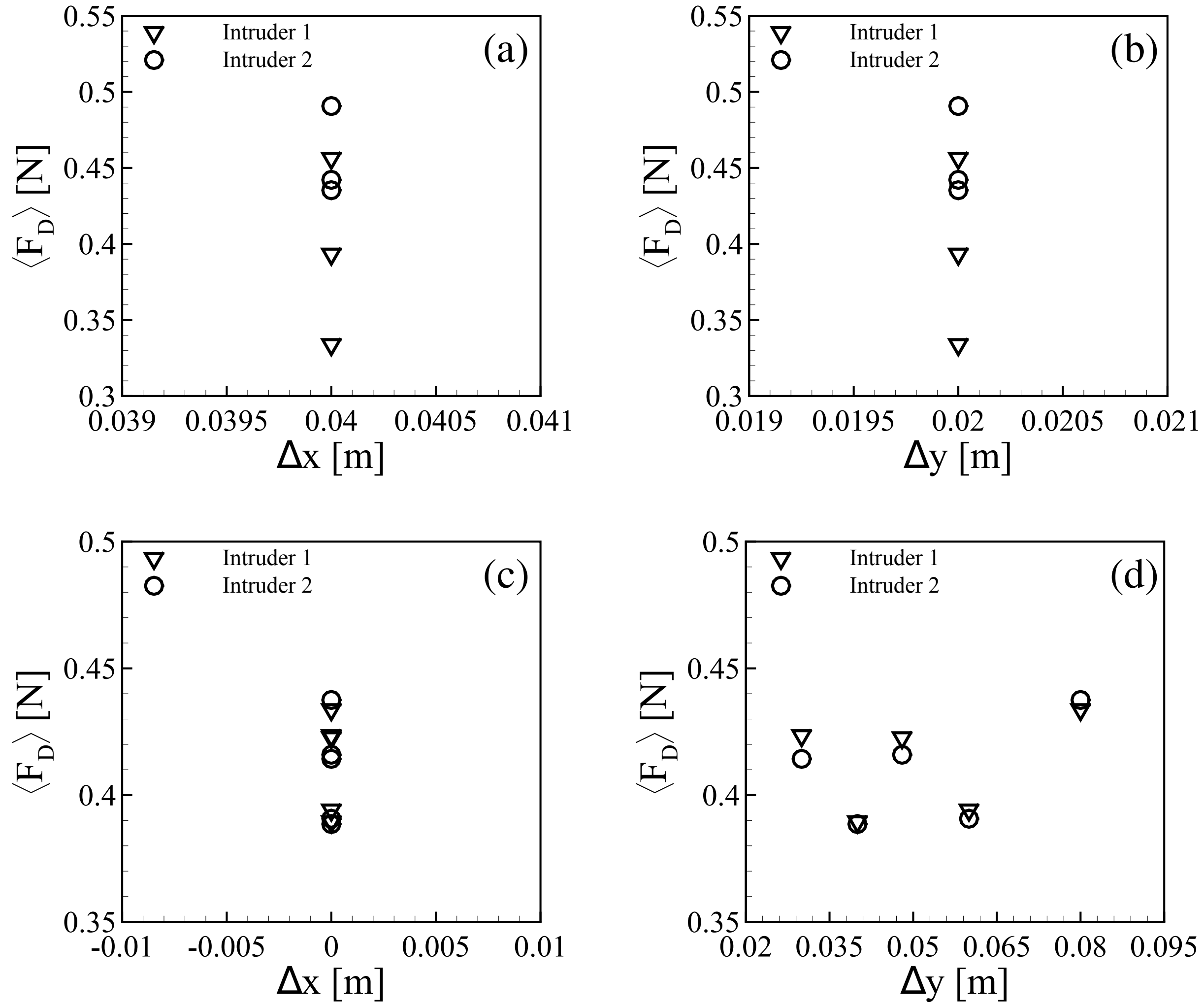

Figure 4.28 – Mean drag on each intruder as functions of initial separations Δx and Δy for (a) and (b) type III and (c) and (d) type IV. Images taken from (Carvalho; Franklin, 2022b).

Additional graphics of the evolution of Z, N, and ρ for some of the cases presented in Fig. (4.14) are shown in Annex A, and a movie showing the motion of grains and force networks within the granular system is available in (Carvalho; Franklin, 2022a).

4.1.2.3.5 Variations with the packing fraction

We investigate in this subsection if some of the patterns shown previously for ϕ = 0.76 change with the packing fraction. For example, Figs. (4.31)a to (4.31)d show snapshots of final positions for simulations of type I with ϕ = 0.72, 0.73, 0.76 and 0.78, respectively, for the same initial separations (same initial configuration of intruders as in Fig. (4.24)a, $(\Delta y - d_{int})/d_{int}$ = 0.875). We observe that the increase in packing fraction boosts the cooperative

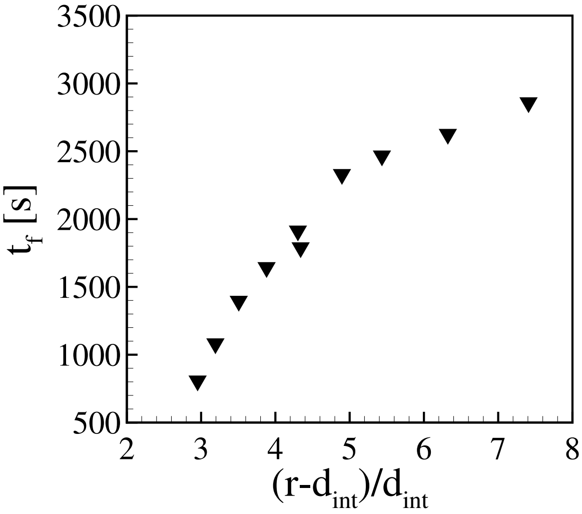

Figure 4.29 – Time to reach the final configuration, t_f, as a function of the initial separation between intruders, $r = \sqrt{\Delta x^2 + \Delta y^2}$, normalized by d_{int}. Configuration of type I. Image taken from (Carvalho; Franklin, 2022b).

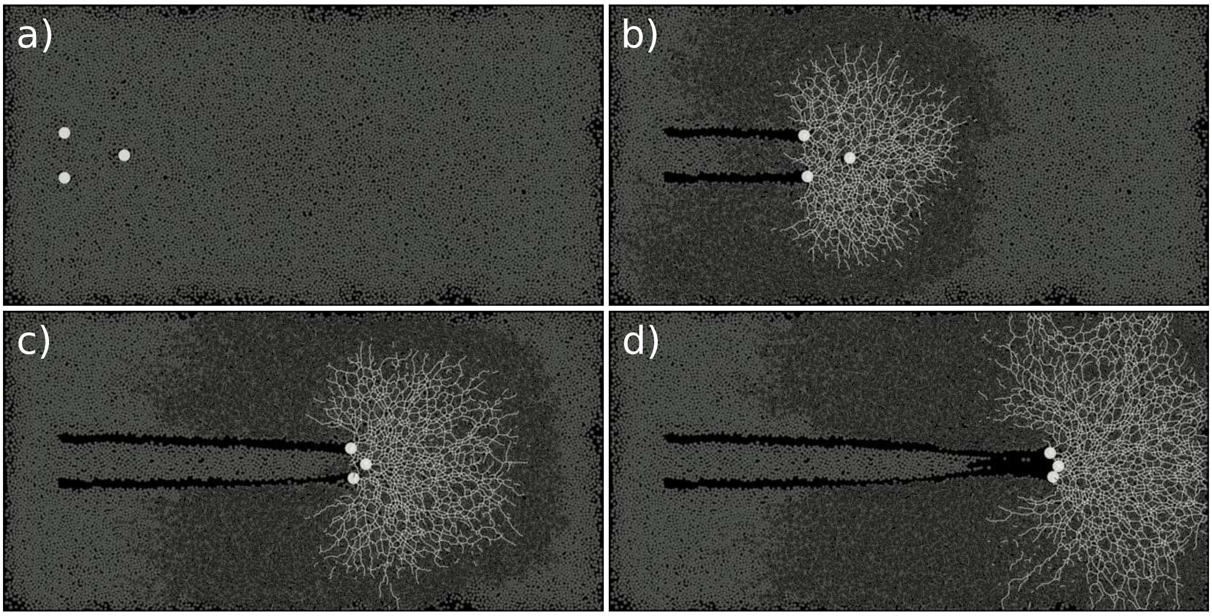

Figure 4.30 – From left to right, snapshots at (a) t = 0 s, (b) t = 710.64 s, (c) t = 1492.80 s and (d) t = 2074.56 s for trios organized in type I being pushed at 0.8 N [each intruder, same of Fig. (4.24)a]. The figures show the load-bearing (clear lines) and dissipative (dark lines) chains, and ϕ = 0.76. Images taken from (Carvalho; Franklin, 2022b).

dynamics between intruders: for the lowest value (ϕ = 0.72), the intruders move as single objects, with virtually no cooperation, while from ϕ = 0.72 to ϕ = 0.78 they tend to form the clumped structure in a time scale that decreases as ϕ increases. Although we show here that ϕ is an important parameter in determining the different patterns observed, we do not inquire into

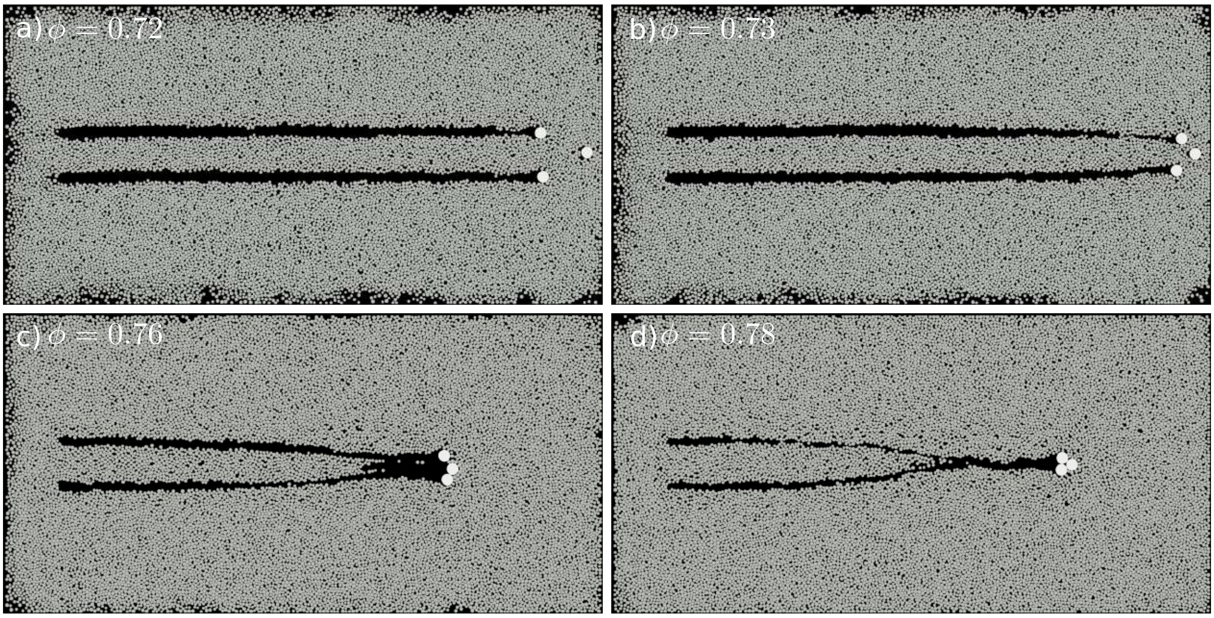

Figure 4.31 – Snapshots of final positions for simulations of type I with (a) ϕ = 0.72, (b) ϕ = 0.73, (c) ϕ =0.76, and (d) ϕ =0.78 [same initial configuration of intruders as in Fig. (4.24)a]. Images taken from (Carvalho; Franklin, 2022b).

its effects, which needs to be investigated further.

In summary, in Sec. 4.1.2 we investigated how a group of intruders interact with each other while moving horizontally in a two-dimensional granular system. Our results show that: (i) there exists a cooperative dynamics between the intruders; (ii) this cooperative dynamics is the result of compaction and expansion of the granular medium in front and behind, respectively, each intruder, with load-bearing chains connecting the intruders and cavities being formed in front of the downstream intruders; (iii) for the cases presenting more drag, load-bearing chains percolate over longer distances, reaching in some cases the vertical walls; (iv) in cases of constant velocity, there is an optimal separation between intruders for not only reaching minimum drag, but also drag reduction (with respect to single intruders). This can be proven useful for designing devices stirring the ground or other granular surfaces; (v) for constant thrust, different patterns appear depending on the initial configurations and distances between intruders; (vi) in addition to initial separations, the packing fraction also influences the observed patterns; (vii) for some initial arrangements, the same spatial configuration is eventually reached, showing an attractor-like behavior. While a cooperative dynamics was shown in the case of intruders falling within light grains by Refs. (Pacheco-Vázquez; Ruiz-Suárez, 2010; Solano-Altamirano *et al.*, 2013; Dhiman *et al.*, 2020; Kawabata *et al.*, 2020; Pravin *et al.*, 2021; Espinosa *et al.*, 2022), and the compaction and expansion of the granular medium in front and behind a single intruder by Refs. (Kolb *et al.*, 2013; Seguin *et al.*, 2016), all the remaining findings are new. On the whole, our results bring new insights into the cooperative dynamics of intruders moving amid grains.

In the next section (Sec. 4.2), we investigate experimentally some aspects of the dynamics behind the cooperative motion of sets of intruders within a granular material.

4.2 Experimental Investigation

This section (Sec. 4.2) reproduces material from Douglas D. Carvalho, Yann Bertho, Antoine Seguin, Erick M. Franklin, and Baptiste Darbois Texier, “Drag reduction during the side-by-side motion of a pair of intruders in a granular medium”, Phys. Rev. Fluids **9**, 114303 (2024), with permission from the American Physical Society (Carvalho *et al.*, 2024b).

Despite the progress made in recent years, many questions remain unanswered concerning the forces resulting from the cooperative behaviors observed when more than one intruder move together within a granular material. Thus, we have conducted experiments, in accordance to the methodology presented in Sec. 3.2.1, in which we forced either one or two spheres to move horizontally at constant velocity at different depths within a granular medium, while measuring the forces (mainly drag) involved in their motion. In this section, we show that we probed the spatial extent of the interaction between the spheres by exploring the influence of the separation distance on the mean drag experienced by each sphere and determining an associated characteristic length of the interaction. We show that for two intruders moving side by side at a constant speed, from a certain separation, the average drag felt by each intruder decreases significantly and that there is an increase in this relative drag reduction with the depth of the intruders. Moreover, at the end of this section, we also explore the possibility of developing a model to predict the measured drag in order to account for the observed cooperative behavior.

4.2.1 Experimental setup

The experiments consist in pulling intruders (polyamide spheres with a diameter $d = 20$ mm) at a constant velocity V_0 inside a granular medium made of slightly polydisperse glass spheres (diameter $d_g = 1 \pm 0.3$ mm and density $\rho \simeq 2.5 \times 10^3$ kg m^{-3}). The grains are contained in a rectangular box 365 mm long, 270 mm wide, filled to a height of 97 mm [Fig. (4.32)a]. The intruders are attached to cylindrical rods of 5 mm in diameter, preventing any tilting or rotation, and immersed in the bed at depth h (h being the distance separating the free surface of grains from the center of the intruder). The rods are connected to force gauges that measure the longitudinal time-varying drag force $f_0(t)$. The whole system is fixed to an x-direction moving plate, controlled by a linear stepper motor ensuring the displacement of the intruders at a velocity V_0 from 10^{-1} to 10 mm s^{-1} [Fig. (4.32)a]. The materials used in these experiments and their properties are shown in Tab. (4.10), and more details regarding the experimental setup can be seen in Sec. 3.2.1.

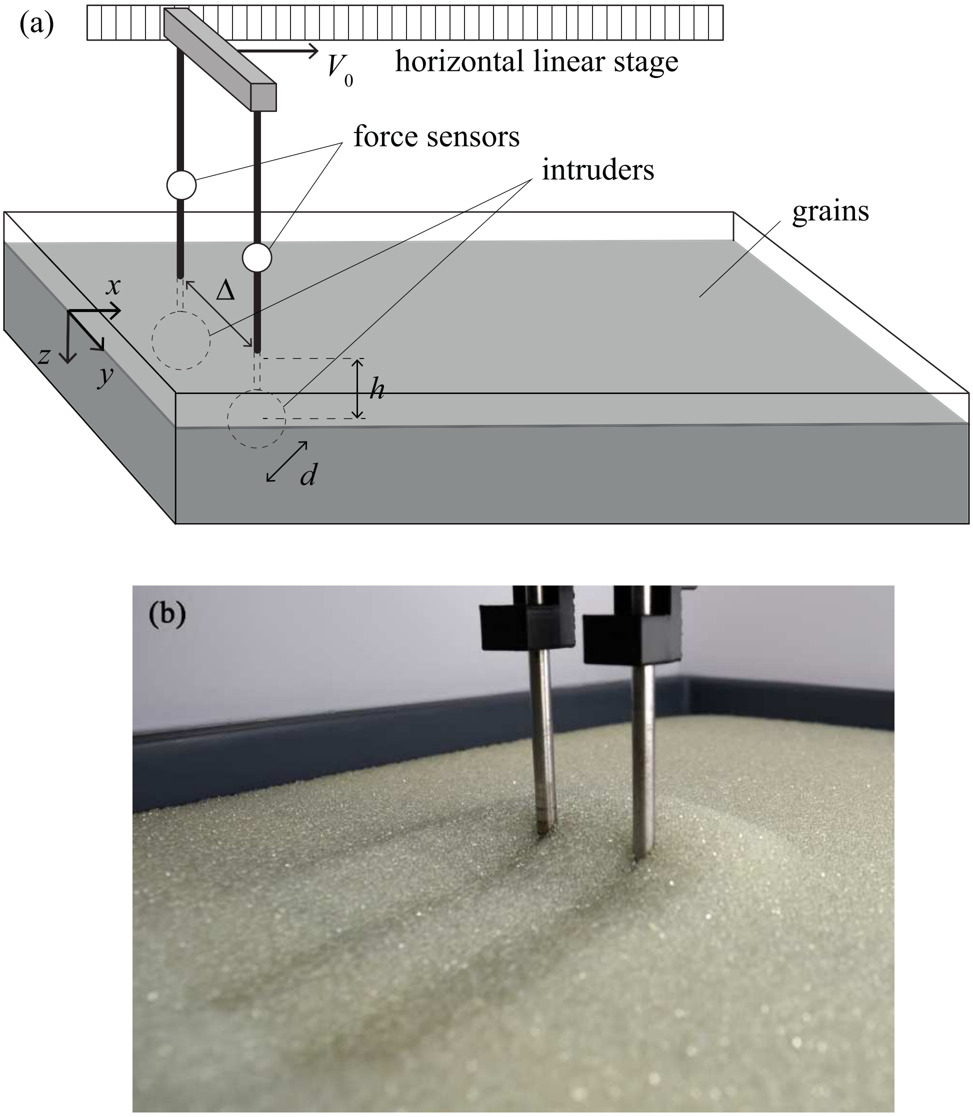

Figure 4.32 – (a) Sketch of the experimental setup for the displacement along the x-axis of two spherical intruders of diameter d, immersed in grains at the depth h. (b) Picture of an experiment for two immersed intruders $\Delta = 30$ mm apart, at depth $h = 14$ mm and moving at the velocity $V_0 = 2.7$ mm s^{-1} during the forward journey. The image is used for visualization purposes to show the surface deformation that occurs at the shallowest depth. Images taken from (Carvalho *et al.*, 2024b). Same images as in Fig. (3.2) and shown here for the sake of completeness.

Table 4.10 – Properties of materials used in the experiments: ρ is the material density and the last column shows the object's dimensions [diameters (d, d_g, and d_{rod})].

	Material	ρ **(kg/m^3)**	**Dimensions (mm)**
Intruder	Polyamide	1122	$d = 20$
Cylindrical rod	Metal alloy	-	$d_{rod} = 5$
Grains	Glass beads	2500	$d_g = 1 \pm 0.3$
Walls	Plastic	-	$365 \times 270 \times 118$

Two distinct configurations will be considered below: (i) the displacement of a single intruder in the x-direction from one edge of the box to the other, and initially placed at $y = 0$ and depth $z = h$; (ii) the displacement of two side-by-side intruders at the same abscissa x and same depth $z = h$, located initially at $y = \pm\Delta/2$ and separated by a distance Δ measured from their centers as seen in Fig. (4.32)a. In addition, in the x-direction, data are acquired in a region of interest (ROI) located at the center of the box, in the range 135 mm $\leq x \leq$ 225 mm. Finally, note that one experiment consists of moving the intruder forward (along positive x) in the undisturbed granular medium, and then, in a second step, making the return path (towards negative x) in the wake generated by the forward path and seen in Fig. (4.32)b. Note that free surface deformation can appear at shallow depth. The surface deformations become less significant as the object is deeper in the granular medium, as observed in previous studies (Gravish *et al.*, 2010). This view is also consistent with our results where only the data at the shallowest depth ($h = 14$ mm) deviates from the others, as shown in Sec. 4.2.2.2. An interesting idea would be to use a lid on top of the granular bed to avoid free surface effects and study their importance. However, these experiments are challenging from a technical point of view because they require the creation of many plates with different groove separation and would be something to be investigated in the future.

4.2.2 Experimental results

4.2.2.1 Journey of a single intruder

We first study the displacement of a single intruder at constant velocity V_0 in the granular medium at depth h. The inset in Fig. (4.33)a shows the typical evolution of the intruder drag force f_0 as it moves at $V_0 = 2.7$ mm s^{-1} at the depth $h = 14$ mm, from one side of the box to the other. Note that here and in the remaining of Sec. 4.2, the drag force measured during the movement of the rod alone (i.e., without the intruder attached to its end) has been subtracted from the force signal for each probed depth h, so as to retain only the force experienced by the intruder [please check Fig. (3.6)]. This method has already been adopted in others experimental studies (Albert *et al.*, 2001). Despite some fluctuations, associated with the creation/breaking of force chains (Kolb *et al.*, 2013; Seguin *et al.*, 2016; Carvalho *et al.*, 2022), we observe distinct zones in the force signal presented in the inset of Fig. (4.33)a. When the movement of the intruder begins, the force increases abruptly when the motion starts, and then, after a transient regime, reaches an extended zone of slow variation which becomes more negligible as the intruder is deeper in the granular medium (Seguin, 2019). This decreasing trend is present in all our measurements with the same magnitude of about 0.1 N within the

ROI. For the moment, we do not have any explanation for this particular trend. However, the variation is smaller than the fluctuations of the force signal for high values of h and comparable for $h = 14$ mm. For these reasons, this trend does not affect significantly the average of the signal force taken inside the ROI. For both signals shown in the inset of Fig. (4.33)a, there is a slight variation of approximately 0.1 N within the ROI, meaning slighter effects for higher forces (i.e., decreasing with the depth). Finally, on approaching the box walls, the force starts to increase again, as already reported in previous studies (Kolb *et al.*, 2013; Carvalho *et al.*, 2022). In the following, we will define the mean drag force F_0 felt by a single intruder, as the average of the instantaneous force f_0 over the 90 mm long region of interest (ROI) located at the center of the box, so that $F_0 = |\langle f_0(x)\rangle_{\mathrm{ROI}}|$, where the absolute value accounts for the mean drag force in both journeys of the intruders (forward and backward).

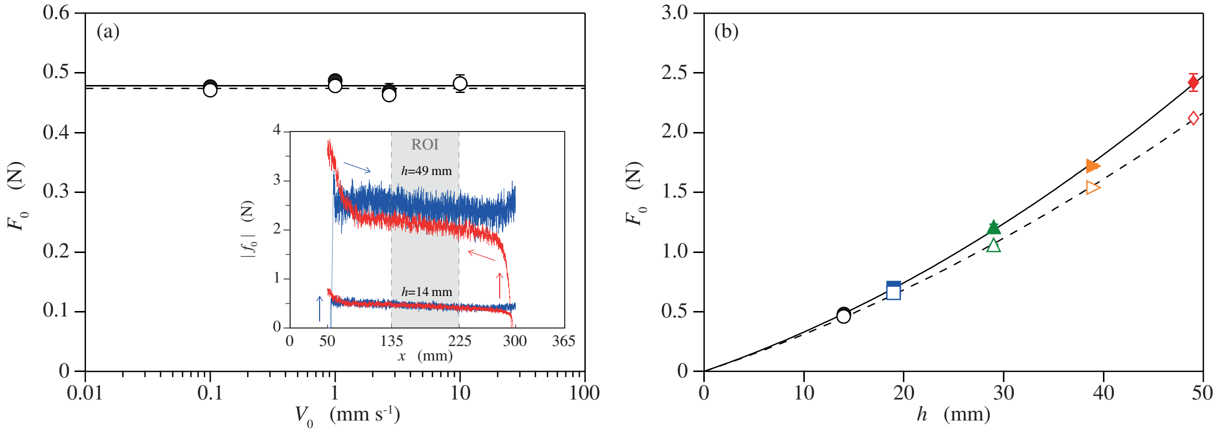

Figure 4.33 – (a) Mean drag force on a single intruder F_0 as a function of its horizontal velocity V_0 at a depth $h = 14$ mm. Solid symbols correspond to forward motion and open symbols to backward motion. Inset: Instantaneous drag force on a single intruder f_0 as a function of the position x at two different depths ($h = 14$ mm and $h = 49$ mm), and a travel velocity of $V_0 = 2.7$ mm s^{-1} for (—) forward and (—) backward motions, respectively. The shaded area corresponds to the region of interest where the measurements are carried out. (b) Mean drag force on a single intruder F_0 as it moves horizontally at $V_0 = 2.7$ mm s^{-1}, as a function of immersion depth h. Solid symbols correspond to forward motion and open symbols to backward motion. The curves are the best fits of the data, of the form $F_0 = A_0\, h + B_0\, h^2$, where the solid line corresponds to $A_0 \simeq 2.9\ 10^{-2} \pm 0.1\ 10^{-2}$ N mm^{-1} and $B_0 \simeq 4.1\ 10^{-4} \pm 0.3\ 10^{-4}$ N mm^{-4}, and the dashed line to $A_0 \simeq 2.8\ 10^{-2} \pm 0.1\ 10^{-2}$ N mm^{-1} and $B_0 \simeq 3.1\ 10^{-4} \pm 0.2\ 10^{-4}$ N mm^{-2}. Images taken from (Carvalho *et al.*, 2024b).

Figure (4.33)a displays the evolution of the mean drag force F_0 as a function of the imposed displacement velocity V_0. Drag force measurements are made during the intruder's first pass (solid symbols), and also during its backward return as it passes through the wake it previously created (open symbols). No significant variation in F_0 is observed with the displacement velocity V_0, over the two-decade range experimentally explored. In granular medium, the fact that the drag force does not depend on velocity is the signature of a quasi-static regime characterized by a Froude number smaller than 1. This Froude number, expressed as the ratio of the kinetic pressure due to collisions between grains to the pressure generated by the gravity field, is written as $\mathrm{Fr} = V_0/\sqrt{gh}$ and has a value smaller than 0.03 for all cases studied here, consistent with the quasi-static regime hypothesis (Hilton; Tordesillas, 2013; Takehara *et al.*, 2010; Takehara; Okumura, 2014; Faug, 2015; Seguin, 2019; Seguin *et al.*, 2022).

Figure (4.33)b shows the evolution of the mean drag force F_0 on a single intruder as a function of burial depth h. The drag force F_0 is observed to increase with the depth h, both in the forward and backward directions. This increase is slightly supralinear and can be modeled by a quadratic function of h, in agreement with observations from a previous experimental study (Albert *et al.*, 2001). We note that the fitting function is only valid in the range $h > 0$ and the zero force solution in the negative range, i.e., $h = -A_0/B_0$, has no physical meaning. It is important to note that the trend of the force as a function of the depth is mainly linear, as expected by the increase of the hydrostatic-like pressure, and the quadratic term is only a correction from this linear trend that has been measured by Albert *et al.* (2001) (Albert *et al.*, 2001). At the present moment, there is not a physical explanation for this non-linearity as underlined by Albert *et al.* (2001) (Albert *et al.*, 2001), that suggests that the nonlinearity is associated with geometrical factors in the drag for which the simple theoretical expectations do not take into account. In addition, we point out that the backward drag force seems to be slightly lower than the forward drag force. This difference can be explained by the fact that the intruder passes in its wake, i.e., in an area that has been slightly “structured" in some way by its first passage (Guillard *et al.*, 2013). Note that the horizontal free surface has also been disturbed by the passage of the rod, slightly modifying the effective burial height.

4.2.2.2 Journey of two side-by-side intruders

4.2.2.2.1 Drag forces

Let us now consider the displacement of two side-by-side intruders separated by a distance Δ, at velocity V_0 and depth h, as sketched in Fig. (4.32)a. Each force sensor provides a signal similar to that shown in the inset in Fig. (4.33)a. The overall drag force F of the system composed of the two intruders is determined as the average of the mean drag forces experienced by each of the intruders, F_0. Figure (4.34) shows the evolution of the mean drag force F as a function of the distance between the intruders $(\Delta - d)$ while the spheres velocity and depth were kept constant to $V_0 = 2.7$ mm $^{-1}$ and $h = 49$ mm respectively. Each point in this figure corresponds to an average of five experiments. The error bars correspond to the standard deviation calculated on these five realizations. The variation of force F with distance between intruders $(\Delta - d)$ follows the same trend, for both the forward and backward journeys. For large separations $(\Delta - d \gtrsim 50$ mm), the mean drag force F remains constant. This constant value corresponds to that measured for a single intruder, on both the forward and backward journeys, as attested by the horizontal lines in Fig. (4.34) depicting the drag force F_0 for a single intruder under similar conditions. Thus, the two intruders do not interact with each other. When the intruders are closer to each other $(\Delta - d \lesssim 50$ mm), the average drag force is significantly lower than at large separation. This decrease can reach up to 30% in relative value when the distance between intruders vanishes, which is well below the usual force fluctuations observed for a single intruder [depicted as grey regions in Fig. (4.34)]. Therefore, they cooperate with each other, resulting in a reduction in drag force. Finally, as already mentioned for a single intruder, we note that the drag force is about 10% lower during the backward journey than during the forward one due to the passage of intruders in their own wake. We also observe that the error bars are smaller in the case of backward motion than in the case of forward motion.

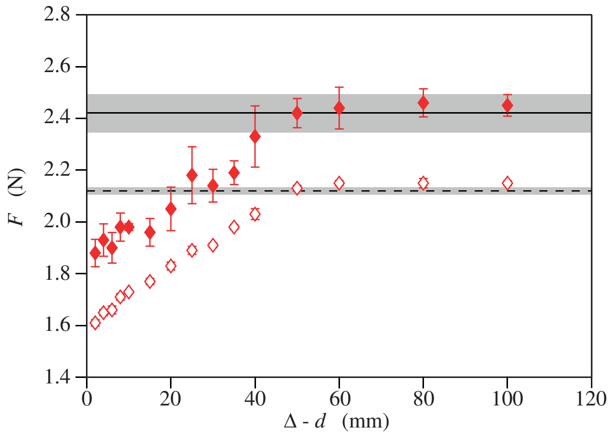

Figure 4.34 – Mean drag force F for both intruders as a function of the space between them $\Delta - d$, for a displacement at $V_0 = 2.7$ mm $^{-1}$ at the depth $h = 49$ mm. Solid symbols correspond to forward motion and open symbols to backward motion, and error bars represent the standard deviation in five realizations. The horizontal lines and shaded areas correspond, respectively, to force values F_0 and their typical fluctuations, obtained with a single intruder under similar conditions. Image taken from (Carvalho *et al.*, 2024b).

Figure (4.35) shows the normalized drag force $\tilde{F} = F/F_0$ as a function of the normalized distance between intruders $\tilde{\delta} = (\Delta - d)/d$ for different burial depths h, on both the forward [Fig. (4.35)a] and backward [Fig. (4.35)b] journeys. The evolution of $\tilde{F}$ with $\tilde{\delta}$ is similar in both cases, and also whatever the burial depth h. It can also be seen that when the two intruders are close enough to each other, the greater the burial depth, the greater the relative drag reduction. Since the force increases roughly linearly with $\tilde{\delta}$ at short distances between intruders, and saturates at a constant value when they are far enough apart, we propose to model the observed behavior with an exponential law of the form

$$\tilde{F} = 1 - \Lambda \exp\left(-\frac{\tilde{\delta}}{\tilde{\delta}_s}\right), \tag{4.5}$$

where Λ is a coefficient corresponding to the relative reduction in drag and $\tilde{\delta}_s$ a normalized characteristic screening length reflecting the typical distance from which intruders can affect each other. When $\tilde{\delta} < \tilde{\delta}_s$, the intruders cooperate and the drag force per intruder is lower than the value for a single intruder moving through the grains. Conversely, when $\tilde{\delta} > \tilde{\delta}_s$, the intruders do not interact with each other, i.e., we recover the case of a single intruder. Note that even in the limit of touching spheres, the separation distance between the two rods is large enough to ensure that there is no interaction between them.

Equation (4.5) allows us to fit our experimental data for each burial depth h shown in Figs. (4.35)a and (4.35)b, and extract the corresponding Λ and $\tilde{\delta}_s$ values. We note that the solid lines plotted in Figs. (4.35)a and (4.35)b were obtained for both the forward and backward journeys together. The evolution of the drag reduction coefficient Λ and the normalized screening length $\tilde{\delta}_s$ as a function of the normalized burial depth $\tilde{h} = h/d$ are plotted in Figs. (4.35)c and (4.35)d, respectively. It can be seen that as the penetration depth increases, the Λ reduction is greater. For the sake of simplicity, the whole data set can be described by a linear behavior of the form $\Lambda \sim \tilde{h}$. The linear fit proposed here should not be valid for larger values of $\tilde{h}$, as it is unreasonable to expect Λ to exceed the value 1. Saturation of Λ is therefore expected for large values of $\tilde{h}$ which are above the depth range possible to be explored with the current experimental setup. The normalized screening length $\tilde{\delta}_s$ is observed to be rather constant with the normalized burial depth $\tilde{h}$, with $\tilde{\delta}_s = 1.2$. We also note that for the shallowest depth ($\tilde{h} \simeq 0.7$), the normalized screening length $\tilde{\delta}_s$ and reduction Λ deviate from these trends. These deviations may be due to a free-surface effect, since they are observed when the burial depth is less than one sphere diameter. It is important to note in Figs. (4.35)c and (4.35)d that additional measurements were carried out at a velocity approximately four times higher (cross symbols in these figures), and we observe that both the coefficients Λ and $\tilde{\delta}_s$ are unaffected, at least in the quasi-static regime.

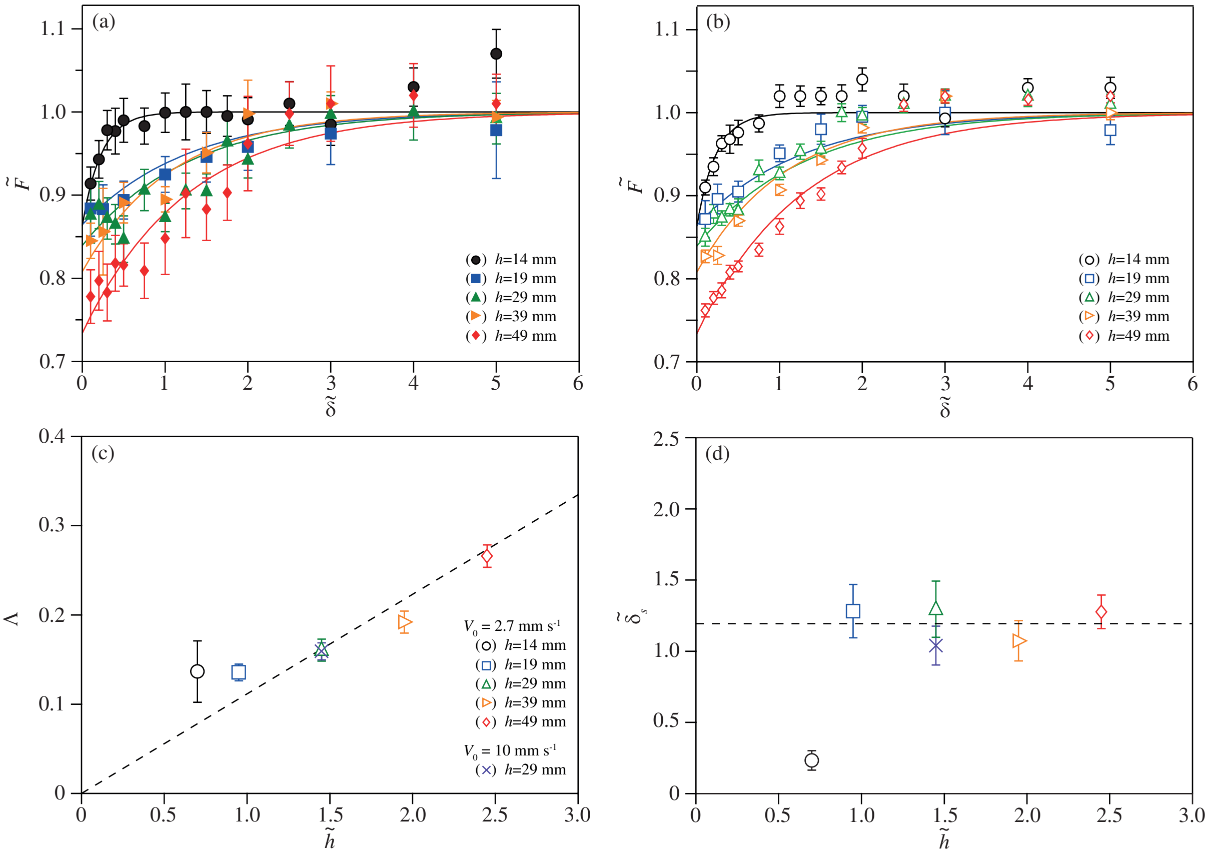

Figure 4.35 – Normalized drag force $\tilde{F} = F/F_0$ as a function of the normalized distance between the intruders $\tilde{\delta} = (\Delta - d)/d$ for (a) a forward motion and (b) a backward motion at $V_0 = 2.7$ mm s^{-1}, and different depths (●,○) $h = 14$ mm, (■, □) $h = 19$ mm, (▲, △) $h = 29$ mm, (▶, ▷) $h = 39$ mm, (♦, ◇) $h = 49$ mm. Solid lines correspond to the best fits of the data with Eq. (4.5). Parameters (c) Λ and (d) $\tilde{\delta}_s$ resulting from the fitting of the data with Eq. (4.5) as a function of the normalized depth $\tilde{h}$. Dashed lines correspond to (c) $\Lambda = 0.1\tilde{h}$ and (d) $\tilde{\delta}_s = 1.2$. In the panels, error bars represent the standard deviation in five realizations. Images taken from (Carvalho *et al.*, 2024b).

Finally, it is possible to propose a master curve on which the data are superposed. Figure (4.36) shows the evolution of $(\tilde{F} - 1)/\Lambda$ as a function of $\tilde{\delta}/\tilde{\delta}_s$. We can see that the data gather around the experimental fit of Eq. (4.5) for both the forward and backward runs. We also observe that measurements at shallow depths deviate from the model due to free-surface effects.

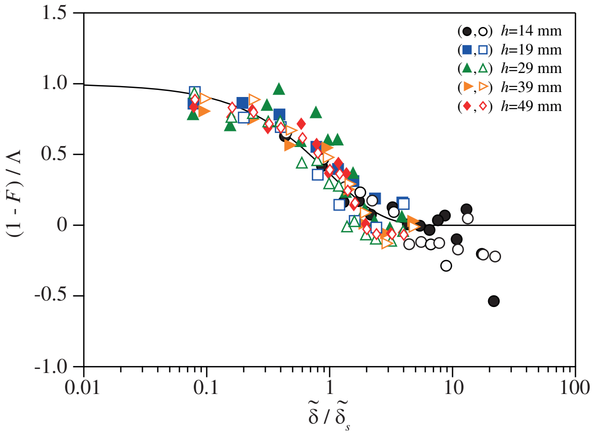

Figure 4.36 – Rescaled drag force $(1-\tilde{F})/\Lambda$ as a function of the rescaled separation distance $\tilde{\delta}/\tilde{\delta}_s$. For each set of data, we use the values of Λ and $\tilde{\delta}_s$ resulting from the best fits obtained in Fig. (4.35). All the data collapse on the solid line which corresponds to Eq. (4.5). Image taken from (Carvalho *et al.*, 2024b).

4.2.2.2.2 Side forces

The side forces have also been measured experimentally for two different depths h for both the forward and backward journeys. These results are shown in Fig. (4.37). We note that the variation of force F (here given by the average of the mean side forces) with distance between intruders ($\Delta - d$) follows the same trend, for both the forward [Fig. (4.37)a] and backward journeys [Fig. (4.37b)]. For large separations ($\Delta - d \gtrsim 50$ mm), the average side force F remains constant. This constant value corresponds to that measured for a single intruder, both in forward and backward journeys, as attested by the horizontal lines in Fig. (4.37) representing the side force for a single intruder under similar conditions (whose value is approximately zero for all cases, as expected). When the intruders are closer to each other ($\Delta - d \lesssim 50$ mm), the average side force begins to decrease in a region where its value is negative, indicating a force of attraction between the intruders. This decrease reaches a minimum value and, if the separation between intruders continues to decrease, the side force begins to increase progressively until it becomes positive, in a condition where the intruders are very close to each other and begin to repel each other. These observations are in agreement with experimental and numerical observations made by other works (Cruz; Caballero-Robledo, 2016; Dhiman *et al.*, 2020; Caballero-Robledo *et al.*, 2021).

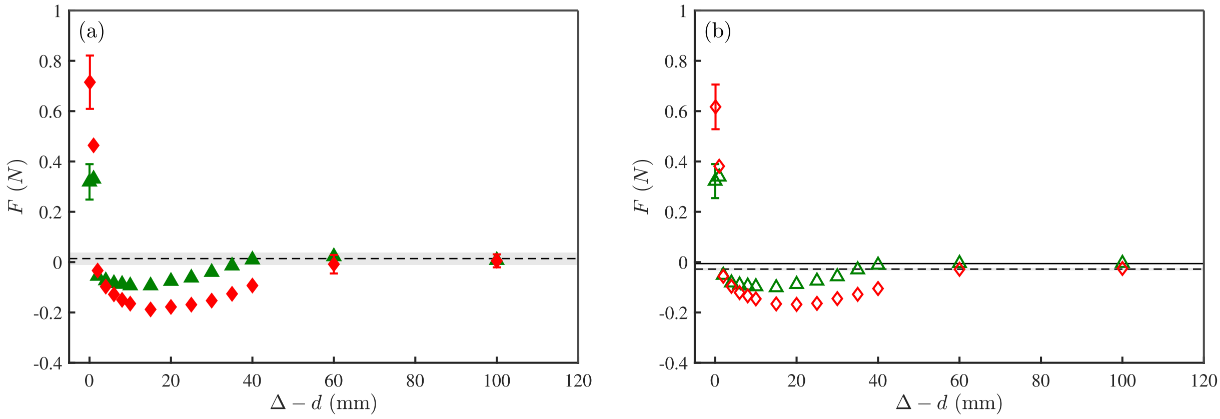

Figure 4.37 – Mean side force F for both intruders as a function of the space between them $\Delta - d$, for a displacement at $V_0 = 2.7$ mm s^{-1} at depths (▲, △) $h = 29$ mm and (♦, ◇) $h = 49$ mm. Solid symbols correspond to (a) forward motion and open symbols to (b) backward motion, and error bars represent the standard deviation in five realizations. The horizontal lines and shaded areas correspond, respectively, to force values and their typical fluctuations, obtained with a single intruder under similar conditions.

4.2.3 Discussion

In this section, we discuss how the interactions between two intruders moving side by side in a granular material can be rationalized. For the side force appearing on two side-by-side cylinders in a granular flow, it has been shown experimentally and numerically that the direction of this force (attraction or repulsion) correlates with the sign of the difference in granular temperature between the inside and outside of the cylinders (Cruz; Caballero-Robledo, 2016; Caballero-Robledo *et al.*, 2021). The same argument of granular temperature difference has been invoked to rationalize the axial-segregation of large spheres in a rotating drum filled with small grains (Zuriguel *et al.*, 2005). However, Dhiman *et al.* (2020) (Dhiman *et al.*, 2020) carried out discrete element method (DEM) simulations of two side-by-side intruders and showed that the temperature and pressure fields do not follow the evolution expected by kinetic theory. They concluded that the difference of granular temperature should rather be a consequence of the interactions rather than its cause. In order to understand the origin of the side forces that appear on the intruders when they are close to each other, Dhiman *et al.* (2020) (Dhiman *et al.*, 2020) studied numerically the dynamics of force chains in their vicinity. They found that the presence of a neighbor shears the force chains of the first intruder and breaks them more often. As a result, the first intruder pushes less on the granular material on its neighbor's side than it does on the other side. In addition, this would also predict a reduction of the drag force on the intruder when its neighbor is close. This scenario is also in agreement with the observations of Reddy *et al.* (2011), who observed that the presence of a shear zone in the vicinity of a cylindrical intruder immersed in grains reduces its yielding force (Reddy *et al.*, 2011).

We therefore formulate the observations of Dhiman *et al.* (2020) (Dhiman *et al.*, 2020) in an empirical model where the force field of the first intruder is perturbed by the velocity field of its neighbor. Our approach is two-dimensional and is based on time-averaged local force and velocity fields within the granular material, which is described as a continuous medium. The velocity field around a cylinder moving amid grains has been studied experimentally (Seguin *et al.*, 2013) with the following relation:

$$\frac{\mathbf{v}(r,\theta)}{V_0} = -A_r(r)\cos\theta\,\mathbf{e}_r + A_\theta(r)\sin\,\theta\,\mathbf{e}_\theta, \tag{4.6}$$

where r and θ are the cylindrical coordinates with origin at the center of the object, as shown in Fig. (4.38)a and the two functions A_r and A_θ write:

$$\begin{aligned} A_r(r) &= \frac{r-d/2+\lambda_s}{r}\left[1-\exp\left(-\frac{r-d/2}{\lambda_0}\right)\right] \quad \text{and} \\ A_\theta(r) &= 1+\frac{r-d/2+\lambda_s-\lambda_0}{\lambda_0}\exp\left(-\frac{r-d/2}{\lambda_0}\right), \end{aligned} \tag{4.7}$$

where λ_0 is the characteristic length over which the velocity varies along the radial direction, and λ_s reflects the velocity slip tangential to the object surface. These two parameters have been shown to depend on the cylinder diameter d and the grain size d_g according to the empirical relations: $\lambda_0 = d/4 + 2d_g$ and $\lambda_s = 0.45\,d$ (Seguin *et al.*, 2013). In our case, i.e., an intruder of 20 mm in diameter moving amid grains of 1 mm, it corresponds to $\lambda_0/d = 0.35$ and $\lambda_s/d = 0.45$. Note that the velocity field given by Eq. (4.6) is expressed in the reference frame of the intruder, and here it should be expressed in the reference frame of the laboratory by adding $+V_0\,\mathbf{e}_x$ to Eq. (4.6). This velocity field is represented with blue arrows in Fig. (4.38)a.

The network of forces around an object moving in a granular medium has been studied in experiments with photoelastic grains (Clark *et al.*, 2012) or by numerical simulations (Carvalho *et al.*, 2022). Both approaches reveal that the force distribution extends over a characteristic length: high stresses are applied close to the object and there are no stress variations far from the intruder (Muthuswamy; Tordesillas, 2006). Furthermore, experiments with 2D photoelastic grains revealed that the force distribution decreases exponentially with the distance from the intruder (Clark *et al.*, 2012; Seguin *et al.*, 2016). From these studies, it is possible to propose an expression for the average local force per unit area in the granular material, which follows an exponential decay and whose pattern resembles that of the force chains usually observed around intruders (Seguin *et al.*, 2016; Carvalho *et al.*, 2022). The force per unit area around the intruder can be described empirically by the following expression:

$$\mathbf{f} = f_r \exp\left(-\frac{r-d/2}{\lambda_0}\right)\cos\theta\,\mathbf{e}_r + f_\theta \exp\left(-\frac{r-d/2}{\lambda_0}\right)\sin\theta\,\mathbf{e}_\theta. \tag{4.8}$$

This expression assumes that the characteristic length over which the force field varies in the radial direction is the same as that of the velocity field, i.e., λ_0. It also introduces two force coefficients, f_r and f_θ, whose ratio reflects the way the force chains deviate from the radial direction. The average force field of Eq. (4.8) corresponds to the space average of the normal forces transmitted by contacts between particles per unit area and is a continuous representation of the discrete contact network. Figure (4.38)a shows with red arrows a typical example of force field resulting from Eq. (4.8). In this approach, the total drag force experienced by an intruder is considered to correspond to the integral of the force field per unit area over a surface bounded by the perimeter of the intruder and a thickness of one grain. We have only considered the frontal part of the object because it is the main contributor to the total drag force (Seguin *et al.*, 2016). Thus the drag force F_0 expresses as

$$F_0 = \int_{-\pi/2}^{\pi/2}\int_{d/2}^{d/2+d_g} \mathbf{f}\cdot\mathbf{e}_x\, dr\, r d\theta, \tag{4.9}$$

and can be calculated analytically as:

$$F_0 = \frac{\pi}{2}(f_r - f_\theta)\lambda_0\left[\lambda_0 + \frac{d}{2} - \left(\lambda_0 + \frac{d}{2} + d_g\right)\exp\left(-\frac{d_g}{\lambda_0}\right)\right]. \tag{4.10}$$

Note that in the limit where $d_g \ll \lambda_0$, the previous expression simplifies to $F_0 \simeq (\pi/4)(f_r - f_\theta)dd_g$. Under these circumstances, the drag force scales linearly with the effective surface area of the object dd_g, as expected in two-dimensional configurations (Seguin, 2019; Seguin *et al.*, 2022). Once again, we point out that the approach followed is a continuum one where the velocity and force fields in the medium are continuous. However, the parameters present in the equations modeling these fields have been shown to depend on the grain size (Seguin *et al.*, 2013) (which is taken into account in our model). To this end, this is a continuum model that includes some granular discreteness effects in these dependencies and also in the computation of the force with Eq. (4.9).

In the following, the forces will be normalized by this reference value F_0 given by Eq. (4.10), which corresponds to the case where there is no interaction, and we will consider the ratio $\tilde{F} = F/F_0$ introduced in Sec. 4.2.2. In order to account for the mechanism proposed by Dhiman *et al.* (Dhiman *et al.*, 2020) in this framework and calculate the drag force in the presence of interactions, we assume that the force field around the first intruder $\mathbf{f}_1$ is perturbed locally by the velocity field of the second intruder $\mathbf{v}_2$. We hypothesize that the perturbed force field $\mathbf{f}_1'$ writes:

$$\mathbf{f}_1' = \mathbf{f}_1 \left(1 - \alpha \frac{|\mathbf{v}_1 \cdot \mathbf{v}_2|}{V_0^2}\right), \tag{4.11}$$

where α is a nondimensional coefficient that represents the strength of the interaction. In this phenomenological formulation, α is an *ad hoc* parameter adjusted from experimental data. In the future, it would be interesting to have a prediction for α on how it depends on other parameters, such as the grain's size, for instance. Note that this expression depends only on the orientation of the local velocity fields of the two intruders and not on their norm. The area of velocity and force interactions between the two intruders is highlighted in purple in Fig. (4.38)a.

Now we study how this interaction modifies the total drag force on one intruder as a function of the separation distance Δ. We solve this problem numerically by computing Eq. (4.9), where the force field $\mathbf{f}$ is replaced by the perturbed force field $\mathbf{f}_1'$ given by Eq. (4.11). This calculation gives the drag force F in the presence of interaction and allows it to be compared with the reference force F_0. We repeat this procedure for different separating distances Δ and compute the resulting drag force ratio $\tilde{F}$ on one intruder. This approach results in a normalized drag force $\tilde{F}$ that tends towards one for large separation distances ($\Delta \gg d$) and decreases as the separation distance is reduced, in agreement with our observations. As we have used renormalization, the drag force ratio $\tilde{F}$ is only a function of α, λ_0 and λ_s. Therefore, we consider λ_0 and α as free parameters, keep $\lambda_s/d = 0.45$ constant, and search for the best fits of the measurements of the normalized drag force at each depth.

Figure (4.38)b presents the normalized drag force as a function of the separation distance for three different depths along with the best fits of the model. We observe that the model correctly captures the reduction in drag force observed experimentally. We also note that the model curve for $h = 49$ mm seems to be a bit non-monotonic for small values of $\tilde{\delta}$. This behavior is a second-order effect and is the result of the complex orientation of the velocity and force fields in the zone of interaction. So, in some sense, it is related to the modification

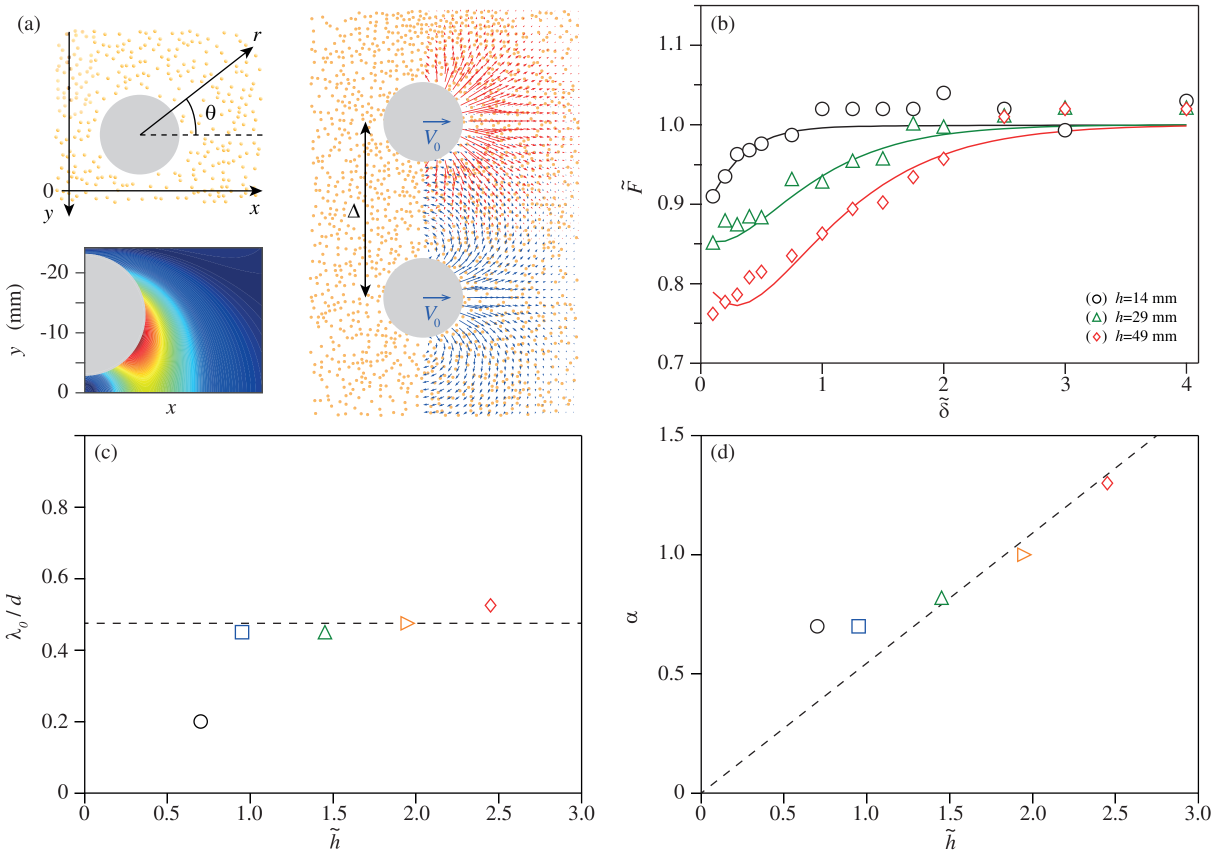

Figure 4.38 – (a) Top view sketches illustrating the model developed to rationalize the interaction between the two intruders: (top left) notations of the problem; (bottom left) area in front of one intruder where the color scale from blue to red encodes increasing values of the interaction term $(\alpha|\mathbf{v}_1 \cdot \mathbf{v}_2|/V_0^2)$ in Eq. (4.11); (right) velocity field (blue arrows) of the neighboring intruder at the bottom disturbs the force field (red arrows) induced by the movement of the intruder at the top (and vice-versa, not shown here for visibility purposes). (b) Normalized drag force $\tilde{F}$ as a function of the normalized separation distance $\tilde{\delta}$. Symbols correspond to experimental data at different depths and solid lines represent the best fit with the model. (c) Parameter λ_0 divided by d resulting from the best fit of the data as a function of the normalized depth $\tilde{h}$. The dashed line indicates $\lambda_0/d \simeq 0.48$. (d) Coefficient α resulting from the best fit of the data as a function of of the normalized depth $\tilde{h}$. The dashed line corresponds to $\alpha \simeq 0.55\,\tilde{h}$. Images taken from (Carvalho *et al.*, 2024b).

of the shearing effect in this regime, which we expect to increase with the intruder's depth [as indirectly shown by the increase of α with h in Fig. (4.38)d]. Note that, given the experimental accuracy, we are not able to distinguish this weak non-monotonic behavior. Consequently, for these values of $\tilde{\delta}$, the model is very sensitive to the parameters used in its calculation [λ_s, λ_0, α and, perhaps, even with d_g due to its presence in Eq. (4.9)]. In addition, we would like to point out that a non-monoticity of the force with the separation between intruders has already been observed in other experimental and numerical works (Pravin *et al.*, 2021; Carvalho; Franklin, 2022b), and shown in Sec. 4.1.2.2.1.

In order to not overload Fig. (4.38)b, we decided to show only part of the data corresponding to the backward motion since they are less dispersed. Similar results are obtained for the forward case with a slight difference in the found fitting coefficients, shown in Tab. (4.11).

Table 4.11 – Fitting coefficients for the solution of the model. In all cases, f_θ = 1 N m^{-2}.

	Forward Journey			Backward Journey		
h/d	λ_0/d	α	f_r ($\times 10^5$) N m^{-2}	λ_0/d	α	f_r ($\times 10^5$) N m^{-2}
0.70	0.200	0.70	0.3297	0.200	0.70	0.3170
0.95	0.550	0.70	0.4430	0.450	0.70	0.4290
1.45	0.525	0.88	0.7721	0.450	0.82	0.6820
1.95	0.475	0.90	1.0990	0.475	1.00	0.9850
2.45	0.550	1.30	1.5370	0.525	1.30	1.3466

The estimated values of λ_0/d and α found with this procedure are plotted as a function of $\tilde{h}$ in Figs. (4.38)c and (4.38)d, respectively. Note that similar parameters are found when adjusting the forces measured in the case of forward motion. We observe in Fig. (4.38)c that the ratio λ_0/d is roughly independent of the depth of the intruder, except at shallow depths where surface effects are not negligible. At large depths, the ratio λ_0/d is about 0.48, in close agreement with the estimate of Seguin *et al.* (Seguin *et al.*, 2013). Figure (4.38)d shows that the coefficient α resulting from the fitting procedure increases linearly with depth. This observation is consistent with the fact that the parameter α is related to the relative magnitude of drag reduction, which follows the same evolution as seen in Fig. (4.35)c.

In addition, this procedure can also be used to calculate the side force experienced by the intruders when they interact with each other. The side force is calculated by integrating the force field projected onto the y-direction in a similar way to Eq. (4.9) as:

$$F_S = \int_{-\pi/2}^{\pi/2} \int_{d/2}^{d/2+d_g} \mathbf{f}_1' \cdot \mathbf{e}_y \, dr \, r d\theta. \tag{4.12}$$

In doing so, we find that the lateral force tends towards zero at large separation distances ($\Delta \gg d$) and is attractive at smaller separation distances. This prediction is in line with previous observations made in experiments and simulations for separation distances that are not too small ($\Delta > 0.1d$) (Cruz; Caballero-Robledo, 2016; Dhiman *et al.*, 2020; Caballero-Robledo *et al.*, 2021). Finally, the framework proposed above, although empirical, provides an extensive prediction of the interaction between two objects moving in a granular material in the quasi-static regime.

Another point that is relevant to discuss is the reference case of two spheres in interaction in a viscous fluid, and how the situation compares with the granular case. The interaction in viscous fluids has been analytically solved using force-point methods by Happel and Brenner (Happel; Brenner, 1983). In the case of two identical spheres moving side by side at a constant velocity (flow perpendicular to the centerline linking the spheres), the drag force is predicted to reduce as the separation between the sphere decreases. At the first order, the drag force on the sphere is predicted to reduce as:

$$\frac{F}{3\pi\eta d V_0} = \frac{1}{1+\frac{3}{8}\frac{d}{\Delta}}, \tag{4.13}$$

where η is the fluid's viscosity. Note that in the limit of touching spheres ($\Delta = d$), the relative drag reduction in the viscous case is approximately equal to 27%, which is the same order of the highest drag reduction measured in our experiments in granular materials [Fig. (4.35)c]. Such drag reduction in viscous flow has been observed experimentally in the case of two bubbles ascending side by side (Saad, 2015), and with two spheres in yield-stress fluid (Merkak *et al.*, 2006). However, in the case of interacting spheres in viscous flows, no depth dependence on drag reduction is predicted. Another important difference between both situations is that side forces are not present in the viscous case.

In summary, we investigated experimentally how drag forces acting on a pair of transversely aligned intruders vary with their depth and transverse separation as they move at constant speed in a granular bed. We found that the mean drag experienced by each intruder is lower than that for a single intruder when separations are small, and that the drag increases with their separation, until it reaches a plateau equal to the single intruder's value for large separations, evincing, therefore, a cooperation dynamics within a given distance range. In addition, we found that the drag reduction for small separations increases with depth and that data for the mean drag varies exponentially with the intruder-intruder separation, and propose a model for the drag reduction based on the breakup of contact chains caused by the local motion of grains. Although the model has some limitations, being two-dimensional and using phenomenological laws, it describes well our experimental results. Our findings shed light on the cooperative dynamics and coupling effects taking place in granular media.

5 RESULTS AND DISCUSSION - COLLISIONAL REGIME - IMPACT PROBLEMS

5.1 Numerical Investigation

5.1.1 Impact of a spherical projectile

This section (Sec. 5.1.1) reproduces material from Douglas D. Carvalho, Nicolao C. Lima, and Erick M. Franklin, "Roles of packing fraction, microscopic friction, and projectile spin in cratering by impact", Phys. Rev. E **107**, 044901 (2023), with permission from the American Physical Society (Carvalho *et al.*, 2023b).

Although considerable progress on the mechanics of impacts and crater formation was made from previous studies, many questions remain open, such as the scaling laws for the penetration depth, and the roles of friction and initial packing fractions. Other questions are still to be investigated, such as how the initial spin of projectiles (rotational kinetic energy) affects cratering. In this section, we inquire into those questions by carrying out DEM computations of the impact of solid projectiles onto a cohesionless granular medium (in the gravity regime), in accordance to the methodology presented in Sec. 3.1.2. For different projectile and grain properties (diameter, density, friction coefficients and packing fraction), we measured the morphology of craters, fluctuations of grains, and resultant force on the projectile. In summary, we show that the scales of craters and the dynamics of projectiles compare well with some of the existing scaling laws, but not with others. We find that, after an initial fluidization, a denser region forms below the projectile, which pushes it back and causes its rebound by the end of its motion, and that solid friction affects considerably the crater morphology. In addition, we show that the penetration length δ increases with the initial spin (angular velocity) of the projectile and that differences in the initial packing fraction ϕ engender the diversity of scaling laws found in the literature. Finally, we propose an *ad hoc* scaling for δ involving ϕ that can, perhaps, unify the existing correlations.

5.1.1.1 Numerical setup

The computed system consisted of $N \sim 10^6$ spheres with diameter d and density ρ, forming a granular bed in a cylindrical container, and a projectile with diameter D_p and density ρ_p. Prior to each simulation, around 10^6 spheres with a Gaussian distribution for d

were randomly arranged in space, and let to fall freely in the container and settle until a low level of kinetic energy was attained. By varying the initial value of the grain-grain friction coefficient μ_{gg}, we obtained different packing fractions ϕ for the bed, after which we changed μ_{gg} back to the correct value. The grains were then allowed to relax, and only afterward the simulations began. The distribution of diameters used in the simulations are shown in Tab. (5.1). We then computed the minimum height necessary for having a horizontal surface and deleted all the grains above that height (around 10^4 grains removed). Depending on the properties of the spheres and their initial number, the number N that remained in the computational domain varied. The granular beds had a diameter D_{bed} = 125 mm and heights h_{bed} = 67.0-76.5 mm (depending on the packing fraction). In order to avoid strong confinement effects, the bed dimensions are equal to the largest dimensions investigated by Seguin *et al.* (2008) (Seguin *et al.*, 2008).

Table 5.1 – Distribution of diameters for the settling grains: number of grains N_d for each diameter d.

d (mm)	0.6	0.8	1.0	1.2	1.4
N_d (ϕ = 0.554)	21524	128125	643002	128053	21421
N_d (ϕ = 0.575-0.632)	21483	128214	642847	127831	21340

Table 5.2 – Properties of materials used in the simulations: E is Young's modulus, ν is the Poisson ratio, and ρ is the material density. The last column corresponds to the diameter of the considered object.

	Material	E **(Pa)**	ν	ρ **(kg/m^3)**	**Diameters (mm)**
Projectile	Steel$^{(1)}$	0.2×10^{11}	0.3	7865	15
Grains	Sand$^{(1)-(2)}$	0.1×10^{9}	0.3	2600	$0.6 \leq d \leq 1.4$
Walls	Steel $^{(1)}$	0.2×10^{12}	0.3	7865	125

(1) Ucgul *et al.* (Ucgul *et al.*, 2014a; Ucgul *et al.*, 2014b; Ucgul *et al.*, 2015)

(2) Derakhshani *et al.* (Derakhshani *et al.*, 2015)

At the beginning of the simulations, the projectile is put into motion in order to collide with the granular bed with collision velocities V_p that are related with the free-fall height h (distance from the bed surface to the initial position of the projectile centroid minus its radius, $V_p = \sqrt{2gh}$). With that, Froude numbers were within $3.75 \times 10^{-3} \leq Fr^{-1} \leq 3$, all of which we consider in the gravity regime. Figure (5.1) shows a layout of the numerical setup. Animations showing impacts and cratering are available in <https://journals.aps.org/pre/supplemental/10.1103/PhysRevE.107.044901>.

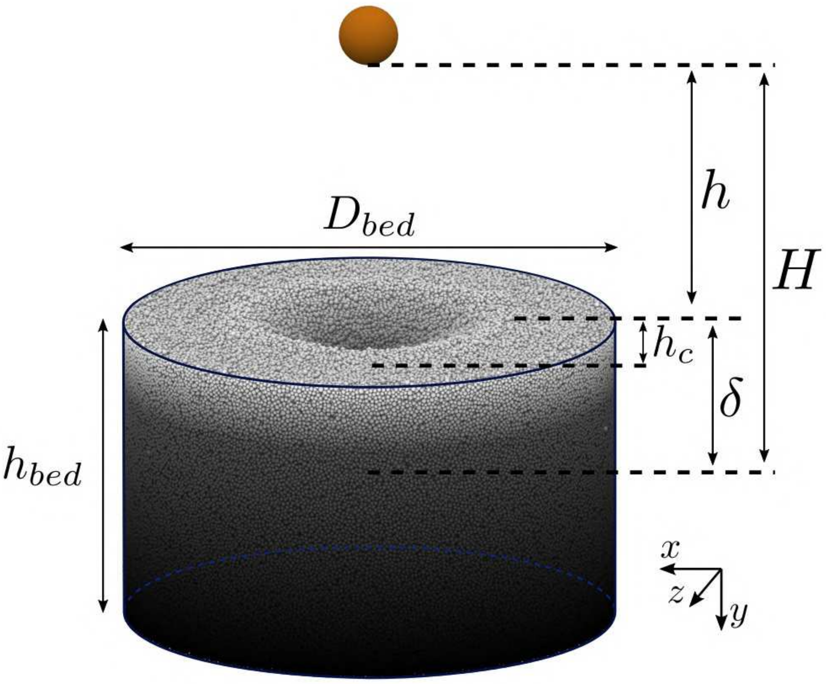

Figure 5.1 – Layout of the numerical setup. The origin of the coordinate system is on the bed surface, in the center of the domain; however, it is shown on the bottom right for better visualization. Image taken from (Carvalho *et al.*, 2023b).

Table 5.3 – Coefficients used in the numerical simulations.

Coefficient	**Symbol**	**Value**
Restitution coefficient (grain-grain)$^{(1)}$	ϵ_{gg}	0.6
Restitution coefficient (grain-projectile)$^{(1)}$	ϵ_{gp}	0.6
Restitution coefficient (grain-wall)$^{(1)}$	ϵ_{gw}	0.6
Fiction coefficient (grain-grain)$^{(1)-(2)}$	μ_{gg}	0.52
Friction coefficient (grain-projectile)$^{(1)}$	μ_{gp}	0.5
Friction coefficient (grain-walls)$^{(1)}$	μ_{gw}	0.5
Coefficient of rolling friction (grain-grain)$^{(2)}$	$\mu_{r,gg}$	0.3
Coefficient of rolling friction (grain-projectile)$^{(1)}$	$\mu_{r,gp}$	0.05
Coefficient of rolling friction (grain-wall)$^{(1)}$	$\mu_{r,gw}$	0.05

(1) Ucgul *et al.* (Ucgul *et al.*, 2014a; Ucgul *et al.*, 2014b; Ucgul *et al.*, 2015)

(2) Derakhshani *et al.* (Derakhshani *et al.*, 2015)

We used different properties for the grains and projectile, listed in Tabs. (5.2) and (5.3) together with those for walls. We used the real Young's modulus E, with the exception of projectiles in steel, for which we used a value that was smaller by one order of magnitude. Because steel has the higher Young's modulus among the used materials, and since the projectile suffers a considerable number of energetic impacts (much larger than the walls), this numerical artifice increased the necessary time step without affecting significantly the results (Lommen *et al.*, 2014). In our simulations, all the coefficients were taken from the literature, and the sand grains were modeled as spherical particles with angularity effects embedded in the rolling friction, for which we used the value μ_r = 0.3 validated by Derakhshani *et al.* (Derakhshani *et al.*, 2015). We validated the friction coefficients listed in Tab. (5.3) by measuring the angles of repose obtained numerically: prior to starting any computation, we evaluated the friction coefficients [listed in Tab. (5.3)] by letting the grains fall freely and form a conical heap, as can be seen in Fig. (5.2). We then measured the angle of repose and compared it with values found in the literature (Ref. (Derakhshani *et al.*, 2015), for example). Because we modeled sand grains as spherical particles with angularity effects embedded in the rolling friction, the agreement was good ($\approx 32°$).

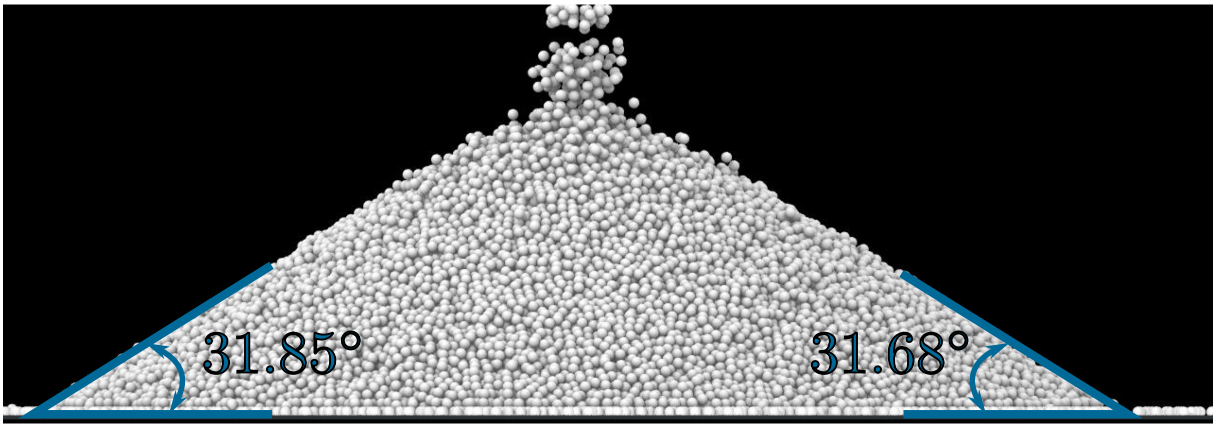

Figure 5.2 – Angle of repose obtained by settling particles with μ_{gg} = 0.52 and $\mu_{r,gg}$ = 0.3. Image taken from (Carvalho *et al.*, 2023b).

Although we present results for fixed ρ_p and D_p [as listed in Tab. (5.2)] in the following, we also carried out simulations with 2685 kg/m^3 $\leq \rho_p \leq$ 11865 kg/m^3 and 5 mm $\leq$ $D_p \leq$ 30 mm, the results being shown at the end of Sec. 5.1.1.2.1.

The time step was $\Delta t = 8 \times 10^{-7}$ s in all our computations, assuring Δt less than 10 % of the Rayleigh time t_R for all particles [Eq. (4.2)] (Derakhshani *et al.*, 2015). More details about the numerical setup are available in an open repository (Lima *et al.*, 2022).

5.1.1.2 Results and discussion

5.1.1.2.1 Morphology of craters

Although extensively investigated over the last decades, the morphological laws for craters are still object of debate (with the exception, perhaps, of the crater diameter D_c), and

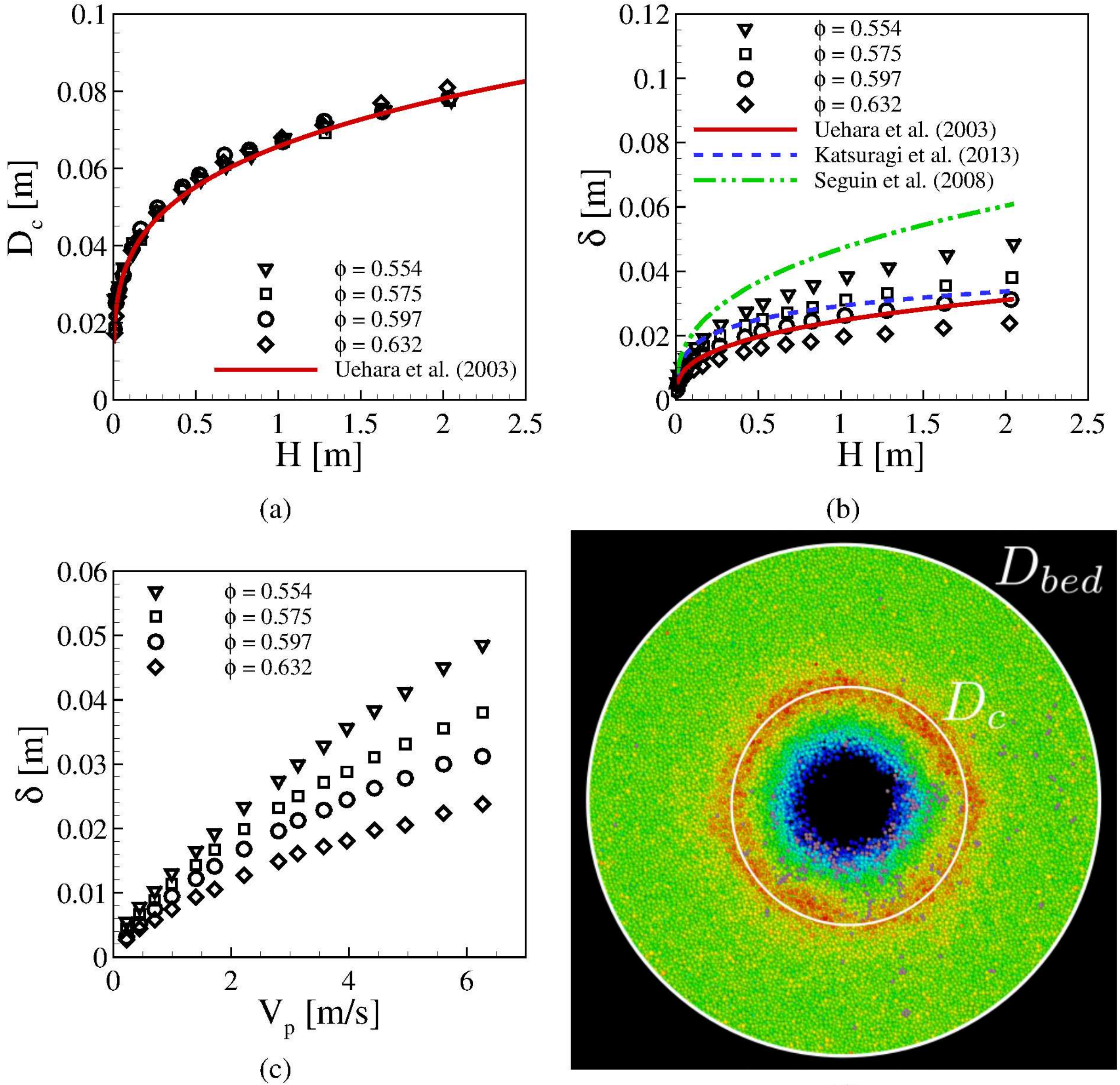

(a) (b) (c) (d)

Figure 5.3 – Morphological aspects: (a) Crater diameter D_c as a function of the total drop distance H; (b) depth δ reached by the projectile as a function of H; and (c) δ as a function of the projectile velocity at the impact V_p. (d) Top view of a crater, showing a circle fitted over the corona. The crater diameter D_c is defined as the diameter of this circle. In Figs. (a) and (b), the corresponding correlations proposed by Uehara *et al.* (2003) (Uehara *et al.*, 2003b), Katsuragi *et al.* (2013) (Katsuragi; Durian, 2013) and Seguin *et al.* (2008) (Seguin *et al.*, 2008) are also plotted, and Figs. (a) to (c) are parameterized by the initial packing fraction. Images (a) to (c) taken from (Carvalho *et al.*, 2023b) and image (d) taken from (Carvalho *et al.*, 2023a).

correlations available in the literature often mix data obtained under different (if not unknown) packing fractions. In other instances, functional relations are based on different parameters (h instead of the total drop height $H = h + \delta$, where δ is the projectile's penetration depth, for example). Therefore, we investigate initially how the crater diameter D_c and the depth δ reached by the projectile behave with varying the drop distance H (or the height to impact h, related to the velocity at the impact V_p), and compare them with morphological laws found in the literature. In addition, different from previous studies, we evaluate how those relations vary with the initial packing fraction ϕ of the bed.

Figure (5.3)a shows the crater diameter D_c [measured as indicated in Fig. (5.3)d] as a function of the total drop distance H, parameterized by the initial packing fraction ϕ, and the correlation proposed by Uehara *et al.* (2003) (Uehara *et al.*, 2003b), given by Eq. (5.1),

$$D_c = 0.90\left(\frac{\rho_p}{\rho\mu_{rep}^2}\right)^{1/4} D_p^{3/4} H^{1/4}\,, \tag{5.1}$$

where μ_{rep} is the macroscopic friction measured as the tangent of the angle of repose, which Uehara *et al.* (2003) (Uehara *et al.*, 2003b) considered equal to μ_{gg}, and ρ is the density of the grains. In fact, we find a consensus in the literature that D_c varies with $H^{1/4}$, and our data shows the same, with a collapse of data for all the different packing fractions used in the simulations. Therefore, D_c is independent of ϕ, and this is the main reason for the existing consensus since the different experiments reported in the literature were conducted at different packing fractions. The same does not occur with the depth δ reached by the projectile. Figure (5.3)b shows δ as a function of H, parameterized by ϕ, and the corresponding correlations proposed by Uehara *et al.* (2003) (Uehara *et al.*, 2003b), Katsuragi *et al.* (2013) (Katsuragi; Durian, 2013) and Seguin *et al.* (2008) (Seguin *et al.*, 2008), given by Eqs. (5.2), (5.3) and (5.5), respectively. We observe a clear dependence of δ on ϕ, and that correlations give different results. The discrepancies between the existing correlations are thus, at least in part, due to the different packing fractions of the experiments they came from. The dependence of δ on ϕ is shown also in Fig. (5.3)c in terms of the projectile velocity at the impact V_p. We observe that the data diverge for increasing values of V_p, presenting a non-linear variation with V_p for higher values of ϕ. This is in contrast with Katsuragi and Durian (2007) (Katsuragi; Durian, 2007) and Goldman and Umbanhowar (2008) (Goldman; Umbanhowar, 2008), who found that δ varies linearly with V_p. However, we note that: (i) most of the data presented by Refs. (Katsuragi; Durian, 2007; Goldman; Umbanhowar, 2008) are within 0 m/s $\leq V_p \leq$ 4 m/s, for which the dependencies tend to appear more linear; and (ii) we controlled the packing fraction in each of our simulations (different from previous works), finding considerable deviations for higher values of ϕ. If we consider 0 m/s $\leq V_p \leq$ 4 m/s, the curves in Fig. (5.3)c become roughly linear. The correlations plotted in

Fig. (5.3)b are presented below.

(i) Correlation proposed by Uehara *et al.* (2003) (Uehara *et al.*, 2003b):

$$\delta = 0.14\left(\frac{\rho_p}{\rho\mu_{rep}^2}\right)^{1/2} D_p^{2/3} H^{1/3}. \tag{5.2}$$

(ii) Correlation proposed by Katsuragi *et al.* (2013) (Katsuragi; Durian, 2013):

$$\frac{2\delta}{d_1} = 1 + \frac{2m_p g}{\kappa d_1} + \mathcal{W}\left(\frac{2m_p V_p^2 - 2m_p g d_1 - \kappa d_1^2}{\kappa d_1^2 e^{1+2m_p g/\kappa d_1}}\right), \tag{5.3}$$

where $\mathcal{W}(x)$ is the Lambert function, and κ and d_1 are constants given by Eq. (5.4):

$$\frac{d_1}{D_p} = \left(\frac{0.25}{\mu_{rep}}\right)\left(\frac{\rho_p}{\rho}\right); \qquad \frac{\kappa D_p}{m_p g} = 12\mu_{rep}\left(\frac{\rho}{\rho_p}\right)^{\frac{1}{2}}. \tag{5.4}$$

OBS: in Eq. (2.3), $\xi = m_p/d_1$.

(iii) Correlation proposed by Seguin *et al.* (2008) (Seguin *et al.*, 2008):

$$\frac{\delta}{D_p} = A\left(\frac{\rho_p}{\rho}\right)^{\beta}\left(\frac{H}{D_p}\right)^{\lambda}, \tag{5.5}$$

where $A = 0.37 \pm 0.01$, $\beta = 0.61 \pm 0.02$ and $\lambda = 0.40 \pm 0.04$. We note that in Fig. (5.3)b we used the lower limit of these constants.

Unlike most of previous experiments, de Bruyn and Walsh (2004) (Bruyn; Walsh, 2004) varied the packing fraction and, by modeling the granular system as a Bingham fluid, found that $\delta \sim \phi$. They proposed a correlation where $\delta \sim h^{1/2}D_p^{1/2}$, which contrasts with the above ones [Eqs. (5.2) to (5.5)]. However, as pointed out by the authors, they expected that inaccuracies in their measurements of ϕ could affect the results. From our numerical data, we also noticed that the penetration depth depends on the packing fraction, producing thus different correlations for δ with H or V_p. We propose an *ad hoc* scaling that collapses our data, but without additional modeling (we maintain the discrete nature of granular matter in our analysis). Our objective in proposing this *ad hoc* scaling is simply to collapse our $\delta(H)$ data for different values of ϕ, showing that, perhaps, the existing correlations can be unified by considering a dependency on ϕ.

Figure (5.4)a shows $\delta(H)$ for our simulations, where a factor $\phi^{9/2}$ was introduced in order to collapse the data into a master curve. We notice that the collapse is reasonable, indicating that ϕ is a parameter to be taken into account. By considering specifically the correlation proposed by Uehara *et al.* (2003) (Uehara *et al.*, 2003b) [Eq. (5.2)], Fig. (5.4)b shows $\delta\phi^{9/2}$ as

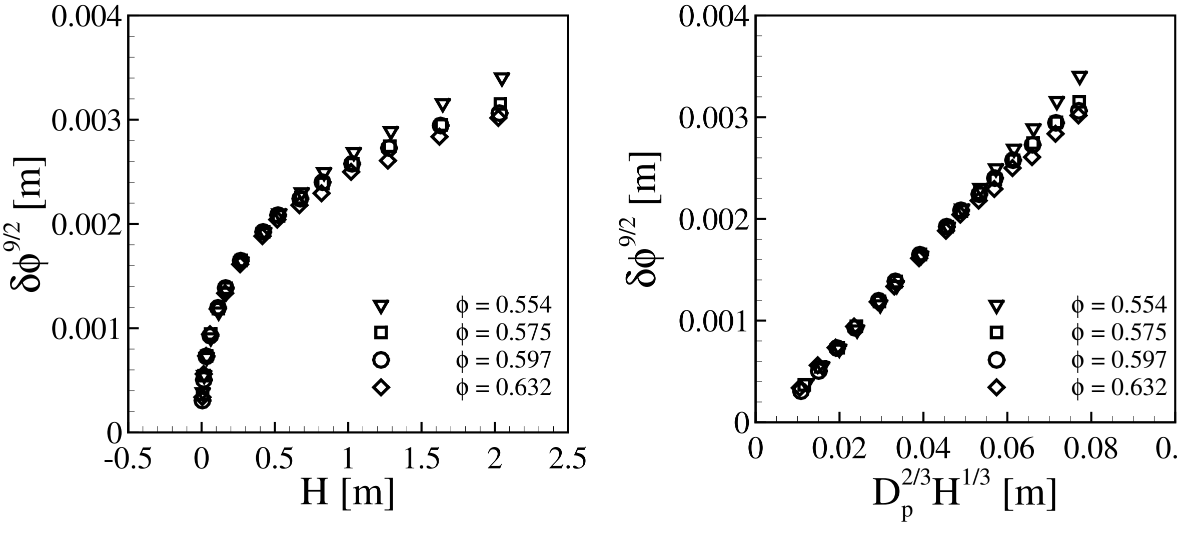

(a) (b)

Figure 5.4 – Depth reached by the projectile multiplied by a power of the packing fraction, $\delta\phi^{9/2}$, as a function of (a) the drop distance H, and (b) $D_p^{2/3}H^{1/3}$, parameterized by ϕ. Images taken from (Carvalho *et al.*, 2023b).

a function of $D_p^{2/3}H^{1/3}$. The data collapse and follow a master line, with some dispersion for higher values of H. This indicates that by taking into account a term ϕ^n [as in Eq. (5.6)], where n is a coefficient, some of the existing expressions may be turned into universal correlations. For our data, n = 9/2 is a reasonable value (please note that n = 4.74 gave a slightly better collapse than 9/2).

$$\delta\phi^n \sim D_p^{2/3}H^{1/3}. \tag{5.6}$$

Although the results presented above were obtained for fixed density ρ_p and diameter D_p of the projectile [as listed in Tab. (5.2)], we also carried out simulations with 2685 kg/m^3 $\leq \rho_p \leq$ 11865 kg/m^3 and 5 mm $\leq D_p \leq$ 30 mm, and the results are shown in Figs. (5.5)a and (5.5)b. Note that the results obtained can be modeled, for both variables, by the powers presented in the correlation proposed by Uehara *et al.* (2003) (Uehara *et al.*, 2003b) [Eq. (5.2)].

5.1.1.2.2 Forces on the projectile and stopping time

We investigate now the projectile dynamics, in particular the accelerations experienced by the projectile and the time t_c that it takes for reaching full stop. In the DEM simulations, positions, velocities and forces are computed for all objects at each time step, so that the time evolution of the projectile acceleration $\vec{a}$ can be obtained from the resultant force ($\vec{a}$ =

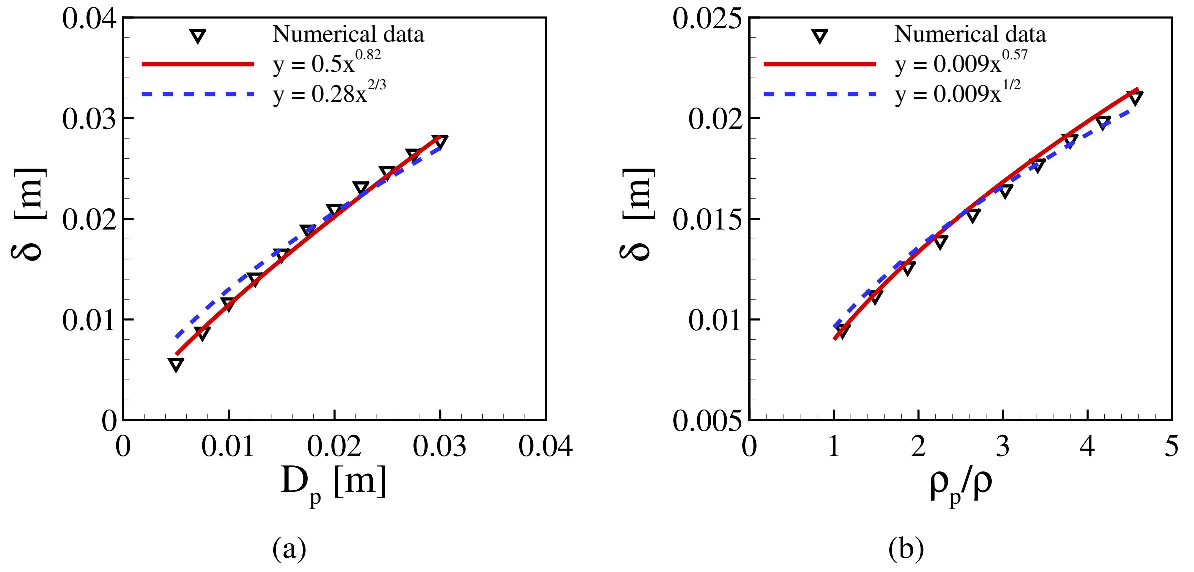

Figure 5.5 – (a) Penetration depth δ as a function of the projectile diameter D_p. The blue-dashed line corresponds to a functional dependence on $D_p^{2/3}$ (as in the correlation of Uehara *et al.* (2003) (Uehara *et al.*, 2003b)), and the red-continuous line to a fitting of our data. In this figure, h = 0.1 m and ρ_p = 7865 kg/m^3. (b) Penetration depth δ as a function of the projectile density ρ_p. The blue-dashed line corresponds to a functional dependence on $\rho_p^{1/2}$ (as in the correlation of Uehara *et al.* (2003) (Uehara *et al.*, 2003b)), and the red-continuous line to a fitting of our data. In this figure, h = 0.1 m and D_p = 15 mm. Images taken from (Carvalho *et al.*, 2023b).

$\vec{F}_p/m_p$), the drag force by subtracting the projectile weight from $\vec{F}_p$, and the stopping time by finding the instant when the projectile velocity V reaches zero. In our analyses, the origin of time is the instant when the bottom of the projectile touches the granular bed, and a_y is positive upwards (as F_p in Eq. (2.3)).

Figure (5.6)a shows the time evolution of the vertical component of the projectile deceleration a_y, normalized by g, for a fixed packing fraction (ϕ = 0.554) and different values of h, i.e., different energies available at the impact. We observe the features described by Goldman and Umbanhowar (2008) (Goldman; Umbanhowar, 2008): (i) a high peak just after the impact has taken place, with its magnitude increasing with h; (ii) the presence of strong fluctuations; (iii) a discontinuity of the deceleration by the end of the motion; and (iv) a slight inversion in the sign of a_y before reaching full stop. The a_y inversion and the full stop is shown in detail in Fig. (5.8). The last instants of the motion (focusing on the rebound region) are presented in Fig. (5.9). In addition, a movie showing the projectile and grains during the impact can be seen in <https://journals.aps.org/pre/supplemental/10.1103/PhysRevE.107.044901>.

Besides reproducing the experimental findings of Goldman and Umbanhowar

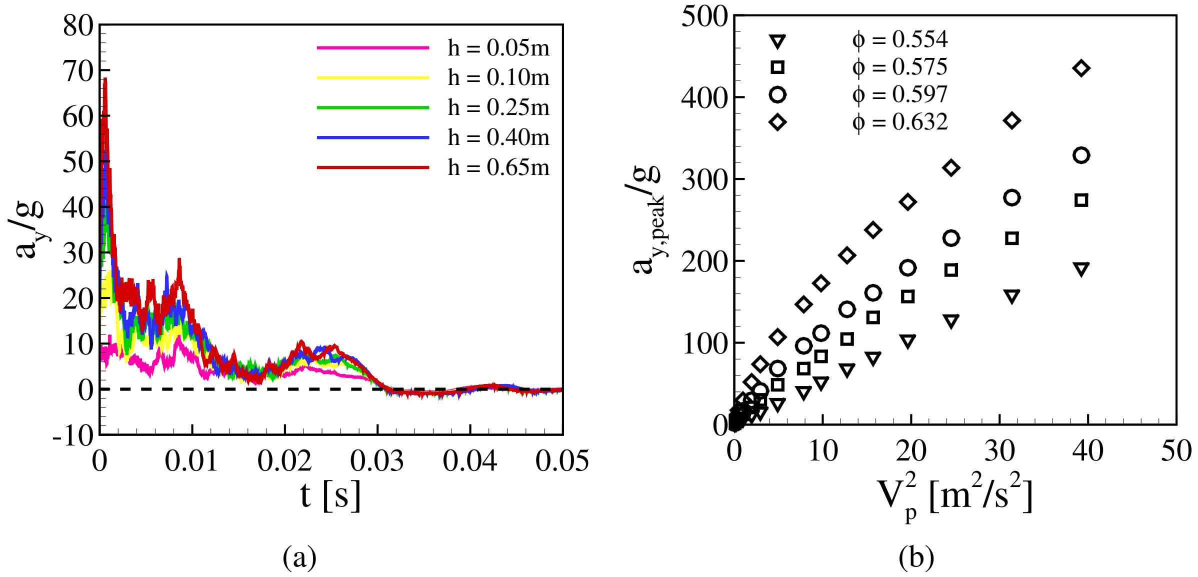

(a)

(b)

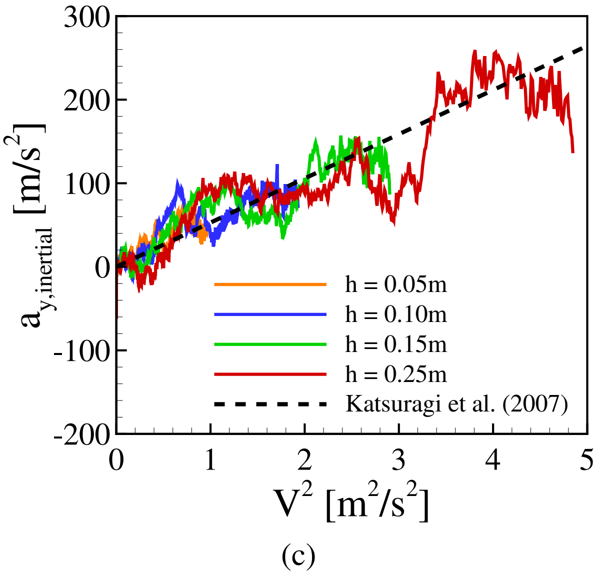

(c)

Figure 5.6 – Projectile dynamics. (a) Time evolution of the vertical component of the deceleration a_y for different initial heights h. (b) Maximum values of the deceleration $a_{y,peak}$ as a function of V_p^2, for different packing fractions ϕ. (c) Inertial component of the vertical deceleration, $a_{y,inertial}$, as a function of V^2 for different values of h. The dashed line corresponds to the model proposed by Katsuragi *et al.* (2007) (Katsuragi; Durian, 2007) (with κ = 37.6287 and d_1 = 0.0189). In Figures (a) and (c), the packing fraction was fixed to ϕ = 0.554. Images taken from (Carvalho *et al.*, 2023b).

(2008) (Goldman; Umbanhowar, 2008), we can now inquire into aspects not previously investigated, such as the effect of the packing fraction and the mechanics of the projectile rebound.

Figure (5.6)b presents the maximum values of the deceleration, $a_{y,peak}$, as a function of the square of the impact velocity V_p, for different packing fractions ϕ. It is clear from

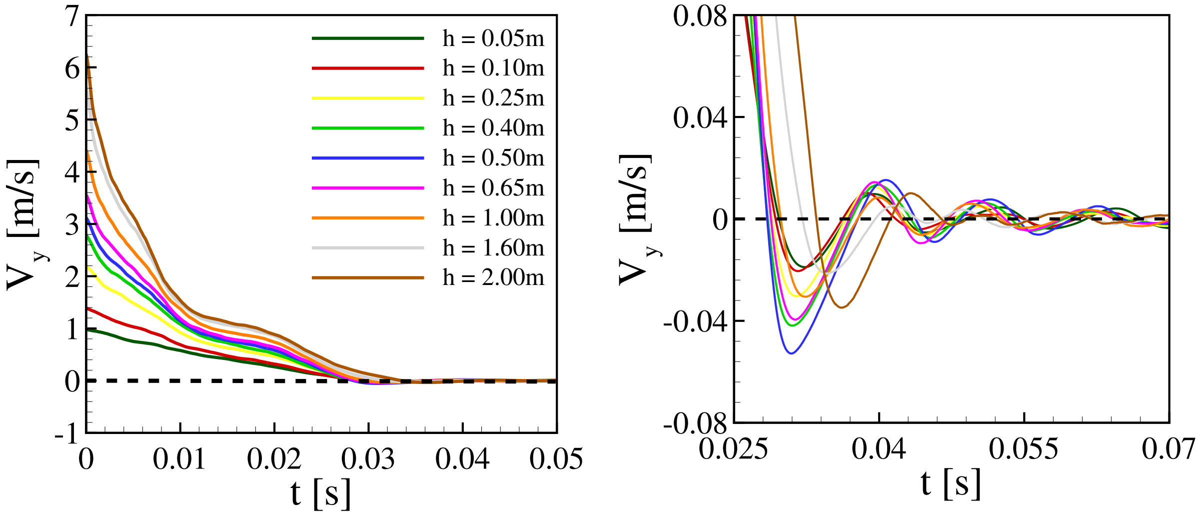

(a) (b)

Figure 5.7 – Time evolution of the vertical component of the projectile velocity V_y for different values of h for (a) the entire simulation and (b) zoomed in the region corresponding to the projectile rebound and final stop. The packing fraction was fixed to ϕ = 0.554. Images taken from (Carvalho *et al.*, 2023b).

Fig. (5.6)b that the value of the peak increases not only with the available energy at the impact, but also with the packing fraction. In mechanical terms, the projectile deceleration is expected to increase with the bed compaction, since more grains are in contact as ϕ increases, hindering their motion and, consequently, that of the projectile. Although previous works showed the deceleration peak and its dependence on h, this is the first time that a parametric study on ϕ is presented, which corroborates the idea of higher a_y for higher ϕ and, in part, the argument advanced by Goldman and Umbanhowar (2008) (Goldman; Umbanhowar, 2008) that Eq. (2.3) should depend on ϕ (and would be valid only close to a critical packing ϕ_{cps}).

In order to inquire if our results agree with the model of Katsuragi *et al.* (2007) (Katsuragi; Durian, 2007), we evaluated the inertial term of the vertical deceleration, $a_{y,inertial}$. By considering F_{drag} = $\xi V^2 + \kappa y$ in Eq. (2.3), where ξV^2 = $m_p\, a_{y,inertial}$ is the inertial term of the drag force (positive upwards), $a_{y,inertial}$ is given by Eq. (5.7):

$$a_{y,inertial} = a_y + g - (\kappa/m_p)y. \tag{5.7}$$

Figure (5.6)c shows $a_{y,inertial}$ as a function of the square of the instantaneous velocity of the projectile, V^2, for ϕ = 0.554 and different values of h, and also the model proposed by Katsuragi *et al.* (2007) (Katsuragi; Durian, 2007) (dashed line). For all initial heights inves-

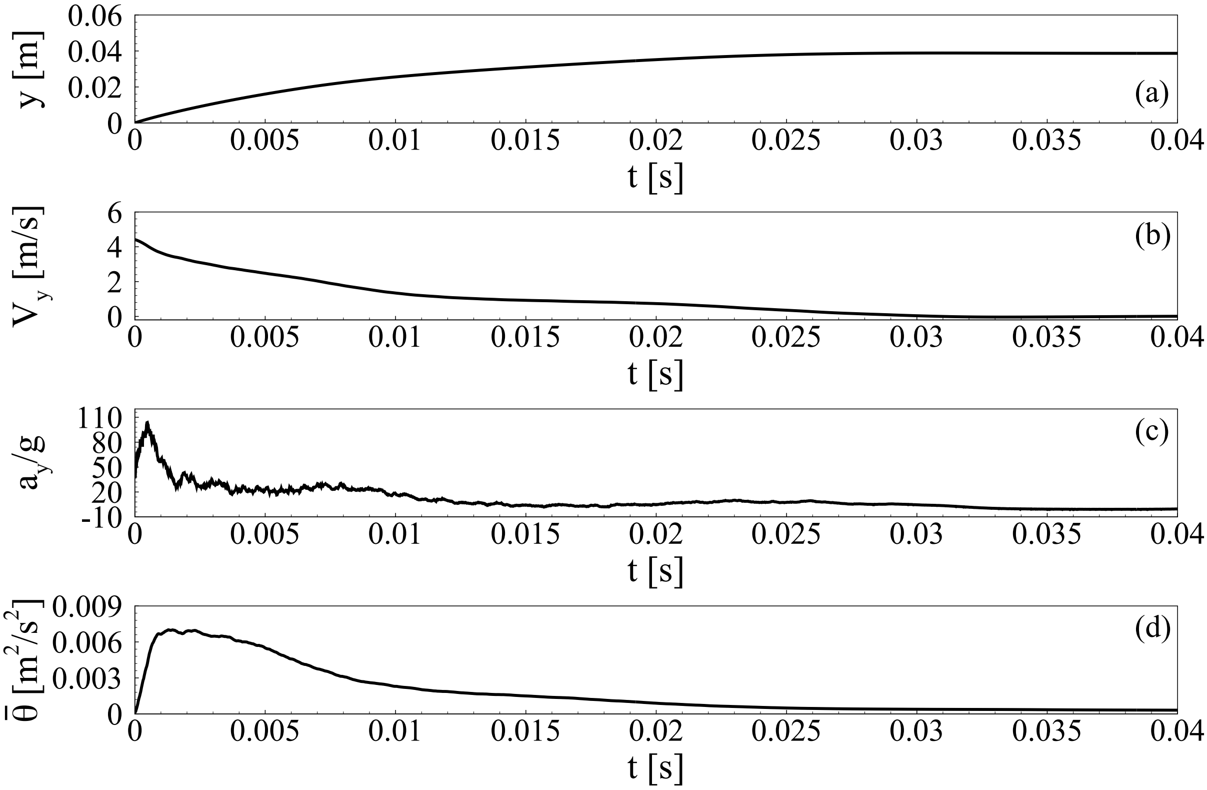

Figure 5.8 – Time evolution of (a) vertical position y of the projectile; (b) vertical velocity V_y of the projectile; (c) vertical deceleration a_y of the projectile, normalized by g; and (d) space-averaged granular temperature $\bar{\theta}$ considering all grains. In this figure, ϕ = 0.554 and h = 1 m. Images taken from (Carvalho *et al.*, 2023b).

tigated (at ϕ = 0.554), the agreement with Katsuragi *et al.* (2007) (Katsuragi; Durian, 2007) is good.

Figure (5.7) presents the time evolution of the vertical component of the projectile velocity, V_y, for different values of h, showing that the time t_c to reach the full stop is independent of the available energy, in agreement with previous works (Ciamarra *et al.*, 2004; Katsuragi; Durian, 2007; Goldman; Umbanhowar, 2008; Seguin *et al.*, 2009) (in Fig. (5.7)a, V_p $\geq$ 0.99 m/s). Furthermore, the stopping time t_c scales well with the timescale t_o proposed by Goldman and Umbanhowar (2008) (Goldman; Umbanhowar, 2008):

$$t_o \sim \left(\frac{\rho_p}{\rho}\right)^{1/4} \left(\frac{D_p}{2g}\right)^{1/2}, \tag{5.8}$$

which is t_o = 0.0365 s in our case [very close to the values of t_c in Fig. (5.7)], and the sign of V_y changes just before the full stop (indicative of the final rebound).

Finally, we investigate the projectile rebounding. We begin by showing how the granular temperature θ evolves as the projectile penetrates into the bed. For that, we computed

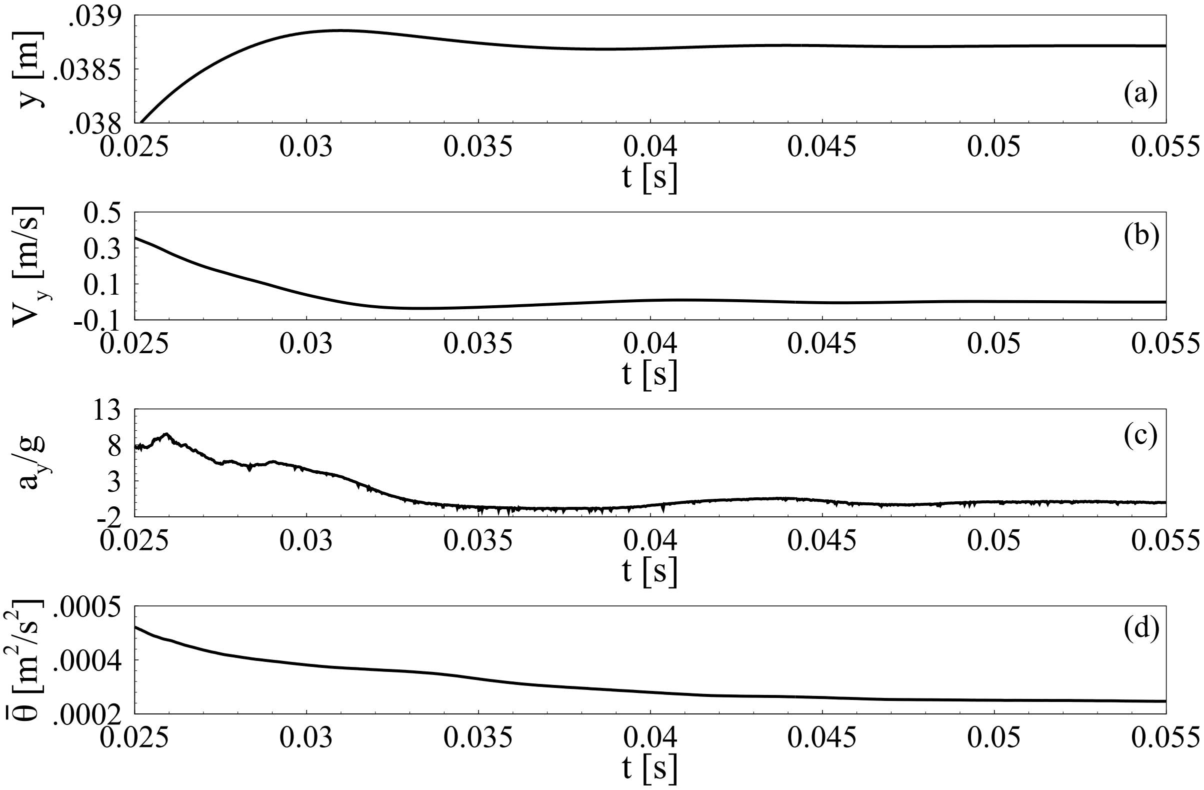

Figure 5.9 – The same graphics of Fig. (5.8) zoomed at the rebound interval. Images taken from (Carvalho *et al.*, 2023b).

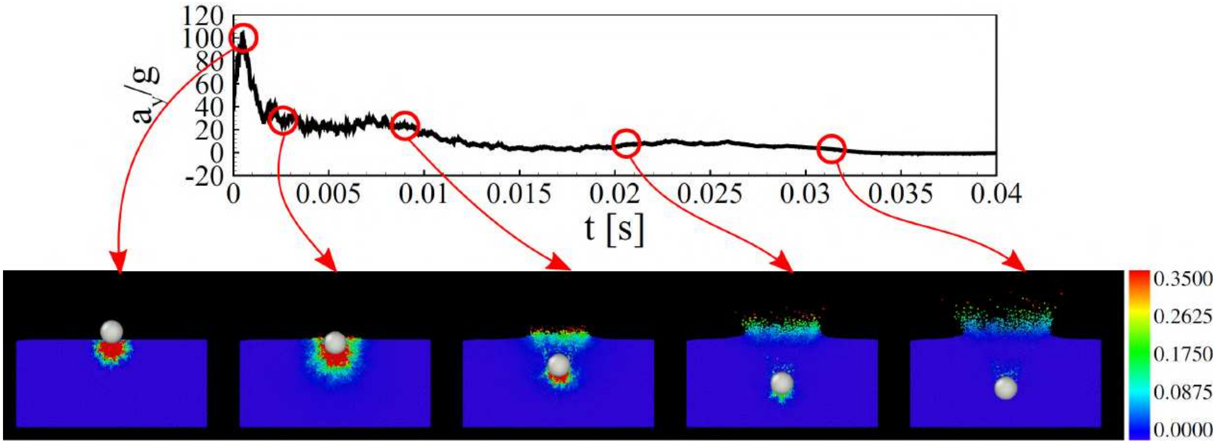

Figure 5.10 – Time evolution of the normalized deceleration in the vertical direction a_y/g, and snapshots of the granular temperature θ at the instants indicated in the a_y/g graphic. The colorbar indicates the values of θ in m^2/s^2, and the figure corresponds to ϕ = 0.554 and h = 1 m. Images taken from (Carvalho *et al.*, 2023b).

the granular temperature of the bed as in Eq. (5.9),

$$\theta(x,y,z,t) = \frac{1}{3}\vec{u_g'}^{\,2} = \frac{1}{3}\left(u'^2 + v'^2 + w'^2\right) \; , \tag{5.9}$$

where $\vec{u_g'}$ is the instantaneous fluctuation velocity of each grain (its velocity relative to the ensemble of grains), and u', v' and w' are the x, y and z components of $\vec{u'_g}$. Therefore, high values of θ indicate more agitation and a fluid-like behavior, while low values indicate less agitation and a solid-like behavior.

Figure (5.10) shows the time evolution of the vertical deceleration of the projectile a_y normalized by g, and snapshots of the granular temperature θ at some instants (indicated in the a_y/g graphic), for ϕ = 0.554 and h = 1 m. A movie showing the time evolution of θ during all the penetration process is available in <https://journals.aps.org/pre/supplemental/10.1103/PhysRevE.107.044901>. From both Fig. (5.10) and the movie, we observe that initially ($t \lessapprox$ 0.005 s) the region of higher granular temperatures is just below the projectile and, with its motion downwards, grains above the projectile reach higher values of θ at a later time (0.01 s $\lessapprox t \lessapprox$ 0.02 s), in particular the ejecta. By the end of its motion and before full stop (0.025 s $\lessapprox t \lessapprox$ 0.04 s), values of θ are considerable smaller, reaching zero below the projectile earlier than above it. This means that the region in front of the projectile (below it) is hardened (solid-like behavior) while that behind it (above the projectile) has still some mobility. Therefore, the rebound can be understood as a result of the faster de-fluidization on the front (bottom) than on the rear (top) of the projectile. We note that we have not inquired into shockwaves propagating from the impact point, toward the walls, and back to the projectile, which can play a role in the projectile rebound, as pointed out by Bourrier *et al.* (2008) (Bourrier *et al.*, 2008). However, Bourrier *et al.* (2008) (Bourrier *et al.*, 2008) propose that the rebound of large projectiles is caused by the compaction of grains below the projectile, in agreement with our results (though we cannot assert that shockwaves are responsible for the rebound).

The vertical position y of the projectile as a function of time for $t >$ 0.025 s, and the displacement in the vertical direction $\Delta y_{rebound}$ for simulations with different values of H, are shown, respectively, in Figs. (5.11)a and (5.11)b. For the latter, we noticed that, although the data oscillate considerably, it seems that $\Delta y_{rebound}$ increases with H for small heights, and then reaches a plateau for $H \approx$ 0.7 m (it remains, however, to be investigated in future works).

5.1.1.2.3 Frictionless grains

The role of friction in the projectile dynamics and cratering is still an open question, with previous works showing that the friction either promotes a strong energy dissipation (Tsimring; Volfson, 2005; Kondic *et al.*, 2012) or does not affect the projectile penetration and stopping time (Seguin *et al.*, 2009) (those results are contradictory). In order to further investi-

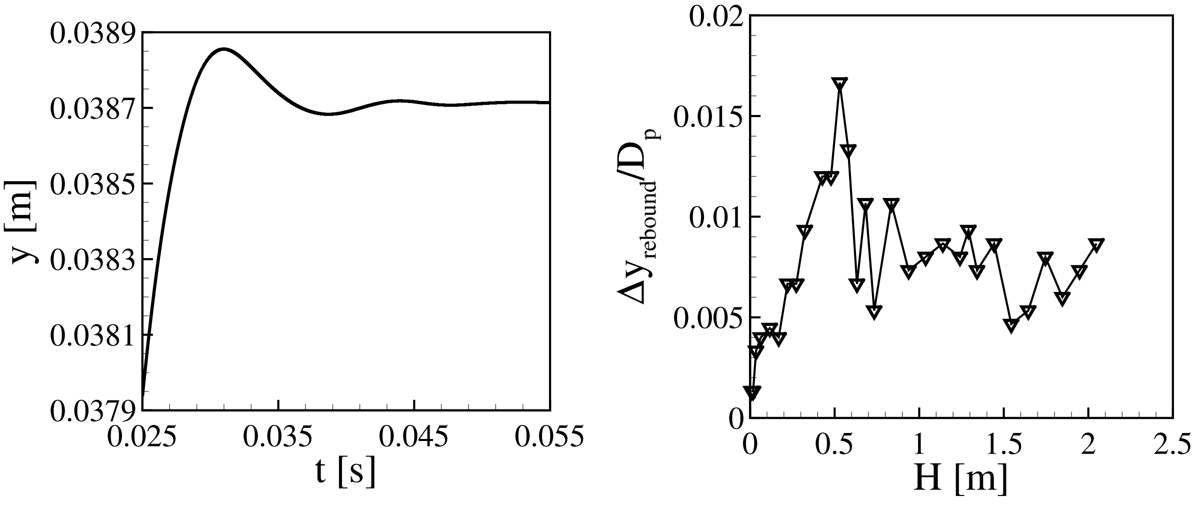

(a) (b)

Figure 5.11 – (a) Vertical position y of the projectile as a function of time for the final phase of the penetration ($t > 0.025$ s), for the case depicted in Fig. (5.10). (b) The vertical displacement during the rebound $\Delta y_{rebound}$, normalized by D_p, for different values of H. Images taken from (Carvalho *et al.*, 2023b).

gate the role of friction, we carried out simulations that considered: (i) all friction coefficients as in Tab. (4.3) (case $\mu \neq 0$); (ii) all friction coefficients equal to zero (case $\mu = 0$); (iii) only the grain-grain friction equal to zero (case $\mu_{gp} \neq 0$ and $\mu_{gw} \neq 0$); and (iv) the friction due to both the grain-grain and grain-wall contacts (but not grain-projectile) equal to zero (case $\mu_{gp} \neq 0$). In all these cases, whenever we indicate that μ_{gp}, μ_{gw} or μ was turned to zero, the corresponding rolling frictions were also zero.

Before each simulation, approximately 10^6 spheres were randomly arranged and let to fall freely in the container and settle. The grains had a Gaussian distribution for d, shown in Tab. (5.1) for the cases with friction, and shown in Tab. (5.4) for frictionless cases. The initial packing fractions were ϕ = 0.641 and 0.640 for μ = 0 and μ_{gg} = 0, respectively.

Table 5.4 – Distribution of diameters of settling grains: number of grains N_d for each diameter d. The table shows values for the absence of friction μ = 0 (frictionless grain-grain, grain-wall and grain-projectile contacts) and for the absence of only the grain-grain friction, μ_{gg} = 0.

d (mm)	0.6	0.8	1.0	1.2	1.4
N_d (μ = 0)	22114	131688	661232	131878	22091
N_d (μ_{gg} = 0)	22092	131523	660681	131675	22068

Figure (5.12) presents the effects of the total or partial absence of friction on the crater diameter D_c [Figs. (5.12)a and (5.12)c], penetration depth δ [Fig. (5.12)b] and projectile

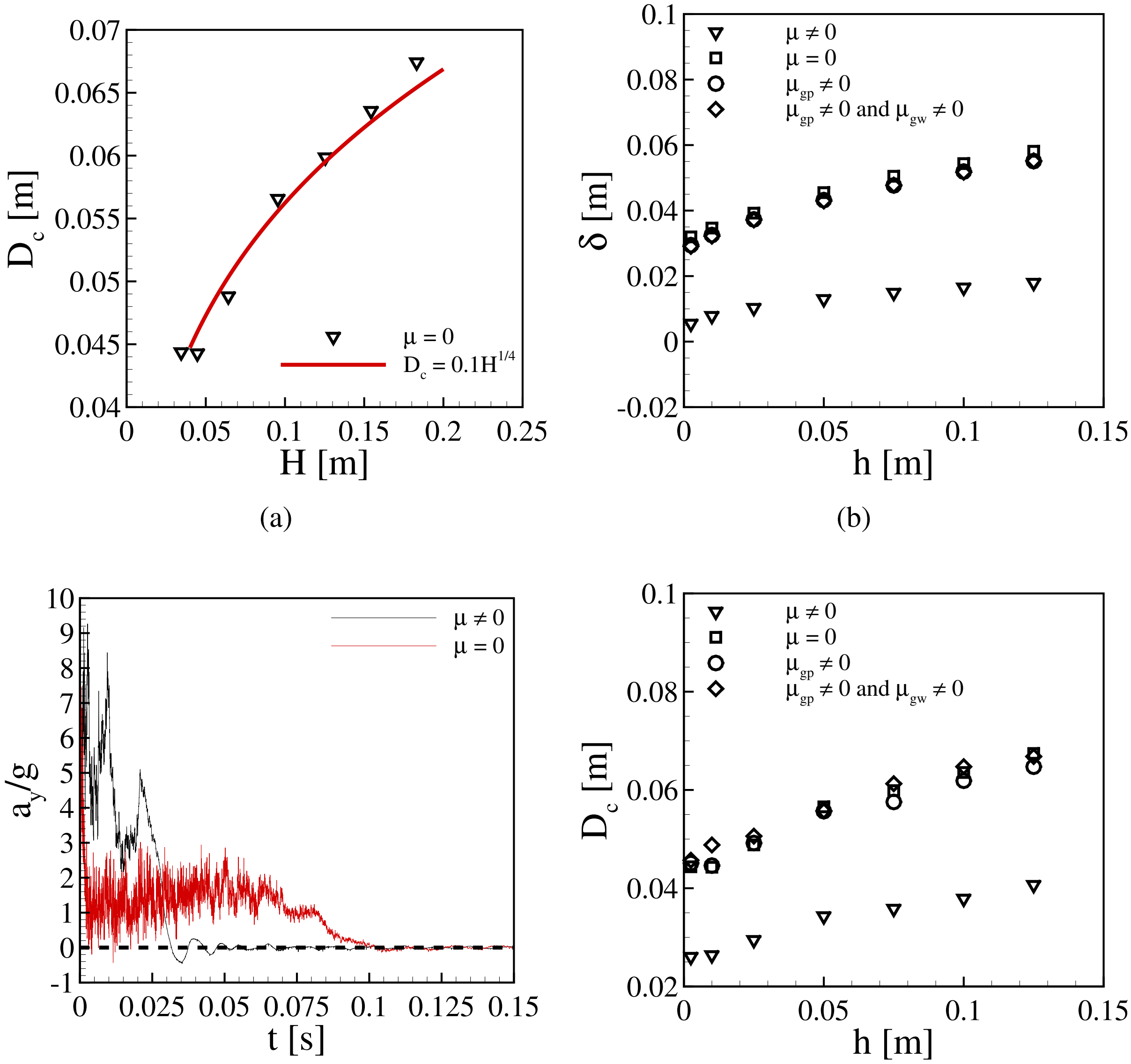

(a) (b)

(c) (d)

Figure 5.12 – (a) Crater diameter D_c as a function of the drop distance H for simulations in the absence of friction (case $\mu = 0$). $\phi = 0.554$ and the red line corresponds to a fitting with $H^{1/4}$. (b) Depth δ reached by the projectile as a function of the initial height h for simulations with all friction coefficients as listed in Tab. (5.3) (case $\mu \neq 0$), without any friction (case $\mu = 0$), with only the grain-projectile friction (case $\mu_{gp} \neq 0$), and with only the grain-grain equal to zero (case $\mu_{gp} \neq 0$ and $\mu_{gw} \neq 0$). (c) For the same cases of figure (b), D_c as a function of h. (d) Time evolution of the normalized deceleration in the vertical direction a_y/g for the cases with (black line) and without (red line) friction. In figure (d), $\phi = 0.554$ when $\mu \neq 0$, and $h = 0.075$ m. Images taken from (Carvalho *et al.*, 2023b).

deceleration in the vertical direction a_y/g [Fig. (5.12)d]. We observe that D_c, δ and a_y are highly affected by the absence of grain-grain friction, and that the presence/absence of the grain-wall and grain-projectile frictions have little effect on them. For the crater diameter, we observe that the $H^{1/4}$ scaling remains valid [Fig. (5.12)a], but the magnitude of D_c increases considerably in the absence of friction between grains, D_c being roughly 50% larger when $\mu = 0$ (or at least $\mu_{gg} = 0$) than when $\mu \neq 0$ [Fig. (5.12)c]. For the penetration depth, δ presents a variation with h that is slighter when the grain-grain friction is present ($\mu \neq 0$), and has much smaller magnitudes than in the frictionless cases [roughly 75% smaller, Fig. (5.12)b]. The vertical deceleration of the projectile, a_y, shows a different behavior in the absence of friction [Fig. (5.12)d]: it presents a smaller peak just after the impact, followed by a fast decrease to values that oscillate around $1.5g$, and finally a fast decrease to zero much after that of the frictional case [t_c is much higher in the frictionless case, approximately by four times in Fig. (5.12)d]. The granular temperature and projectile rebounding of a projectile colliding with a frictionless bed are shown, respectively, in Figs. (5.13) and (5.14), where we notice that in the frictionless case grains reach and maintain a much higher degree of fluctuation and an absence of rebound in the absence of friction. In addition, a movie of a projectile colliding with a frictionless bed is available in <https://journals.aps.org/pre/supplemental/10.1103/PhysRevE.107.044901>.

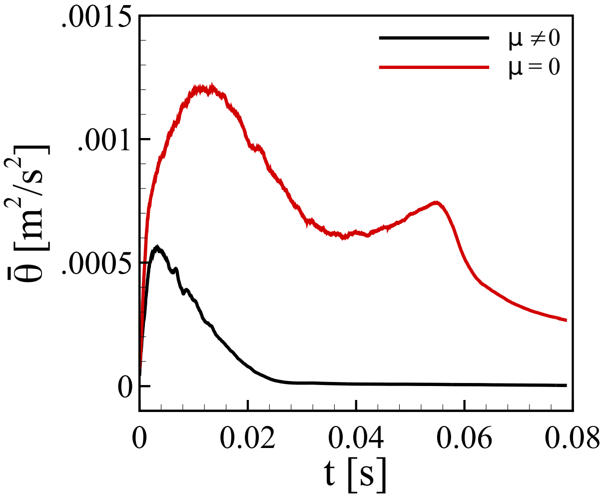

Figure 5.13 – Time evolution of the space-averaged granular temperature $\bar{\theta}$ considering all grains. The red line corresponds to frictionless objects (μ = 0) and the black line to grains with friction ($\mu \neq 0$). ϕ = 0.554 and h = 1 m. Image taken from (Carvalho *et al.*, 2023b).

In summary, our results show a strong influence of the grain-grain friction in both the morphology of craters and the projectile dynamics, which reflects the lower resistance to the projectile penetration when grain-grain friction is absent. The disagreement of our conclusions with those of Seguin *et al.* (2009) (Seguin *et al.*, 2009) is probably due to their highly confined

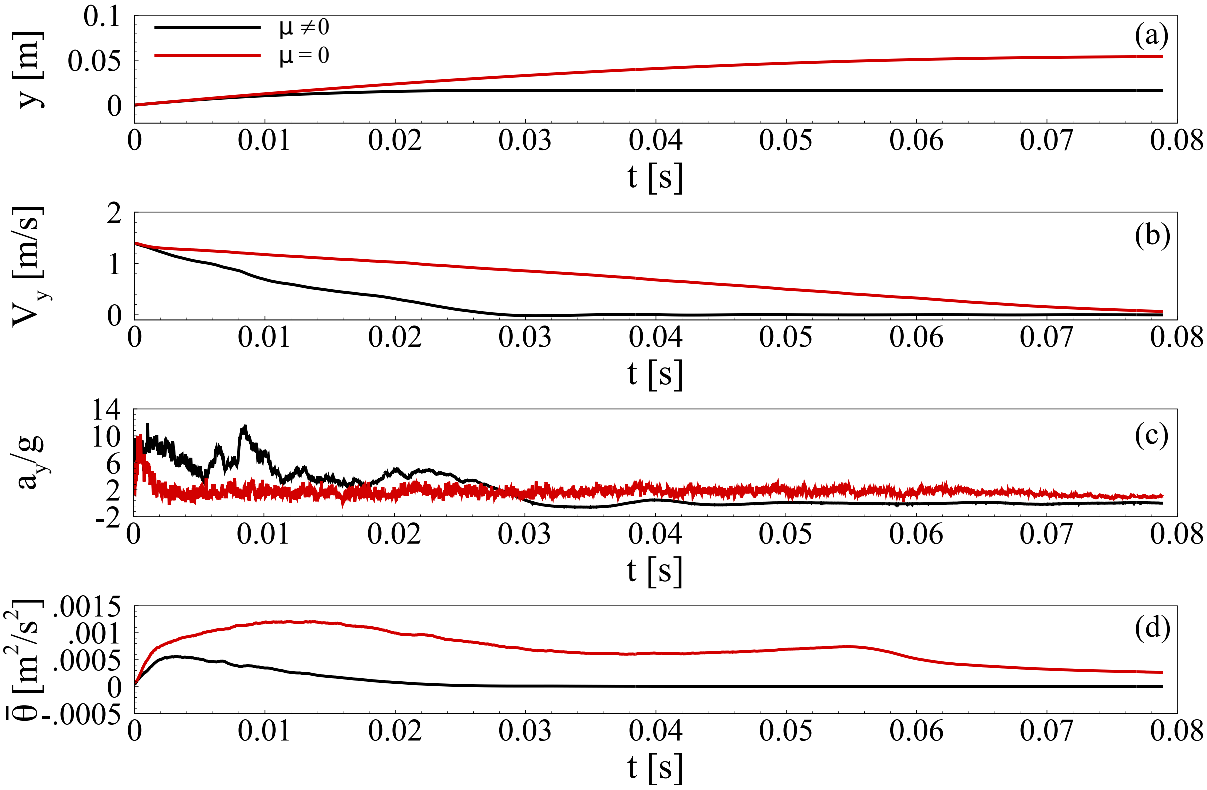

Figure 5.14 – Time evolution of (a) vertical position y of the projectile; (b) vertical velocity V_y of the projectile; (c) vertical deceleration a_y of the projectile, normalized by g; and (d) space-averaged granular temperature $\bar{\theta}$ considering all grains. The red line corresponds to frictionless objects (μ = 0) and the black line to grains with friction ($\mu \neq 0$). ϕ = 0.554 and h = 1 m. Images taken from (Carvalho *et al.*, 2023b).

2D case. In our case, the simulations are 3D and wall effects are much less pronounced. Our results are important for deciding on the pertinence of the grain-grain friction and, therefore, for modeling and computing cratering in various scenarios.

5.1.1.2.4 Rotating projectile (initial spin)

A question that has remained without investigation over the last decades, and that we scrutinize now, is the effect of the angular velocity of the projectile (rotational kinetic energy) on cratering. Our studies are motivated by the presence of spinning projectiles in natural and artificial processes, such as the fall of asteroids, weapon projectiles (spin imposed in order to stabilize their ballistic trajectory) and seeds (which acquire spin during their fall). To investigate this question, we carried out simulations where we imposed an initial angular velocity (initial spin) $\vec{\omega}$ to the projectile impacting the bed and computed the crater diameter, penetration

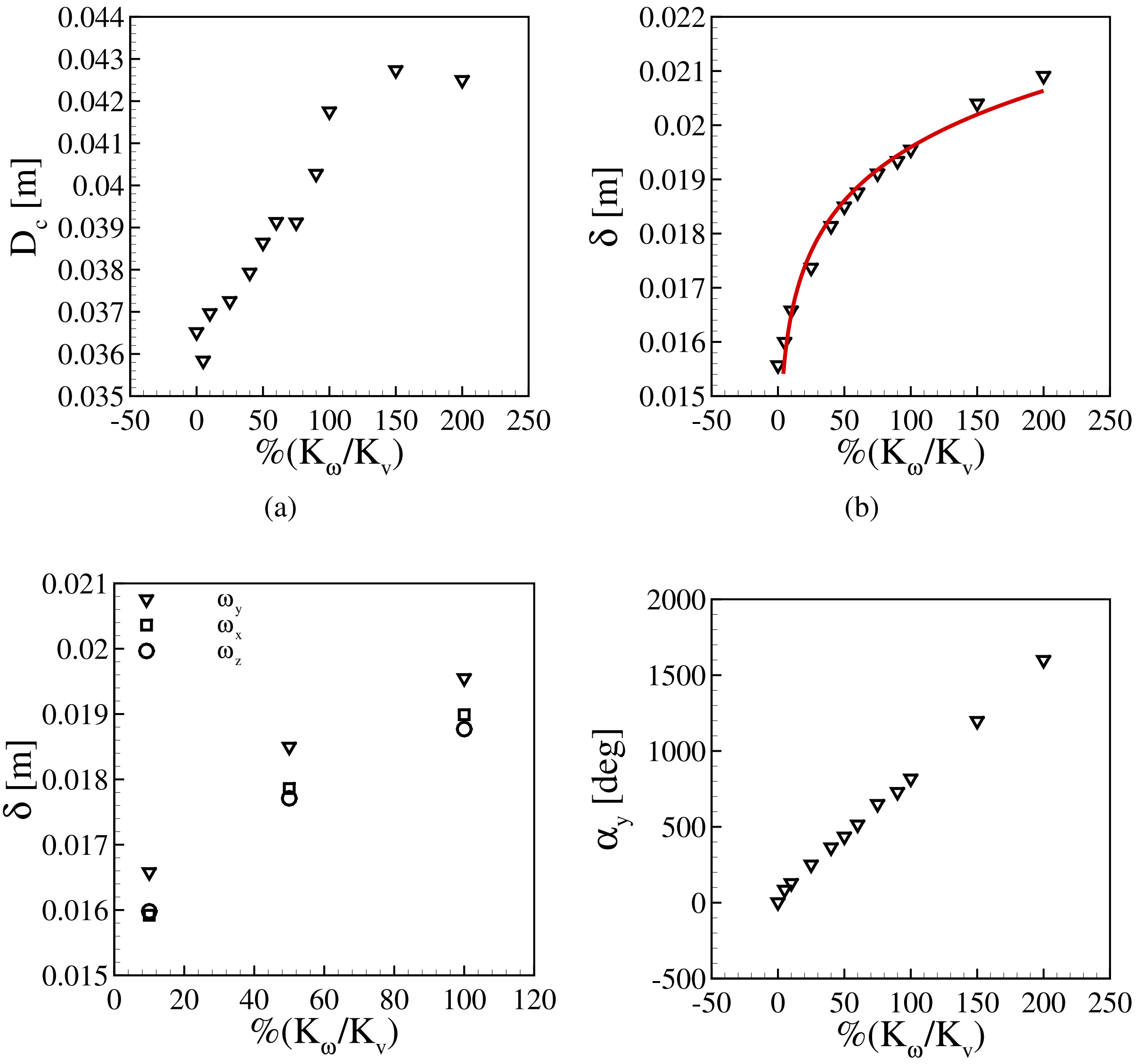

(a) (b)

(c) (d)

Figure 5.15 – (a) Crater diameter D_c as a function of the ratio of rotational to linear kinetic energies, K_ω/K_v, in percentage, by considering only ω_y. (b) Penetration depth δ as a function of K_ω/K_v by considering only ω_y, and (c) for either ω_x, ω_y or $\omega_z \neq 0$. (d) Total revolution angle (in degrees), α_y, that the projectile effectuate after colliding with the bed as a function of K_ω/K_v (by considering only ω_y). In figures (a) to (d), $\phi = 0.554$ and $h = 0.1$ m. In figure (b), the line corresponds to $\delta = 0.014 + (K_\omega/K_v)^{0.075}$. Images taken from (Carvalho *et al.*, 2023b).

depth and projectile dynamics for different $\vec{\omega}$ in terms of magnitude and direction. The angular velocity $\vec{\omega}$ was imposed only as an initial condition, the projectile being free to rotate or stop rotating in any direction after the impact has taken place (there was no constraint), so that it went to zero as the projectile finished penetrating the bed (excepting for frictionless solids, as explained next). In the following, we consider ω_x, ω_y and ω_z the x, y and z components of

$\vec{\omega}$, respectively, and $K_v = (1/2) m_p V_p^2$ and $K_\omega = (1/2) I |\vec{\omega}|^2$ the linear and rotational kinetic energies of the projectile, where $I = (2/5) m_p (D_p/2)^2$ is its moment of inertia.

Figures (5.15)a and (5.15)b show, respectively, the crater diameter D_c and penetration depth δ as functions of the ratio of rotational to linear kinetic energies, K_ω/K_v, by varying only the y component of the angular velocity, ω_y (both ω_x and ω_z were set to zero). We observe that both D_c and δ vary with the rotation rate of the projectile, with D_c and δ increasing by roughly 20 and 40%, respectively, when K_ω/K_v varies from zero to two. Apparently, part of the rotational kinetic energy further agitates the bed, helping to dislodge more grains and excavate it. Figure (5.16)a compares the granular temperatures for rotating and non-rotating cases, where we notice that the rotating case maintains a higher degree of fluctuation.

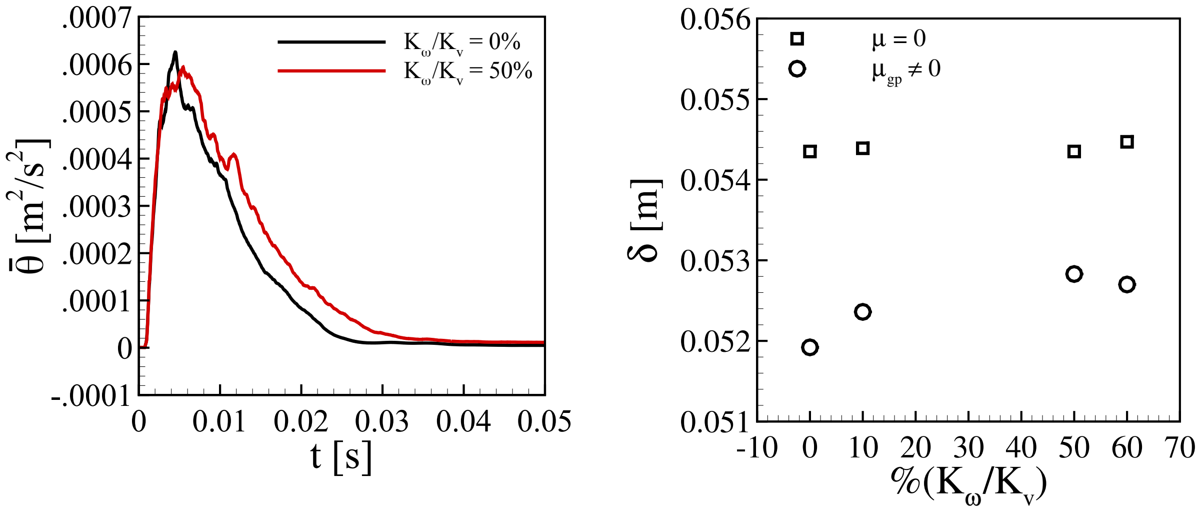

(a) (b)

Figure 5.16 – (a) Time evolution of the space-averaged granular temperature $\bar{\theta}$ considering all grains. The red line corresponds to a rotating projectile (K_ω/K_v = 0.5) and the black line to a non-rotating projectile. ϕ = 0.554 and h = 1 m. (b) Penetration depth δ as a function of K_ω/K_v by considering only ω_y, for frictionless grains. In the figure, squares correspond to simulations where all friction coefficients are zero ($\mu = 0$), and circles to those where only the grain-projectile friction is nonzero ($\mu_{gp} \neq 0$). Images taken from (Carvalho *et al.*, 2023b).

In addition, we notice that, while a clear fitting cannot be found for D_c (it seems to increase and then reach a plateau for $K_\omega/K_v > 1$, but we cannot assert it for the moment), δ follows a curve as in Eq. (5.10),

$$\delta \sim (K_\omega/K_v)^n , \tag{5.10}$$

where n = 0.075. In terms of the total rotation α_y that the projectile effectuate after colliding with the bed, Fig. (5.15)d shows a linear variation with K_ω/K_v. In order to investigate the effect of the direction of $\vec{\omega}$ on the penetration depth δ, we set either ω_x, ω_y or ω_z to a nonzero value for K_ω/K_v equal to 10, 50 and 100%. This is presented in Fig. (5.15)c, which shows that in all cases δ follows the same trend with K_ω/K_v, but with higher values for ω_y (by symmetry, ω_x and ω_z are equivalent).

In the specific case of frictionless solids, δ reaches higher values and the projectile takes more time to stop rotating (when $\mu_{gp} \neq 0$) or even keeps rotating (when $\mu = 0$), though δ reaches a final value. Figure (5.16)b shows δ as a function of K_ω/K_v for frictionless grains. We note that for simulations with $\mu = 0$ the angular velocity of the projectile, ω_y, remained constant during our simulations, though δ reached a final (stable) value. For the simulations with $\mu_{gp} \neq 0$, ω_y decreased slowly in time, but δ reached a final value much before ω_y reached zero.

Concerning the general morphology of the crater, Fig. (5.17) shows top views of final forms resulting from projectiles with angular velocities in the y, x and z directions ($-\omega_y$, ω_x and $-\omega_z$, respectively). We observe strong asymmetries when either ω_x or ω_z are nonzero, with grains accumulating (forming the corona) mostly in the direction of the tangential velocity, since they are partially excavated by the projectile rotation.

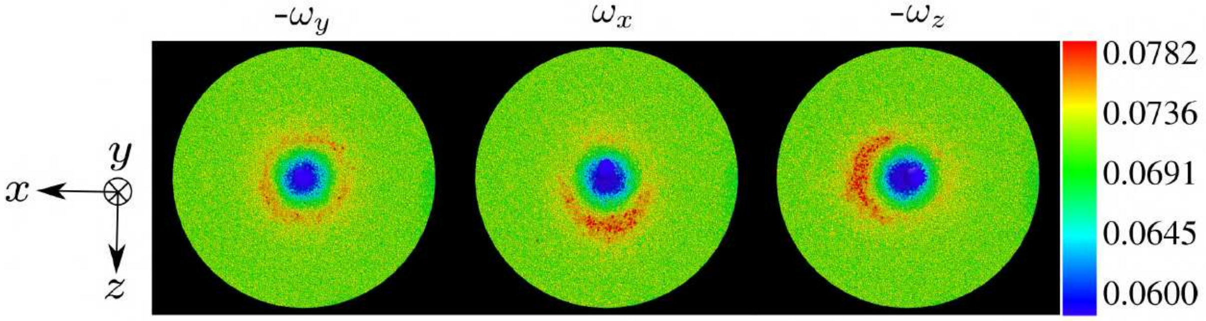

Figure 5.17 – Top views of final forms of craters resulting from projectiles with angular velocities in the y, x and z directions ($-\omega_y$, ω_x and $-\omega_z$, respectively). The colors correspond to $h_{bed} - y$ (the bed height measured from the bottom) and the values in the colorbar are in m. In this figure, K_ω/K_v = 1, ϕ = 0.554 and h = 0.1 m. Image taken from (Carvalho *et al.*, 2023b).

Finally, we measured the final rebound and time to reach the full stop for different values of K_ω/K_v, which we present in Fig. (5.18), Fig. (5.18)a showing the vertical displacement of the projectile during the rebound $\Delta y_{rebound}$ and Fig. (5.18)b the time evolution of the vertical component of the projectile velocity V_y. We observe in Fig. (5.18)a that $\Delta y_{rebound}$ is

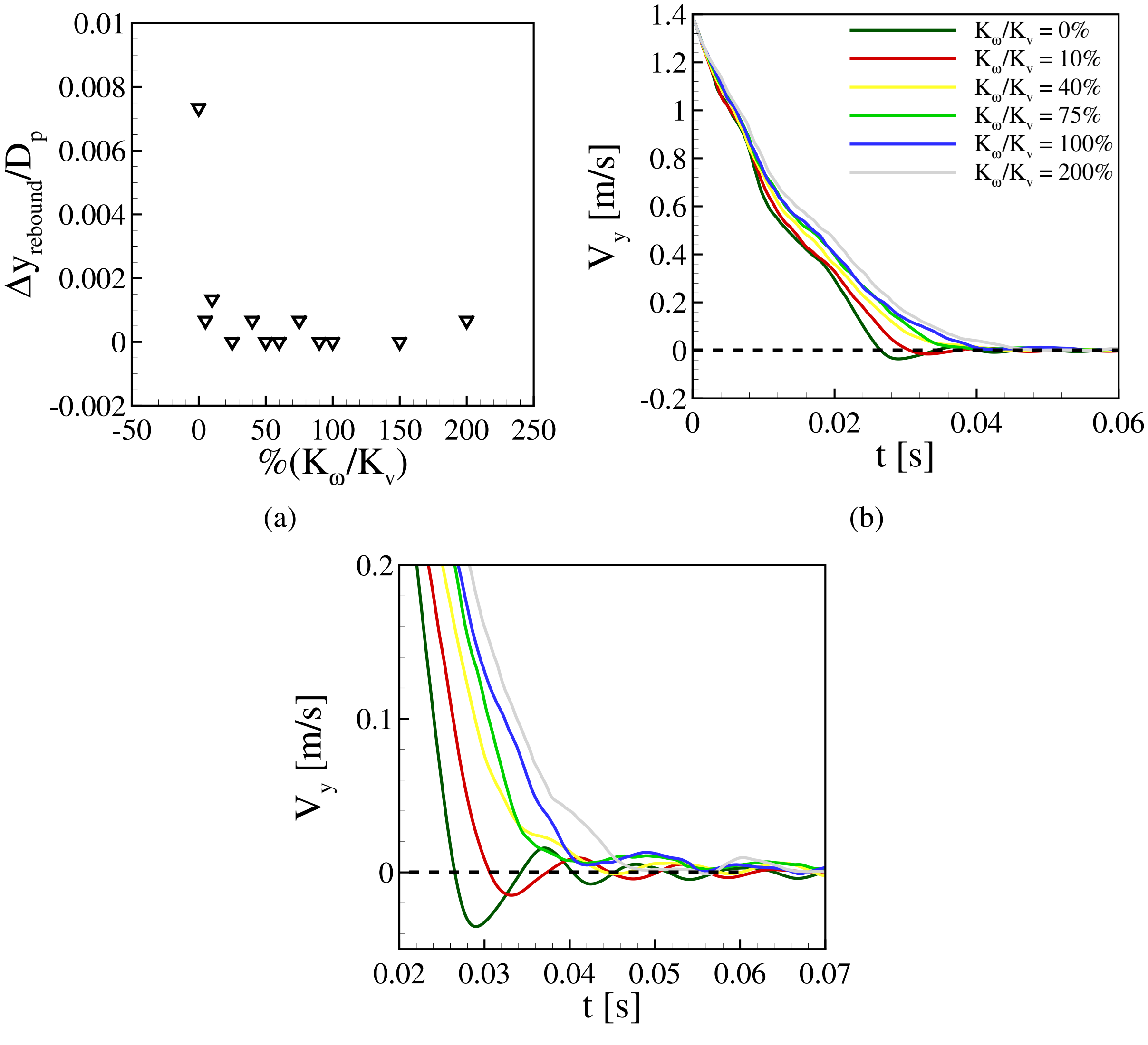

(a)

(b)

(c)

Figure 5.18 – (a) Vertical displacement during the rebound $\Delta y_{rebound}$, normalized by D_p, as a function of the ratio of rotational to linear kinetic energies, K_ω/K_v, in percentage. (b) Time evolution of the vertical component of the projectile velocity V_y for different values of K_ω/K_v and the entire simulation, and (c) zoomed in the region corresponding to the projectile rebound and final stop. In figures (a) to (c), we consider only ω_y, and ϕ = 0.554 and h = 0.1 m. Images taken from (Carvalho *et al.*, 2023b).

approximately zero for rotating projectiles, indicating that in this case the rebound is suppressed even for small angular velocities (K_ω/K_v = 0.1), as can be see in detail in Fig. (5.18)c. While the rebound is suppressed, Figs. (5.18)b and (5.18)c show that the stopping time t_c increases slightly with the angular velocity of the projectile. Figure (5.19) presents a full comparison between a rotating and non-rotating case, on which we observe the absence of the rebound for a rotating case.

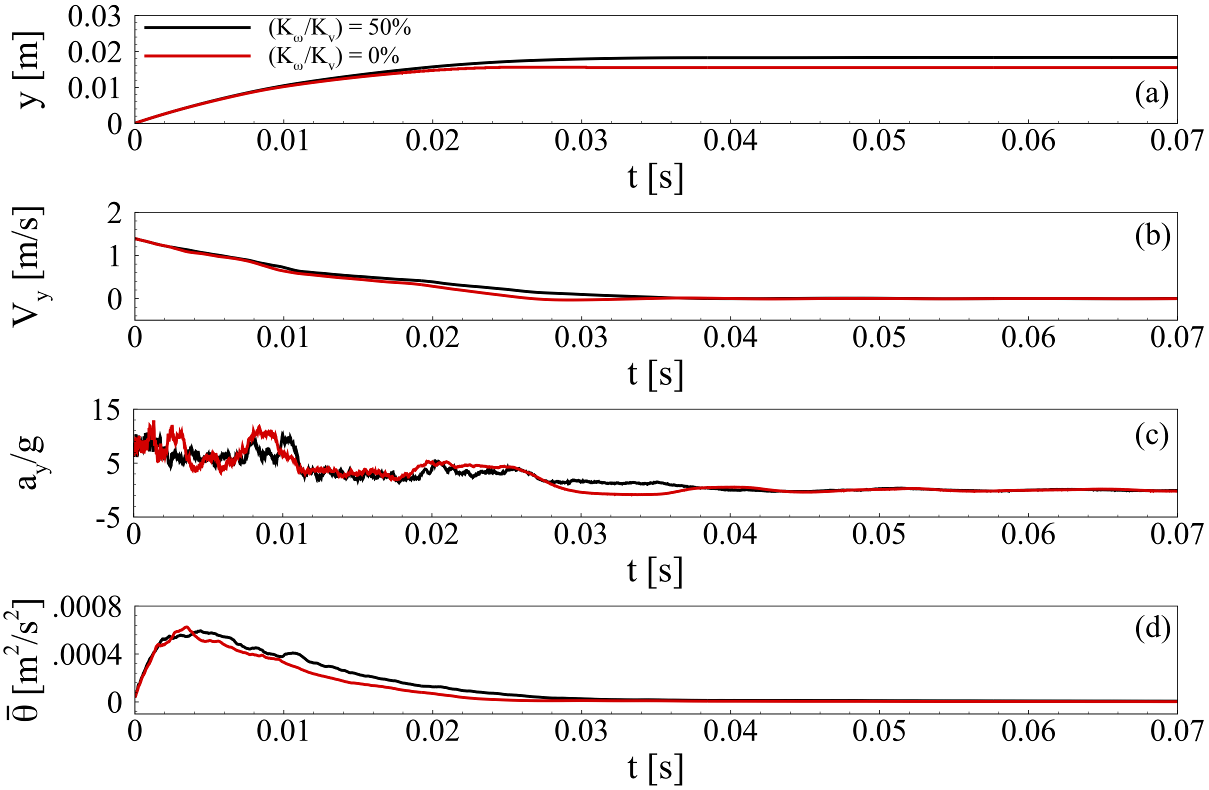

Figure 5.19 – Time evolution of (a) vertical position y of the projectile; (b) vertical velocity V_y of the projectile; (c) vertical deceleration a_y of the projectile, normalized by g; and (d) space-averaged granular temperature $\bar{\theta}$ considering all grains. The red line corresponds to a rotating projectile (K_ω/K_v = 0.5) and the black line to a non-rotating projectile. ϕ = 0.554 and h = 1 m. Images taken from (Carvalho *et al.*, 2023b).

Finally, Tab. (B.1) in Annex B summarizes results obtained for rotating projectiles with different angular velocities $\vec{\omega}$.

In summary, we investigated numerically the formation of craters by an object impacting a granular bed, and concentrated our efforts into questions that were still open or to be investigated, such as the effects on cratering of the packing fraction of beds, solid friction of grains, and initial spin of projectiles. We found that the packing fraction ϕ does not affect the crater diameter D_c, both in terms of magnitude and functional relation with the drop distance H, while the depth δ reached by the projectile is highly influenced by ϕ. By observing a lack of consensus in the literature, with diverging correlations for $\delta(H)$, and based on our results for different packing fractions, we proposed an *ad hoc* scaling law that collapsed our data and indicates that some of the existing $\delta(H)$ correlations may be turned universal by considering ϕ. For the projectile dynamics, we showed that it presents a high dependency on ϕ, and explained the final rebound as the result of a faster de-fluidization on the front (bottom) than on the rear (top) of the projectile. We also showed that both the morphology of craters and the projectile dynamics are highly affected by the presence of fricionless grains (both D_c and δ increase with the absence of friction, a_y oscillates around a constant value during great part of the penetration, and the projectile rebound is suppressed), evidencing the importance of grain-grain friction in models and computations. Finally, we revealed how D_c and δ increase with the initial spin (angular velocity) $\vec{\omega}$ of the projectile, and that the final rebound is suppressed by $\vec{\omega}$. Our results represent a new step toward understanding the mechanics of impact cratering in granular matter.

In the next section (Sec. 5.1.2), we investigate numerically some aspects of the dynamics behind the cratering process when the projectile is formed as an aggregate (cohesive) of smaller particles.

5.1.2 Impact of a cohesive projectile (aggregate)

This section (Sec. 5.1.2) reproduces material from Douglas D. Carvalho, Nicolao C. Lima, and Erick M. Franklin, "Impact craters formed by spinning granular projectiles", Phys. Rev. E **108**, 054904 (2023), with permission from the American Physical Society (Carvalho *et al.*, 2023a).

Even though previous studies explained important aspects of impact cratering, many questions remain open. One of them concerns the mechanics of cratering for spinning aggregates impacting a granular ground. In this specific case, close to impacts observed in nature, the total or partial collapse of projectiles can engender different crater structures, explaining some of the crater shapes observed in nature and how materials from the projectile spread below and over the ground. This section inquires into these questions. For that, we carried out 3D DEM computations of spinning granular projectiles (aggregates) impacting onto a bed consisting of cohesionless grains, for different bonding stresses (between the projectile's grains), initial spins and initial heights, in accordance to the methodology presented in Sec. 3.1.2, with the additional modeling of Sec. 3.1.2.2. In summary, we show that, as the bonding stresses decrease and the initial spin increases, the projectile's grains spread farther from the collision point, and, in consequence, the crater shape becomes flatter, with peaks around the rim and in the center of craters. In addition, we found that the penetration depth of rotating projectiles varies with their angular velocity and degree of collapse (number of detached particles), but not necessarily with the bonding stresses, indicating that under high spinning velocities the excess of breaking energy contributes only for the larger spreading in the horizontal plane and formation of peaks. Our results shed light on the different shapes of craters found on planets and moons, as well as on the distribution of the projectile material below and over the ground.

5.1.2.1 Numerical setup

The numerical domain consisted of: (i) $N \sim 10^6$ spheres with diameter 0.6 mm $\leq d \leq$ 1.4 mm following a Gaussian distribution and fixed density ρ = 2600 kg/m^3, which formed a granular bed in a cylindrical container [the distribution of diameters used in the simulations is shown in Tab. (5.5)]; and (ii) N_p = 1710 spheres with d_p = 1 mm and ρ_p = 15523 kg/m^3 bonded together [please check Fig. (3.1)b], which formed a round projectile with total diameter D_p = 0.015 m and bulk density $\rho_{p,bulk}$ = 7865 kg/m^3 (packing fraction ϕ_p = 0.507). A scheme of the numerical setup and an image of the granular projectile are shown in Fig. (5.20)a and (5.20b), respectively.

Prior to each simulation, around 10^6 grains (bed spheres) were let to fall freely and settle, and grains that were above that height were deleted in order to have a horizontal surface (around 10^4 grains were removed), the number N then depending on the initialization (being always $\sim 10^6$). With that, we obtained a granular bed with diameter D_{bed} = 125 mm, height h_{bed} = 76.5 mm, and packing fraction ϕ = 0.554. For the projectile, the value of ρ_p assured that the agglomerated material had the same size and mass of solid projectiles investigated in (Carvalho *et al.*, 2023b), and we applied a given bonding stress σ_p to all grain-grain contacts. In our simulations, σ_p was modeled through a breakup-tension threshold, and we used either σ_p = 1×10^7, 5×10^7 or 1×10^{32} N/m^2 in order to investigate the effect of bonding stresses on cratering. The highest value was chosen to avoid the projectile collapse, and the others to have partial or total collapses. The material that bonds two or more particles together can be modeled in several ways (Guo *et al.*, 2013; Schramm *et al.*, 2019; Chen *et al.*, 2022a; Gong *et al.*, 2023). In this work, it acts as a spring and damper system, where the bonds can twist, bend, stretch and break due to both normal and tangential stresses. The damping system is based on Guo *et al.* (2013) (Guo *et al.*, 2013), whereas the bond normal force and the bending and torsional moments are determined using linear models. More details can be seen in Sec. 3.1.2.2, and validation and details of the used model can be found in Guo *et al.* (2013) (Guo *et al.*, 2013) and Schramm *et al.* (2019) (Schramm *et al.*, 2019).

Table 5.5 – Distribution of diameters for the settling grains: number of grains N_d for each diameter d.

d (mm)	0.6	0.8	1.0	1.2	1.4
N_d	21524	128125	643002	128053	21421

Table 5.6 – Properties of materials used in the simulations: E is Young's modulus, ν is the Poisson ratio, and ρ is the material density. The last column corresponds to the diameter of the considered object.

	Material	E **(Pa)**	ν	ρ **(kg/m^3)**	**Diameters (mm)**
Bed grains	Sand$^{(1)-(2)}$	0.1×10^9	0.3	2600	$0.6 \leq d \leq 1.4$
Projectile grains	-	0.2×10^{11}	0.3	15523	1.0
Bond material	-	0.2×10^{11}	0.3	-	0.1
Walls	Steel $^{(1)}$	0.2×10^{12}	0.3	7865	125

(1) Ucgul *et al.* (Ucgul *et al.*, 2014a; Ucgul *et al.*, 2014b; Ucgul *et al.*, 2015)

(2) Derakhshani *et al.* (Derakhshani *et al.*, 2015)

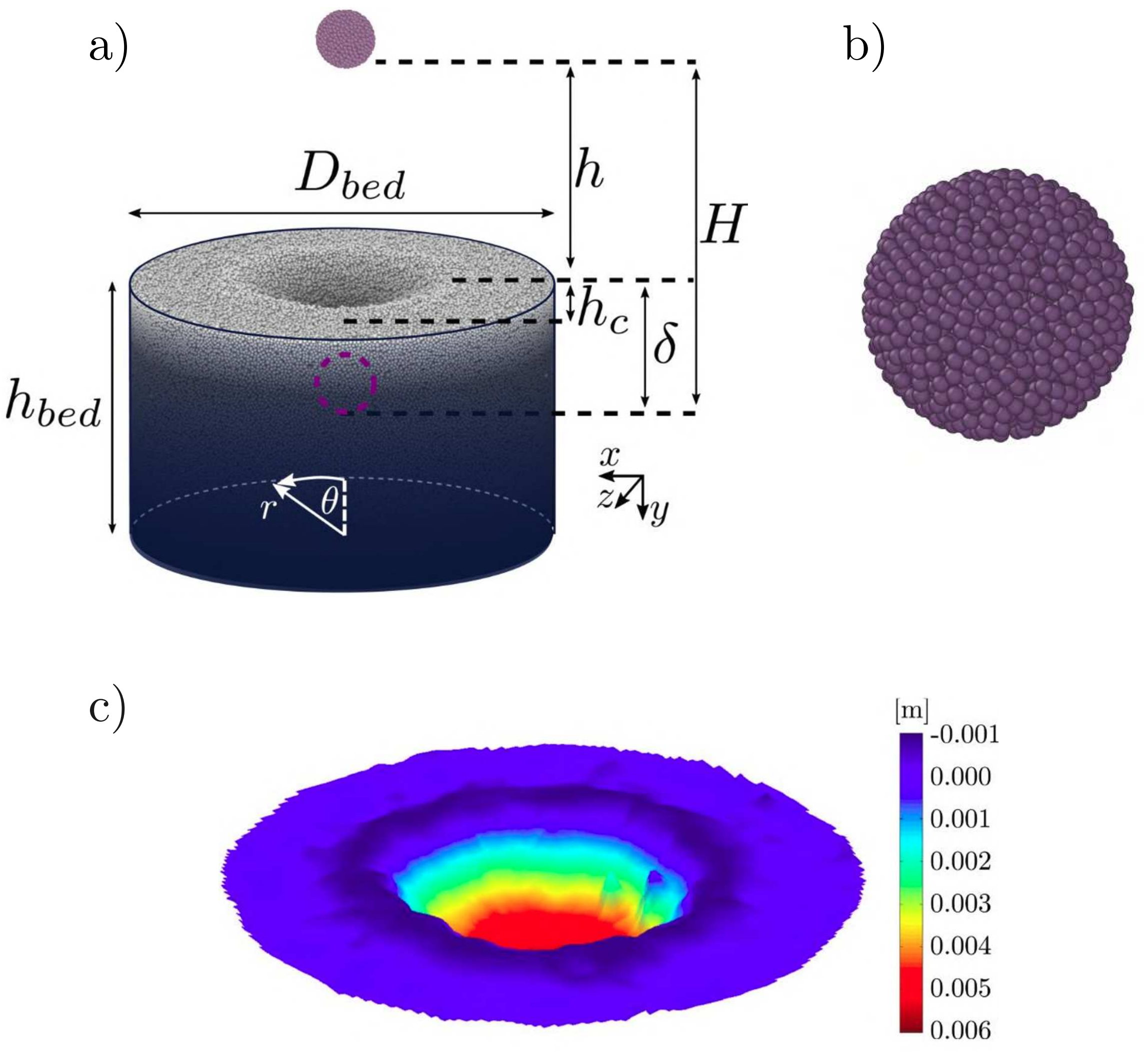

Figure 5.20 – (a) Layout of the numerical setup (the y coordinate points downwards, and, although shown on the bottom, the origin of the coordinate system is on the bed surface centered horizontally in the domain); (b) Detail of the granular projectile (aggregate); (c) Topography (elevation) of a crater formed by a spinning projectile consisting of bonded grains (we notice at least one internal peak close to the rim). In this figure, the bonding stresses are 10^7 N/m^2, the ratio between linear and angular kinetic energies is 1, and the colorbar shows the elevation from the undisturbed surface (pointing downwards). Images taken from (Carvalho *et al.*, 2023a).

The properties and coefficients of grains forming the bed and projectile were taken from the literature, and are listed in Tabs. (5.6) and (5.7) (together with those for the walls). In addition, we validated the friction coefficients listed in Tab. (5.7) by measuring the angles of repose obtained numerically, as shown in Sec. 5.1.1.1. Because we used spherical particles, we embedded angularity in the rolling friction μ_r (for typical sand, Derakhshani *et al.* (2015) (Derakhshani *et al.*, 2015) showed that μ_r = 0.3). The simulations began by imposing to the

Table 5.7 – Coefficients used in the numerical simulations.

Coefficient	**Symbol**	**Value**
Restitution coefficient (bed grain-bed grain)$^{(1)}$	ϵ_{gg}	0.60
Restitution coefficient (bed grain-projectile grain)$^{(1)}$	ϵ_{gp}	0.60
Restitution coefficient (projectile grain-projectile grain)$^{(2)}$	ϵ_{pp}	0.56
Restitution coefficient (bed grain-wall)$^{(1)}$	ϵ_{gw}	0.60
Restitution coefficient (projectile grain-wall)$^{(1)}$	ϵ_{pw}	0.60
Fiction coefficient (bed grain-bed grain)$^{(1),(3)}$	μ_{gg}	0.52
Friction coefficient (bed grain-projectile grain)$^{(1)}$	μ_{gp}	0.50
Friction coefficient (projectile grain-projectile grain)	μ_{pp}	0.57
Friction coefficient (bed grain-wall)$^{(1)}$	μ_{gw}	0.50
Friction coefficient (projectile grain-wall)	μ_{pw}	1.00
Coefficient of rolling friction (bed grain-bed grain)$^{(3)}$	$\mu_{r,gg}$	0.30
Coefficient of rolling friction (bed grain-projectile grain)$^{(1)}$	$\mu_{r,gp}$	0.05
Coefficient of rolling friction (projectile grain-projectile grain)	$\mu_{r,pp}$	0.30
Coefficient of rolling friction (bed grain-wall)$^{(1)}$	$\mu_{r,gw}$	0.05
Coefficient of rolling friction (projectile grain-wall)	$\mu_{r,pw}$	1.00

(1) Ucgul *et al.* (Ucgul *et al.*, 2014a; Ucgul *et al.*, 2014b; Ucgul *et al.*, 2015)

(2) Zaikin *et al.* (Zaikin *et al.*, 2017)

(3) Derakhshani *et al.* (Derakhshani *et al.*, 2015)

projectile a collision velocity V_p corresponding to the free-fall height h, i.e., $V_p = \sqrt{2gh}$. For the values used in our simulations, Froude numbers were within $3.8 \times 10^{-3} \leq \mathrm{Fr}^{-1} \leq 7.5 \times 10^{-2}$, and we used a time step $\Delta t = 1 \times 10^{-7}$ s, which corresponds to less than 10 % of the Rayleigh time t_R [Eq. (4.2)] (Derakhshani *et al.*, 2015). Figure (5.20)a shows a layout of the numerical setup, and animations showing impacts and cratering are available in <https://journals.aps.org/pre/supplemental/10.1103/PhysRevE.108.054904>. The numerical setup of our simulations, output files, and scripts for post-processing the outputs are available in an open repository (Lima *et al.*, 2023).

5.1.2.2 Results and discussion

Figure (5.21) shows top view images of the final position of grains for non-rotating and rotating projectiles with different bonding stresses σ_p. The bonding stresses are listed on the left, the corresponding elevation (from the undisturbed surface) of each grain is shown on the right, and initial heights h (non-rotating cases) and ratios of rotational to linear kinetic energies K_ω/K_v available at the impact (for spinning projectiles) are shown on the top. We used three different values of σ_p: $\sigma_p = 10^{32}$ N/m^2, which is strong enough to ensure that the agglomerate behaves as a single solid (no breaking) for the range of energies simulated; $\sigma_p = 5 \times 10^7$ N/m^2, for which the aggregate collapses partially within the ranges of energy simulated; and $\sigma_p = 1 \times$

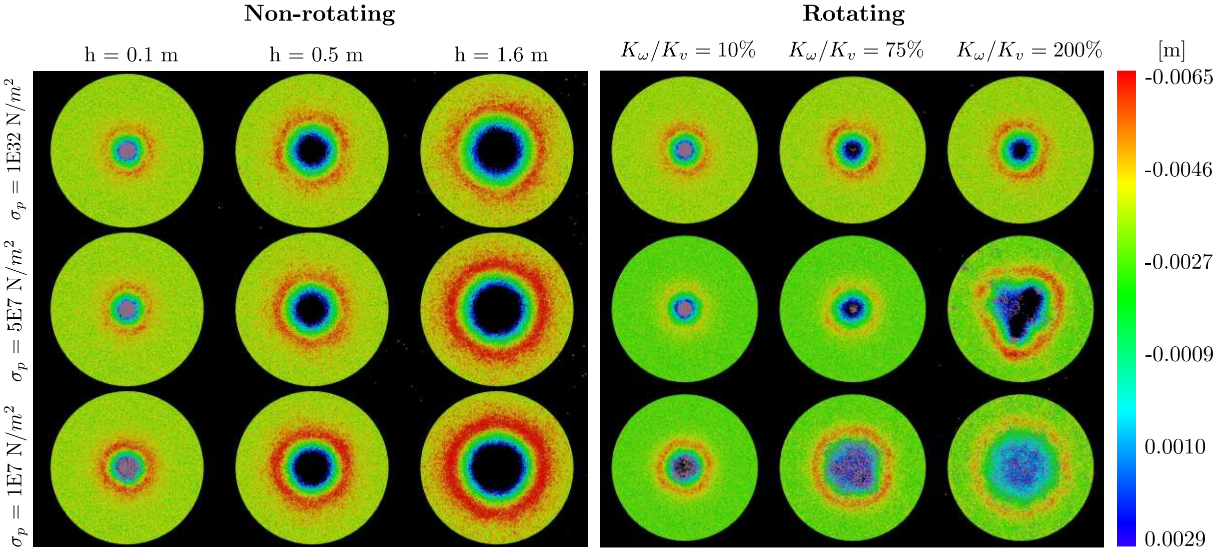

Figure 5.21 – Top view of final positions of grains, showing the final morphology of craters for non-rotating and rotating projectiles with different bonding stresses. For spinning projectiles, $h = 0.1$ m. The colorbar on the right shows the elevation of each grain from the undisturbed surface (coordinate pointing downwards). The same figure in gray scale is shown in Fig. (C.1), in Annex C. Images taken from (Carvalho *et al.*, 2023a).

10^7 N/m^2, for which the projectile collapses completely for the highest energies simulated. For the non-rotating case, we observe that the crater diameter D_c remains roughly constant and the height of the corona (rim) increases with the decrease in the bonding stresses, and, consequently, with the number of broken bonds [shown next in Fig. (5.28)c]. In the rotating case, craters are shallower, wider, and with lower rims when compared to the non-rotating case. This is caused by the stronger spreading of grains when the projectile has an initial spin, which we inquire further in the following. In addition, we observe that large asymmetries can appear for rotating cases in which partial breaking occurs, such as when $\sigma_p = 5 \times 10^7$ N/m^2 and $K_\omega/K_v = 200\%$ [the partial breaking is confirmed in Fig. (5.28)f]. The asymmetries come then from a small number of chunks spreading in the horizontal plane (when $\sigma_p = 5 \times 10^7$ N/m^2 and $K_\omega/K_v = 200\%$, three large pieces were spread by centrifugal effect. For a clearer view, Figs. (5.22) and (5.23) show snapshots of the final positions of grains originally in the projectile. A movie of the entire process can be found at <https://journals.aps.org/pre/supplemental/10.1103/PhysRevE.108.054904>.

Most of the aforementioned comments can be observed in Figs. (5.24) and (5.25), which show the topography (elevation) of the final craters for non-rotating and rotating projectiles, respectively, for the same variations of the bonding stress and available energy of

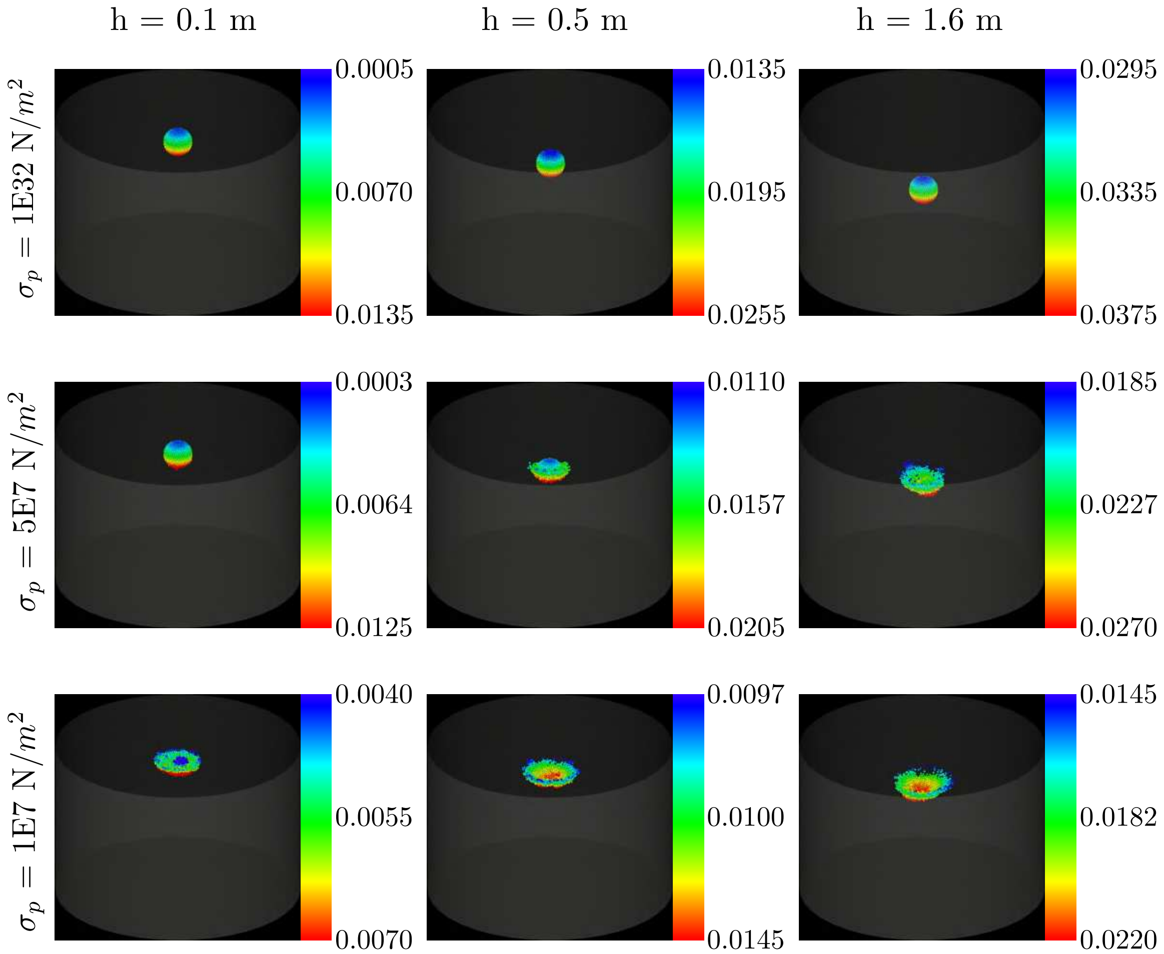

Figure 5.22 – Snapshots of the final positions of grains originally in the projectile, for the non-rotating cases. The colorbar on the right of each graphic shows the corresponding depth measured from the initial bed surface in m. Images taken from (Carvalho *et al.*, 2023a).

Fig. (5.21). Although variations of D_c are easier observed in Fig. (5.21), Figs. (5.24) and (5.25) allow for easier and direct observations of the crater depth and the formation of small peaks (we note that the scales of figures are not the same). We notice that the crater shape becomes flatter, with peaks around the rim and in the center of craters as the bonding stresses decrease and the initial spin increases (although peaks can also appear in low-energy cases without fragmentation). Some of these observations are corroborated by Fig. (5.26), which shows profiles of the elevations of final craters for both non-rotating and rotating projectiles, with different bonding stresses. Profiles corresponding to different heights are superimposed for non-rotating cases and to different rotational energies for rotating cases, allowing direct comparisons. We observe that craters have higher diameters and lower depths when projectiles have large rotational energies and low bonding stresses, and that some oscillations appear in the region near the corona (cor-

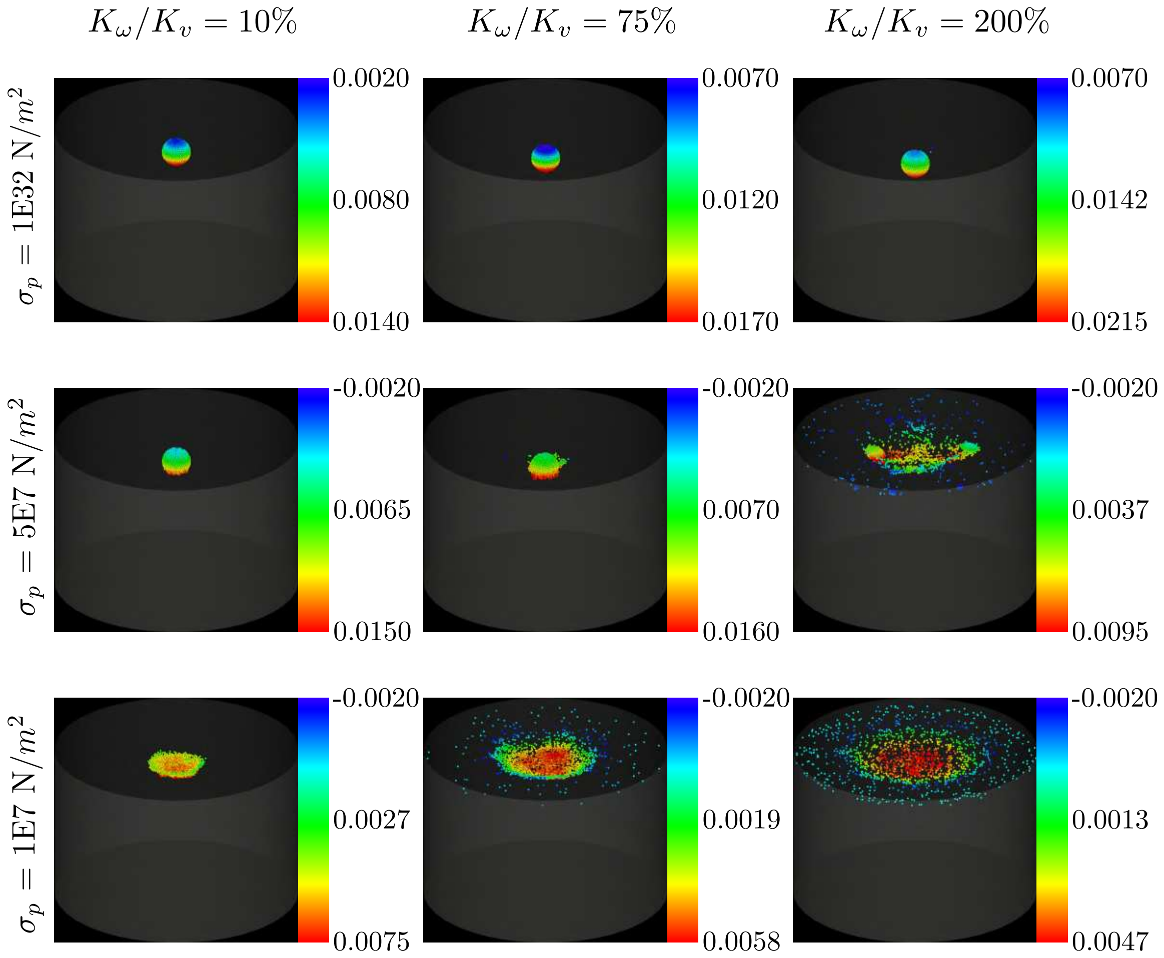

Figure 5.23 – Snapshots of the final positions of grains originally in the projectile, for the rotating cases. The colorbar on the right of each graphic shows the corresponding depth measured from the initial bed surface in m, and h = 0.1 m for all figures. Images taken from (Carvalho *et al.*, 2023a).

responding to peripheral peaks). We can observe a central peak in low-energy non-fragmenting cases, but they correspond to the projectile itself (which was not completely buried). Check Fig. (5.27) for profiles excluding the projectile's grains. Therefore, the final topographies indicate that the formation of central and peripheral peaks are due to the stronger spreading of grains when the projectile has higher rotational energies. In addition, the central peak can also be formed by a partially penetrating projectile when the available energy is relatively low.

In order to inquire further into the crater shape and the level of fracture of the projectile, we plot in Fig. (5.28) the crater diameter D_c, the penetration depth δ, and the percentage of broken bonds as functions of the initial height h or the ratio of rotational to linear kinetic energies K_ω/K_v for, respectively, non-rotating and rotating projectiles. The crater diameter D_c was determined as the diameter of a circle fitted over the corona, as shown in Fig. (5.3)d,

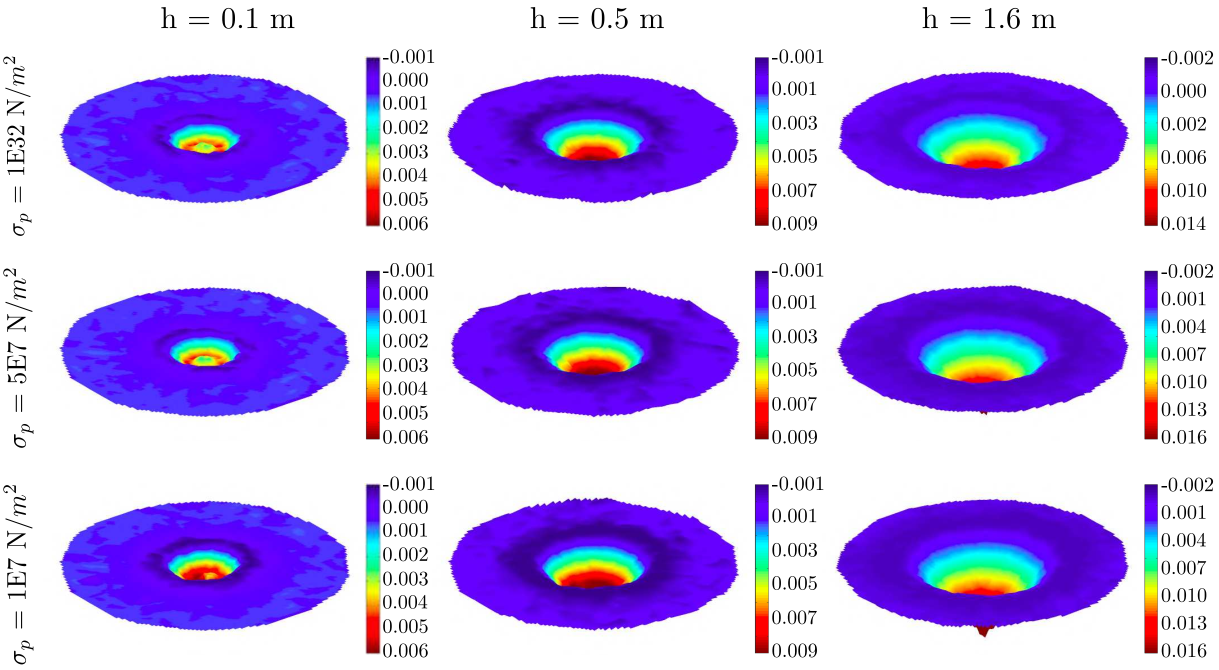

Figure 5.24 – Topography (elevation) of the final craters for non-rotating projectiles with different bonding stresses. The colorbar on the right of each panel shows the elevation from the undisturbed surface in m. The same figure in gray scale is shown in Fig. (C.2), in Annex C. Images taken from (Carvalho *et al.*, 2023a).

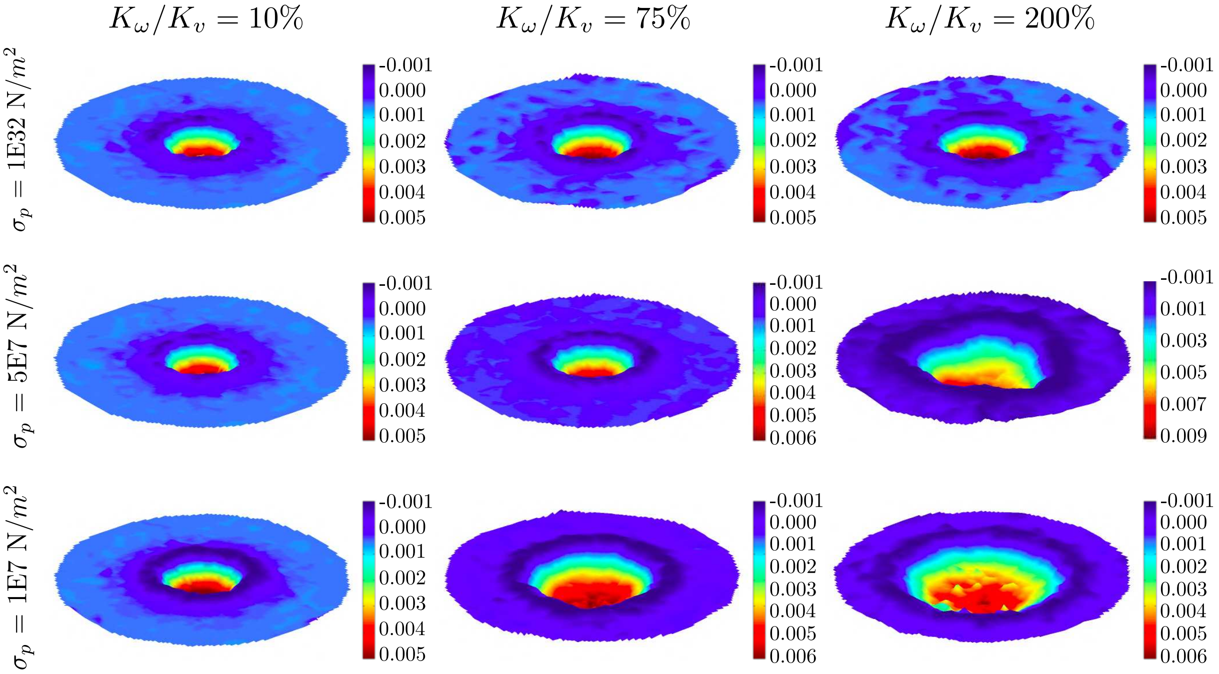

Figure 5.25 – Topography (elevation) of the final craters for rotating projectiles with different bonding stresses. The colorbar on the right of each panel shows the elevation from the undisturbed surface in m, and h = 0.1 m for all panels. The same figure in gray scale is shown in Fig. (C.3), in Annex C. Images taken from (Carvalho *et al.*, 2023a).

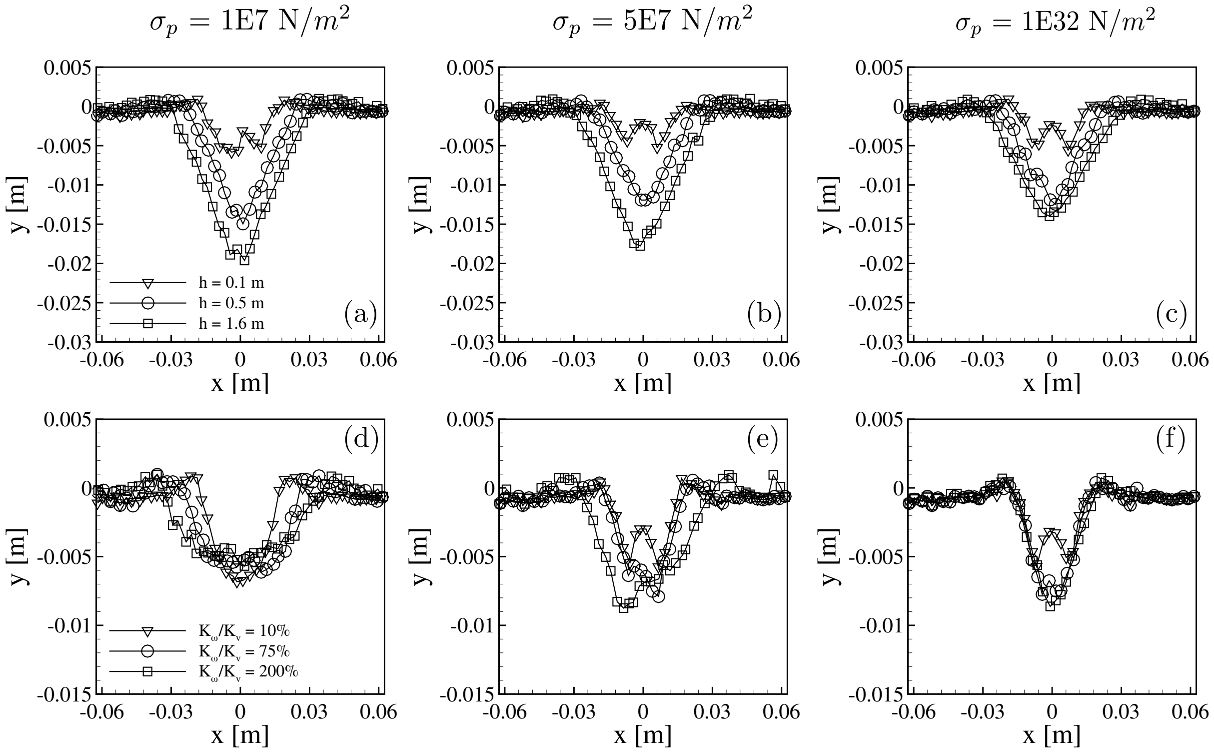

Figure 5.26 – Profiles of the elevations of final craters for both non-rotating and rotating projectiles, with different bonding stresses. The heights and rotational energies are shown in the figure key, and h = 0.1 m for non-rotating projectiles. All profiles were plot in a vertical plane of symmetry (therefore, include the crater center). These profiles include the projectile's grains. Figure (5.27) presents profiles excluding the projectile's grains. Images taken from (Carvalho *et al.*, 2023a).

and corresponds to an equivalent diameter in the case of asymmetric craters. Whenever the projectile collapsed, we computed δ based on the center of mass of the projectile's grains. For the non-rotating case, we observe that D_c [Fig. (5.28)a] is roughly independent of σ_p (for the levels of energy investigated here), varying as $D_c \sim h^{1/4}$, in agreement with Pacheco-Vázquez and Ruiz-Suárez (2011) (Pacheco-Vázquez; Ruiz-Suárez, 2011), although they measured the packing fraction of agglomerates instead of σ_p (to which we have access in our simulations). However, Pacheco-Vázquez and Ruiz-Suárez (2011) (Pacheco-Vázquez; Ruiz-Suárez, 2011) identified a discontinuity in D_c as a result of fragmentation, which depended on the projectile packing fraction. We did not observe the discontinuity, perhaps because our projectiles were lighter than those in Ref. (Pacheco-Vázquez; Ruiz-Suárez, 2011) (13.9 g in our simulations, against 33.0–45.5g in their experiments). The penetration depth δ [Fig. (5.28)b], on the other hand, depends on σ_p, varying with the percentage of broken bonds [Fig. (5.28)c]. In addition, the rate of change of δ with h decreases as h increases, and it is possible that a plateau is reached

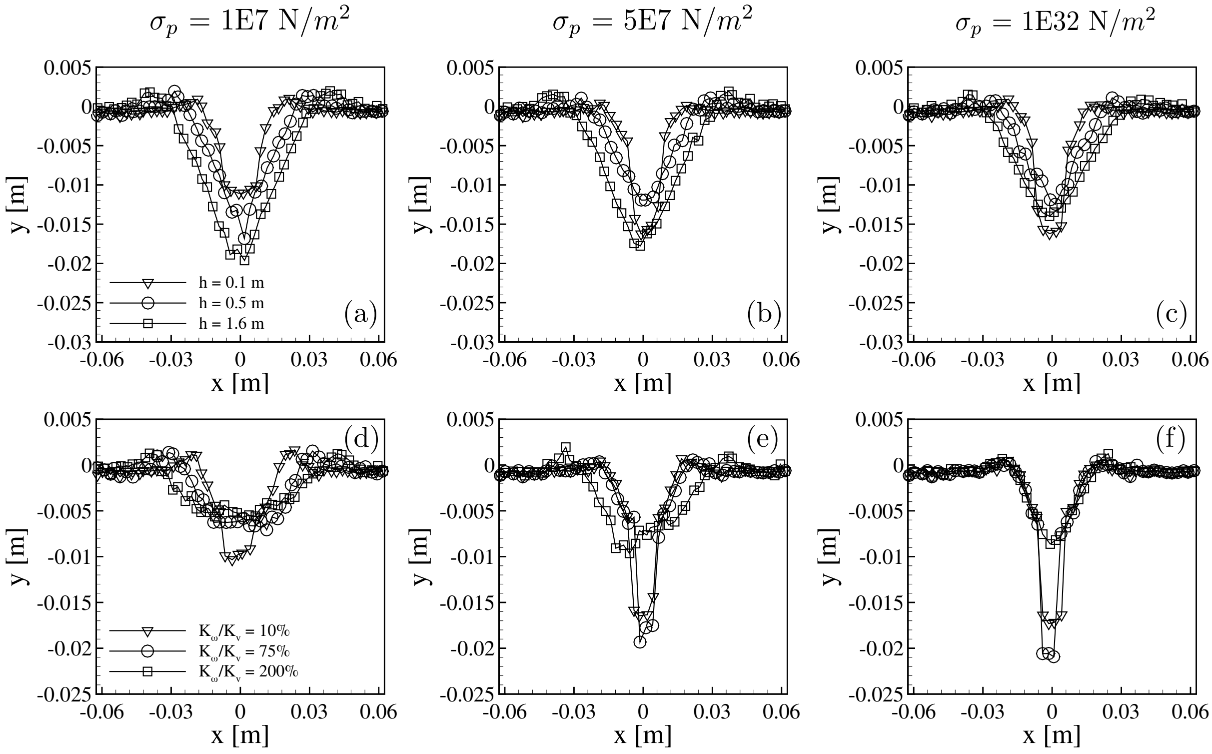

Figure 5.27 – Same as Fig. (5.26), however these profiles do not include the projectile's grains. Images taken from (Carvalho *et al.*, 2023a).

for values of h higher than those simulated in this work. This would be in agreement with the results of Ref. (Pacheco-Vázquez; Ruiz-Suárez, 2011), but remains to be investigated further. For δ, Pacheco-Vázquez and Ruiz-Suárez (2011) (Pacheco-Vázquez; Ruiz-Suárez, 2011) also found a discontinuity resulting from fragmentation, which our simulations did not show. As stated for D_c, the absence of discontinuity is due, perhaps, to the lighter weight of our projectiles. For the rotating case, the situation is different: D_c varies strongly with σ_p [Fig. (5.28)d], and variations for δ are even stronger [Fig. (5.28)e]. Figure (5.28)d shows that D_c increases up to approximately 2 times when σ_p varies from the largest (non-breaking) to the lowest (breaking) values (for K_ω/K_v varying between 0 and 200%), and for moderate stresses (σ_p = 5 × 10^7 N/m^2) we notice that partial breaking makes D_c to deviate from the curve for the non-breaking case toward to that for the breaking case []which occurs for K_ω/K_v around 100% in Fig. (5.28)d]. The inverse behavior occurs for δ: it decreases by one order of magnitude when σ_p varies from the largest to the lowest value, with also partial breaking (σ_p = 5 × 10^7 N/m^2) leading to the breaking case as K_ω/K_v increases. Finally, Fig. (5.28)f shows that, indeed, the percentage of broken bonds is 0% for the largest σ_p, and 100% for the lowest σ_p when $K_\omega/K_v \geq 30\%$, while that for moderate σ_p evolves toward 100% for increasing K_ω/K_v. At the same time, values

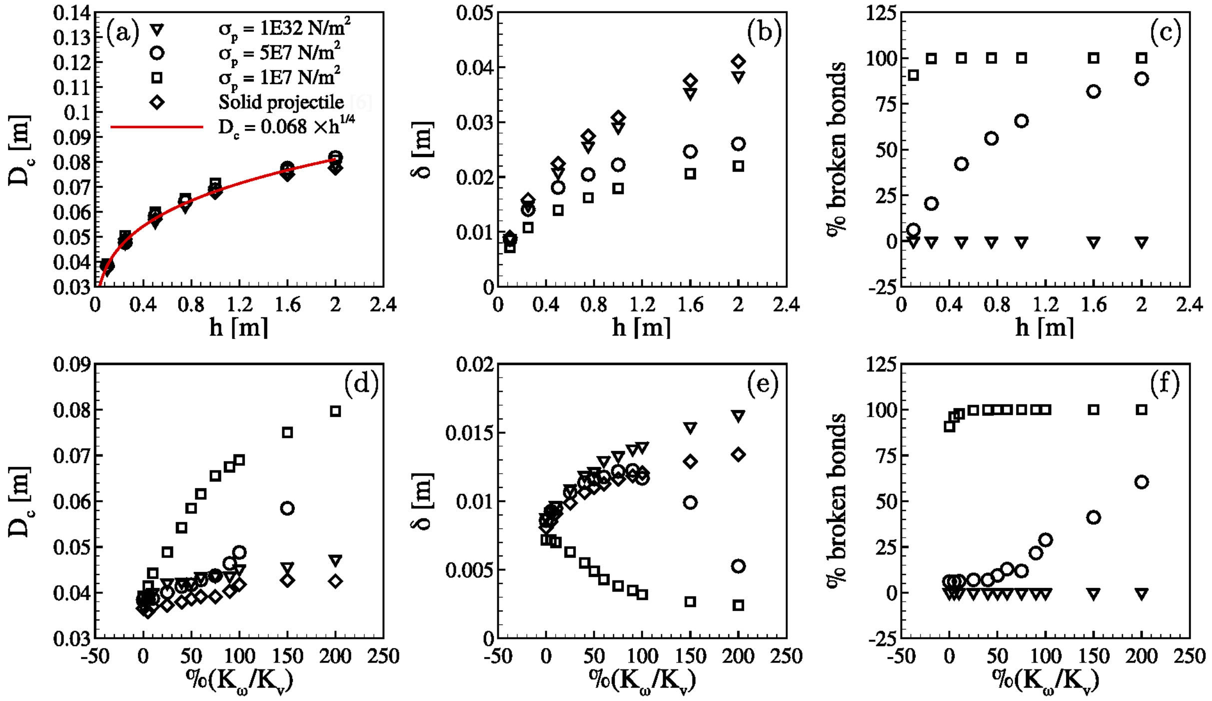

Figure 5.28 – (a) Crater diameter D_c, (b) penetration depth δ, and (c) the percentage of broken bonds as functions of the initial height h for a non-rotating projectile; panels (d), (e) and (f) show D_c, δ and the percentage of broken bonds as functions K_ω/K_v for spinning projectiles falling from h = 0.1 m, respectively. The graphics are parameterized by the bonding stresses (shown in the key of panel (a)), and the results for the solid projectile reported in Carvalho *et al.* (2023) (Carvalho *et al.*, 2023b) and showed in Sec. 5.1.1 are shown for reference. Images adapted from (Carvalho *et al.*, 2023a).

of δ for $\sigma_p = 5 \times 10^7$ N/m^2 evolve toward those for $\sigma_p = 1 \times 10^7$ N/m^2 [Fig. (5.28)e]. This implies that the penetration depth of rotating projectiles varies with their angular velocity and degree of collapse (number of detached particles), but not necessarily with the bonding stresses, indicating that under high spinning velocities the excess of breaking energy contributes only for the larger spreading in the horizontal plane and the formation of peaks.

After the impact has occurred, the projectile collapses if the bonding stresses are not strong enough to maintain the agglomerate integrity. In these cases, besides changing considerably the crater shape, the once agglomerated material is spread on or within the ground, over distances that depend on the initial height, bonding stresses and initial spin of the projectile. Understanding how this process occurs can help us, for example, to interpret whether materials found today under the ground have their origin on the ancient impact of asteroids, and how they are distributed, with important applications in geophysics and mining. Therefore, we inquire now into the dispersion of the projectile's grains.

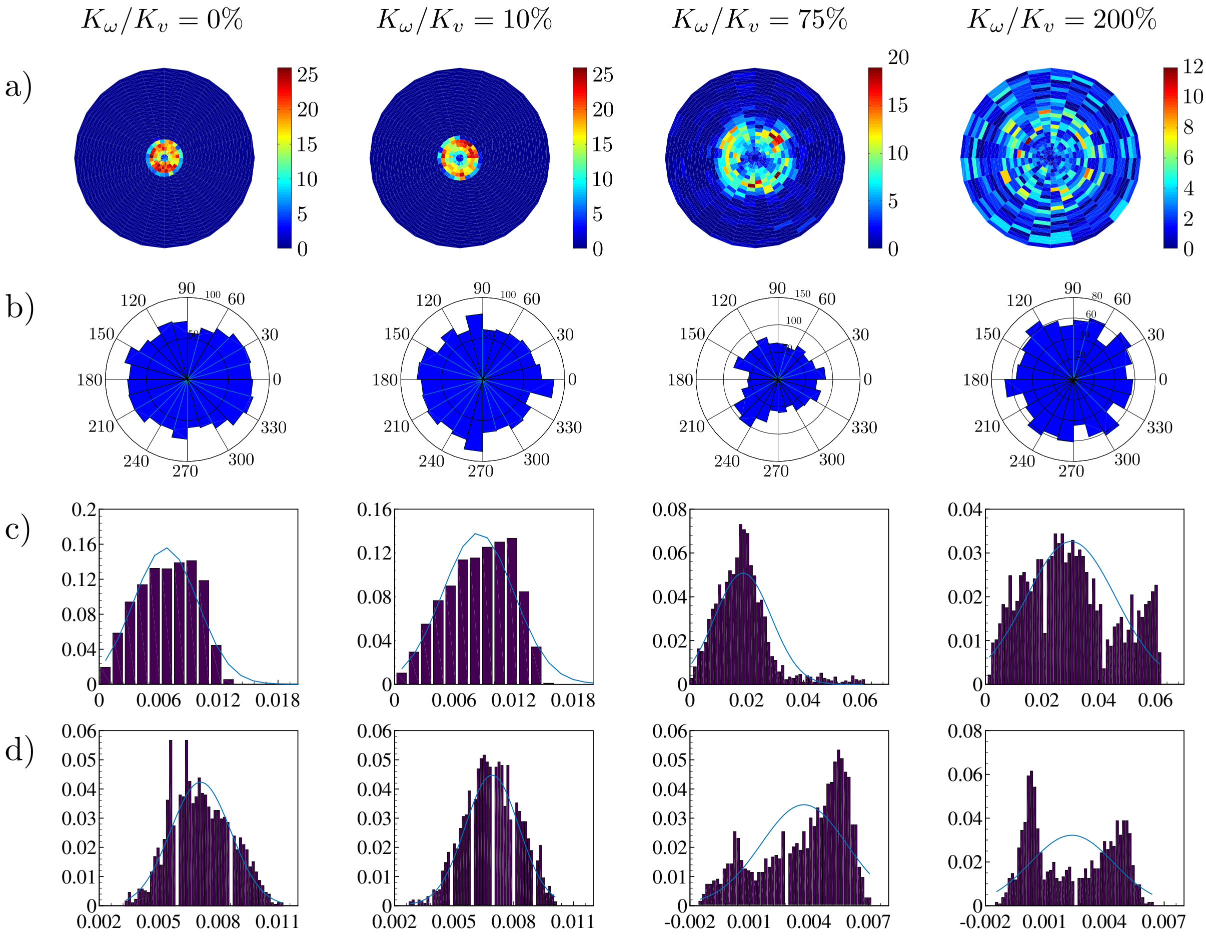

Figure 5.29 – Final positions the projectile's grains after the impact has taken place, for σ_p = 1 × 10^7 N/m^2 and different values of K_ω/K_v. From top to bottom: (a) Frequencies of occurrence of the projectile's grains in the r–θ plane (radius–angle plane, independent of the depth); (b) frequencies of occurrence of final positions in terms of the angle (all depths); (c) frequencies of occurrence of final positions in terms of radius (all depths); (d) frequencies of occurrence of final positions in the y coordinate (depths for all angles and radii). Images taken from (Carvalho *et al.*, 2023a).

Figure (5.29) shows the final positions of grains initially forming the projectile, for σ_p = 1 × 10^7 N/m^2 and different K_ω/K_v. The first row [Fig. (5.29)a] shows the frequencies of occurrence of the projectile's grains in the r–θ plane (radius–angle plane, independent of the depth), corresponding then to top views of the distributions of the projectile's grains (in the polar plane). We clearly observe that the projectile material reaches distances farther from the collision point as the rotational energy increases. In order to have more quantitative measurements, the second [Fig. (5.29)b] and third [Fig. (5.29)c] rows show the frequencies of occurrence of final positions in terms of the angle θ and radius r, for all depths, where the angles are given in degrees and the radius in m [see Fig. (2.1)c for θ and r]. We observe that in this weak-bond case the projectile's grains spread in a roughly symmetrical way along the angles, and distances reached in the radial direction increase with K_ω/K_v: the most probable values of the radius increase from approximately 0.007 m when K_ω/K_v = 0 to 0.03 m (one order of magnitude greater) when K_ω/K_v = 200%. Finally, the last row [Fig. (5.29)d] shows the frequencies of occurrence of final positions in terms of depth (all angles and radii). Interestingly, we observe that the most probable value decreases with K_ω/K_v, so that in average the projectile's grains tend to remain closer to the surface for higher spinning velocities, different from the behavior of solid projectiles (which reach deeper depths for increasing K_ω/K_v, as shown in Sec. 5.1.1.2.4). However, the depth distribution widens, so that the projectile's grains populate depths that spans over larger values, including negative ones corresponding to peaks or the corona. Snapshots of the final positions of grains originally in the projectile are shown in Figs. (5.22) and (5.23).

We note that we did not investigate here the effect of initial packing fractions on the dynamics of cratering (as done in Sec. 5.1). However, we measured how the bed packing fraction far from the collision point varies with the linear and rotational energies, for the different bonding stresses used. For that, we selected a 20-mm-height cylindrical region occupying the bottom of the cylindrical container (corresponding to 26% of the container) and measured the average packing fraction before and after the impact. For rotating projectiles, we found no change at all in the packing fraction, while negligible variations (increasing with h) were measured for non-rotating projectiles. The maximum variations were of 0.34%, 0.30% and 0.20% for σ_p = 10^7, 5×10^7 and 10^{32}, respectively, and h = 2 m. We also note that, under some conditions, the dynamics of both cratering and projectile fragmentation change with the stiffness of grains and bonds. Due to the presence of bonds, the effect of stiffness is rather complex and needs to be investigated further.

In summary, we investigated numerically how the projectile spin and cohesion lead to different crater shapes, and how the projectile's materials spread over and below the ground. We found that, as the bonding stresses decrease and the initial spin increases: (i) the projectile's grains spread radially farther from the collision point; (ii) the projectile's grains remain in average closer to the surface (lower penetration depths), but spread horizontally over longer distances, with some grains buried deep in the bed while others are above the surface populating peaks or the corona; (iii) as a consequence, the crater shape becomes flatter, with peaks around the rim and in the center of craters. In addition, we found that the penetration depth of rotating projectiles varies with their angular velocity and degree of collapse (number of detached particles), but not necessarily with the bonding stresses themselves, indicating that under high spinning velocities the excess of breaking energy contributes only for the larger spreading in the horizontal plane and formation of peaks. Our results represent a significant step for understanding how cratering occurs, helping us, for example, to interpret whether materials found today under the ground have their origin on the ancient impact of asteroids, and how they are distributed, with important applications in geophysics and engineering.

In the next section (Sec. 5.2), we investigate experimentally some consequences of spinning in the cratering process of a solid spherical projectile.

5.2 Experimental Investigation

This section (Sec. 5.2) reproduces material from Douglas D. Carvalho, Yann Bertho, Erick M. Franklin, and Antoine Seguin, “Penetration of a spinning sphere impacting a granular medium”, Phys. Rev. E **109**, 054902 (2024), with permission from the American Physical Society (Carvalho *et al.*, 2024a).

In this section, we investigate experimentally the impact dynamics of a sphere colliding with a granular bed, considering rotational effects, in accordance to the methodology presented in Sec. 3.2.3. In summary, we observe that the rotation has an influence on the penetration dynamics, increasing the sphere penetration as it rotates faster. Additionally, we develop a first-order model that takes the effect of spinning into account to describe our experimental observations. The resulting model can be used for estimating the depth reached by spinning projectiles, with important applications in agriculture, reforestation, civil constructions, and planetary exploration.

5.2.1 Experimental setup

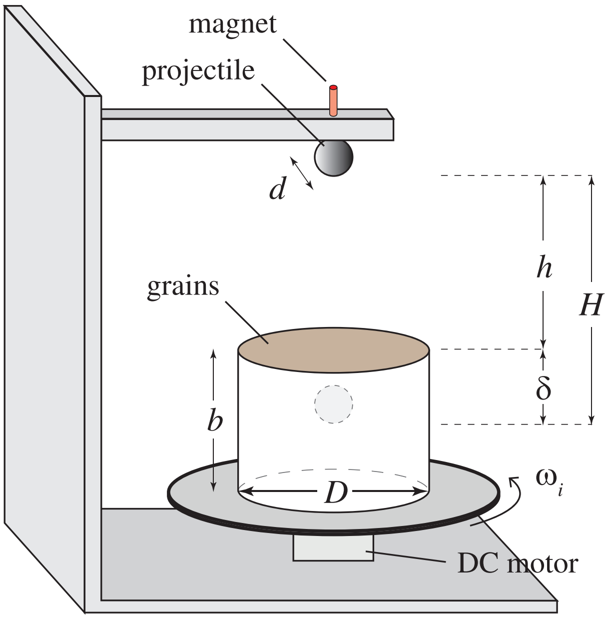

Figure 5.30 – Sketch of the experimental setup and notations introduced. Image taken from (Carvalho *et al.*, 2024a). Same image as in Fig. (3.14)a and shown here for the sake of completeness.

The penetration depth δ of a spherical projectile of diameter d and density ρ is investigated by dropping it onto a fine granular material confined in a cylindrical container of diameter D and height b [Fig. (5.30)]. The granular medium consists of slightly polydisperse glass spheres (diameter $d_g = 1 \pm 0.3$ mm and density $\rho_g \simeq 2.5 \times 10^3$ kg m^{-3}) with an initial packing fraction of $\phi \approx 0.6$.

Different materials and sizes of spherical projectiles were used to highlight the influence of the sphere density ρ and diameter d on the penetration depth δ. For a container of diameter $D = 140$ mm and height $b = 90$ mm, three different metallic projectiles were used, with diameters $d = 20$, 25, and 30 mm and densities $\rho \simeq 14920$, 8160, and 7710 kg m^{-3}, respectively. For a plastic projectile with diameter $d = 80$ mm and density $\rho \simeq 1150$ kg m^{-3}, two different cylindrical containers were used, with diameter $D = 400$ mm and heights equal to $b = 50$ mm and $b = 180$ mm. This allows us to keep a ratio $D/d \gtrsim 5$, avoiding any confinement effects (Seguin *et al.*, 2008). All materials properties used in this study are shown in Tab. (5.8). Note that for all cases studied here, the grain size d_g remains much smaller than the projectile diameter d, with $d_g/d \leq 0.05$.

Table 5.8 – Properties of materials used in the experiments: ρ is the material density and the last column shows the object's dimensions [diameters (d, d_g, and D) and height (b)].

	Material	**ρ (kg/m^3)**	**Dimensions (mm)**
Projectile	Metal (ferrous alloys)	8160 and 7710	d = 25 and 30
Projectile	Tungsten	14920	d = 20
Projectile	Polyamide	1150	d = 80
Grains	Glass beads	2600	$d_g = 1 \pm 0.3$
Walls	Plexiglass	-	i) $D = 140$ mm and $b = 90$ mm ii) $D = 400$ mm and $b = 50$ mm iii) $D = 400$ mm and $b = 180$ mm

The impact velocity is adjusted by varying the releasing height h from 2 mm to 2.17 m. Hence, the corresponding speed at impact v_i, given by $v_i = \sqrt{2gh}$, where g is the gravitational acceleration, varies from 0.2 to 6.5 m s^{-1}. Note that the projectile is released just above the center of the cylindrical container and falls along its axis.

As a means to investigate rotational effects and as described in Sec. 3.2.3, rather than releasing a rotating projectile to impact a nonrotating granular bed, it is experimentally more feasible to release a nonrotating projectile onto a rotating granular medium. In the absence of relatively strong centrifugal effects, these situations are equivalent, since they induce the same relative motion between the projectile and grains. Hence, the cylindrical container is placed on a rotating platform allowing its rotation around its main axis at a constant angular velocity ω_i in the range 0 – 10 rad s^{-1}. In the following, we will denote by an index "0" the quantities referring to the case without any rotation ($\omega_i = 0$).

5.2.2 Results and discussion

5.2.2.1 Impact without rotation

Figure (5.31) displays the penetration depth δ_0 as a function of the total distance $H_0 = h + \delta_0$ traveled by the projectile, for a motionless reservoir ($\omega_i = 0$) and four different projectiles of different diameters d and densities ρ.

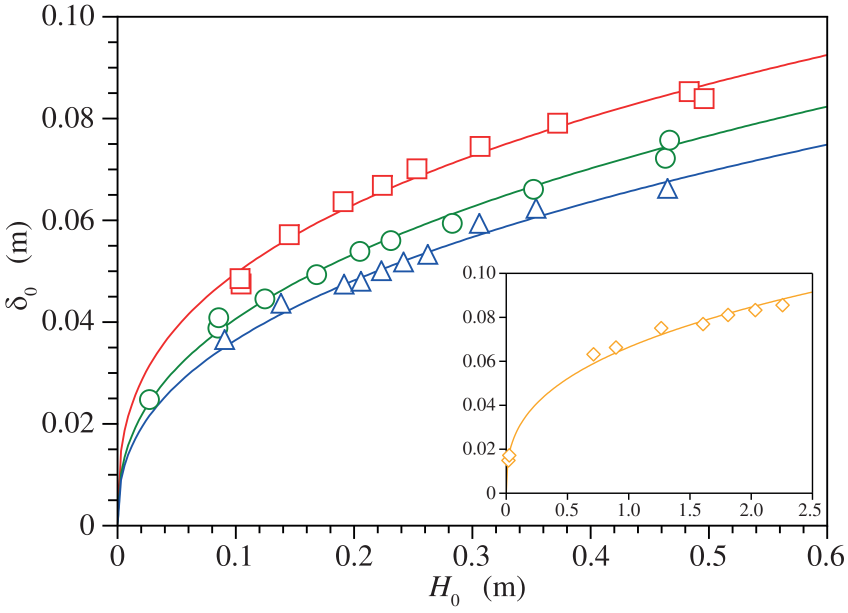

Figure 5.31 – Penetration depth δ_0 as a function of the total distance $H_0 = h + \delta_0$ traveled by the projectile for (□) $d = 20$ mm, $\rho \simeq 14920$ kg m^{-3}, and $55 \leq h \leq 412$ mm; (△) $d = 25$ mm, $\rho \simeq 8160$ kg m^{-3}, and $54.5 \leq h \leq 400$ mm; and (○) $d = 30$ mm, $\rho \simeq 7710$ kg m^{-3}, and $2 \leq h \leq 391$ mm. Inset: δ_0 as a function of H_0 for (◇) $d = 80$ mm, $\rho \simeq 1150$ kg m^{-3}, and $3 \leq h \leq 2170$ mm. Solid lines are the best fits of experimental data following $\delta_0 \propto H_0^{\alpha}$, with $\alpha = 0.35$, 0.40, 0.39, and 0.35 for increasing projectile sizes. Image taken from (Carvalho *et al.*, 2024a).

As expected, and as already observed in several studies, the bigger and/or denser the projectile, the deeper it sinks into the granular medium (Seguin *et al.*, 2008). Moreover, the greater the drop height, the deeper the penetration depth, with a power-law dependence close to $\delta_0 \propto H_0^{0.4}$ in good agreement with the empirical power laws proposed in previous studies (Uehara *et al.*, 2003b; Ambroso *et al.*, 2005; Bruyn; Walsh, 2004; Seguin *et al.*, 2008).

Let us then write the equation describing the dynamics of the projectile. The projectile experiences its own weight and a force resulting from its interactions with the granular medium, the latter having collisional and frictional origins that are proportional to v^2 and z, respectively (Katsuragi; Durian, 2007). Hence, the equation of motion for the projectile can be written as

$$\rho \frac{\pi d^3}{6} \frac{d^2 z}{dt^2} = \frac{\pi d^3}{6} \rho g - K_v \rho_g \phi d^2 v^2 - K_z \rho_g \phi g d^2 z, \tag{5.11}$$

where K_v and K_z are coefficients. Based on previous theoretical studies (Guo, 2018), we can define a dimensionless depth $\tilde{z}$ and a dimensionless time $\tilde{t}$ as

$$\tilde{z} = \frac{6\rho_g \phi}{\pi \rho d} z \qquad \text{and} \qquad \tilde{t} = \left(\frac{6\rho_g \phi g}{\pi \rho d} \right)^{1/2} t. \tag{5.12}$$

This allows one to build the dimensionless penetration depth $\tilde{\delta}_0$ and the dimensionless total distance $\tilde{H}_0 = \tilde{h} + \tilde{\delta}_0$, which are plotted in Fig. (5.32). We observe that all the experimental data collapse remarkably well on a single curve following the scaling law:

$$\tilde{\delta}_0 = A \tilde{H}_0^{\alpha}, \tag{5.13}$$

with $A \simeq 0.49$ and $\alpha \simeq 0.4$ [dashed line in Fig. (5.32)].

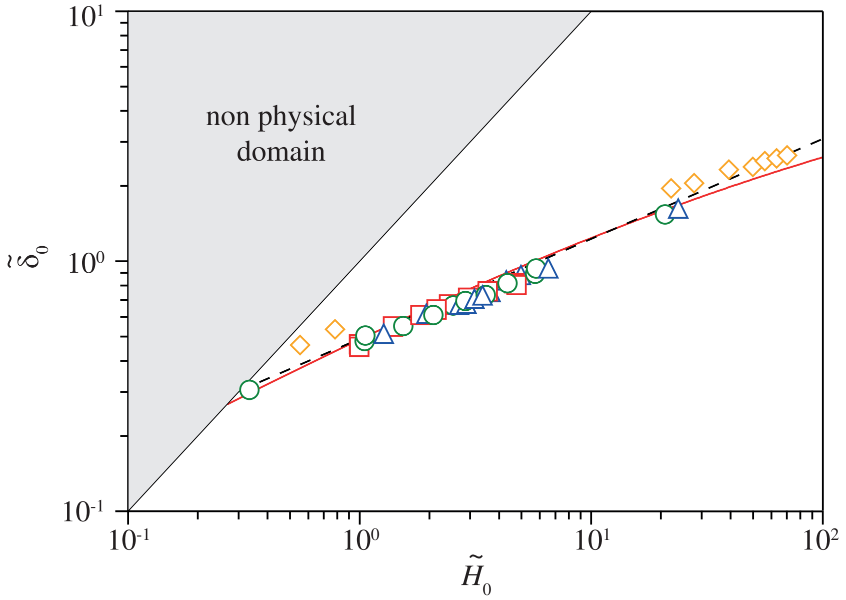

Figure 5.32 – Nondimensional penetration depth $\tilde{\delta}_0$ as a function of the nondimensional total distance $\tilde{H}_0 = \tilde{h} + \tilde{\delta}_0$ traveled by the projectile in log-log scales for the same data as in Fig. (5.31). (- - -) Best fit of the data, with $\tilde{\delta}_0 = 0.49\ \tilde{H}_0^{0.4}$. (—) Solution of Eq. (5.14), with $K_v = 0.39$ and $K_z = 7.2$. Image taken from (Carvalho *et al.*, 2024a).

By using the same scaling from Eqs. (5.12), Eq. (5.11) can be made dimensionless,

$$\frac{d^2 \tilde{z}}{d\tilde{t}^2} = 1 - K_v \left(\frac{d\tilde{z}}{d\tilde{t}} \right)^2 - K_z \tilde{z}, \tag{5.14}$$

and be solved numerically with the initial conditions $z = 0$ and $dz/dt = v_i = \sqrt{2gh}$ at $t = 0$, for the position and the impact velocity of the projectile, respectively, i.e., in dimensionless notations:

$$\tilde{z} = 0; \qquad \tilde{v}_i = \left(\frac{6\rho_g\phi}{\pi\rho g d}\right)^{1/2} v_i. \tag{5.15}$$

The final penetration depth $\tilde{\delta}_0$ corresponds to the depth where the velocity vanishes, the characteristic time of the penetration linked to the impact being typically:

$$T_v = \left(\frac{6\rho_g\phi g}{\pi\rho d}\right)^{-1/2}. \tag{5.16}$$

At this point, a small discussion on the definition of T_v should be addressed. We note that the more "natural" characteristic penetration time d/v_i is partially inappropriate. Two time scales can be extracted from Eq. (5.11) by considering independently its two force terms. By considering only the depth-dependent force term, the characteristic time is T_v. Whereas, by considering only the non-linear velocity-dependent force term, the characteristic time is $\rho d/(\rho_g v_i)$, which depends on the impact velocity v_i. The velocity-dependent force term decreases from its maximal value at impact to zero at the stop, whereas the depth-dependent force term increases from zero at impact to its maximal value at the stop. So, the timescale d/v_i is valuable for very low impact velocities, corresponding to small penetration depths. Conversely, the greater the impact velocity, the closer the characteristic time is to T_v, since d/v_i tends to zero. This topic has already been addressed in some previous studies supported with both experimental and numerical data (Katsuragi; Durian, 2007; Goldman; Umbanhowar, 2008; Seguin *et al.*, 2009).

Integrating Eq. (5.14) with the values $K_v = 0.39$ and $K_z = 7.2$ leads to the red solid curve shown in Fig. (5.32), which is very close to the empirical power-law fit (dashed line in the same figure). A large range of variations is reported in the literature for the K_v and K_z coefficients, depending on material properties (density, friction coefficient, shape) and/or packing fraction ϕ (Kang *et al.*, 2018; Katsuragi; Durian, 2013; Guo, 2018). In particular, note that we expect these coefficients to increase with ϕ, leading to a decrease of the penetration depth $\tilde{\delta}_0$ with ϕ (Umbanhowar; Goldman, 2010; Carvalho *et al.*, 2023b). For instance, based on the model proposed by Katsurati & Durian (2013) (Katsuragi; Durian, 2013), the coefficients K_v and K_z from Eq. (5.11) should be calculated as:

$$K_v = \frac{2\pi}{3}\mu; \qquad K_z = 2\pi\mu\Big(\frac{\rho}{\phi\rho_g}\Big)^{\frac{1}{2}}, \tag{5.17}$$

where μ is the internal friction coefficient, defined as the tangent of the angle of repose, reported by the authors to be $\mu \approx 0.45$ for glass beads (as is the case in our experiments). The predicted values of the coefficients for each one of the spheres used in our experiments are then:

Table 5.9 – Coefficients K_v and K_z calculated using Eq. (5.17).

ρ (kg m^{-3})	K_v	K_z
14920	0.9425	8.9173
8160	0.9425	6.5947
7710	0.9425	6.4102
1150	0.9425	2.4757

We note that the values of K_v are a bit higher than that used in the manuscript. As for K_z, the value used here is very close for the spheres with densities $\rho = 8160$ kg m^{-3} and $\rho = 7710$ kg m^{-3}, a bit higher for the sphere with $\rho = 1150$ kg m^{-3} and smaller for that with $\rho = 14920$ kg m^{-3} [for small impact speeds and low density projectiles, the shape of the projectile during penetration should be considered (Katsuragi; Durian, 2013)]. As a basis for comparison, $K_v = 0.8$ and $K_z = 9$ are reported for the data in Katsuragi *et al.* (2007) (Katsuragi; Durian, 2007). In addition to that, Kang *et al.* (2018) (Kang *et al.*, 2018) show a large variation for the values predicted for K_z. They highlight that $10^1 < K_z < 10^2$ when $0.4 < \mu < 0.8$.

Finally, contrasting with the model by Katsuragi & Durian (2013) (Katsuragi; Durian, 2013) [Eq. (5.17)], Guo (2018) (Guo, 2018) proposes that these coefficients might depend only on the packing fraction ϕ. Since our experiments are performed with the same grains and at approximately the same packing fraction, we decided to use a single pair of coefficients K_v and K_z that fit well all our experimental data [Fig. (5.32)]. Having said that, we point out that our values for both coefficients are in the same order of magnitude as compared to these other similar studies (Katsuragi; Durian, 2007; Pacheco-Vázquez *et al.*, 2011; Katsuragi; Durian, 2013; Hinch, 2014; Guo, 2018).

5.2.2.2 Impact with rotation

5.2.2.2.1 Experimental and numerical results

In the reference frame of the tank, the spherical projectile has an initial spin ω_i. This rotational velocity can be compared to the impact velocity using the velocity ratio ν:

$$\nu = \frac{\omega_i\, d}{v_i}. \tag{5.18}$$

Note that ν can be interpreted as the square root of the ratio between angular and translational kinetic energies.

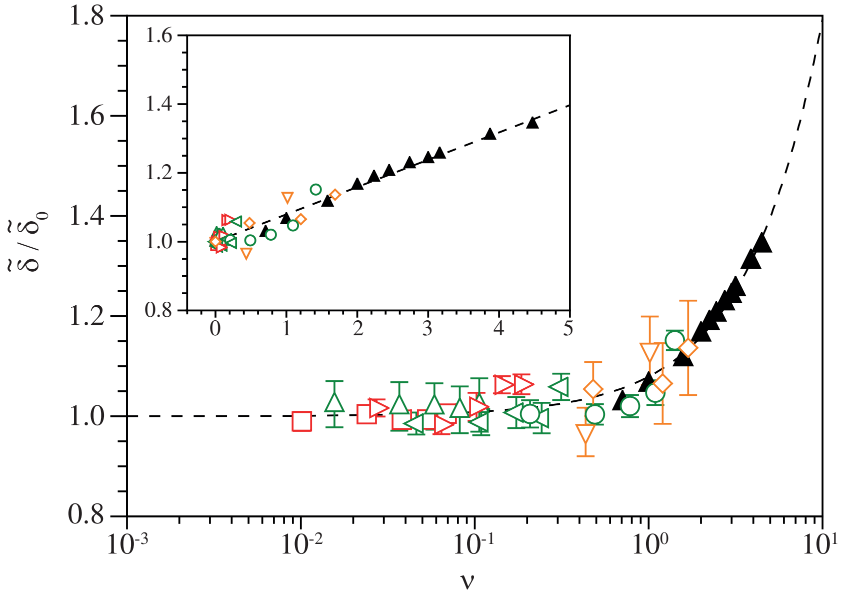

Figure 5.33 – Nondimensional penetration depth $\tilde{\delta}$ divided by the nondimensional penetration depth without rotation $\tilde{\delta}_0$, as a function of the nondimensional velocity ratio $\nu = \omega_i\, d/v_i$, for the following configurations: $d = 20$ mm and (▷) $h = 57$ mm, (□) $h = 412$ mm ; $d = 30$ mm and (○) $h = 2$ mm, (◁) $h = 45$ mm, (△) $h = 391$ mm ; $d = 80$ mm and (◇) $h = 3$ mm, (▽) $h = 8$ mm. (▲) Numerical simulations from Ref. (Carvalho *et al.*, 2023b). (- - -) Best fit of both experimental and numerical data with $\tilde{\delta}/\tilde{\delta}_0 = 1 + 0.08\,\nu$. Inset: Same data in linear plot. Image taken from (Carvalho *et al.*, 2024a).

Figure (5.33) displays the evolution of the relative penetration depth $\tilde{\delta}/\tilde{\delta}_0$ as a function of the velocity ratio ν (note that $\tilde{\delta}/\tilde{\delta}_0$ is also simply δ/δ_0). We observe that the data collapse on a single curve, as well as a slight increase in penetration depth with rotation. Indeed, within the experimental range of ν, the relative rotation between the projectile and the grains leads to variations in the penetration depth of up to approximately 15%.

To enhance the experimental data, we supplement them with numerical results extracted from a previous study obtained from three-dimensional discrete element method computations (Carvalho *et al.*, 2023b) and presented in Sec. 5.1.1.2.4. Just as reminder, in that case (numerical), the granular medium consisted of spheres ($d_g = 1 \pm 0.4$ mm, $\rho_g = 2600$ kg m^{-3}) confined in a cylindrical container ($D = 125$ mm, $b = 76.5$ mm), leading to a granular packing fraction of $\phi \simeq 0.554$. The projectile ($d = 15$ mm, $\rho = 7865$ kg m^{-3}) was released from a height $h = 10$ mm, with an angular velocity ω_i that varied from 0 to 418 rad s^{-1}. The results of these simulations are plotted in Fig. (5.33) (dark symbols) and complement our experimental findings at large ν, in a range of parameters that are difficult to access experimentally, since if ω_i is too large, then the grains tend to be ejected due to centrifugal forces. A very good agreement between experimental and numerical data is observed, with an overlap zone around $\nu \simeq 1$. For rotating projectiles impacting a granular bed (Carvalho *et al.*, 2023b), part of the rotational kinetic energy of the projectile agitates the bed, helping to dislodge more grains and excavate it, leading to an increase in the penetration depth.

The inset in Fig. (5.33) shows the same data in linear plot and suggests that the relative penetration depth $\tilde{\delta}/\tilde{\delta}_0$ increases linearly with the velocity ratio ν, following a law of the form $\tilde{\delta}/\tilde{\delta}_0 = 1 + B\nu$, with $B \simeq 0.08$. Finally, considering that $\tilde{\delta}_0 = A\tilde{H}_0^{\alpha}$, the data are well described by the general fit,

$$\tilde{\delta} = A\tilde{H}_0^{\alpha}\left(1 + B\nu\right), \tag{5.19}$$

where $A \simeq 0.49$ and $\alpha \simeq 0.4$ come from the case without rotation ($\nu \to 0$). The penetration depth δ of the projectile, expressed in terms of impact velocity v_i and rotation velocity ω_i, writes

$$\delta = Ad\left(\frac{\pi\rho}{6\rho_g\phi}\right)^{1-\alpha}\left(\frac{v_i^2}{2gd} + \frac{\delta_0}{d}\right)^{\alpha}\left(1 + B\frac{\omega_i\, d}{v_i}\right). \tag{5.20}$$

We note that the scaling drawn in Fig. (5.33) is not a master curve since Eq. (5.20) cannot be written in a separable form with v_i and ω_i. Consequently, $\tilde{\delta}/\tilde{\delta}_0$ is still a function of both variables v_i and ω_i. However, the dependence of $\tilde{\delta}/\tilde{\delta}_0$ with v_i is quite soft, which is why we observe that all the data collapse on a single curve for the range of ω_i and v_i explored.

5.2.2.2.2 Model update and discussion

We observed in Fig. (5.33) that the penetration depth varies continuously across the different angular velocities (spins), for all initial heights and angular velocities tested ex-

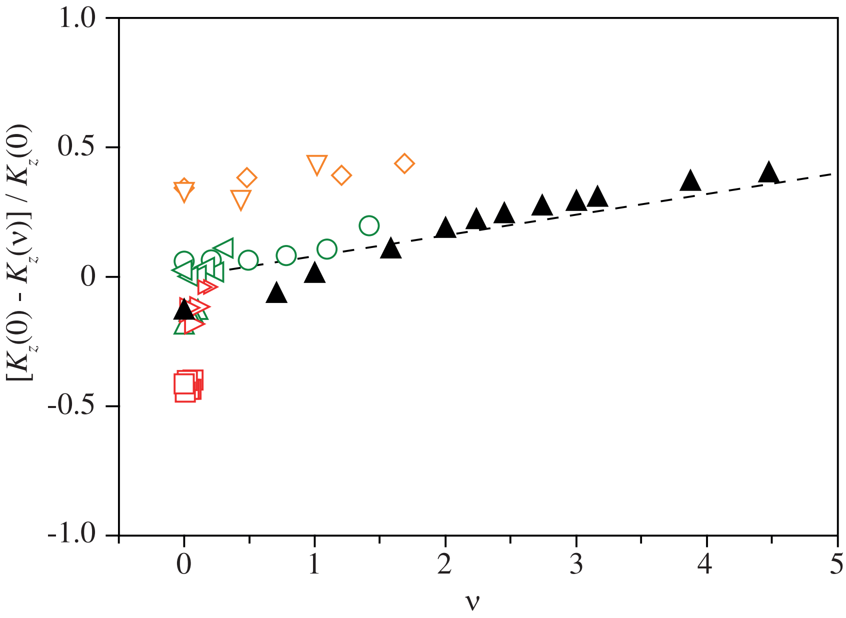

Figure 5.34 – $[K_z(0) - K_z(\nu)]/K_z(0)$ as a function of the nondimensional ratio velocity $\nu = \omega_i\, d/v_i$. Symbols correspond to the same data as in Fig. (5.33). Numerical data have been integrated with $K_z(0) = 26.84$ and $K_v = 0.68$ corresponding to values for the nonrotating projectile in numerical simulations. (- - -) Fit of both experimental and numerical data with $[K_z(0) - K_z(\nu)]/K_z(0) = 0.08\,\nu$. Image taken from (Carvalho *et al.*, 2024a).

perimentally and numerically (Carvalho *et al.*, 2023b). This suggests that the dynamics of the projectile should be continuous across different initial spins as it penetrates the granular bed. Therefore, we aim at modifying Eq. (5.14) by incorporating the contribution of the projectile spin.

The increase in penetration depth with the initial spin indicates that rotation enhances the fluidization of part of the granular medium around the projectile. As a result, the pressure beneath the projectile decreases, with its angular velocity decreasing over a characteristic time T_ω due to a resisting torque exerted by the granular medium on the sphere (T_ω is the characteristic time for stopping the rotation of an initially spinning projectile, i.e., the time interval for reaching a zero angular velocity).

The conservation of momentum for a sphere's rotation is written as follows:

$$\rho d^5 \frac{d\omega}{dt} \sim C_f, \tag{5.21}$$

where C_f corresponds to the resisting torque exerted by the granular medium on the object during penetration. This resisting torque corresponds to a local solid friction force per unit area between the grains and the sphere, noted τ_f. This solid friction force cannot be reasonnably linked to the object's angular velocity nor its geometrical properties. As it is applied to the entire sphere of area $\sim d^2$, a reasonable scale for the resistive torque should be $C_f \sim d^3\tau_f$. This scaling of the spin deceleration, $d\omega/dt$, can be obtained by carrying out a dimensional analysis:

$$\frac{d\omega}{dt} \sim \frac{\omega_i - 0}{T_\omega}. \tag{5.22}$$

Working on the two previous relationships leads to $\rho d^5\omega_i/T_\omega \sim d^3\tau_f$, so the characteristic time T_ω should be proportional to the rotational inertia, i.e., $T_\omega \sim \rho d^2\omega_i/\tau_f$. Even if we have no clear idea of what τ_f is, it does not depend on ρ, d and ω_i. This way:

$$T_\omega \propto \rho d^2\omega_i. \tag{5.23}$$

As rotation and vertical penetration are decoupled in our experiments, there is no obvious reason for the two corresponding timescales T_ω and T_v to be of the same order of magnitude. For example, for low rotational velocity, the characteristic time T_ω is such as $T_\omega \ll T_v$, so that the rotation of the projectile can be neglected. Conversely, for high rotational velocity ($T_\omega \gg T_v$), the projectile can keep on rotating while final penetration is reached. It is then reasonable to assume that the resisting torque arises from contact between the grains and the projectile and is therefore frictional rather than collisional in origin. Hence, we will suppose that only the coefficient K_z will be affected by the rotation of the projectile $\omega(t)$, while the coefficient K_v will not depend on it. Let us consider two limiting cases: (*i*) The first one is the regime where the impact velocity v_i dominates and leads to a penetration time T_v much greater than the characteristic time for spinning T_ω. In this situation, rotation will have no effect on penetration depth. (*ii*) The second one is the regime where the characteristic time due to rotation T_ω is much greater than that due to translation T_v. In this case, the angular velocity can be considered constant over time, so that $\omega(t) \sim \omega_i$. Both extreme cases are well describe by the relevant dimensionless number $\nu = \omega_i\, d/v_i$. Consequently, in first approximation, the effect of rotation can be modeled by defining a function $K_z(\nu)$. Let us set

$$K_z(\nu) = K_z(0)[1 - |\chi(\nu)|]. \tag{5.24}$$

Note that the absolute value allows to overcome the direction of rotation of the projectile.

Let us determine $\chi(\nu)$ in our experiments. To do so, we set $K_z(0) = 7.2$ and $K_v = 0.39$ (same values as for the nonrotating projectile) and determine χ for solving

Eq. (5.14) continuously across different values of ν. Figure (5.34) shows the evolution of $[K_z(0) - K_z(\nu)]/K_z(0)$ as a function of ν for both experimental and numerical data. Although with a significant dispersion of data at low values of ν, we observe that the coefficient K_z decreases with ν, which is consistent with the fact that the penetration depth δ increases with the angular velocity. This decrease is rather linear, so that we can define the function χ such that $\chi(\nu) = C\nu$ with $C \simeq 0.08$ to fit the data [dashed line in Fig. (5.34)].

We point out that the coefficients of the linear correction B in Eq. (5.19) and C in Eq. (5.25) are equal to 0.08. We believe that it is only a coincidence that they are equal, however we are not sure of the origin of the equality of both coefficients. We note that the coefficient B originally comes from the fit of the data of the relative penetration depth $\tilde{\delta}/\tilde{\delta}_0$ as a function of ν in Fig. (5.33), while the coefficient C only appears when the dependence of K_z on ν is analyzed in Fig. (5.34). Thus, both coefficients were obtained from a simple linear fit of the data which they represent, being linked to the dilation/fluidization of the granular material due to rotational effects.

In this way, we are now able to modify the initial model [Eq. (5.14)] for taking rotation effects into account, leading to:

$$\frac{d^2\tilde{z}}{d\tilde{t}^2} = 1 - K_v\left(\frac{d\tilde{z}}{d\tilde{t}}\right)^2 - K_z(0)(1 - |C\nu|)\tilde{z}. \tag{5.25}$$

We observe a discrepancy between the experimental data for the highest diameter ($d = 80$ mm) and the dashed line on Fig. (5.34). These experiments always exhibit a penetration depth smaller than the projectile diameter ($\delta/d < 1$). Since the model is based on the assumption that the projectile is a point object, it is not precise enough to capture such limiting cases. It should be noted, however, that the trend remains consistent, since these data follow a curve parallel to the dashed line. In addition, we believe the dispersion observed for the densest sphere ($d = 20$ mm) to be associated with the fact that $K_z(0)$ and K_v are supposed to be constant [although the data are well described by one single pair of coefficients, as seen in Fig. (5.32)]. To calculate the values present in Fig. (5.34), we consider the spheres individually (not all together as previously done in the other figures) and, since this sphere is twice as dense as the other metalic spheres that we used in our experiments, and as Tab. (5.9) suggests, $K_z(0)$ could be different (probably larger) for this specific sphere. We point out again that we made the choice of using of a single pair of K_z and K_v (Guo, 2018) because they describe well all our experimental data [Fig. (5.32)]. In the end, the data collapses reasonably well by using the proposed scales and model, as can be seen in Fig. (5.33). What Fig. (5.34) is showing is only part of our assumptions for the model (for obtaining the results of Fig.(5.35), for example): it shows some linearity between K_z and ν, with some deviations (as the case of d = 20 mm). Therefore, we understand that our model works well at first order, and that Fig. (5.34) shows some second-order deviations (which seems to affect little the final results). Moreover, the linear model proposed in Eq. (5.25) works only for cases where $|\chi(\nu)| < 1$, ensuring energy dissipation.

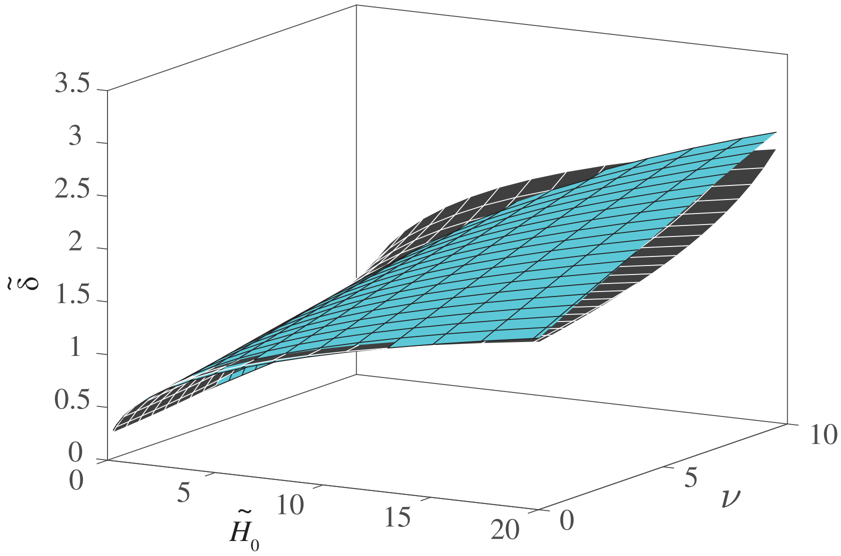

Figure 5.35 – Nondimensional penetration depth $\tilde{\delta}$ as a function of the dimensionless total distance $\tilde{H}_0$ and the nondimensional velocity ratio ν. Black surface corresponds to the solution of Eq. (5.25). Blue surface corresponds to the scaling law (5.19). Image taken from (Carvalho *et al.*, 2024a).

The resolution of Eq. (5.25) generates the black surface displayed in the three-dimensional graphic of Fig. (5.35), which describes the penetration depth $\tilde{\delta}(\tilde{H}_0, \nu)$ as a function of the total height and the velocity ratio. Figure (5.35) also shows a blue surface that represents the scaling law described by relation (5.19). We can see that both surfaces are very close to each other, showing that the proposed model correctly captures the observed scaling law.

In summary, we have shown that rotational velocity increases the penetration depth of a projectile impacting a granular material. However, the effect of rotation on the penetration depth is of a lower order than that of impact velocity. It is possible to take the effect of rotation ν into account in the penetration depth $\tilde{\delta}$ by modifying the usual scaling law for penetration depth without rotation $\tilde{\delta}_0$. The new scaling law is an affine relation that reads $(\tilde{\delta} - \tilde{\delta}_0)/\tilde{\delta}_0 \sim \nu$. Moreover, by implementing rotation effects, we have adapted the dynamic equation for penetration of a projectile into granular materials. The influence of rotation ν essentially reduces the frictional drag term (proportional to depth). The resolution of this updated equation leads to a solution $\tilde{\delta}(\tilde{H}_0, \nu)$ represented by a nonplanar surface very close to the aforementioned new scaling law. Nevertheless, the model proposed can be used to estimate the depth reached by spinning projectiles, with important industrial, geotechnical and environmental applications. Overall, our results represent a new step for understanding the mechanics of impact in granular media.

6 CONCLUSIONS AND FUTURE WORKS

This Thesis presents an investigation of the dynamics of solid objects (intruders) moving in granular materials using numerical simulations, experimental approaches, and mathematical modeling. The work covers a variety of scenarios, including single and multiple intruders moving horizontally in granular media, as well as the impact of projectiles on granular beds. The role of key parameters in the dynamics of these movements, such as intruder velocity, basal friction, packing fraction, spatial arrangement of intruders, projectile rotation, bonding stresses in particle aggregates, among others, are analyzed. The results provide new insights into the mechanics of granular media when interacting with intruders, which are crucial for applications in various fields, such as geophysics, engineering, and planetary science.

Through the use of the Discrete Element Method (DEM) and the open source code LIGGGHTS, the study revealed complex mechanisms of force transmission in granular systems. The force network around a moving intruder was observed to be composed of two main types of chains: load-bearing and dissipative. Load-bearing chains transmit large forces, leading to the formation of jammed regions and high drag forces, while dissipative chains percolate smaller forces and contribute less to drag. The study also highlighted that anisotropy is more pronounced in load-bearing chains, with a noticeable increase in anisotropy in regions downstream of the intruder path. Furthermore, variations in basal friction significantly influenced the extent and strength of these force networks, as well as the formation of downstream cavities, demonstrating the critical role of friction in granular displacement. In addition, it has been shown that load-bearing contact networks creep before breaking, thus allowing the intruders to continue moving.

The interaction between multiple intruders moving in a granular bed was numerically explored, revealing a cooperative dynamics that is not present in single intruder scenarios. The cooperative behavior arises from the compaction (in front of the intruder) and expansion (downstream of the intruder) of the granular medium. For the case of two intruders moving side by side at constant velocity, the study identified the optimal intruder spacing that minimizes drag, offering potential applications for designing systems that need to navigate or agitate granular media efficiently. It was also found that the initial configuration and packing fraction play crucial roles in determining the interaction patterns for intruders moving freely in granular media. Certain configurations led to attractor-like behaviors, where intruders settled into stable formations, indicating that granular systems can exhibit complex and stable cooperative dynamics depending on their initial states. Experimentally, we showed that for two intruders moving side by side at a constant speed, from a certain separation, the average drag felt by each intruder decreases significantly and that there is an increase in this relative drag reduction with the depth of the intruders. These findings were rationalized by the proposition of a phenomenological model, based on the breakdown of contact networks between intruders when they move side by side.

The research extended to projectile impacts on granular beds, a scenario relevant to planetary science and engineering. Numerical simulations showed that the packing fraction of the granular bed significantly affects the penetration depth of the projectile, while the crater diameter remains apparently unchanged. The influence of friction between grains was also critical; lower friction led to deeper penetration and larger craters, highlighting the importance of friction in granular impact processes. In addition, the study explored the role of projectile spin, finding that increasing spin leads to greater penetration depths and changes the final crater shape. These findings suggest that both the mechanical properties of the granular bed and the characteristics of the impacting object must be taken into account to accurately predict cratering outcomes. Through experiments, we confirmed that increasing rotational speed leads to increasing penetration depth, leading to the proposal of an updated model that incorporates rotational effects to provide a refined scaling law for penetration depth, with potential applications in geotechnical engineering and planetary exploration.

Further investigation into the effects of cohesion and rotational speed on crater formation dynamics by the impact of aggregates revealed that decreasing bond stresses (between the constituents of the aggregate) and increasing spin lead to more pronounced radial spreading of projectile material. This results in flatter crater shapes with peaks around the rim and center, and variable penetration depths, highlighting the diversity of crater shapes found in nature. These results indicate that the interplay between cohesion, rotational speed, and granular strength plays a crucial role in determining the final distribution of materials after an impact. These results can be used for interpreting geological formations and the distribution of materials in natural impact events.

Overall, the findings of this Thesis contribute to the understanding of the behavior of granular materials when in the presence of an intruder. By elucidating the importance of some important mechanisms and parameters, both in cooperative dynamics and in crater formation, this research provides a basis for the development of better predictive models and engineering solutions for systems that interact with granular materials. Although this Thesis presents an advance in the understanding of the dynamics of these movements, several aspects remain to be better investigated in the future to deepen our understanding and enhance practical applications, some of which are listed below.

Our current numerical studies for intruders moving in the quasi-static regime focus on two-dimensional representations of granular systems. Extending these analyses to three-dimensional systems would provide a more realistic and comprehensive understanding of intruder dynamics. Three-dimensional models can capture additional complexities, such as out-of-plane force chains and three-dimensional flow patterns, which are essential for accurately predicting behavior in natural and industrial environments. As shown in the experimental results for the interaction between intruders moving side by side, the deeper the intruders are, the greater the relative drag reduction. Future investigations, both numerical and experimental, performed at greater depths, could predict a saturation of this behavior and help elucidate the physical mechanisms underlying this drag reduction.

Future research should investigate how varying the shapes (e.g., elliptical, angular, irregular) and sizes of intruders affect the force transmission, drag, and stability of granular systems, especially when in the presence of multiple intruders. Experimental techniques involving photoelasticity could be employed as a means to achieve it, aiming at better understanding the internal structure os these materials when under load or in the presence on intruders. Understanding these variations could lead to the development of optimized designs for tools and devices that interact with granular media, such as agricultural machinery for soil preparation, excavation equipment, and robotic systems for exploration in extraplanetary granular environments.

Further studies are needed to explore the effects of different levels of friction and cohesion on granular behavior. In particular, incorporating other models for friction forces into numerical simulations would be very valuable, especially for understanding events such as jamming and stick-slip motion.

Examining the behavior of intruders at higher speeds and with multidirectional capabilities (e.g., lateral movements, rotations) would provide a more comprehensive and realistic understanding of dynamic interactions in granular media, especially in characterizing the cooperative motion between intruders moving side by side.

The effects of oblique impacts at different impact angles on crater dynamics should be explored. Understanding how these factors influence crater morphology and penetration depth would be valuable for interpreting planetary surface features and designing impact mitigation strategies, since real impacts do not always occur perpendicular to the granular material. Developing more sophisticated models that take into account the deceleration of projectile spin over time and complex collision dynamics could improve predictions for various impact scenarios, especially in predicting crater diameter and projectile penetration depth.

For mathematical modeling of numerical and experimental observations, it would be interesting to develop universal scaling laws that incorporate various factors, such as packing fraction, friction, intruder shape, rotational effects, and high-energy impacts, thus allowing more accurate predictions of granular behavior in impact dynamics.

Overall, exploring more realistic and complex conditions of intruder motion could help bridge the gap between theoretical research and practical implementation. Likewise, the motion of intruders through wet granular materials would be an interesting topic to be covered in the future.

By pursuing these future research directions, we can further unravel the complexities of granular materials when interacting with intruders, leading to more accurate models, better predictions, and improved engineering solutions for various applications. Continued exploration of this topic could contribute to helping solve practical challenges in fields ranging from fundamental physics to planetary exploration.

BIBLIOGRAPHY

Abdalla, A.; Hettiaratchi, D.; Reece, A. The mechanics of root growth in granular media. **J. Agric. Eng. Res**, v. 14, n. 3, p. 236–248, 1969.

Albert, I.; Sample, J. G.; Morss, A. J.; Rajagopalan, S.; Barabási, A.-L.; Schiffer, P. Granular drag on a discrete object: Shape effects on jamming. **Phys. Rev. E**, v. 64, p. 061303, Nov 2001.

Albert, R.; Pfeifer, M. A.; Barabási, A.-L.; Schiffer, P. Slow drag in a granular medium. **Phys. Rev. Lett.**, v. 82, p. 205–208, Jan 1999.

Alvesgaspar. **Piles of soil with various compositions used for levelling the terrain**. <https://commons.wikimedia.org/wiki/File:Soil_July_2010-1.jpg>. [Licensed under Creative Commons Attribution-Share Alike 3.0 Unported, Wikimedia Commons], Accessed August 13, 2024.

Amato, J. C.; Williams, R. E. Crater formation in the laboratory: An introductory experiment in error analysis. **Am. J. Phys.**, v. 66, n. 2, p. 141–143, 1998.

Ambroso, M. A.; Kamien, R. D.; Durian, D. J. Dynamics of shallow impact cratering. **Phys. Rev. E**, v. 72, p. 041305, 2005.

Andreotti, B.; Forterre, Y.; Pouliquen, O. **Les milieux granulaires - Entre fluide et solide**. [S.l.]: EDP Sciences - CNRS Éditions, 2011.

Arvidson, R. E. Morphologic classification of martian craters and some implications. **Icarus**, v. 22, n. 3, p. 264–271, 1974.

Arvidson, R. E.; Bell III, J. F.; Bellutta, P.; Cabrol, N. A.; Catalano, J.; Cohen, J.; Crumpler, L. S.; Des Marais, D.; Estlin, T.; Farrand, W. *et al.* Spirit mars rover mission: Overview and selected results from the northern home plate winter haven to the side of scamander crater. **J. Geophys. Res. Planets**, v. 115, n. E7, 2010.

Askari, H.; Kamrin, K. Intrusion rheology in grains and other flowable materials. **Nat. Mater.**, v. 15, n. 12, p. 1274–1279, 2016.

Barlow, N. G.; Ferguson, S. N.; Horstman, R. M.; Maine, A. Comparison of central pit craters on mars, mercury, ganymede, and the saturnian satellites. **Meteorit. Planet. Sci.**, v. 52, n. 7, p. 1371–1387, 2017.

Behringer, R. P.; Chakraborty, B. The physics of jamming for granular materials: A review. **Rep. Prog. Phys.**, v. 82, n. 1, p. 012601, 2018.

Benito, J.; Bertho, Y.; Ippolito, I.; Gondret, P. Stability of a granular layer on an inclined "fakir plane". **EPL**, v. 100, n. 3, p. 34004, 2012.

Benito, J.; Bertho, Y.; Ippolito, I.; Gondret, P. Stability of a granular layer on an inclined "fakir plane". **EPL**, v. 100, p. 34004, 2012.

Berger, R.; Kloss, C.; Kohlmeyer, A.; Pirker, S. Hybrid parallelization of the LIGGGHTS open-source DEM code. **Powder Technol.**, v. 278, p. 234–247, 2015.

Berns, W. **Sandfish lizard (*Scincus scincus*)**. <https://en.wikipedia.org/wiki/Scincus_scincus>. [Licensed under CC BY-SA 2.0 DE], Accessed August 13, 2024.

Bester, C. S.; Behringer, R. P. Collisional model of energy dissipation in three-dimensional granular impact. **Phys. Rev. E**, v. 95, p. 032906, Mar 2017.

Bi, D.; Zhang, J.; Chakraborty, B.; Behringer, R. P. Jamming by shear. **Nature**, v. 480, p. 355–358, 2011.

Blum, J. Dust evolution in protoplanetary discs and the formation of planetesimals: What have we learned from laboratory experiments? **Space Sci. Rev.**, v. 214, n. 2, p. 52, 2018.

Bourrier, F.; Nicot, F.; Darve, F. Physical processes within a 2D granular layer during an impact. **Granul. Matter**, v. 10, p. 415–437, 2008.

Brilliantov, N. V.; Spahn, F.; Hertzsch, J.-M.; Pöschel, T. Model for collisions in granular gases. **Phys. Rev. E**, v. 53, n. 5, p. 5382, 1996.

Bruyn, J. R. de; Walsh, A. M. Penetration of spheres into loose granular media. **Can. J. Phys.**, v. 82, n. 6, p. 439–446, 2004.

Butko, A. **Maize for popcorn, cultivated in Hungary, producer UNO FRESCO TRADEX.** <https://commons.wikimedia.org/wiki/File:Ab_food_06.jpg>. [Licensed under Creative Commons Attribution-Share Alike 3.0 Unported, Wikimedia Commons. Observation: this image has been cropped.]; Accessed August 13, 2024.

Caballero-Robledo, G.; Acevedo-Escalante, M.; Mandujano, F.; Málaga, C. Attraction and repulsion between objects in a granular flow. **Phys. Rev. Fluids**, v. 6, p. 084303, 2021.

Candelier, R.; Dauchot, O. Creep motion of an intruder within a granular glass close to jamming. **Phys. Rev. Lett.**, v. 103, n. 12, p. 128001, 2009.

Candelier, R.; Dauchot, O. Journey of an intruder through the fluidization and jamming transitions of a dense granular media. **Phys. Rev. E**, v. 81, n. 1, p. 011304, 2010.

Carlevaro, C. M.; Kozlowski, R.; Pugnaloni, L. A.; Zheng, H.; Socolar, J. E. S.; Kondic, L. Intruder in a two-dimensional granular system: Effects of dynamic and static basal friction on stick-slip and clogging dynamics. **Phys. Rev. E**, v. 101, p. 012909, Jan 2020.

Carvalho, D. D.; Bertho, Y.; Franklin, E. M.; Seguin, A. Penetration of a spinning sphere impacting a granular medium. **Phys. Rev. E**, v. 109, n. 5, p. 054902, 2024.

Carvalho, D. D.; Bertho, Y.; Seguin, A.; Franklin, E.; Texier, B. Drag reduction during the side-by-side motion of a pair of intruders in a granular medium. **Phys. Rev. Fluids**, v. 9, p. 114303, 2024.

Carvalho, D. D.; Franklin, E. M. **LIGGGHTS input and output files, a code implemented in LIGGGHTS to introduce basal friction effects, and Octave scripts for post-processing the outputs are available on Mendeley Data, https://data.mendeley.com/datasets/39wgn3jtxb**, 2022.

Carvalho, D. D.; Franklin, E. M. Collaborative behavior of intruders moving amid grains. **Phys. Fluids**, v. 34, n. 12, 2022.

Carvalho, D. D.; Lima, N. C.; Franklin, E. M. Contacts, motion, and chain breaking in a two-dimensional granular system displaced by an intruder. **Phys. Rev. E**, v. 105, p. 034903, Mar 2022.

Carvalho, D. D.; Lima, N. C.; Franklin, E. M. Impact craters formed by spinning granular projectiles. **Phys. Rev. E**, v. 108, n. 5, p. 054904, 2023.

Carvalho, D. D.; Lima, N. C.; Franklin, E. M. Roles of packing fraction, microscopic friction, and projectile spin in cratering by impact. **Phys. Rev. E**, v. 107, n. 4, p. 044901, 2023.

Cates, M. E.; Wittmer, J. P.; Bouchaud, J.-P.; Claudin, P. Jamming, force chains, and fragile matter. **Phys. Rev. Lett.**, v. 81, p. 1841–1844, Aug 1998.

Chen, G.; Qiao, L.; Zhou, Z.; Richter, L.; Ji, A. Development of a lizard-inspired robot for mars surface exploration. **Biomimetics**, v. 8, n. 1, p. 44, 2023.

Chen, X.; Wang, L.; Morrissey, J.; Ooi, J. Y. DEM simulations of agglomerates impact breakage using Timoshenko beam bond model. **Granul. Matter**, v. 24, n. 74, 2022.

Chen, X.; Wang, L. G.; Morrissey, J. P.; Ooi, J. Y. Dem simulations of agglomerates impact breakage using timoshenko beam bond model. **Granul. Matter**, v. 24, n. 3, p. 74, 2022.

Chien, P. le. **Torrefied coffee beans**. <https://commons.wikimedia.org/wiki/File:Coffee_beans2.jpg>. [Licensed under Creative Commons Attribution-Share Alike 4.0 International, Wikimedia Commons], Accessed August 13, 2024.

Ciamarra, M. P.; Lara, A. H.; Lee, A. T.; Goldman, D. I.; Vishik, I.; Swinney, H. L. Dynamics of drag and force distributions for projectile impact in a granular medium. **Phys. Rev. Lett.**, v. 92, p. 194301, May 2004.

Clark, A. H.; Kondic, L.; Behringer, R. P. Particle scale dynamics in granular impact. **Phys. Rev. Lett.**, v. 109, n. 23, p. 238302, 2012.

CNRS-Ingénierie. **Comment la rotation des projectiles les fait s'enfoncer dans les milieux granulaires**. 2024. <https://www.insis.cnrs.fr/fr/cnrsinfo/comment-la-rotation-des-projectiles-les-fait-senfoncer-dans-les-milieux-granulaires>. Accessed September 26, 2024.

Costantino, D. J.; Scheidemantel, T. J.; Stone, M. B.; Conger, C.; Klein, K.; Lohr, M.; Modig, Z.; Schiffer, P. Starting to move through a granular medium. **Phys. Rev. Lett.**, v. 101, p. 108001, Sep 2008.

Coulomb, C. A. Essai sur une application des regles de maximis et minimis a quelques problemes de statique relatifs a l'architecture (essay on maximums and minimums of rules to some static problems relating to architecture). **Mem. Div. Sav. Acad.**, v. 7, 1773.

De La Cruz, R. L.; Caballero-Robledo, G. Lift on side-by-side intruders within a granular flow. **J. Fluid Mech.**, v. 800, p. 248, 2016.

Cundall, P. A.; Strack, O. D. A discrete numerical model for granular assemblies. **Géotechnique**, v. 29, n. 1, p. 47–65, 1979.

Daniels, K. E.; Kollmer, J. E.; Puckett, J. G. Photoelastic force measurements in granular materials. **Rev. Sci. Instrum.**, v. 88, n. 5, p. 051808, 2017.

Derakhshani, S. M.; Schott, D. L.; Lodewijks, G. Micro–macro properties of quartz sand: Experimental investigation and DEM simulation. **Powder Technol.**, v. 269, p. 127–138, 2015.

Dhiman, M.; Kumar, S.; Anki Reddy, K.; Gupta, R. Origin of the long-ranged attraction or repulsion between intruders in a confined granular medium. **J. Fluid Mech.**, v. 886, p. A23, 2020.

Di Renzo, A.; Di Maio, F. P. An improved integral non-linear model for the contact of particles in distinct element simulations. **Chem. Eng. Sci.**, v. 60, n. 5, p. 1303–1312, 2005.

Duran, J. **Sables, poudres et grains**. [S.l.]: Eyrolles Sciences, 1997.

Espinosa, M.; Díaz-Melián, V.; Serrano-Muñoz, A.; Altshuler, E. Intruders cooperatively interact with a wall into granular matter. **Granul. Matter**, v. 24, n. 39, 2022.

Fakih, M.; Delenne, J.-Y.; Radjai, F.; Fourcaud, T. Root growth and force chains in a granular soil. **Phys. Rev. E**, v. 99, p. 042903, 2019.

Faug, T. Macroscopic force experienced by extended objects in granular flows over a very broad froude-number range: macroscopic granular force on extended object. **Eur. Phys. J. E**, v. 38, p. 1, 2015.

Featherstone, J.; Bullard, R.; Emm, T.; Jackson, A.; Reid, R.; Shefferman, S.; Dove, A.; Colwell, J.; Kollmer, J. E.; Daniels, K. E. Stick-slip dynamics in penetration experiments on simulated regolith. **Planet. Sci. J.**, v. 2, n. 6, p. 243, dec 2021.

FelixMittermeier. **Unknown**. <https://pixabay.com/pt/photos/faia-%C3%A1rvore-ra%C3%ADzes-floresta-3385957/>. [Pixabay], Accessed August 13, 2024.

Ferdowsi, B.; Ortiz, C. P.; Houssais, M.; Jerolmack, D. J. River-bed armouring as a granular segregation phenomenon. **Nat. Commun.**, v. 8, n. 1, p. 1363, 2017.

fr/MIDI/, G. M. gdrmidi@ polytech. univ-mrs. fr http://www. lmgc. univ-montp2. On dense granular flows. **Eur. Phys. J. E**, v. 14, p. 341–365, 2004.

Ganapathy, R. A major meteorite impact on the earth 65 million years ago: Evidence from the cretaceous-tertiary boundary clay. **Science**, v. 209, n. 4459, p. 921–923, 1980.

Geng, J.; Behringer, R. P. Slow drag in two-dimensional granular media. **Phys. Rev. E**, v. 71, p. 011302, Jan 2005.

Gladkov, S. O. Stokes' force for a stationary rotating sphere. **Russ. Phys. J.**, v. 65, n. 5, p. 856, 2022.

Gloss, K. T. **A Photoelastic Investigation Into The Effects Of Cracks And Boundary Conditions On Stress Intensity Factors In Bonded Specimens**. Tese (Doutorado) — Virginia Tech, 2000.

Godwin, R. J.; O'Dogherty, M. J. Integrated soil tillage force prediction models. **J. Terramech.**, v. 44, n. 1, p. 3–14, 2007.

Goldman, D. I.; Umbanhowar, P. Scaling and dynamics of sphere and disk impact into granular media. **Phys. Rev. E**, v. 77, p. 021308, Feb 2008.

Gondret, P.; Lance, M.; Petit, L. Bouncing motion of spherical particles in fluids. **Phys. Fluids**, v. 14, n. 2, p. 643–652, 2002.

Gong, Z.; Yang, Y.; Cui, L.; He, J.; Liu, X. Dem investigation on the size effect in the fragmentation of intact aggregates. **Powder Technol.**, v. 425, p. 118585, 2023.

Gonzalez, J. O.; Cúñez, F. D.; Franklin, E. M. Bidisperse beds sheared by viscous fluids: Grain segregation and bed hardening. **Phys. Fluids**, v. 35, n. 10, 2023.

Gravish, N.; Umbanhowar, P. B.; Goldman, D. I. Force and flow transition in plowed granular media. **Phys. Rev. Lett.**, v. 105, n. 12, p. 128301, 2010.

Guillard, F.; Forterre, Y.; Pouliquen, O. Depth-independent drag force induced by stirring in granular media. **Phys. Rev. Lett.**, v. 110, p. 138303, 2013.

Guo, J. Exact solution for depth of impact crater into granular bed. **J. Eng. Mech.**, v. 144, n. 1, p. 06017018, 2018.

Guo, Y.; Wassgren, C.; Hancock, B.; Ketterhagen, W.; Curtis, J. Validation and time step determination of discrete element modeling of flexible fibers. **Powder Technol.**, v. 249, p. 386–395, 2013.

Happel, J.; Brenner, H. **Low Reynolds number hydrodynamics: with special applications to particulate media**. [S.l.]: Springer Science & Business Media, 1983. v. 1.

Hashemnia, K.; Spelt, J. K. Particle impact velocities in a vibrationally fluidized granular flow: measurements and discrete element predictions. **Chem. Eng. Sci.**, v. 109, p. 123–135, 2014.

Herman, A. Molecular-dynamics simulation of contact and force networks in fragmented sea ice under shear deformation. In: CIMNE. **PARTICLES III: proceedings of the III International Conference on Particle-Based Methods: fundamentals and applications**. [S.l.], 2013. p. 659–669.

Herman, A. Numerical modeling of force and contact networks in fragmented sea ice. **Ann. Glaciol.**, v. 54, n. 62, p. 114–120, 2013.

Herman, A. Discrete-Element bonded-particle Sea Ice model DESIgn, version 1.3 a–model description and implementation. **Geosci. Model Dev.**, v. 9, n. 3, p. 1219–1241, 2016.

Hestroffer, D.; Sánchez, P.; Staron, L.; Bagatin, A. C.; Eggl, S.; Losert, W.; Murdoch, N.; Opsomer, E.; Radjai, F.; Richardson, D. C. *et al.* Small solar system bodies as granular media. **Astron. Astrophys. Rev.**, v. 27, p. 1–64, 2019.

Hilton, J.; Cleary, P. Granular flow during hopper discharge. **Phys. Rev. E**, v. 84, n. 1, p. 011307, 2011.

Hilton, J. E.; Tordesillas, A. Drag force on a spherical intruder in a granular bed at low froude number. **Phys. Rev. E**, v. 88, p. 062203, 2013.

Hinch, J. Particles impacting on a granular bed. **J. Eng. Math.**, v. 84, n. 1, p. 41–48, 2014.

Holsapple, K. A. The scaling of impact processes in planetary sciences. **Ann. Rev. Earth Pl. Sc.**, v. 21, n. 1, p. 333–373, 1993.

Hosoi, A. E.; Goldman, D. I. Beneath our feet: strategies for locomotion in granular media. **Annu. Rev. Fluid Mech.**, v. 47, p. 431–453, 2015.

Houssais, M.; Ortiz, C. P.; Durian, D. J.; Jerolmack, D. J. Onset of sediment transport is a continuous transition driven by fluid shear and granular creep. **Nat. Commun.**, v. 6, n. 1, p. 1–8, 2015.

Huang, C.; Yu, Y.; Cheng, B.; Zhang, K.; Qiao, D.; Baoyin, H. Sand creep motion in slow spin-up experiment: An analog of regolith migration on asteroids. **Phys. Rev. E**, v. 104, p. L042901, 2021.

Iagnemma, K.; Kang, S.; Shibly, H.; Dubowsky, S. Online terrain parameter estimation for wheeled mobile robots with application to planetary rovers. **IEEE Trans. Robot.**, v. 20, n. 5, p. 921–927, 2004.

Inaglory, B. **Mesquite Dunes in Death Valley National Park**. <https://commons.wikimedia.org/wiki/File:Mesquite_Sand_Dunes_in_Death_Valley.jpg>. [Licensed under Creative Commons Attribution-Share Alike 3.0 Unported, Wikimedia Commons], Accessed August 13, 2024.

Irie, T.; Yamaguchi, R.; Watanabe, S.-I.; Katsuragi, H. Deformation of a rotated granular pile governed by body-force-dependent friction. **Phys. Rev. E**, v. 104, p. 064902, 2021.

Ishigami, G.; Miwa, A.; Nagatani, K.; Yoshida, K. Terramechanics-based model for steering maneuver of planetary exploration rovers on loose soil. **J. Field Robot.**, v. 24, n. 3, p. 233–250, 2007.

Jaeger, H. M.; Nagel, S. R.; Behringer, R. P. Granular solids, liquids, and gases. **Rev. Mod. Phys.**, v. 68, n. 4, p. 1259, 1996.

Jaggard, V. **Mars Rover to Roam No More – It's Official (National Geographic)**. 2010. <www.nationalgeographic.com/science/article/100126-mars-rover-spirit-nasa-stuck>. [Accessed February 28, 2024].

Janda, A.; Maza, D.; Garcimartín, A.; Kolb, E.; Lanuza, J.; Clément, E. Unjamming a granular hopper by vibration. **EPL**, v. 87, n. 2, p. 24002, 2009.

Jiang, M.; Zhang, W. Dem analyses of shear band in granular materials. **Eng. Comput.**, v. 32, n. 4, p. 985–1005, 2015.

Jung, S. Caenorhabditis elegans swimming in a saturated particulate system. **Phys. Fluids**, v. 22, n. 3, 2010.

Jung, S.; Winter, A. G.; Hosoi, A. Dynamics of digging in wet soil. **Int. J. Non-Linear Mech.**, v. 46, n. 4, p. 602–606, 2011.

Jung, W.; Choi, S. M.; Kim, W.; Kim, H.-Y. Reduction of granular drag inspired by self-burrowing rotary seeds. **Phys. Fluids**, v. 29, n. 4, 2017.

Kang, W.; Feng, Y.; Liu, C.; Blumenfeld, R. Archimedes' law explains penetration of solids into granular media. **Nat. Commun.**, v. 9, n. 1, p. 1–9, 2018.

Katsuragi, H.; Durian, D. Unified force law for granular impact cratering. **Nature Phys.**, v. 3, p. 420–423, 2007.

Katsuragi, H.; Durian, D. J. Drag force scaling for penetration into granular media. **Phys. Rev. E**, v. 87, p. 052208, May 2013.

Kawabata, D.; Yoshida, M.; Shimosaka, A.; Shirakawa, Y. Discrete element method simulation analysis of the generation mechanism of cooperative behavior of disks falling in a low-density particle bed. **Adv. Powder Technol.**, v. 31, n. 4, p. 1381–1390, 2020.

Kloss, C.; Goniva, C. LIGGGHTS: a new open source discrete element simulation software. In: **Proc. 5th Int. Conf. on Discrete Element Methods**. London, UK: [s.n.], 2010.

Kloss, C.; Goniva, C.; Hager, A.; Amberger, S.; Pirker, S. Models, algorithms and validation for opensource dem and cfd–dem. **Prog. Comput. Fluid Dyn.**, v. 12, n. 2-3, p. 140–152, 2012.

Kolb, E.; Cixous, P.; Gaudouen, N.; Darnige, T. Rigid intruder inside a two-dimensional dense granular flow: Drag force and cavity formation. **Phys. Rev. E**, v. 87, p. 032207, Mar 2013.

Kolb, E.; Legué, V.; Bogeat-Triboulot, M.-B. Physical root–soil interactions. **Phys. Biol.**, v. 14, p. 065004, 2017.

Kondic, L.; Fang, X.; Losert, W.; O'Hern, C. S.; Behringer, R. P. Microstructure evolution during impact on granular matter. **Phys. Rev. E**, v. 85, p. 011305, Jan 2012.

Kozlowski, R.; Carlevaro, C. M.; Daniels, K. E.; Kondic, L.; Pugnaloni, L. A.; Socolar, J. E. S.; Zheng, H.; Behringer, R. P. Dynamics of a grain-scale intruder in a two-dimensional granular medium with and without basal friction. **Phys. Rev. E**, v. 100, p. 032905, Sep 2019.

Kozlowski, R.; Zheng, H.; Daniels, K. E.; Socolar, J. E. S. Stress propagation in locally loaded packings of disks and pentagons. **Soft Matter**, v. 17, p. 10120–10127, 2021.

Kozlowski, R.; Zheng, H.; Daniels, K. E.; Socolar, J. E. S. Stick-slip dynamics in a granular material with varying grain angularity. **Front. Phys.**, v. 10, p. 916190, 2022.

Krisp, H. **Saharan Horned Viper (*Cerastes cerastes*)**. <https://commons.wikimedia.org/wiki/File:Hornviper_Cerastes_cerastes.jpg>. [Licensed under CC BY 3.0, Wikimedia Commons], Accessed August 13, 2024.

Krüger, T.; van der Bogert, C.; Hiesinger, H. Geomorphologic mapping of the lunar crater tycho and its impact melt deposits. **Icarus**, v. 273, p. 164–181, 2016.

Kumar, S.; Dhiman, M.; Reddy, K. A. Magnus effect in granular media. **Phys. Rev. E**, v. 99, n. 1, p. 012902, 2019.

Lätzel, M.; Luding, S.; Herrmann, H. J. Macroscopic material properties from quasi-static, microscopic simulations of a two-dimensional shear-cell. **Granul. Matter**, v. 2, p. 123–135, 2000.

Li, C.; Zhang, T.; Goldman, D. I. A terradynamics of legged locomotion on granular media. **Science**, v. 339, n. 6126, p. 1408–1412, 2013.

Li, C.; Zhang, T.; Goldman, D. I. A terradynamics of legged locomotion on granular media. **Science**, v. 339, n. 6126, p. 1408–1412, 2013.

LIGGGHTS(R)-PUBLIC Documentation, Version 3.X. 2016. <https://www.cfdem.com/media/DEM/docu/Manual.html>. Accessed August 13, 2024.

Lima, N. C.; Carvalho, D. D.; Franklin, E. M. **LIGGGHTS input and output files, a code implemented in LIGGGHTS to introduce basal friction effects, and Octave scripts for post-processing the outputs are available on Mendeley Data, https://data.mendeley.com/datasets/7x2mj8nvbn**, 2021.

Lima, N. C.; Carvalho, D. D.; Franklin, E. M. **LIGGGHTS input and output files, and Octave scripts for post-processing the outputs are available on Mendeley Data, http://dx.doi.org/10.17632/y38prf7hmc**, 2022.

Lima, N. C.; Carvalho, D. D.; Franklin, E. M. **LIGGGHTS input and output files, and Octave scripts for post-processing the outputs are available on Mendeley Data, http://dx.doi.org/10.17632/d49b9p6f4r.1**, 2023.

Lommen, S.; Schott, D.; Lodewijks, G. DEM speedup: Stiffness effects on behavior of bulk material. **Particuology**, v. 12, p. 107–112, 2014.

Majmudar, T.; Sperl, M.; Luding, S.; Behringer, R. P. Jamming transition in granular systems. **Phys. Rev. Lett.**, v. 98, n. 5, p. 058001, 2007.

Majmudar, T. S.; Behringer, R. P. Contact force measurements and stress-induced anisotropy in granular materials. **Nature**, v. 435, n. 7045, p. 1079–1082, 2005.

Maladen, R. D.; Ding, Y.; Li, C.; Goldman, D. I. Undulatory swimming in sand: subsurface locomotion of the sandfish lizard. **Science**, v. 325, n. 5938, p. 314–318, 2009.

Maladen, R. D.; Ding, Y.; Umbanhowar, P. B.; Kamor, A.; Goldman, D. I. Mechanical models of sandfish locomotion reveal principles of high performance subsurface sand-swimming. **J. R. Soc. Interface**, v. 8, n. 62, p. 1332–1345, 2011.

Maladen, R. D.; Ding, Y.; Umbanhowar, P. B.; Goldman, D. I. Undulatory swimming in sand: experimental and simulation studies of a robotic sandfish. **Int. J. Robotic Res.**, v. 30, n. 7, p. 793–805, 2011.

Marvi, H.; Gong, C.; Gravish, N.; Astley, H.; Travers, M.; Hatton, R. L.; Mendelson III, J. R.; Choset, H.; Hu, D. L.; Goldman, D. I. Sidewinding with minimal slip: Snake and robot ascent of sandy slopes. **Science**, v. 346, n. 6206, p. 224–229, 2014.

McDonald, I.; Andreoli, M.; Hart, R.; Tredoux, M. Platinum-group elements in the Morokweng impact structure, South Africa: Evidence for the impact of a large ordinary chondrite projectile at the Jurassic-Cretaceous boundary. **Geochim. Cosmochim. Ac.**, v. 65, n. 2, p. 299–309, 2001.

Melosh, H. J.; Ivanov, B. A. Impact crater collapse. **Ann. Rev. Earth Pl. Sc.**, v. 27, n. 1, p. 385–415, 1999.

Merceron, A.; Sauret, A.; Jop, P. Cooperative effects induced by intruders evolving through a granular medium. **EPL**, v. 121, n. 3, p. 34005, 2018.

Merceron, A.; Sauret, A.; Jop, P. Influence of the size of the intruder on the reorganization of a 2d granular medium. **Granul. Matter**, v. 21, n. 3, p. 81, 2019.

Merkak, O.; Jossic, L.; Magnin, A. Spheres and interactions between spheres moving at very low velocities in a yield stress fluid. **J. Nonnewton. Fluid Mech.**, v. 133, p. 99, 2006.

Modesto, J.; Dorbolo, S.; Katsuragi, H.; Pacheco-Vázquez, F.; Sobral, Y. D. Experimental and numerical investigation of the compression and expansion of a granular bed of repelling magnetic disks. **Granul. Matter**, v. 24, n. 4, p. 105, 2022.

Muthuswamy, M.; Tordesillas, A. How do interparticle contact friction, packing density and degree of polydispersity affect force propagation in particulate assemblies? **J. Stat. Mech.: Theory Exp.**, v. 2006, p. P09003, 2006.

Mynhardt, S. **A tunnel used by the De Winton's golden mole in Port Nolloth, South Africa**. <https://theconversation.com/golden-mole-that-swims-through-sand-is-rediscovered-in-south-africa-after-86-years-219022?mc>. [Licensed under CC BY 4.0], Accessed August 13, 2024.

Mynhardt, S. **Golden mole that swims through sand is rediscovered in South Africa after 86 years**. 2023. <https://theconversation.com/golden-mole-that-swims-through-sand-is-rediscovered-in-south-africa-after-86-years-219022?mc>. Accessed July 13, 2024.

Nguyen, M.-L. **Marine sandglass**. <https://commons.wikimedia.org/wiki/File:Marine_sandglass_MMM.jpg>. [Licensed under Creative Commons Attribution 2.5 Generic, Wikimedia Commons], Accessed August 13, 2024.

Pacheco-Vázquez, F.; Caballero-Robledo, G. A.; Solano-Altamirano, J. M.; Altshuler, E.; Batista-Leyva, A. J.; Ruiz-Suárez, J. C. Infinite penetration of a projectile into a granular medium. **Phys. Rev. Lett.**, v. 106, n. 21, p. 218001, 2011.

Pacheco-Vázquez, F.; Ruiz-Suárez, J. Cooperative dynamics in the penetration of a group of intruders in a granular medium. **Nat. Commun.**, v. 1, n. 123, 2010.

Pacheco-Vázquez, F.; Ruiz-Suárez, J. C. Impact craters in granular media: Grains against grains. **Phys. Rev. Lett.**, v. 107, p. 218001, Nov 2011.

Pennestrì, E.; Rossi, V.; Salvini, P.; Valentini, P. P. Review and comparison of dry friction force models. **Nonlinear Dyn.**, v. 83, p. 1785–1801, 2016.

Poncelet, J. V. **Cours de Mécanique Industrielle**. [S.l.: s.n.], 1829.

Pouliquen, O. Scaling laws in granular flows down rough inclined planes. **Phys. Fluids**, v. 11, n. 3, p. 542–548, 1999.

Pouliquen, O.; Cassar, C.; Jop, P.; Forterre, Y.; Nicolas, M. Flow of dense granular material: towards simple constitutive laws. **J. Stat. Mech.: Theory Exp.**, v. 2006, n. 07, p. P07020, 2006.

Pouliquen, O.; Forterre, Y. Friction law for dense granular flows: application to the motion of a mass down a rough inclined plane. **J. Fluid Mech.**, v. 453, p. 133–151, 2002.

Pouliquen, O.; Forterre, Y. A non-local rheology for dense granular flows. **Philos. Trans. R. Soc. A**, v. 367, n. 1909, p. 5091–5107, 2009.

Pravin, S.; Chang, B.; Han, E.; London, L.; Goldman, D. I.; Jaeger, H. M.; Hsieh, S. T. Effect of two parallel intruders on total work during granular penetrations. **Phys. Rev. E**, v. 104, p. 024902, Aug 2021.

Pugnaloni, L. A.; Carlevaro, C. M.; Kozlowski, R.; Zheng, H.; Kondic, L.; Socolar, J. E. S. Universal features of the stick-slip dynamics of an intruder moving through a confined granular medium. **Phys. Rev. E**, v. 105, p. L042902, 2022.

Radjai, F.; Jean, M.; Moreau, J.-J.; Roux, S. Force distributions in dense two-dimensional granular systems. **Phys. Rev. Lett.**, v. 77, n. 2, p. 274, 1996.

Radjai, F.; Wolf, D. E.; Jean, M.; Moreau, J.-J. Bimodal character of stress transmission in granular packings. **Phys. Rev. Lett.**, v. 80, p. 61–64, Jan 1998.

Reddy, K.; Forterre, Y.; Pouliquen, O. Evidence of mechanically activated processes in slow granular flows. **Phys. Rev. Lett.**, v. 106, n. 10, p. 108301, 2011.

Reichhardt, C. O.; Reichhardt, C. Fluctuations, jamming, and yielding for a driven probe particle in disordered disk assemblies. **Phys. Rev. E**, v. 82, n. 5, p. 051306, 2010.

Ren, D.; Leslie, L. M.; Karoly, D. Landslide risk analysis using a new constitutive relationship for granular flow. **Earth Interact.**, v. 12, n. 4, p. 1–16, 2008.

Reynolds, O. Lvii. on the dilatancy of media composed of rigid particles in contact. with experimental illustrations. **Lond. Edinb. Dubl. Phil. Mag.**, v. 20, n. 127, p. 469–481, 1885.

Robins, B. New principles of gunnery. 1742, euler's annotations appear in later edition (Berlin: 1745).

Roletschek, R. **Farmer plowing at plowing competition 2004 in Fahrenwalde, Mecklenburg-Vorpommern, Germany**. <https://commons.wikimedia.org/wiki/File:04-09-12-Schaupfl%C3%BCgen-Fahrenwalde-RalfR-IMG_1232.jpg>. [Licensed under Creative Commons Attribution-Share Alike 2.5, Wikimedia Commons], Accessed August 13, 2024.

Roux, J. L. **The De Winton's golden mole**. <https://theconversation.com/golden-mole-that-swims-through-sand-is-rediscovered-in-south-africa-after-86-years-219022?mc>. [Licensed under CC BY 4.0], Accessed August 13, 2024.

Ruiz-Suárez, J. C. Penetration of projectiles into granular targets. **Rep. Prog. Phys.**, v. 76, n. 6, p. 066601, 2013.

Saad, E. Interactions of two slip spheres moving side by side in a viscous fluid. **Fluid Dyn. Res.**, v. 48, p. 015502, 2015.

Sawlowicz, Z. Iridium and other platinum-group elements as geochemical markers in sedimentary environments. **Palaeogeogr. Palaeocl.**, v. 104, n. 1, p. 253–270, 1993.

Schramm, M.; Tekeste, M. Z.; Plouffe, C.; Harby, D. Estimating bond damping and bond young's modulus for a flexible wheat straw discrete element method model. **Biosyst. Eng.**, v. 186, p. 349–355, 2019.

Schwager, T. Coefficient of restitution for viscoelastic disks. **Phys. Rev. E**, v. 75, n. 5, p. 051305, 2007.

Seguin, A. Hysteresis of the drag force of an intruder moving into a granular medium. **Eur. Phys. J. E**, v. 42, p. 1, 2019.

Seguin, A. Experimental study of some properties of the strong and weak force networks in a jammed granular medium. **Granul. Matter**, v. 22, n. 48, 2020.

Seguin, A.; Bertho, Y.; Gondret, P. Influence of confinement on granular penetration by impact. **Phys. Rev. E**, v. 78, p. 010301, Jul 2008.

Seguin, A.; Bertho, Y.; Gondret, P.; Crassous, J. Sphere penetration by impact in a granular medium: A collisional process. **EPL**, v. 88, n. 4, p. 44002, 2009.

Seguin, A.; Bertho, Y.; Martinez, F.; Crassous, J.; Gondret, P. Experimental velocity fields and forces for a cylinder penetrating into a granular medium. **Phys. Rev. E**, v. 87, p. 012201, Jan 2013.

Seguin, A.; Bertho, Y.; Darbois Texier, B. Penetrating a granular medium by successive impacts. **Phys. Rev. E**, v. 106, p. 054904, 2022.

Seguin, A.; Coulais, C.; Martinez, F.; Bertho, Y.; Gondret, P. Local rheological measurements in the granular flow around an intruder. **Phys. Rev. E**, v. 93, n. 1, p. 012904, 2016.

Solano-Altamirano, J. M.; Caballero-Robledo, G. A.; Pacheco-Vázquez, F.; Kamphorst, V.; Ruiz-Suárez, J. C. Flow-mediated coupling on projectiles falling within a superlight granular medium. **Phys. Rev. E**, v. 88, p. 032206, Sep 2013.

Speedy, R. J. Glass transition in hard disc mixtures. **J. Chem. Phys.**, v. 110, n. 9, p. 4559–4565, 1999.

Stephens, M. **“Spin” Leaves Its Mark on Some Meteorite Craters**. 2023. <https://physics.aps.org/articles/v16/s166>. Accessed September 03, 2024.

Stone, M. B.; Barry, R.; Bernstein, D. P.; Pelc, M. D.; Tsui, Y. K.; Schiffer, P. Local jamming via penetration of a granular medium. **Phys. Rev. E**, v. 70, p. 041301, Oct 2004.

Sun, B.; Wei, S.; Yang, L.; Li, P.; Tong, S. Optimizing of particle accelerated rotor parameters using the discrete element method. **Sci. Rep.**, v. 13, n. 1, p. 18878, 2023.

Takehara, Y.; Fujimoto, S.; Okumura, K. High-velocity drag friction in dense granular media. **EPL**, v. 92, n. 4, p. 44003, 2010.

Takehara, Y.; Okumura, K. High-velocity drag friction in granular media near the jamming point. **Phys. Rev. Lett.**, v. 112, p. 148001, 2014.

Takkk. **No name - Pharmaceutics**. <https://commons.wikimedia.org/wiki/File:Pharmaceutic.jpg>. [Licensed under Creative Commons Attribution-Share Alike 3.0 Unported, Wikimedia Commons], Accessed August 13, 2024.

Tang, J.; Behringer, R. How granular materials jam in a hopper. **Chaos**, v. 21, n. 4, 2011.

Darbois Texier, B.; Bertho, Y.; Gondret, P. Downslope granular flow through a forest of obstacles. **Phys. Rev. Fluids**, v. 8, p. 034303, 2023.

To, K.; Lai, P.-Y.; Pak, H. Jamming of granular flow in a two-dimensional hopper. **Phys. Rev. Lett.**, v. 86, n. 1, p. 71, 2001.

Tordesillas, A. Force chain buckling, unjamming transitions and shear banding in dense granular assemblies. **Philos. Mag.**, v. 87, n. 32, p. 4987–5016, 2007.

Tordesillas, A.; Hilton, J. E.; Tobin, S. T. Stick-slip and force chain evolution in a granular bed in response to a grain intruder. **Phys. Rev. E**, v. 89, p. 042207, Apr 2014.

Torquato, S.; Truskett, T. M.; Debenedetti, P. G. Is random close packing of spheres well defined? **Phys. Rev. Lett.**, v. 84, n. 10, p. 2064, 2000.

Tripura, B. K.; Kumar, S.; Anyam, V. K. R.; Reddy, K. A. Drag on a circular intruder traversing a shape-heterogeneous granular mixture. **Phys. Rev. E**, v. 106, p. 014901, Jul 2022.

Tsimring, L. S.; Volfson, D. **Powders and Grains 2005**. [S.l.]: A.A. Balkema, 2005. 1215–1223 p.

Ucgul, M.; Fielke, J. M.; Saunders, C. 3D DEM tillage simulation: Validation of a hysteretic spring (plastic) contact model for a sweep tool operating in a cohesionless soil. **Soil Till. Res.**, v. 144, p. 220–227, 2014.

Ucgul, M.; Fielke, J. M.; Saunders, C. Three-dimensional discrete element modelling of tillage: Determination of a suitable contact model and parameters for a cohesionless soil. **Biosyst. Eng.**, v. 121, p. 105–117, 2014.

Ucgul, M.; Fielke, J. M.; Saunders, C. Three-dimensional discrete element modelling (dem) of tillage: Accounting for soil cohesion and adhesion. **Biosyst. Eng.**, v. 129, p. 298–306, 2015.

Uehara, J. S.; Ambroso, M. A.; Ojha, R. P.; Durian, D. J. Erratum: Low-speed impact craters in loose granular media [phys. rev. lett.prltao0031-9007 90, 194301 (2003)]. **Phys. Rev. Lett.**, v. 91, p. 149902, Oct 2003.

Uehara, J. S.; Ambroso, M. A.; Ojha, R. P.; Durian, D. J. Low-speed impact craters in loose granular media. **Phys. Rev. Lett.**, v. 90, p. 194301, May 2003.

Umbanhowar, P.; Goldman, D. I. Granular impact and the critical packing state. **Phys. Rev. E**, v. 82, p. 010301, Jul 2010.

Vet, S. J. de; Bruyn, J. R. de. Shape of impact craters in granular media. **Phys. Rev. E**, v. 76, p. 041306, Oct 2007.

Vogel, G. **Unknown**. <https://pixabay.com/pt/photos/raiz-relva-natureza-crescimento-6742800/>. [Pixabay], Accessed August 13, 2024.

Walsh, A. M.; Holloway, K. E.; Habdas, P.; Bruyn, J. R. de. Morphology and scaling of impact craters in granular media. **Phys. Rev. Lett.**, v. 91, p. 104301, Sep 2003.

Wei, H.; Zhang, Y.; Zhang, T.; Guan, Y.; Xu, K.; Ding, X.; Pang, Y. Review on bioinspired planetary regolith-burrowing robots. **Space Sci. Rev.**, v. 217, p. 1–39, 2021.

Wieghardt, K. Experiments in granular flow. **Annu. Rev. Fluid Mech.**, v. 7, n. 1, p. 89–114, 1975.

Xiao, X.; Murphy, R. A review on snake robot testbeds in granular and restricted maneuverability spaces. **Robotics Auton. Syst.**, v. 110, p. 160–172, 2018.

Yao, Z.; Wang, J.-S.; Liu, G.-R.; Cheng, M. Improved neighbor list algorithm in molecular simulations using cell decomposition and data sorting method. **Comput. Phys. Commun.**, v. 161, n. 1-2, p. 27–35, 2004.

Ye, X.; Wang, D.; Zhang, X.; Zhang, C.; Du, W.; Su Xiyangand Li, G. Projectile oblique impact on granular media: penetration depth and dynamic process. **Granul. Matter**, v. 23, n. 48, 2021.

Ye, X.; Wang, D.; Zheng, X. Influence of particle rotation on the oblique penetration in granular media. **Phys. Rev. E**, v. 86, n. 6, p. 061304, 2012.

Ye, X.; Wang, D.; Zheng, X. Effects of density ratio and diameter ratio on penetration of rotation projectile obliquely impacting a granular medium. **Eng. Comput.**, v. 32, n. 4, p. 1025–1040, 2015.

Abed Zadeh, A.; Barés, J.; Brzinski, T. A.; Daniels, K. E.; Dijksman, J.; Docquier, N.; Everitt, H. O.; Kollmer, J. E.; Lantsoght, O.; Wang, D. *et al.* Enlightening force chains: a review of photoelasticimetry in granular matter. **Granul. Matter**, v. 21, p. 1–12, 2019.

Zadeh, A. A.; és, J. B.; Brzinski, T.; Daniels, K. E.; Dijksman, J.; Docqiuer, N.; Everitt, H.; Kollmer, J.; Lantsoght, O.; Wang, D.; Workamp, M.; Zhao, Y.; Zheng., H. **Photoelastic methods wiki**. 2018. <https://git-xen.lmgc.univ-montp2.fr/PhotoElasticity/Main/-/wikis/home>. Accessed October 5, 2024.

Zaikin, O.; Korablin, A.; Dyulger, N.; Barnenkov, N. Model of the relationship between the velocity restitution coefficient and the initial car velocity during collision. **Transp. Res. Proc.**, v. 20, p. 717–723, 2017.

Zhang, H.; Makse, H. Jamming transition in emulsions and granular materials. **Phys. Rev. E**, v. 72, n. 1, p. 011301, 2005.

Zhang, J.; Majmudar, T.; Tordesillas, A.; Behringer, R. Statistical properties of a 2d granular material subjected to cyclic shear. **Granul. Matter**, v. 12, n. 2, p. 159–172, 2010.

Zhang, T.; Goldman, D. I. The effectiveness of resistive force theory in granular locomotion. **Phys. Fluids**, v. 26, n. 10, 2014.

Zhang, T.; Qian, F.; Li, C.; Masarati, P.; Hoover, A. M.; Birkmeyer, P.; Pullin, A.; Fearing, R. S.; Goldman, D. I. Ground fluidization promotes rapid running of a lightweight robot. **Int. J. Robotic Res.**, v. 32, n. 7, p. 859–869, 2013.

Zheng, H.; Dijksman, J. A.; Behringer, R. P. Shear jamming in granular experiments without basal friction. **EPL**, v. 107, n. 3, p. 34005, 2014.

Zheng, H.; Wang, D.; Chen, D. Z.; Wang, M.; Behringer, R. P. Intruder friction effects on granular impact dynamics. **Phys. Rev. E**, v. 98, p. 032904, Sep 2018.

Zhou, Y. A theoretical model of collision between soft-spheres with hertz elastic loading and nonlinear plastic unloading. **Theor. Appl. Mech. Lett.**, v. 1, n. 4, p. 041006, 2011.

Zhu, H.; Zhou, Z.; Yang, R.; Yu, A. Discrete particle simulation of particulate systems: a review of major applications and findings. **Chem. Eng. Sci.**, v. 63, n. 23, p. 5728–5770, 2008.

Zuriguel, I.; Boudet, J.; Amarouchene, Y.; Kellay, H. Role of fluctuation-induced interactions in the axial segregation of granular materials. **Phys. Rev. Lett.**, v. 95, p. 258002, 2005.

Appendix

APPENDIX A – INTERACTIONS AT THE GRAINS SCALE

The contact force between two dry grains is usually decomposed into a normal and tangential reaction, which for particles large enough are dominated by the elastic repulsion (Hertz contact) and solid friction (Amontons-Coulomb's law), respectively (Andreotti *et al.*, 2011). When flowing, these materials are also subjected to inelastic collisions between the particles. A brief description of these interactions is given below.

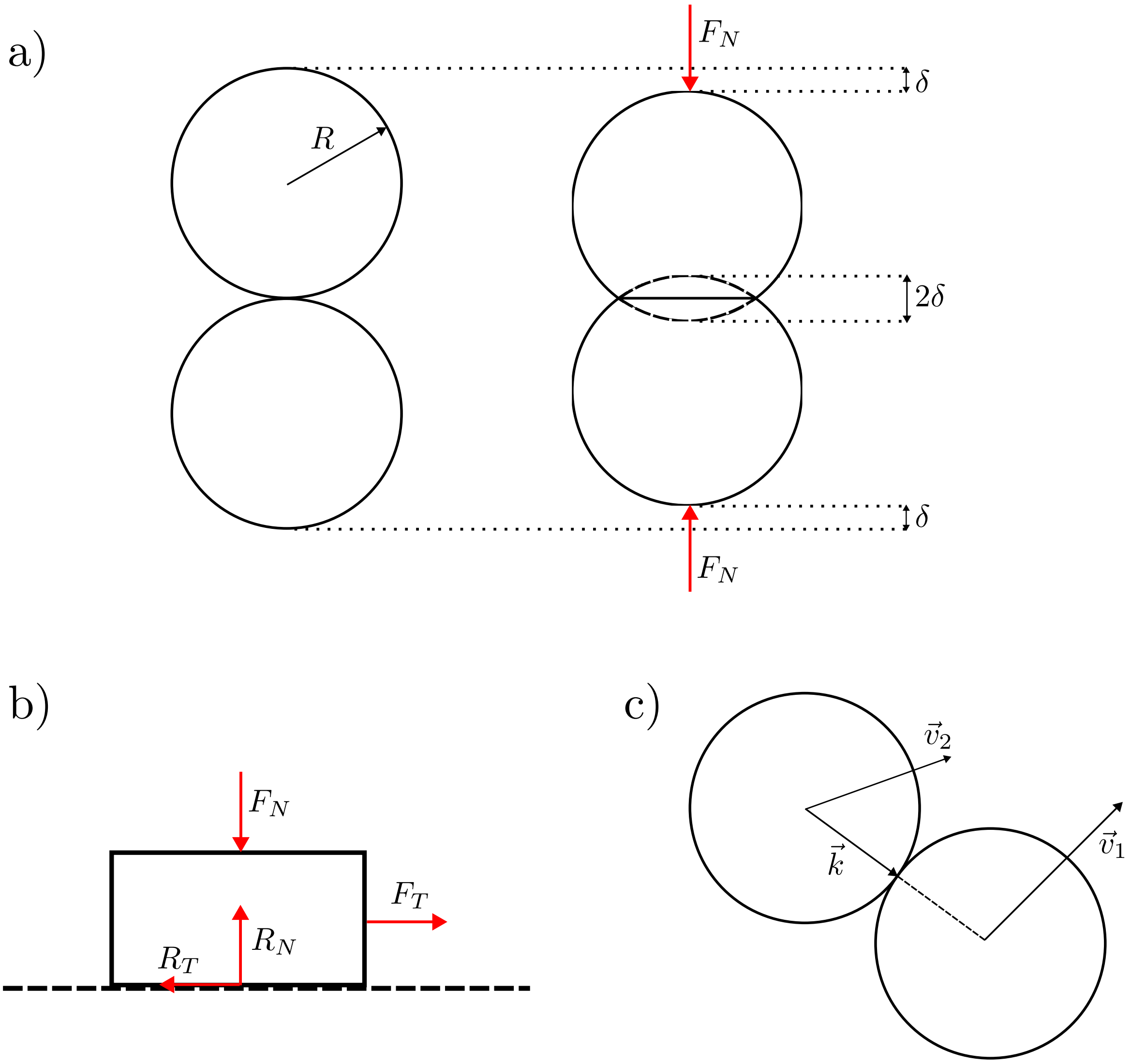

Figure A.1 – (a) Elastic contact between two spheres with a deformation of 2δ. (b) Free body diagram of a block sliding over a surface. (c) Collision between two particles. Images adapted from (Andreotti *et al.*, 2011).

A.1 Hertz elastic contact

The normal reaction force between two spherical grains of radius R forced against each other by a force F_N originates, at a first approximation, of the elastic repulsion during the deformation of the grains at the contact zone (Andreotti *et al.*, 2011). Considering the hypothesis that the two spheres are elastic and perfectly smooth (frictionless), the relation between the force F_N and the deformation δ (check Fig. A.1a) is given by:

$$F_N = \frac{E\sqrt{2R}}{3(1-\nu^2)}\delta^{3/2}, \tag{A.1}$$

where E is the particle Young modulus and ν is the Poisson coefficient.

Note that the force does not depend linearly on the deformation δ. Usually $\delta \ll 2R$, and small deformations are present for rigid grains, however, the hypothesis that the deformations remain in the elastic domain is less certain (Andreotti *et al.*, 2011).

A.2 Solid friction - Amontons-Coulomb's law

The tangential force between two grains comes from the friction between the surfaces in contact. By considering a block on top of a solid surface (Fig. A.1b), over which a normal ($\mathbf{F_N}$) and tangential ($\mathbf{F_T}$) force is applied, the laws of Amontons-Coulomb are given by (Andreotti *et al.*, 2011):

1. Starting from rest, to make the block move, it is necessary that the norm of the tangential reaction $\mathbf{R_T}$ reachs $|\mathbf{R_T}| = \mu_s|\mathbf{R_N}|$, where $\mathbf{R_N}$ is the normal reaction and μ_s is the static friction coefficient between the two solids in contact. If there is no motion, the friction force $\mathbf{R_T}$ is unknown, and just the inequality $|\mathbf{R_T}| \leq \mu_s|\mathbf{R_N}|$ is verified;

2. If the block is moving, the friction force is given by $|\mathbf{R_T}| = \mu_d|\mathbf{R_N}|$, where μ_d is the dynamic friction coefficient between the two solids in contact, and it is in the direction opposite to the block's velocity;

3. The constants μ_s and μ_d depend only on the nature of the materials in contact, with typically $1 > \mu_s > \mu_d > 0.1$.

A.2.1 Stick-slip motion

One important phenomenon associated with friction in granular materials is the stick-slip motion, where the material alternates between phases of sticking (no movement) and sliding (sudden movement). It usually occurs due to the intermittent rearrangement of force chains. When external forces are applied, these force chains resist movement until the stress exceeds a critical threshold. Once the threshold is exceeded, the structure of the granular material breaks down locally, resulting in a sliding event. This may be followed by a period of sticking, where the granular medium reorganizes and the force chains reform before the next sliding event occurs (Kozlowski *et al.*, 2019; Carlevaro *et al.*, 2020).

A.3 Inelastic collisions between two particles

Consider two identical spherical particles of mass m, radius R and velocities $\mathbf{v_1}$ and $\mathbf{v_2}$ (Fig. A.1c) experiencing a frontal collision, the impact is inevitably followed by a loss of kinetic energy and the velocities of the sphere after the impact $\mathbf{v'_1}$ and $\mathbf{v'_2}$ are always smaller than those previous to the impact, with the relation between these velocities given by (Andreotti *et al.*, 2011):

$$(\mathbf{v'_2} - \mathbf{v'_1}) \cdot \mathbf{k} = -\epsilon(\mathbf{v_2} - \mathbf{v_1}) \cdot \mathbf{k}, \tag{A.2}$$

where $\mathbf{k}$ is the unit vector connecting the center of the particles during the impact and ϵ is the restituent coefficient.

For smooth spheres, the velocities after impact are written as (Andreotti *et al.*, 2011):

$$\mathbf{v'_1} = \mathbf{v_1} + \frac{1+\epsilon}{2}[(\mathbf{v_2} - \mathbf{v_1}) \cdot \mathbf{k}]\mathbf{k}, \tag{A.3}$$

$$\mathbf{v'_2} = \mathbf{v_2} - \frac{1+\epsilon}{2}[(\mathbf{v_2} - \mathbf{v_1}) \cdot \mathbf{k}]\mathbf{k}, \tag{A.4}$$

And the variation in kinetic energy ΔE_c during the collision is (Andreotti *et al.*, 2011):

$$\Delta E_c = -\frac{m}{4}(1-\epsilon^2)[(\mathbf{v_2} - \mathbf{v_1}) \cdot \mathbf{k}]^2. \tag{A.5}$$

APPENDIX B – FABRIC TENSOR $\hat{R}$

The fabric tensor is a mathematical tool used to describe the structure of a granular material by quantifying the orientation and distribution of contacts between particles. In a granular assembly, each contact between two particles contributes to the overall organization of the material, and the fabric tensor is derived from these contacts. Mathematically, it is expressed as (Lätzel *et al.*, 2000; Bi *et al.*, 2011):

$$\hat{R} = \frac{1}{N} \sum_{i \neq j} \frac{\mathbf{r}_{ij}}{|\mathbf{r}_{ij}|} \otimes \frac{\mathbf{r}_{ij}}{|\mathbf{r}_{ij}|}, \tag{B.1}$$

where N is the number of non-rattler particles (particles with at least two contacts), $\mathbf{r}_{ij}$ is the contact vector from the center of particle i to the contact between particles i and j, and $\otimes$ denotes the vector outer product. For two particles in contact, the outer product $\mathbf{n}_{ij} \otimes \mathbf{n}_{ij}$, where $\mathbf{n}_{ij} = \mathbf{r}_{ij}/|\mathbf{r}_{ij}|$ is a unit vector, gives a tensor that captures how much the contact is oriented in various directions. In 2D, for $\mathbf{n} = [n_x, n_y]$, the outer product is:

$$\mathbf{n}_{ij} \otimes \mathbf{n}_{ij} = \begin{bmatrix} n_x^2 & n_x n_y \\ n_y n_x & n_y^2 \end{bmatrix} \tag{B.2}$$

This matrix describes how the contact vector $\mathbf{n}_{ij}$ contributes to the material's structure. Each entry in this matrix reflects how much the contact aligns with the x or y directions, both individually (diagonal terms) and in combination (off-diagonal terms): diagonal elements (e.g., n_x^2) reflect contact alignment along the principal axes, while off-diagonal terms (e.g., $n_x n_y$) represent cross-axis interactions. The structure of the granular material can vary between isotropic and anisotropic states, depending on the orientation of the contacts. If contacts are randomly oriented, the sum of the outer products will yield an isotropic fabric tensor, meaning all directions contribute equally, with no directional bias. If contacts are aligned in specific directions (e.g., due to external forces like compression or shear), the fabric tensor becomes anisotropic, indicating that some directions are more dominant than others.

The sum of the outer products over all N_c contacts provides a macroscopic description of the contact network's distribution. The resulting fabric tensor offers a statistical representation of contact orientation across the entire granular material. For example, in a material undergoing vertical compression, more contacts will form along the vertical axis, and the fabric tensor will reflect this anisotropy by showing a larger value in the direction of compression. Similarly, in simple shear, the contacts reorient along the shear direction, leading to a fabric tensor that captures this directional bias.

The diagonal elements of the fabric tensor ($\hat{R}_{xx}$ and $\hat{R}_{yy}$), represent the strength of contact alignment along the principal axes. If $\hat{R}_{xx} \gg \hat{R}_{yy}$, it indicates that most contacts are aligned in the x direction, suggesting anisotropy in the material's contact network. The off-diagonal elements ($\hat{R}_{xy}$ and $\hat{R}_{yx}$), capture the correlation between different directions. If $\hat{R}_{xy}$ is large, it shows that contacts are not purely aligned with the x or y axis, but skewed between them, contributing to overall anisotropy.

When the fabric tensor is diagonalized, we obtain its eigenvalues and eigenvectors, which provide a clear physical interpretation of the internal structure of granular materials. The eigenvectors represent the principal directions of the contact network, indicating the directions along which the contacts (or force chains) are most aligned. In 2D, the fabric tensor has two eigenvectors corresponding to two principal directions of alignment. The eigenvalues, on the other hand, represent the magnitude of contact alignment in each of these principal directions. A larger eigenvalue indicates stronger alignment of contacts along the associated eigenvector, meaning more contacts are concentrated in that direction. Conversely, a smaller eigenvalue indicates weaker alignment, with fewer contacts oriented along that direction. With the eigenvalues R_1 and R_2 of the tensor $\hat{R}$, we can compute the average number of contacts per particle $Z = R_1 + R_2$ and the anisotropy of the contact network $\rho = R_1 - R_2$ (Bi *et al.*, 2011).

The sum of the eigenvalues represents the total contribution of contact alignment in all directions. This sum is related to the mean contact number Z, which is the average number of contacts per particle. The trace of the fabric tensor (the sum of its diagonal components) is proportional to the mean contact number. This reflects the material's overall connectivity, with a larger sum indicating a higher number of contacts and a more interconnected granular assembly. The difference between the eigenvalues measures the anisotropy ρ of the material. If the eigenvalues are all equal, the material is isotropic, with contacts uniformly distributed in all directions. When the eigenvalues differ, the material becomes anisotropic, showing a directional preference in its contact structure. The larger the difference between eigenvalues, the more pronounced the anisotropy.

For example, in 2D: if the eigenvalues R_1 and R_2 are equal, the material is isotropic; if $R_1 \neq R_2$, the material is anisotropic, with more contacts aligned along one principal direction.

The difference R_1 - R_2 quantifies this anisotropy.

In an isotropic material, each particle has roughly the same number of contacts, and these contacts are evenly distributed in all directions. However, under external loading (e.g., compression or shear), the contact network becomes anisotropic, with more contacts forming in specific directions to resist the applied forces. The sum of the eigenvalues of the fabric tensor still reflects the total number of contacts, while the difference between the eigenvalues captures the directional bias introduced by the loading. For example: under vertical compression, more contacts form in the vertical direction, leading to a fabric tensor with a larger eigenvalue corresponding to the vertical axis. The sum of the eigenvalues increases as more contacts form, and the difference between the eigenvalues grows, reflecting the anisotropy caused by the external load. In simple shear, contacts realign with the shear direction, and the fabric tensor becomes anisotropic. The eigenvalue associated with the shear direction increases, while those in other directions may decrease. Off-diagonal terms may also become significant, reflecting the complex interactions between the directions under shear. In both cases, the sum of the eigenvalues remains related to the mean contact number, while the difference between the eigenvalues provides a measure of anisotropy.

Annex

ANNEX A – ADDITIONAL GRAPHICS OF THE EVOLUTION OF SOME FABRIC TENSOR $\hat{R}$ QUANTITIES

Additional graphics of the evolution of the mean number of contacts per particle Z, the number of non-rattler particles N, and anisotropy level ρ for the different cases presented in Sec. 4.1.2 and illustrated in Fig. (4.14) are given below.

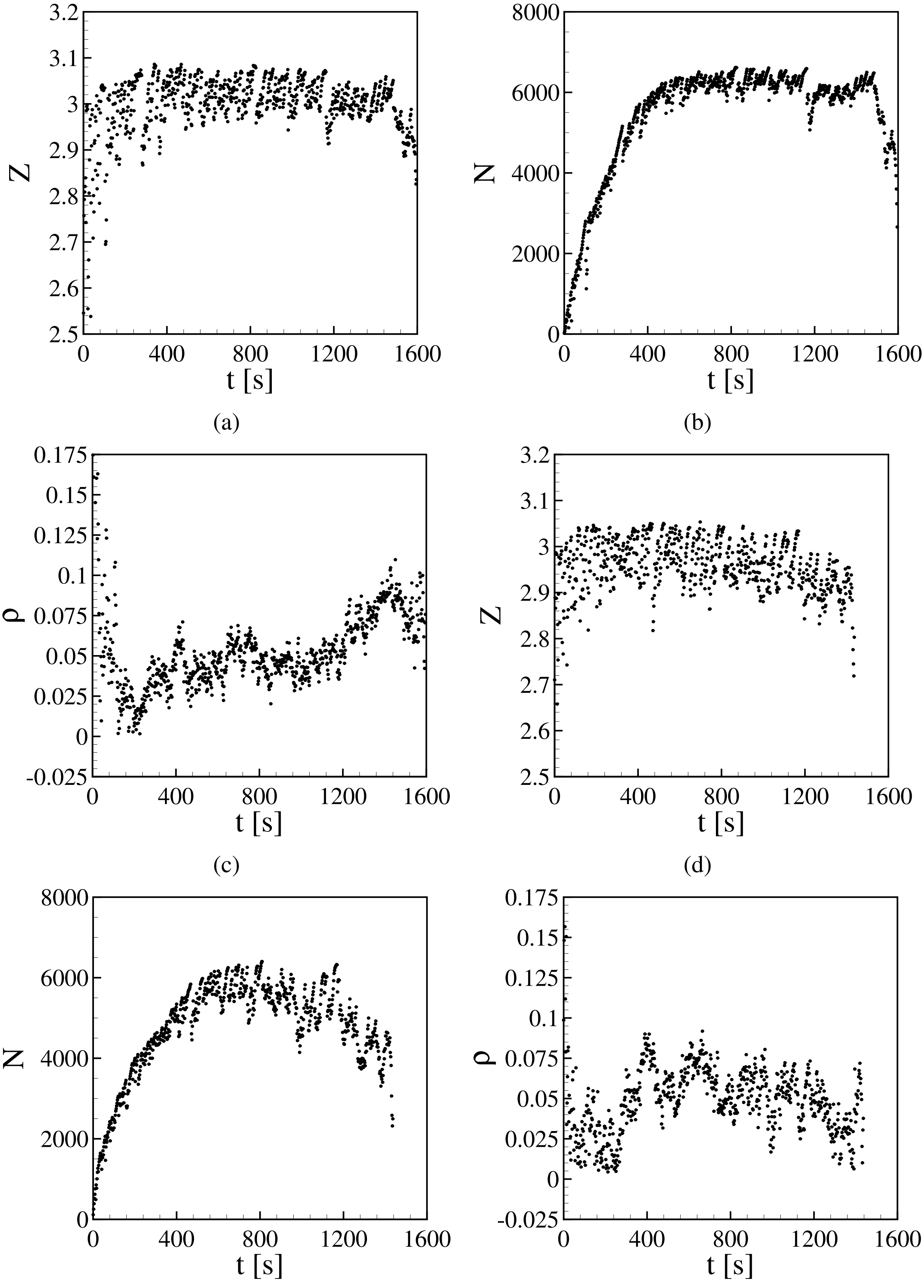

(a) (b) (c) (d) (e) (f)

Figure A.1 – Time evolution of [(a) , (d)] the mean number of contacts per particle Z; [(b) , (e)] number of non-rattler particles N; and [(c) , (f)] anisotropy level ρ for duos in configuration of type IV. (a)-(c) correspond to Fig. (4.22c), and (d)-(f) correspond to Fig. (4.22d). $\phi = 0.76$. Images taken from (Carvalho; Franklin, 2022b).

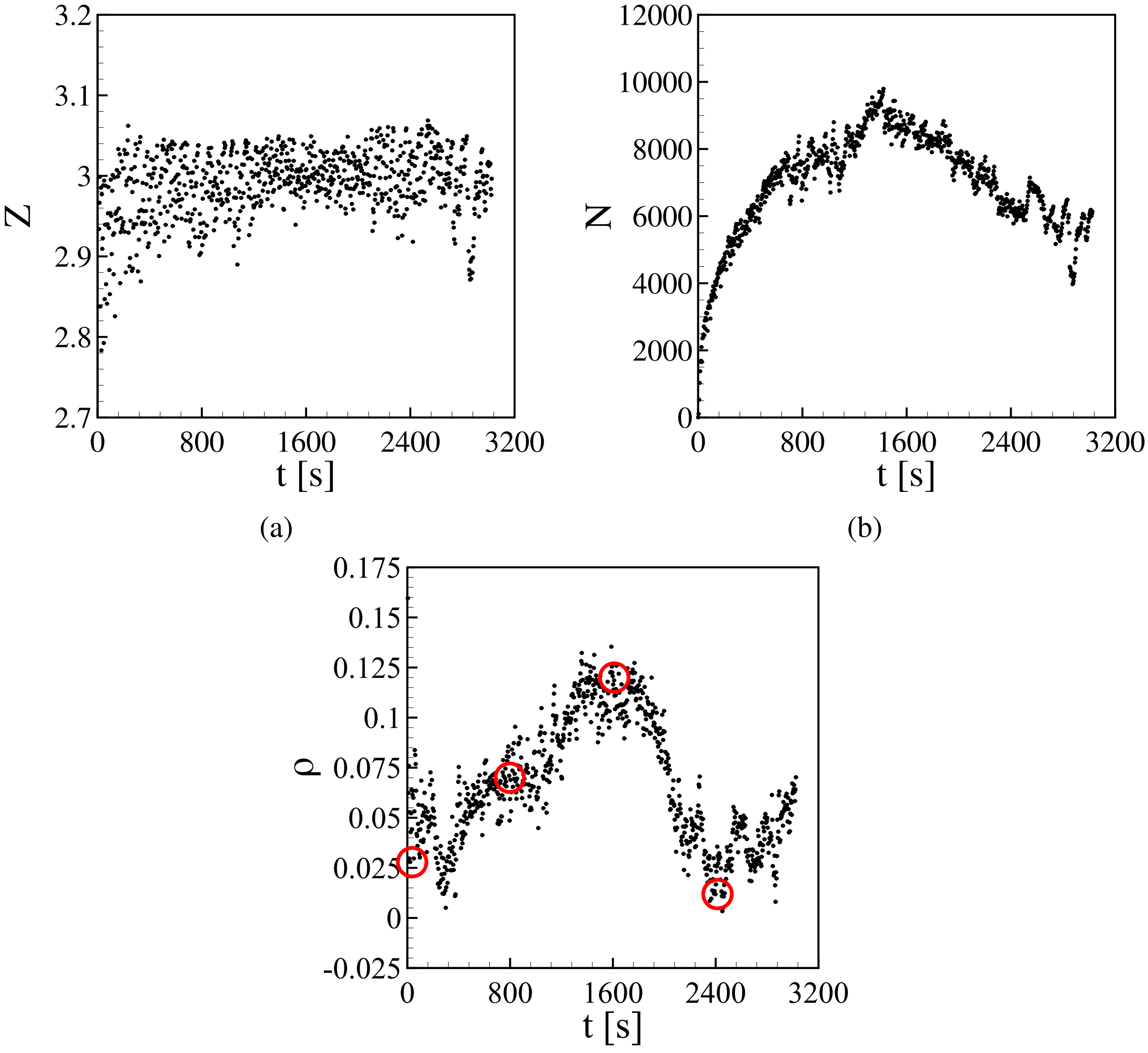

(a)

(b)

(c)

Figure A.2 – Time evolution of (a) the mean number of contacts per particle Z; (b) number of non-rattler particles N; and (c) anisotropy level ρ for trios in configuration of type I. The figures correspond to Fig. (4.24b) and ϕ = 0.76. Snapshots of the intruders and grains at the instants marked up in figure (c) are shown in Fig. A.3. Images taken from (Carvalho; Franklin, 2022b).

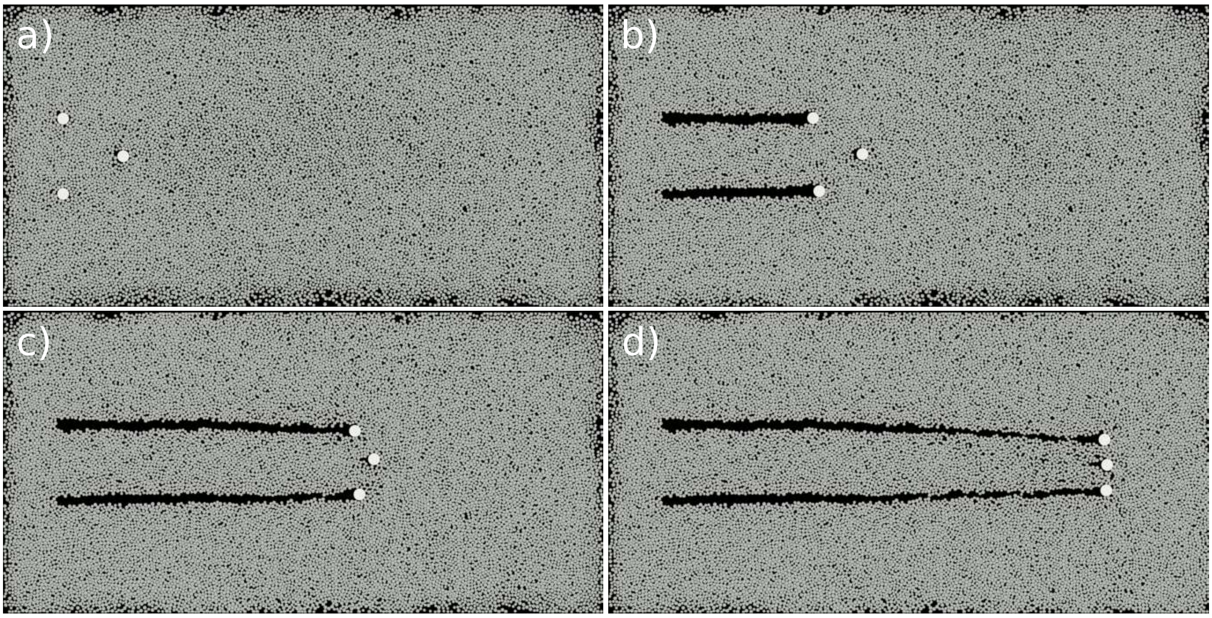

Figure A.3 – Snapshots showing the positions of the intruders and grains at the instants marked up in Fig. A.2. Figures (a) to (d) follow the temporal sequence. Images taken from (Carvalho; Franklin, 2022b).

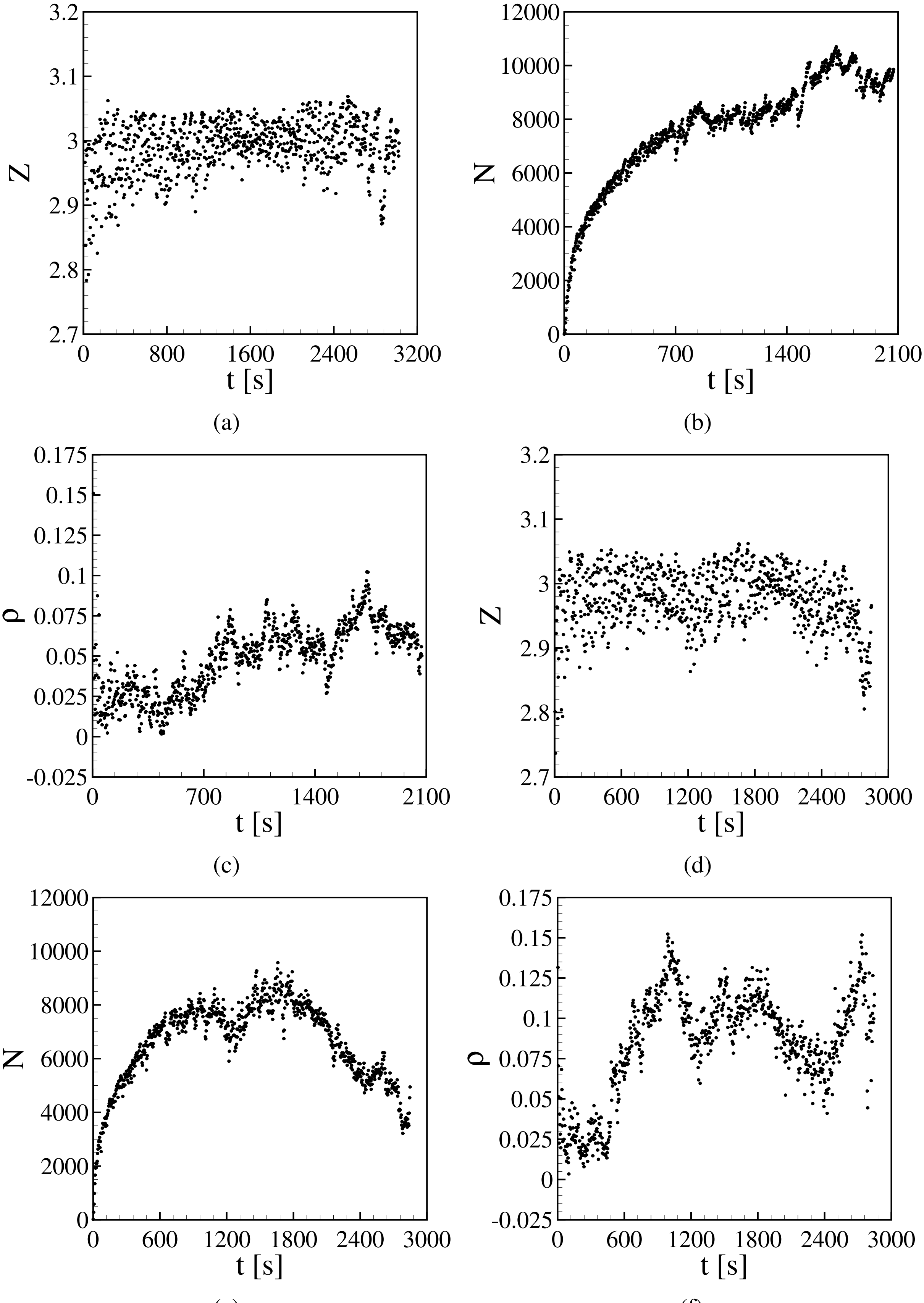

(a) (b)

(c) (d)

(e) (f)

Figure A.4 – Time evolution of [(a) , (d)] the mean number of contacts per particle Z; [(b) , (e)] number of non-rattler particles N; and [(c) , (f)] anisotropy level ρ for trios in configuration of type I. (a)-(c) correspond to Fig. (4.24)a, and (d)-(f) correspond to Fig. (4.24)c. $\phi = 0.76$. Images taken from (Carvalho; Franklin, 2022b).

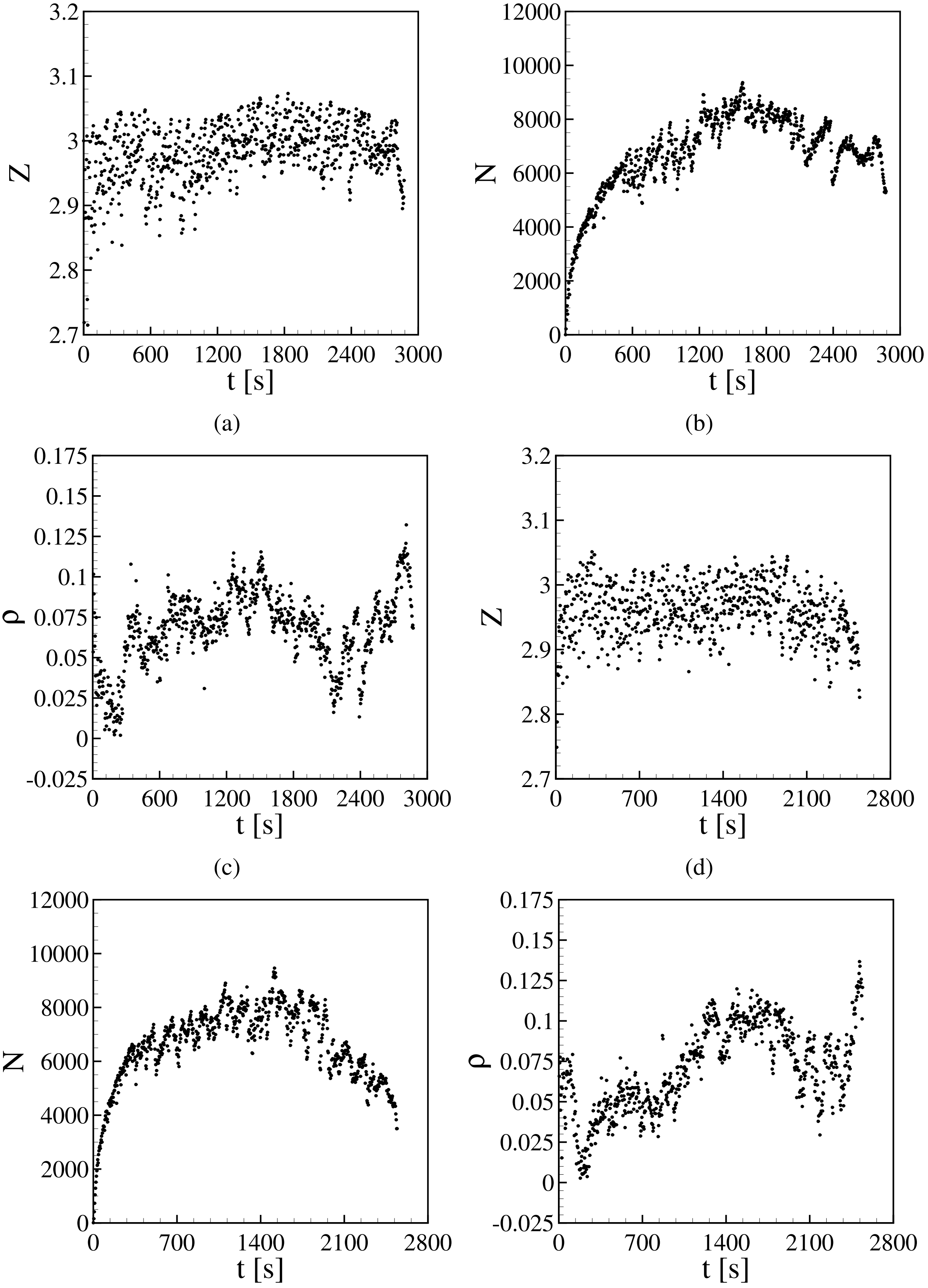

(a) (b)

(c) (d)

(e) (f)

Figure A.5 – Time evolution of [(a) , (d)] the mean number of contacts per particle Z; [(b) , (e)] number of non-rattler particles N; and [(c) , (f)] anisotropy level ρ for trios in configuration of type II. (a)-(c) correspond to Fig. (4.24)d, and (d)-(f) correspond to Fig. (4.24e). $\phi = 0.76$. Images taken from (Carvalho; Franklin, 2022b).

ANNEX B – RESULTS OBTAINED FOR ROTATING PROJECTILES WITH DIFFERENT ANGULAR VELOCITIES

Table B.1 – Results for rotating projectiles, for different angular velocities $\vec{\omega}$. In the simulations, $\phi = 0.554$ and $h = 0.1$ m. In the table, ω_x, ω_y and ω_z are, respectively, the x, y and z components of $\vec{\omega}$, K_ω/K_v is the ratio of rotational to linear kinetic energies, δ is the penetration depth, H is the drop distance, D_c is the crater diameter, and α_x, α_y and α_z are the total revolution angles in the x, y and z directions, respectively, that the projectile effectuate after colliding with the bed.

ω_x [rad/s]	$-\omega_y$ [rad/s]	$-\omega_z$ [rad/s]	$\%(K_\omega/K_v)$	δ [m]	H [m]	D_c [m]	α_x [deg]	α_y [deg]	α_z [deg]
0	0	0	0.00	0.01557	0.11557	0.036518	2.0383	2.9477	-0.8956
0	66.03	0	5.00	0.016	0.116	0.035843	-0.2620	85.5668	3.2127
0	93.38	0	10.00	0.01658	0.11658	0.036969	1.0113	129.2425	-0.3182
0	147.65	0	25.00	0.01737	0.11737	0.037255	6.4758	251.5411	5.9961
0	186.76	0	40.00	0.01814	0.11814	0.03793	2.5180	364.6921	11.8591
0	208.81	0	50.00	0.0185	0.1185	0.038642	4.4041	435.9747	0.7824
0	228.74	0	60.00	0.01876	0.11876	0.039132	0.2990	515.2882	14.5778
0	255.73	0	75.00	0.01911	0.11911	0.039121	-7.2992	650.6434	11.7363
0	280.14	0	90.00	0.01934	0.11934	0.040275	12.1994	729.8618	9.0175
0	295.3	0	100.00	0.01955	0.11955	0.041756	-8.1795	818.4327	-1.4472
0	361.66	0	150.00	0.0204	0.1204	0.042735	-27.6934	1197.9582	18.9867
0	417.61	0	200.00	0.02091	0.12091	0.042501	-6.1338	1600.0990	35.6820
93.38	0	0	10.00	0.01592	0.11592	-	72.2799	-0.2211	4.9696
208.81	0	0	50.00	0.01786	0.11786	-	191.9507	-0.4330	5.0885
295.3	0	0	100.00	0.01899	0.11899	-	359.0656	-0.4052	2.0154
0	0	93.38	10.00	0.01598	0.11598	-	5.3938	0.7996	70.5628
0	0	208.81	50.00	0.01771	0.11771	-	2.4195	3.3089	195.7117
0	0	295.3	100.00	0.01877	0.11877	-	2.1327	6.9920	365.2602

ANNEX C – GRAYSCALE IMAGES FOR THE CRATERING PROCESS OF A COHESIVE (AGGREGATE) PROJECTILE

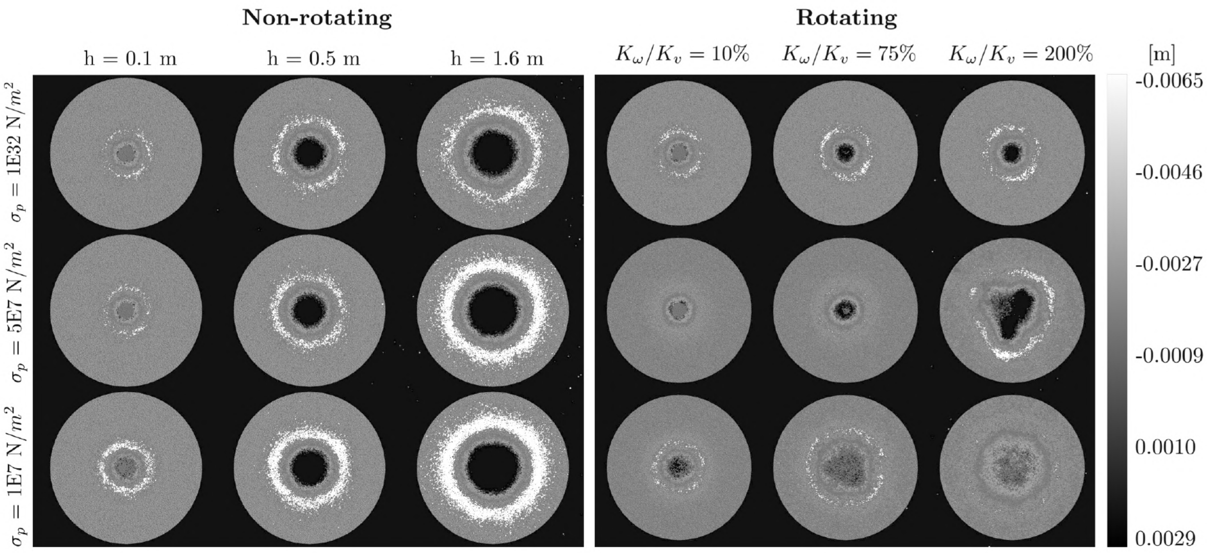

Figure C.1 – Same as Fig. 5.21. The colorbar (in gray scale) on the right shows the elevation of each grain from the undisturbed surface (coordinate pointing downwards). Images taken from (Carvalho *et al.*, 2023a).

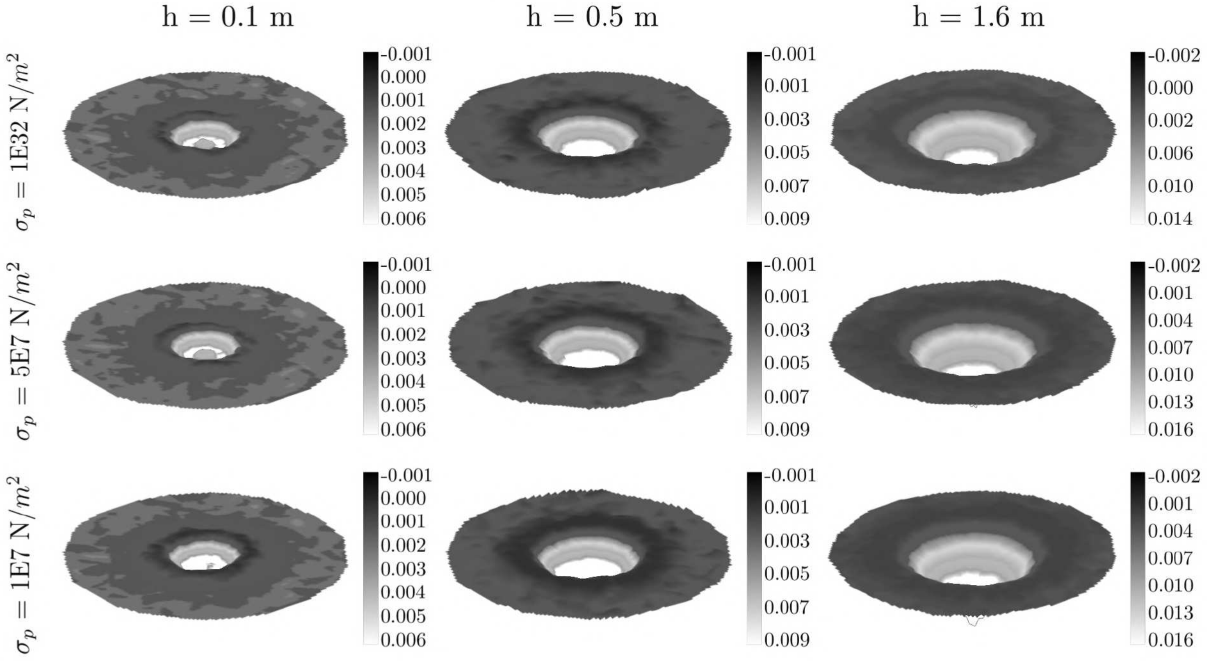

Figure C.2 – Same as Fig. 5.24. The colorbar (in gray scale) on the right of each panel shows the elevation from the undisturbed surface in m. Images taken from (Carvalho *et al.*, 2023a).

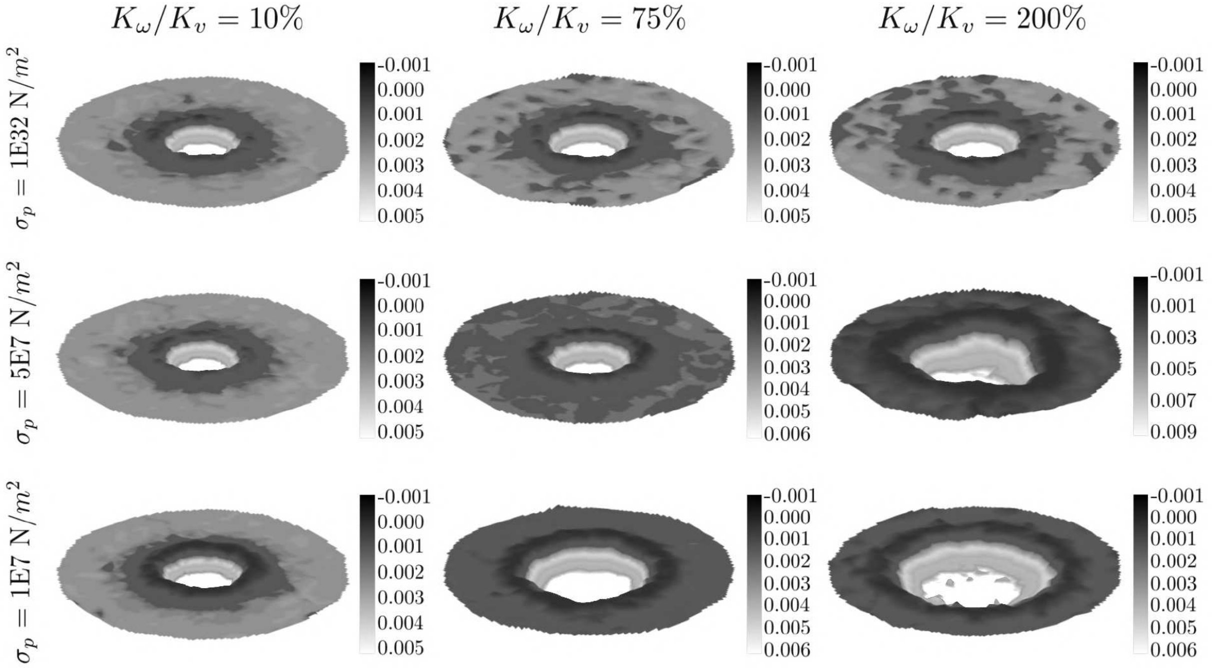

Figure C.3 – Same as Fig. 5.25. The colorbar (in gray scale) on the right of each panel shows the elevation from the undisturbed surface in m, and h = 0.1 m for all panels. Images taken from (Carvalho *et al.*, 2023a).